

# **Assessment of air quality in Northern China by using the COSMO-ART model in conjunction with satellite and ground-based data**

Zur Erlangung des akademischen Grades eines  
DOKTORS DER NATURWISSENSCHAFTEN  
von der Fakultät für  
Bauingenieur-, Geo- und Umweltwissenschaften  
des Karlsruher Instituts für Technologie (KIT)

genehmigte  
DISSERTATION

von

Dipl.-Geogr. Stefanie Ines Schrader

aus

Ulm

Tag der mündlichen Prüfung: 11.07.2014  
Referent: PD Dr. Stefan Norra  
Korreferent: Prof. Dr. Klaus Schäfer



# Content

<b>Content</b> .....	<b>III</b>
<b>Abstract</b> .....	<b>VII</b>
<b>Zusammenfassung</b> .....	<b>IX</b>
<b>1 State of the Art</b> .....	<b>12</b>
1.1 Aerosol characteristics in Northern China .....	12
1.1.1 Mineral dust.....	13
1.1.2 Anthropogenic aerosols.....	16
1.1.3 Impact of aerosols on climate, visibility, air quality and health .....	16
1.1.4 Air quality in Beijing .....	18
1.2 Satellite-based measurement of aerosol .....	20
1.3 Aerosol modeling .....	21
1.4 Scope of the present work .....	22
<b>2 Methodology</b> .....	<b>26</b>
2.1 Methodological approach .....	26
2.2 Data .....	27
2.2.1 Ground-based measurement data.....	27
2.2.1.1 Meteorological data.....	28
2.2.1.2 PM <sub>10</sub> , PM <sub>2.5</sub> and anthropogenic trace gas data.....	28
2.2.2 Satellite data .....	29
2.2.2.1 AOD .....	30
2.2.2.2 Passive sensors .....	30
2.2.2.3 Active sensor – CALIOP-CALIPSO .....	32
2.2.3 The model system COSMO-ART.....	32
2.2.3.1 The weather forecasting model COSMO .....	33
2.2.3.2 Aerosols in COSMO-ART .....	33
2.2.3.3 Treatment of mineral dust in COSMO-ART.....	35
2.2.3.4 Aerosol distribution – transport and deposition .....	39
2.2.3.5 Radiation in COSMO-ART .....	41
2.2.3.6 Model handling .....	42
2.2.4 External input datasets for COSMO-ART .....	42
2.2.4.1 Meteorological data and background pollution data .....	42
2.2.4.2 Soil dataset.....	43
2.2.4.3 Anthropogenic emission inventory.....	43
2.3 Methodological constraints on data comparability .....	45
2.3.1 Comparison of model, ground-based and satellite-based data with different temporal and spatial scales .....	45
2.3.2 Effects of comparison of satellite derived and modelled AOD at different wavelengths .....	45

---

<b>3 Calibration and validation of the COSMO-ART mineral dust module and anthropogenic emission inventory</b> .....	<b>47</b>
3.1 Testing and calibration of the mineral dust module.....	47
3.1.1 Impact of parameter variations on dust emission fluxes – 1D-studies .....	47
3.1.2 Variability of dust emissions – 2D-sensitivity studies.....	51
3.2 Testing and adaption of the anthropogenic emission inventory.....	52
3.2.1 Diurnal variations of gaseous pollutants .....	52
3.2.2 Adaption of the anthropogenic emission inventory for the Olympic Summer Games case study .....	53
3.2.3 Effects of emission factor variations on gaseous pollutant concentrations.....	54
<b>4 Qualitative analysis of airborne mineral dust dynamics in Northern Chinese dust source regions using COSMO-ART in conjunction with satellite data</b> .....	<b>56</b>
4.1 Introduction.....	56
4.2 Case study, study domain, model set-up and data .....	57
4.3 Methodological approach for satellite and model image processing.....	58
4.4 Results .....	59
4.4.1 Characterization of the spatio-temporal variability of AOD in Northern China .....	59
4.4.1.1 Characterization of dust distribution by passive satellite AOD .....	59
4.4.1.2 Identification of active dust source regions.....	62
4.4.1.3 Simulation of dust distribution by COSMO-ART AOD.....	62
4.4.2 Application of satellite derived AOD for model validation .....	63
4.4.3 Simulation of dust emissions inside the source regions using COSMO-ART .....	68
4.4.4 Analysis of the vertical distribution of dust in the major dust source regions using COSMO-ART and CALIPSO spaceborne lidar data.....	69
4.4.5 Assessment of the impact of dust on air quality in the major source regions and dust storm type definition .....	72
4.5 Discussion.....	74
4.5.1 AOD variations of passive satellite sensors .....	74
4.5.2 Analysis of modelled and satellite derived total AOD variations .....	75
4.5.3 Analysis of modelled dust emissions during the case study.....	77
4.5.4 Analysis of the combined use of CALIPSO and COSMO-ART data for determination of aerosol types and vertical profiles.....	78
4.5.5 Alternative methods of near-ground PM <sub>x</sub> concentration determination by combined use of passive sensor and mixing layer height data .....	79
4.5.6 Air quality in Northeast Asian desert areas .....	80
4.6 Summary and conclusions.....	80
<b>5 In-depth study of airborne mineral dust mid-range transport in Northeast China and its impact on Beijing’s air quality using COSMO-ART and ground-based network data</b> .....	<b>83</b>
5.1 Introduction.....	83
5.2 Case study .....	85
5.3 Results .....	85
5.3.1 Mineral dust dynamics in Northern China .....	85

---

5.3.1.1	Simulation of mineral dust dynamics in Northern China.....	86
5.3.1.2	Analysis of dust mobilization in the source regions .....	88
5.3.2	Mid-range transport of mineral dust towards Beijing .....	91
5.3.2.1	Synoptic weather conditions .....	91
5.3.2.2	Horizontal movement of dust plumes .....	92
5.3.2.3	Vertical distribution of airborne dust .....	93
5.3.3	Assessment of the impact of mineral dust on air quality in Beijing .....	97
5.3.3.1	Mixing of dust with local particulate pollutants .....	97
5.3.3.2	Simulation of the spatial variability of PM <sub>10</sub> and PM <sub>2.5</sub> concentrations using COSMO-ART .....	99
5.3.3.3	Quantifying the impact of mineral dust on air quality .....	101
5.4	Discussion.....	106
5.4.1	Relating dust mobilization in Gobi Desert and wind conditions.....	106
5.4.2	Analyzing dust event definitions.....	107
5.4.3	Assessing the uncertainty of simulating meteorological fields .....	108
5.4.4	Relating the observed dust event transport route to existing classifications .....	110
5.4.5	Analyzing the influence of orography on dust distribution .....	110
5.4.6	Estimating orographic effects on dust impact on PM <sub>10</sub> and PM <sub>2.5</sub> .....	112
5.4.7	Assessing constraints which cause discrepancies between modelled and measured PM <sub>10</sub> and PM <sub>2.5</sub> concentrations .....	113
5.5	Summary and conclusions.....	115
<b>6</b>	<b>Assessment of air quality in Greater Beijing during the Olympic Summer Games in 2008 using COSMO-ART in conjunction with MODIS satellite data and ground-based measurements .....</b>	<b>119</b>
6.1	Introduction.....	119
6.2	Case study and model set-up .....	121
6.3	Results .....	122
6.3.1	Meteorological conditions during the Olympic Summer Games.....	122
6.3.1.1	Observed weather conditions.....	122
6.3.1.2	Comparison of modelled and observed weather conditions .....	125
6.3.2	Spatio-temporal distribution and variability of TSP, PM <sub>10</sub> and PM <sub>2.5</sub> concentrations .....	127
6.3.2.1	Spatio-temporal variability of AOD.....	127
6.3.2.2	Spatio-temporal distribution and variability of TSP, PM <sub>10</sub> , PM <sub>2.5</sub> concentrations and air mass origins .....	129
6.3.2.3	Comparison of modelled and observed TSP, PM <sub>10</sub> and PM <sub>2.5</sub> in Beijing .....	133
6.3.3	Composition of urban TSP, PM <sub>10</sub> and PM <sub>2.5</sub> .....	136
6.3.3.1	Relative chemical composition of urban aerosol in Beijing .....	137
6.3.4	Comparison of modelled and observed daily-mean atmospheric nitrate and sulfate concentrations .....	141
6.5	Discussion.....	143
6.5.1	Assessing the level of accuracy of modelled meteorological conditions and its impact on air quality .....	143
6.5.2	Defining horizontal distribution patterns of TSP, PM <sub>10</sub> and PM <sub>2.5</sub> concentrations .....	144
6.5.3	Air mass movement, topographic effects and aerosol distribution .....	145

---

6.5.4	Defining reasons for discrepancies of modelled and observed PM <sub>10</sub> and PM <sub>2.5</sub> concentration levels and its relative chemical compositions .....	147
6.5.5	Assessing effects of anthropogenic emission reductions on NO <sub>3</sub> <sup>-</sup> and SO <sub>4</sub> <sup>2-</sup> .....	150
6.5.6	Spatio-temporal distribution of modelled mineral dust and identification of source regions .....	152
6.6	Summary and conclusions.....	155
<b>7</b>	<b>Conclusions and Outlook.....</b>	<b>158</b>
7.1	Conclusions.....	158
7.2	Outlook.....	162
	<b>Appendix.....</b>	<b>163</b>
A	Visualization of dust storm movement .....	163
	<b>List of figures.....</b>	<b>164</b>
	<b>List of tables.....</b>	<b>172</b>
	<b>List of abbreviations.....</b>	<b>185</b>
	<b>Danksagung .....</b>	<b>187</b>
	<b>Erklärung .....</b>	<b>188</b>

## Abstract

The in-depth study about airborne dust dynamics and mid-range transport towards downwind regions in Northeastern China during the case study period shows that Beijing is affected by a moving dust storm event originating in the Central Chinese Deserts and Gobi Desert. Analyzing vertical atmospheric profiles of the dust storm shows two dust fronts moving on southeastern paths towards Beijing. The plume on the more southern path arrives first in Beijing, followed by the second front on the more northern path. After one day, both dust plumes merge and cover almost all of Northeastern China. Vertical profiles also show that dust transport is highly dynamic due to strong winds and topographic effects downwind the mountains surrounding Beijing. This strong dynamic leads to an uplift of dust up to 10 km, but most dust is still located near the ground.  $PM_{10}$  and  $PM_{2.5}$  concentrations in Beijing show a steep increase due to the airborne dust. A mixing of dust with anthropogenic particulates is not detected.

To date processes triggering air quality depletion in Northern China by geogenic and anthropogenic particulates are still not fully understood.

However, knowledge about these processes and the impact of particulates on Beijing's urban air quality can be enhanced by understanding the spatio-temporal dynamics and transport patterns of mid-range transported airborne mineral dust and local anthropogenic particulates during varying weather conditions.

Therefore, the scope of this work is an in-depth study of the spatio-temporal dynamics of mid-range transported mineral dust and locally produced anthropogenic particulates in Northern China during spring and summer. The aim of this investigation is to improve the understanding of dust emission and distribution within source regions and dust transport and its impact on air quality in downwind regions. In addition, interactions and physical mixing of dust with local anthropogenic particulates are investigated under varying weather conditions during a short-term summer episode.

The model system COSMO-ART is used in conjunction with data of passive and active satellite sensors and ground-based measurements. Two specific case studies during spring 2011 and summer 2008 are analyzed. The focus of the spring case study is the investigation of dust emission and distribution within the source regions, dust transport towards the regions located downwind and the impact of dust on air quality in Beijing. The summer case study is set within the period of the Olympic Summer Games. Anthropogenic particulates are modelled in addition to mineral dust to study the spatio-temporal variability and dynamical mixing of different kinds of particulates.

The analysis of modelled and satellite derived airborne dust within the dust source regions shows that there are continuously significant amounts of aerosol in the ambient air of the major Chinese and Mongolian Deserts. Aerosol-optical thickness (AOD) in these regions reaches values far beyond the global background. Modelled dust emission source strengths show that Kumtaq Desert, Taklimakan Desert and

Gobi Desert are active dust source regions during the study time. Vertical atmospheric profiles recorded by the spaceborne lidar system CALIPSO show that almost the whole amount of the atmospheric particulate loading consists of mineral dust and that most of these dust layers are located near the ground. This situation leads to a drastic decrease of air quality in these regions.

The in-depth study about airborne dust dynamics and mid-range transport towards downwind regions in Northeastern China during the case study period shows that Beijing is affected by a moving dust storm event originated in the Central Chinese Deserts and Gobi Desert. Analyzing the vertical profile of the dust storm shows two dust fronts moving on southeastern paths towards Beijing. The plume on the more southern pathway arrives first in Beijing, followed by the second front on the more northern pathway. After one day, both dust plumes merge and cover almost all of Northeastern China. Vertical atmospheric profiles show that dust transport is highly dynamic due to strong winds and topographic effects downwind of the mountains surrounding Beijing. This strong dynamic leads to an uplift of dust up to 10 km, but most dust is still located near the ground.  $PM_{10}$  and  $PM_{2.5}$  concentrations in Beijing show a steep increase due to the airborne dust. A mixing of dust with anthropogenic particulates is not detected.

Studying particulates in Beijing during the Olympic Summer Games shows that there are significant amounts of particulates in the urban atmosphere during this time. The particulate loading in Beijing in summer is a heterogeneous mixture of different kind of species. The most abundant species of TSP are secondary formed organic and anorganic particles ( $SOA$ ,  $NH_4^+$ ,  $SO_4^{2-}$ ,  $NO_3^-$ ) and mineral dust. In  $PM_{2.5}$  secondary particles and soot have highest amounts. These particulates show spatio-temporal variations with highest ratios of mineral dust during weather conditions when air masses are originated from Northwest. It is shown that the major Asian Deserts are also active in summer with a significant influence of mineral dust on Beijing air quality. Gobi Desert is identified as major source region. During weather conditions with air masses transported from south to east, anthropogenic species are dominating. Highest levels of TSP concentrations during these conditions are always found close to emission sources, whereas  $PM_{10}$  and  $PM_{2.5}$  concentrations show a much more regional distribution. Moreover, a distinct border between areas of high and low concentrations is identified for the area along the Taihang Mountains surrounding Beijing. They act as natural barrier towards anthropogenic air pollutant transport from polluted regions towards the west during weather conditions with low wind speeds.

On the basis of numerical simulations of airborne particulate load by a meso-scale chemistry-transport model and the use of satellite-based and ground-based data, the influence of Asian mineral dust on air quality in Beijing is found during spring and summer. However, during spring dust events, particulates of anthropogenic origin are less important in comparison to the Asian mineral dust, whereas anthropogenic particulate species always dominate during summer time. This result demonstrates the need of measures to reduce the anthropogenic emissions of particulates and precursor compounds.

## Zusammenfassung

Luftverschmutzung durch luftgetragene Partikel ist eines der größten Umweltprobleme in China. Hohe Emissionen partikel- und gasförmiger Schadstoffe der zahlreichen natürlichen und anthropogenen Quellen können in Verbindung mit unvorteilhaften Wetterlagen zu einer drastischen Verschlechterung der Luftqualität führen. Dabei gibt es zwei typische Situationen, (1) im Frühjahr, wenn in den Asiatischen Trockengebieten große Mengen loser Partikel durch starke Windböen vom Boden in die Luft und anschließend in Richtung der ostchinesischen Gebiete transportiert werden und (2) während stagnierender Wetterlagen im Sommer, in denen sich anthropogene Schadstoffe aus lokalen und regionalen Quellen in der städtischen Atmosphäre ansammeln. Beide Situationen bergen ein großes Gesundheitsrisiko für die Bevölkerung.

Die verursachenden Prozesse und Auslöser dieser starken Luftverschmutzungsepisoden durch geogene und anthropogene Partikel werden bis heute nicht vollständig verstanden.

Die Untersuchung der raumzeitlichen Dynamik und des Transportverhaltens dieser luftgetragenen Partikel unter dem Einfluss verschiedener Wetterlagen kann jedoch dazu beitragen, diese Prozesse und die Auswirkungen der Partikel auf die städtische Luftqualität besser zu verstehen.

Im Fokus dieser Arbeit steht deshalb eine eingehende Studie über die raumzeitliche Dynamik von ferntransportiertem Mineralstaub und lokal produzierten anthropogenen Partikeln in Nordchina im Frühjahr und Sommer. Diese Untersuchung hat das Ziel, die vorhandenen Kenntnisse über Prozesse der Mineralstaub-Emission und -Ausbreitung innerhalb der Quellgebiete sowie dessen Transports und Einfluss auf die Luftqualität in den Abluftgebieten zu verbessern. Zusätzlich sollen Interaktionen und physikalische Vermischungsprozesse von Mineralstaub mit anthropogenen Partikeln in der Atmosphäre unter wechselnden Wetterbedingungen analysiert werden.

Im Rahmen dieser Arbeit wird das Modell-System COSMO-ART zusammen mit passiven und aktiven Satellitendaten sowie Daten bodengebundener Messstationen verwendet. Dabei werden zwei spezifische Fallstudien im Frühjahr 2011 und im Sommer 2008 durchgeführt. Der Fokus der Frühjahrsstudie liegt dabei auf der Untersuchung von Emission und Ausbreitung von Mineralstaub innerhalb der Quellgebiete, dem Transport von Mineralstaub in die Abluftgebiete und dessen Einfluss auf die Luftqualität in Peking. Die Sommerstudie liegt im selben Zeitraum wie die 29. Olympischen Sommerspiele. In dieser Studie wird zusätzlich zu Mineralstaub auch die raumzeitliche Verbreitung anthropogener Partikel modelliert und deren dynamische Vermischung untersucht.

Die Frühjahrsstudie zeigt, dass sich über den Chinesischen und Mongolischen Wüsten eine dauerhafte Mineralstaubschicht befindet. Die modellierte und vom Satelliten erfasste Aerosol-optische Dicke (AOD) in diesen Gebieten übersteigt bei weitem die Werte des globalen Hintergrundes. Die Simulationen zeigen,

dass vor allem die Wüsten Kumtaq, Taklamakan und Gobi aktive Quellgebiete während des Untersuchungszeitraumes sind. In Vertikalprofilen, aufgenommen mit dem Satellitengetragenen Lidar an Bord von CALIPSO, ist zu sehen, dass fast der gesamte Anteil dieser atmosphärischen Partikel aus Mineralstaub besteht und dass sich der meiste Staub in Bodennähe befindet. Dadurch wird die Luftqualität in diesen Gebieten drastisch gesenkt.

Die eingehende Studie über die Dynamik und den Transport von Mineralstaub ins nordöstliche China zeigt, dass Peking im Zeitraum der Frühjahrsstudie durch einen wandernden Staubsturm aus den Zentralchinesischen Wüsten und der Wüste Gobi beeinflusst wird. Bei Betrachtung von Horizontalprofilen des Sturms, zeigt sich, dass der Staub durch zwei südöstlich ziehende Fronten nach Peking transportiert wird. Die südlichere Staubwolke erreicht dabei zuerst Peking, gefolgt von der nördlicheren Front. Anhand von Vertikalprofilen wird deutlich, dass der Staubtransport durch die hohen Windgeschwindigkeiten und topographischen Effekte im Lee der Bergketten um Peking sehr dynamisch ist. Diese hohe Dynamik führt dazu, dass sich Staub bis zu einer Höhe von 10 km ausbreiten kann, jedoch ist der Großteil noch immer in Bodennähe zu finden und hat damit einen starken Einfluss auf die Luftqualität. Der Mineralstaub verursacht einen starken Anstieg der  $PM_{10}$  und  $PM_{2.5}$  Konzentrationen in Peking. Eine Vermischung von Mineralstaub und anthropogenen Partikeln findet nicht statt.

Die Sommer Studie zeigt, dass auch während der Olympischen Sommer Spiele gewisse Mengen an Partikeln in der städtischen Atmosphäre von Peking zu finden sind. Diese städtischen Partikel sind eine heterogene Mischung aus verschiedensten Bestandteilen. Im Untersuchungszeitraum sind sekundär gebildete organische und anorganische Partikel ( $SOA$ ,  $NH_4^+$ ,  $SO_4^{2-}$ ,  $NO_3^-$ ) und Mineralstaub die häufigsten Bestandteile in TSP, während in  $PM_{2.5}$  neben sekundär gebildeten Partikeln vor allem Ruß vorkommt. Die prozentuale Zusammensetzung ist raum-zeitlichen Schwankungen unterworfen, wobei der Anteil von Mineralstaub während nordwestlicher Wetterlagen am größten ist. Dadurch wird deutlich, dass die Asiatischen Wüstengebiete auch im Sommer aktive Mineralstaubquellen darstellen und einen signifikanten Einfluss auf die Luftqualität in Peking haben. Wenn hingegen die Luftmassen hauptsächlich aus südlichen und östlichen Richtungen stammen, dominiert der Anteil anthropogener Bestandteile. Während solcher Wetterbedingungen sind höchste TSP Konzentrationen stets in Quellnähe zu finden, während  $PM_{10}$  und  $PM_{2.5}$  eine eher gleichmäßigere regionale Verteilung aufweisen. Des Weiteren kann eine deutliche räumliche Grenze zwischen hohen und niedrigen Konzentrationen im Bereich des Peking umgebenden Taihang Gebirges identifiziert werden. Der Höhenzug stellt insbesondere bei Wetterbedingungen mit schwachem Südost-Winden eine natürliche Barriere für die Ausbreitung atmosphärischer Schadstoffe aus den stark verschmutzten Gebieten in Richtung Westen dar.

In dieser Studie wird anhand von numerischen Partikel-Simulationen mittels eines meso-skaligen Chemie-Transport Modells und der Verwendung von satelliten- und bodengestützten Messdaten der

Einfluss von Asiatischem Mineralstaub auf die Luftqualität in Peking aufgezeigt. Mineralstaub ist sowohl im Frühjahr als auch im Sommer in der städtischen Atmosphäre zu finden. Dieser Anteil schwankt jedoch und ist vor allem während des Staubsturms im Frühjahr sehr groß, während im Sommer hauptsächlich anthropogene Schadstoffe dominieren. Diese Ergebnisse unterstreichen die Notwendigkeit, dass Maßnahmen zur Verringerung der anthropogenen Emissionen von Partikeln und Vorläufersubstanzen ergriffen werden.

# 1 State of the Art

Aerosols are small airborne particles originating from different kind of natural and anthropogenic sources. They are emitted directly into the atmosphere or can be formed in the ambient air by chemical reactions of gaseous precursors [Andreae et al., 2009]. Mineral dust is considered to be one of the most abundant primary aerosol types, regarding its environmental impact. Every year large quantities of dust are released from bare soils into the atmosphere. Strong winds induce mid and long-range transport of dust towards areas far away from the source regions [Prospero, 1999; McKendry et al., 2001]. Secondary formed aerosols are generally smaller in size and mainly accumulate in urban atmospheres or downwind of densely populated and industrialized areas [Husar et al., 1997]. Both aerosol types have direct and indirect effects on the Earth's radiation budget and the atmospheric hydrological cycle [Kaufman et al., 2002]. Besides these environmental effects, aerosols have a strong impact on air quality and the human health [Fenger, 1999; Pope, 2000; Colbeck and Lazaridis, 2010].

## 1.1 Aerosol characteristics in Northern China

Northern China is mainly dominated by two types of aerosols, mineral dust originating from natural deserts and desertified areas and secondary formed anthropogenic aerosols which are produced in and downwind of urbanized and industrialized areas.

As anthropogenic sources are negligible in the remote desert areas of Northwest China, mineral dust is the dominating air pollutant in these regions. Each year, several billion tons of mineral dust particles are emitted and remain in the air from seconds to weeks. When mineral dust is lifted to high altitudes, strong winds transport it to Eastern China or even to the American continent [McKendry et al., 2001; Kim, 2008; Wang et al., 2011]. The Chinese capital Beijing is located downwind of the widespread Asian dust regions. To date, the metropolitan region of Beijing is densely urbanized and populated, accommodating 19.6 million permanent residents in 2010. Beijing is surrounded by Hebei province and Tianjin municipality, accommodating 71.9 million, and 12.9 million permanent residents, respectively [NBSC, 2011]. The population of Beijing grew by 44% between 2000 and 2010 and estimates for the year 2050 predict the population to rise to 50 million permanent residents. Beijing's economy is still growing by 8-10% per year [WPR, 2013].

### 1.1.1 Mineral dust

#### *Source regions and emission rates*

China and South Mongolia are complex and heterogeneous dust regions, comprising large areas of sandy deserts, stony deserts (Gobi) and loess areas located between 35° to 54° N and 73° to 135° E. Major dust source regions are Gobi Desert, Taklimakan Desert, Badain Jaran, Tengger Desert, Ulan Buh Desert, Mu Us Sandy Land, Horqin Sandy Land and the Loess Plateau (see Figure 1). A region can be considered to be a dust source when the annual mean dust storm frequency exceeds 5 days per year [Xuan *et al.*, 2004]. The Chinese and Mongolian source regions can be classified into three types. Type 1 comprises deserts in dry agricultural areas, type 2 characterizes Gobi Deserts and deserts located on plateaus and type 3 comprehends all deserts and Gobi Deserts in topographical lows. Type 1 describes all desertified areas of Inner Mongolia, Horqin and Mu Us Sandy Land located in the east of China, type 2 deserts are the Central Chinese Deserts Badain Jaran, Tengger, Ulan Buh, Hexi corridor and Gobi in South Mongolia, and type 3 comprises Taklimakan Desert in West China [Xuan and Sokolik, 2002].

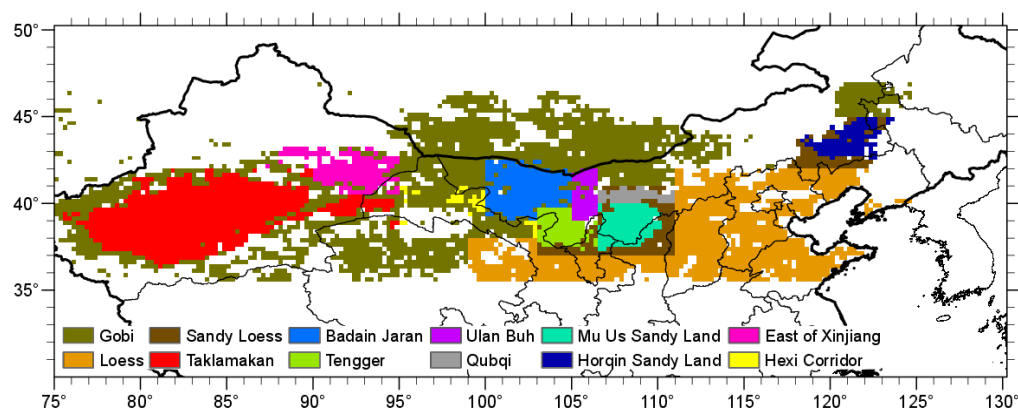


Figure 1: Desert areas in Northern China and Southern Mongolia according to Laurent *et al.* [2005].

China and Southern Mongolia are considered to be the second largest source for global dust emissions [Xuan and Sokolik, 2002]. An overview of current global dust emission estimates is given in Zender *et al.* [2004]. Estimated yearly dust emissions range from 1000 to 2150 Tg yr<sup>-1</sup> and the atmospheric dust burden ranges from 8 to 36 Tg. Tegen and Fung [1995] estimated global dust source to be 1222 Tg yr<sup>-1</sup>. The contribution of the different dust source regions to the global emissions and dust burden shows significant variations. Tanaka and Chiba [2006] estimated for the Chinese dust source regions emissions of 214 Tg yr<sup>-1</sup> and an atmospheric dust loading of 1.1 Tg. The total dust emission and dust load contribution of the Chinese Deserts accounts for 11% and 6% of the nine main dust source regions of the world (Africa, Arabian Peninsula, Central Asia, China, North and South America, and Australia). Luo *et al.* [2003] estimated annual dust emissions of the Chinese deserts of 54 Tg yr<sup>-1</sup>, accounting for 3.2% of the global

emission fluxes. *Xuan and Sokolik* [2002] calculated an annual mean PM<sub>10</sub> emission rate of all Chinese dust sources of 8.4 Tg yr<sup>-1</sup>. *Xuan et al.* [2004] estimated total PM<sub>10</sub> emissions of 10.4 Tg yr<sup>-1</sup> and total PM<sub>50</sub> emissions of 51.3 Tg yr<sup>-1</sup>.

About 70% of the dust loading in China originates from the Chinese dust sources, whereas 30% can be assigned to Mongolian source regions [*Tanaka and Chiba*, 2006]. The main dust emission areas in China are the Tarim Basin in the center of Taklimakan Desert and Badain Jaran Desert, accounting for about 21%, and 22% of the total Asian dust emissions, respectively. Gobi Desert accounts for 29% and the most eastern part of Taklimakan (Kumtaq Desert), Mu Us Sandy Land and Horqin each for a few percent [*Zhang et al.*, 2003b]. *Shao and Dong* [2006] propose that the Tarim Basin in the Central Taklimakan Desert and the Gobi Desert at the Chinese-Mongolian border are the most frequent dust sources in Northeast Asia. High dust frequencies also occur inside the Hexi Corridor, as it is the main transport pathway for dust from the Western and Central Chinese Deserts towards the East. *Shao and Dong* [2006] claim that there are no emissions from the Loess Plateau as they suppose it to be only a deposition area for dust but not an active source region. However, *Laurent et al.* [2005] consider the Loess plateau as a significant source region of dust emissions.

*Xuan and Sokolik* [2002] assume that the contribution among the desert areas show seasonal changes caused by wind speed and precipitation variations. In general, most dust events in China occur during spring, with a maximum frequency in April, accounting for 58% of all events in this season [*Sun et al.*, 2001]. Taklimakan has the highest contribution to the total dust emissions during spring and fall accounting for 69% among all desert areas [*Xuan and Sokolik*, 2002]. Weak dust events in Taklimakan Desert occur throughout the year, whereas heavy dust events show a maximum occurrence during May [*Shao and Dong*, 2006]. The deserts of Central China have a contribution of 30% in spring, 17% in fall, and much higher contribution in winter and summer with 70%, and 53%, respectively. Inner Mongolia and Horqin Sandy Land contribute only to small amounts up to 1% [*Xuan and Sokolik*, 2002]. Dust events in Gobi and the Central Chinese Deserts show highest frequencies in spring, with a maximum in April [*Shao and Dong*, 2006].

Further studies focusing on dust regions indicate that the contribution of naturally produced dust to the overall atmospheric dust burden became less over the last decades, as anthropogenic sources are increasing. Dust from anthropogenic sources originates from agricultural degraded areas, dried lakes like the Aral Sea or industrially used areas and construction zones [*Solomon*, 2007]. *Tegen and Fung* [1995] estimated the contribution of such anthropogenic dust to be 30-50% of the total atmospheric dust loading. In China the total area covered by deserts increased since 1960 between 2 and 7%. Especially the contribution of Inner Mongolia, Horqin Sandy Land and Mu Us Sandy Land increased over the last four decades due to desertification processes [*Zhang et al.*, 2003b]. Especially the region of Inner Mongolia is

highly desertified due to farming, improper use of water resources and over-grazing [Xuan and Sokolik, 2002]. Ongoing desertification of land and changing precipitation and circulation patterns could be the reason for increasing trends of dust event frequency since the 1980s described by Kim [2008].

### ***Distribution and deposition***

Dispersion of dust is initiated as soon as a specific threshold wind friction velocity is exceeded and particles are lifted up in the air. In the atmosphere dust is transported in varying altitudes from the source regions towards the surrounding. The distribution patterns of dust can be classified in four categories, (1) dust-in-suspension or widespread dust conditions describe dust which stays near the ground or source and visibility falls below 10 km; (2) during blowing dust conditions sand or dust is lifted up to higher altitudes than during widespread dust conditions and visibility is reduced to 1-10 km; (3) dust storms lift large amounts of particles in the air and reduce visibility to 200-1000 m; and (4) severe dust storms, when heavy wind raises extreme large amounts of particles and reduce visibility to less than 200 m [Shao and Dong, 2006]. Severe dust storms mainly occur in South and Inner Mongolia and less often in the Central and Eastern Chinese Deserts. However, dust storms which are less strong than severe ones but have higher frequencies mainly occur in the Tarim Basin and Inner Mongolia. Blowing-dust and widespread dust events occur mostly in Northeast China, Korea and Japan. Widespread dust events are often reported in the Tarim Basin, as wind speeds are much lower here due to its location in a topographic low [Shao and Dong, 2006].

Dust events in the Gobi and Central Chinese Deserts are mainly driven by strong low-pressure systems. Wind speeds during such events mainly range between 8-18 m s<sup>-1</sup>. Dust events in the Taklimakan Desert occur more often, even under weaker wind conditions. The lack of vegetation in the central areas of Taklimakan lead to a reduction of surface roughness and a low threshold wind friction velocity of 4 m s<sup>-1</sup>. Friction velocities over the Gobi and the Central Chinese Deserts are higher with values around 7 m s<sup>-1</sup>, because of the high amount of stones and gravel. Dust events in Taklimakan Desert are onset when (1) strong winds from northeast pass the eastern inlet and initialize dust uplift in the eastern and southeastern regions; (2) air flows over the Tian Mountains at the northern rim of the basin and initializes dust events in the north; (3) local winds exceed the threshold wind velocity and (4) convective systems trigger the formation of dust devils [Shao and Dong, 2006].

Xuan *et al.* [2004] classify the Chinese and Mongolian dust sources into two systems, the moving dust storm type originating mostly in the Central, Eastern and Mongolian Deserts and the stationary dust storm type typically occurring in Taklimakan Desert. Dust in Taklimakan Desert mainly stays local and is deposited in the source region due to the specific topographic conditions of the basin [Sun *et al.*, 2001; Xuan *et al.*, 2004]. However, under strong vertical wind speeds dust can be lifted up to higher altitudes and can be transported over long distances [Husar *et al.*, 2001; McKendry *et al.*, 2001; Sun *et al.*, 2001; Wang *et al.*, 2011]. Dust from the Gobi and Central Chinese Deserts are often transported near the ground in maximum

altitudes of 3000 m [Sun *et al.*, 2001]. Therefore the main deposition areas are located in North- and Southeast China, the Yellow Sea, Korea and Japan. The Loess Plateau between the Central Chinese Deserts and the Taihang Mountains west of Beijing is one of the main deposition areas for this dust.

There are four to five main dust routes over China [Sun *et al.*, 2001; Zhang *et al.*, 2003a]. The northeast path transports dust from the Horqin Sandy Land towards the south, the northerly Mongolia path brings dust from Mongolia to Northeast China and the northern desert path enables transport of dust from the Central Chinese Deserts and South Mongolia to the northeast of China [Zhang *et al.*, 2003a]. The western path follows the Hexi Corridor, which can be considered as the main transport pathway of mineral dust from the West Chinese Deserts towards the east. It is a narrow valley surrounded by high mountains in the south and the north. The corridor also has some smaller dust sources, due to the strong increase of aridity from east to west [Xuan and Sokolik, 2002].

### 1.1.2 Anthropogenic aerosols

Besides mineral dust, carbonaceous species such as elemental carbon (BC) and organic carbon (OC), and secondary formed particles such as nitrate ( $\text{NO}_3^-$ ), sulfate ( $\text{SO}_4^{2-}$ ) and ammonium ( $\text{NH}_4^+$ ) are the main contributors to the particle pollution in Beijing [Sun *et al.*, 2004; Chan and Yao, 2008]. Nitrate, sulfate and ammonium are formed by oxidation of gaseous precursors such as nitrogen oxides ( $\text{NO}_x$ ) sulfur dioxide ( $\text{SO}_2$ ), ammonia ( $\text{NH}_3$ ) and volatile organic compounds (VOC) [Zhang *et al.*, 2004]. Secondary particles are either formed locally or they are built-up during transport.

### 1.1.3 Impact of aerosols on climate, visibility, air quality and health

Aerosols have a direct impact on the climate system by scattering and absorbing long- and shortwave radiation. The radiative forcing of aerosols is driven by the wavelength dependent optical properties, the atmospheric concentration level and the vertical and horizontal distribution in the atmosphere [Solomon, 2007]. Scattering aerosols mainly have a negative radiative forcing, which leads to cooling of the atmosphere; whereas absorbing aerosols like black carbon exert a negative forcing at the top of the atmosphere (TOA) over dark surfaces such as forests and a positive effect over bright surfaces such as glaciers or deserts [Solomon, 2007]. Mixing of aerosols can alter the radiative forcing of the single aerosol types, as size, chemical composition and shape of the particles change. Furthermore, the heating or cooling effect of aerosol induces changes of atmospheric thermodynamics and dynamics [Solomon, 2007] which can cause semi-direct effects by altering relative humidity and cloud formation processes. The modeled direct radiative forcing of all atmospheric aerosol ranges between  $-0.2 (\pm 0.2)$  and  $0.4 \text{ W m}^{-2}$ ; whereas satellite-based measurements estimate the radiative forcing to be  $-0.55 \text{ W m}^{-2}$  with high regional

and local variability [Solomon, 2007]. The radiative forcing of dust over China is estimated to range between -1 to -14 W m<sup>-2</sup> in summer and fall, and -1 to -9 W m<sup>-2</sup> in winter and spring [Qian et al., 2003].

The indirect effect of aerosol on the climate system characterizes changes of cloud properties, formation processes, lifetime and precipitation. The indirect effect is mainly driven by the effectiveness of particles to act as cloud condensation nuclei (CCN), which is determined by size, shape, mixing state and chemical composition [Penner et al., 2001].

Several studies about the direct and indirect radiative forcing of aerosols over China were conducted during the last years with varying results [Seinfeld et al., 2004; Li et al., 2007; Han et al., 2012b]. Han et al. [2012b] conducted simulations with a regional climate-chemistry model and estimated a monthly mean shortwave radiative forcing of dust of -3.9 W m<sup>-2</sup> near the ground and +0.9 W m<sup>-2</sup> at TOA; indicating a near surface cooling effect and a slight warming effect in higher altitudes. They also estimate that the radiative forcing of dust in springtime in China accounts for about 42% of the total aerosol forcing. Seinfeld et al. [2004] estimate a radiative forcing of dust during April 2001 of -9.3 W m<sup>-2</sup> at the surface and -5.5 W m<sup>-2</sup> at TOA. Sulfate, organic and black carbon, have a negative radiative forcing near the surface and a positive forcing at TOA.

The radiative effects of aerosol also lead to a reduction of atmospheric visibility and cause a dimming effect. As aerosol loads in China are high, visibility in most megacities is often low. Cao et al. [2012] found an average visibility reduction of 6.4 km in Xian, China. A study of Chang et al. [2009] focused on annual mean visibilities in six Chinese megacities and found decreasing trends of visibility in five of them. Beijing has a mean annual visibility of 10.67 km, with highest values during spring due to high wind speeds from north and west on non-dust days. Days with low aerosol concentrations are called 'blue sky' days. This term is used as air quality indicator by the Chinese Government.

Besides the impact of aerosols on visibility, degradation of air quality can also be captured by an increase of near-ground PM<sub>10</sub> and PM<sub>2.5</sub> concentrations. Particulate matter with an aerodynamic diameter smaller than 10 µm (PM<sub>10</sub>) and 2.5 µm (PM<sub>2.5</sub>) are, besides visibility, the common terms to describe the impact of aerosols on air quality.

In recent years several epidemiological studies were conducted to investigate the effects of aerosols on the human health. Many of these studies focused on the analysis of connections between short- and long-term exposure to high loadings of ambient PM<sub>10</sub> and PM<sub>2.5</sub> with the increase of respiratory symptoms, decrease of lung function and the triggering of cardiopulmonary diseases [Pope, 2000]. It became obvious that a loss of life expectancy is caused by short-term exposures to high PM<sub>x</sub> levels as well as by long-term exposure to lower levels due to accumulative effects [Pope, 2000]. Zhang et al. [2000] analyzed the correlation between atmospheric sulfate particle concentrations and chronic disease mortality and found a connection with cardiovascular diseases, lung cancer and malignant tumors. A significant impact of

atmospheric particle concentrations on total morbidity and mortality was shown by follow up studies of the Harvard Six Cities Study and the American Cancer Society Study for several cities in the U.S. These studies showed that already a decrease of  $10 \mu\text{m m}^{-3}$  of  $\text{PM}_{2.5}$  can enhance life expectancy of the urban population in the U.S. of  $0.61 (\pm 0.2)$  years [Pope *et al.*, 2009]. Bell *et al.* [2008] conducted a study in Taiwan, which focused on the relation between Asian sand- and dust storms and hospital admissions. The results indicated that there is an increase of hospital admissions due to heart diseases by 16-21% on days with elevated mineral dust loadings. The studies of Senlin *et al.* [2008] focused on the connection between toxicity of  $\text{PM}_{2.5}$  particles and plasmid DNA damage of residents in Shanghai. The authors came to the conclusion that heavy metals might have a negative effect on the human DNA. Recent studies in Beijing used the Poisson Generalized Additive Model (GAM) to examine the effects of  $\text{PM}_{10}$  on case specific daily mortality in the districts of Beijing and came to the conclusion that an increase of  $88 \mu\text{g m}^{-3}$  of  $\text{PM}_{10}$  leads to an increase of 2.6% of respiratory mortality within the whole city area [Zhang *et al.*, 2012]. Guo *et al.* [2009b]; [2010] studied the relationship between ambient  $\text{PM}_{10}$  and  $\text{PM}_{2.5}$  concentrations and hospital visits for cardiovascular diseases and hypertension in Beijing. Results showed that an increase of  $10 \mu\text{g m}^{-3}$  in  $\text{PM}_{10}$  and  $\text{PM}_{2.5}$  leads to an increasing number of emergency hospital visits due to hypertension and that there is a significant correlation between increased levels of  $\text{PM}_{2.5}$ ,  $\text{SO}_2$  and  $\text{NO}_2$  and hospital visits for cardiovascular diseases. Epidemiological studies of Breitner *et al.* [2011] and Liu *et al.* [2013] focused on the association between number concentrations of ultrafine particles smaller 100 nm and cardiovascular emergency visits and mortality in Beijing. Results showed that especially short-term exposure to ultrafine particles increase the risk of mortality caused by cardiovascular diseases.

The study of Zhang *et al.* [2008b] focused on the investigation about relations between adverse health effects caused by high loadings of particulate matter and related economic costs in China. They estimated an economic loss caused by  $\text{PM}_{10}$  pollution of approximately 1.5% of the gross domestic product (GDP) of China, which corresponds to US\$ 29,178.7 million per year.

#### 1.1.4 Air quality in Beijing

Particulate matter is the major air pollutant on most days in metropolitan Beijing [Chan and Yao, 2008], as the high dimensions of population and industrialization growth over the past decades led to a severe increase of anthropogenic pollutants in the urban atmosphere and the following degradation of air quality.

Seasonal variations of  $\text{PM}_{10}$  and  $\text{PM}_{2.5}$  are significant in Beijing with highest concentrations in winter and spring, and lowest in summer [He *et al.*, 2001; Chan and Yao, 2008; Schleicher *et al.*, 2010b].  $\text{PM}_{2.5}$  during spring is mainly dominated by crustal elements, whereas secondary and carbonaceous particles dominate during fall, winter and summer [Yu *et al.*, 2011]. The major contributors for emissions of carbonaceous particles and precursors for secondary aerosol formation are industry, traffic and coal burning. The main

local emission sources in Beijing are power plants, domestic heating, industry and traffic. Over the past decades especially coal burning in industry and domestic heating was a major source for high SO<sub>2</sub> and PM<sub>2.5</sub> concentrations. In addition, the traffic volume increased tremendously over the past decade, leading to an increase of NO<sub>x</sub>, VOC, ozone and particulate matter concentrations [Zhang *et al.*, 2004].

Secondary particle formation is reduced in winter due to low air temperature. However, frequently occurring stagnant weather conditions lead to an accumulation of particles in the air and degradation of air quality. In addition, emissions of primary particles are higher in winter due to domestic heating [Chan and Yao, 2008]. Lowest daily PM<sub>10</sub> and PM<sub>2.5</sub> concentrations are found in summer, when precipitation events occur most frequently among all seasons. In spring dust events have a strong negative impact on air quality in Beijing as dust increases PM<sub>10</sub> and PM<sub>2.5</sub> concentrations and provide an effective surface for chemical reactions of precursors like SO<sub>2</sub> and nitrogen dioxide (NO<sub>2</sub>), enhancing the formation of atmospheric sulfate and nitrate concentrations [Han *et al.*, 2007; Huang *et al.*, 2013]. Dust accounts for 10 to 70% of total PM<sub>2.5</sub> concentrations on non-dust days and up to 90% during dust storm days [Han *et al.*, 2007]. During fall, concentrations of carbonaceous species are mainly enhanced due to biomass burning [Chan and Yao, 2008].

Streets *et al.* [2007] suggest that most of the anthropogenic aerosols are formed locally in metropolitan Beijing, but estimate a contribution from sources outside of Beijing to be 34% on non-dust days. He *et al.* [2001] assume a contribution of carbonaceous species to the overall yearly total PM<sub>2.5</sub> mass of 37-42%, and a ratio of nitrate, sulfate and ammonium of 25-30%. Crustal species account for 11-12% throughout the year. Reported total carbon concentrations show strong variations between 10.8 and 51.9 µg m<sup>-3</sup> [He *et al.*, 2001; Sun *et al.*, 2004].

To increase air quality, several international and national air quality standards and limits have been introduced during the last years and the reduction of aerosol concentrations became a major task for environmental policy and decision making in China [WHO, 2006]. China has several laws and standards to regulate national air pollution, such as the Law of the People's Republic of China on the Prevention and Control of Atmospheric Pollution, the National Ambient Air Quality Standards (GB3095-1996 and 2012) and the Emission Standards of Air Pollutants for Thermal Power Plants (GB13223-2003) [Chan and Yao, 2008]. Since 2000, a nationwide daily air pollution index (API) and an air quality classification system is available to the public. Air quality is classified within three grades ranging from Grade I (good air quality) to Grade III (hazardous air quality). The current daily PM<sub>10</sub> concentration limits for the Chinese National Ambient Air Quality Standard (CNAAQs) are 50 µg m<sup>-3</sup> for Grade-I, 150 µg m<sup>-3</sup> for Grade-II and 250 µg m<sup>-3</sup> for Grade-III. These limits will not change with introduction of the new CNAAQs (GB3095-2012). However, for the first time nationwide daily PM<sub>2.5</sub> limits will be introduced, restricting concentrations to 35 µg m<sup>-3</sup> for Grade-I and 75 µg m<sup>-3</sup> for Grade-II; Grade-III will be abolished. The current daily WHO limit for PM<sub>10</sub> is 50 µg m<sup>-3</sup>

and  $25 \mu\text{g m}^{-3}$  for  $\text{PM}_{2.5}$ . The annual limits of CNAAQs (GB3095-1996) are  $40 \mu\text{g m}^{-3}$  for Grade-I,  $100 \mu\text{g m}^{-3}$  for Grade-II and  $150 \mu\text{g m}^{-3}$  for Grade-III. The value for Grade-II will change to  $70 \mu\text{g m}^{-3}$ ; Grade-III will be abolished. The future annual  $\text{PM}_{2.5}$  limits will be  $15 \mu\text{g m}^{-3}$  for Grade-I and  $35 \mu\text{g m}^{-3}$  for Grade-II. The current annual  $\text{PM}_{10}$  limit of WHO is  $20 \mu\text{g m}^{-3}$  and 10 for  $\text{PM}_{2.5}$  [WHO, 2006; Chan and Yao, 2008].

Comprehensive studies about aerosol pollution and air quality were conducted by He *et al.* [2001]; Norra *et al.* [2010]; Schleicher *et al.* [2010b]; 2010a]; Sun *et al.* [2004]; Duan *et al.* [2006]; Guinot *et al.* [2007]; Gurjar *et al.* [2008] and Wu *et al.* [2011]. The chemical composition of  $\text{PM}_{10}$  and  $\text{PM}_{2.5}$  has been studied by He *et al.* [2001], Sun *et al.* [2004], Zhang *et al.* [2004], Guinot *et al.* [2007], Schleicher *et al.* [2012] and Yu *et al.* [2011]

## 1.2 Satellite-based measurement of aerosol

The optical effects of aerosol in the atmosphere facilitated the rapid development of the use of satellite data for aerosol and air quality studies during the past two decades. Due to their high spatial coverage, satellite data address spatial gaps of ground-based monitoring sites. To date there are several satellite aerosol products, with different spatial and temporal resolutions available for these studies.

Aerosol-optical thickness (AOD) is the common metric to assess the aerosol loading of the whole column of the atmosphere, as it is a quantity for the light extinction of the column of the atmosphere for given wavelengths due to the existence of aerosols.

A general overview about recommendations for the use of satellite data for air quality assessment is given in Engel-Cox *et al.* [2004]. Satellite derived AOD in China has been studied by Zhao [2012] who used data from the Moderate Resolution Imaging Spectroradiometer (MODIS) aboard the NASA satellites AQUA and TERRA. Li *et al.* [2011] conducted a study about applications of MODIS like sensors for air quality monitoring and forecasting in Asia and found appropriate correlations between AOD and near-ground  $\text{PM}_{10}$  concentrations. Within their study, they used the MODIS Deep Blue aerosol product, described in Hsu *et al.* [2006]. The MODIS Deep Blue algorithm is most appropriate for the detection of carbonaceous aerosol like mineral dust over bright surfaces such as deserts, snow fields and glaciers. Mineral dust was also studied by Huang *et al.* [2007] and Uno *et al.* [2008] who used data from the space-borne Cloud-Aerosol Lidar with Orthogonal Polarization (CALIOP) to study the horizontal and vertical aerosol distribution in China. They detected the existence of several atmospheric aerosol layers and significant amounts of aerosol in higher altitudes.

### 1.3 Aerosol modeling

Since the strong impact of mineral dust on air quality and climate change came into scientific and political focus, existing weather-chemistry models for simulation of anthropogenic gases and aerosols were extended with dust modules to model dust on different temporal and spatial scales.

To date, dust models are mainly used for quantification of the global dust cycle and the total atmospheric dust burden, assessment of the effect of dust aerosol on climate change, dust storm monitoring and prediction. Models are available for global to local scales. The main differences of these models in general are the horizontal and temporal resolution.

Fundamental research about saltation processes were conducted by *Whitby et al.* [1991], *Alfaro and Gomes* [1995], *Gomes et al.* [2003] and *Park and Park* [2013]. Regional models used for the main worldwide dust sources are DREAM by *Nickovic et al.* [2001]; CFORS used by *Uno et al.* [2003]; COSMO-ART developed by *Vogel et al.* [2006]; MM5-ARPS-CMAQ by *Cheng et al.* [2007]; CUACE-DUST by *Gong and Zhang* [2008]; WRF-DuMo by *Darmenova et al.* [2009]; RAMS-CMAQ by *Ge et al.* [2011] and *Han et al.* [2012b]; and ADAM2/ MGLADAM by *Park and Lee* [2004] and *Lee et al.* [2013]. Currently available global models are ECHAM5-HAM with the emission scheme of *Tegen and Fung* [1994]; MIRAGE, MOZGN, UMI and GOCART with a dust flux scheme by *Ginoux et al.* [2001]; CAM and MATCH with schemes by *Zender et al.* [2003] and MASINGAR by *Tanaka and Chiba* [2006]. Detailed model intercomparison studies are given in *Huneus et al.* [2010] for global model systems and *Uno et al.* [2006] for Asian dust studies.

There are only few dust emission parameterization schemes available for global and regional models. These schemes can be classified into three categories following an approach of *Shao and Dong* [2006]. (1) in alpha schemes the vertical dust flux in terms of the power of the 10-m wind speed or friction velocity  $u_*$  is parameterized and subsequently assigned to different particle sizes by use of particle-size distribution [*White, 1979; Tegen and Fung, 1994; Marticorena et al., 1997; Gong et al., 2003; Uno et al., 2003*]; (2) beta schemes are used in global models and comprise simplified wind-erosion parameterizations and dust climate data [*Ginoux et al., 2001; Zender et al., 2003*]; and (3) gamma schemes are spectral dust emission schemes which are similar to alpha schemes but take into account wind erosion parameterization which are derived from soil properties [*Shao, 2004*]. Models of the first and second category are based on the assumption that the vertical dust flux is proportional to the horizontal saltation flux, which is not the fact for gamma scheme models. Currently gamma schemes produce the most accurate dust results for regional and local scale simulations.

Although several model studies were conducted on global and regional scales over the last years, several problems of anthropogenic and dust aerosol simulation remain. The simulation of anthropogenic gases and aerosols strongly depend on up-to-date high resolved emission inventories. However, even in Europe these inventories show a high level of uncertainty even on local scales. Detailed information about

emissions from industry, households and traffic are necessary input data and have to be kept up-to-date. The simulation of mineral dust renders similar problems, as comprehensive datasets of soil properties are often not available for drylands and deserts. Key surface parameters are soil particle size distribution, soil surface characteristics, vegetation cover and leaf area index. Modelled dust emissions, concentrations and deposition show severe variations, and uncertainties are large due to missing measurement data for validation. Validation of models with satellite data poses a promising tool as satellite images offer a full spatial coverage and mainly a daily temporal resolution. However, aerosol retrievals show huge discrepancies among different satellite products, which constitutes a problem to model validation [Shao and Dong, 2006]. The complexity and broad spatio-temporal scale of the different dust processes, which ranges from saltation processes with a temporal resolution of seconds and a spatial scale of  $\mu\text{m}$  to long-range transport of dust from one continent to another which can take months, remains a challenge for dust modeling in principle. Moreover, interactions of dust with gaseous species and anthropogenic aerosols are still not included in any available model system. This circumstance lead to a loss of accuracy when it comes to dust and air quality simulations, as a study of Han *et al.* [2007] showed that mineral dust has a significant positive effect on secondary particle formation.

#### 1.4 Scope of the present work

The analysis of the state of the art showed, that to date several studies have been conducted focusing on aerosols in China, and especially in Beijing. However, there are still several open scientific questions considering especially the processes of dust source activation, atmospheric dust dynamics, the vertical layering of aerosols in the atmosphere, the impact of dust on air quality and the interactions of dust and anthropogenic aerosols in the urban atmosphere. Besides these scientific questions, also methodological tasks are still not solved, such as the simulation of mineral dust on regional scale, the simulation of anthropogenic aerosols, the use of external input data such as soil property datasets and emission inventories, the use of passive satellite data for air quality applications and the assessment of the potential of active satellite sensors for these applications. Moreover, up to now, most studies focused on the use of one single instrument or method to characterize urban air quality. However, ground-based measurements on their own can never provide a spatial coverage as satellite and model data. But these instruments need specific calibration and validation, which is only possible by ground-based measurements.

On the basis of these open questions major hypotheses can be addressed:

- Air quality in Beijing is strongly determined by airborne mineral dust, not only in spring but also during summer
- In spring mineral dust is a strong pollutant in Beijing on its own and does not act as substitute to local anthropogenic pollution levels

- There is less mixing of airborne mineral dust with locally produced pollutants in spring
- In summer mineral dust is an substitute pollutant to existing anthropogenic dominated pollution levels
- There is an influence of the regional topography of Beijing on spatio-temporal changes of local air quality
- Topography has a strong impact on atmospheric mineral dust transport and transport pathways
- A combined approach of aerosol model, satellite and ground-based measurements is a suitable tool for studying mineral dust dynamics and its impact on air quality
- The spaceborne lidar aboard CALIPSO is a suitable tool for determine the vertical location of mineral dust layers

To help answering these open questions and testing the related hypotheses the scope of this study focuses on the investigation of spatio-temporal variability, dynamics and impact of mineral dust and anthropogenic aerosols on air quality in the Beijing region. This work is strongly motivated by the fact, that mineral dust and anthropogenic substances can lead to a severe depletion of air quality which has a strong negative effect on the residents' health. This happens inside the mineral dust source regions and in the Chinese megacities located downwind of the Asian desert areas, where  $PM_{10}$  and  $PM_{2.5}$  levels strongly increase during unfavorable weather conditions.

Two case studies are conducted. The first study is during spring 2011, when a dust storm was reported for Northern China and Beijing. First of all, active source regions are captured and emission strengths of the dust outbreak are estimated to quantify the amount of dust in the atmosphere. The spatio-temporal variability of dust and its impact on the local air quality in the source regions is analyzed. Therefore, a closer look is taken on the analysis of vertical layering of dust in the atmosphere. The second aspect of this case study focuses on the transport of dust towards Beijing and its impact on the urban air quality. The dispersion of dust in the region is studied in detail and the contribution of dust on  $PM_{10}$  and  $PM_{2.5}$  levels is quantified. The second case study features August 2008. During this period anthropogenic emissions were reduced in Beijing and its vicinity because of the Olympic Summer Games. However, during this time not only particles from anthropogenic sources but also mineral dust particles were detected in the urban atmosphere by geochemical analysis. This leads to the question if these particles are from desert dust sources or if they are mainly emitted by local sources as construction sites and agricultural areas. The focus of this study lies on the estimation of the contribution of anthropogenic aerosols and mineral dust on the local  $PM_{10}$  and  $PM_{2.5}$  concentrations. Moreover, the effects of reduction measures and meteorological conditions on local and regional  $PM_{10}$  and  $PM_{2.5}$  concentrations are studied.

The meso-scale fully-online coupled model system COSMO-ART, a weather forecast and reactive trace gas and aerosol model, is used for this study. Aerosol mass and number concentrations, AOD, TSP (Total Suspended Matter),  $PM_{10}$  and  $PM_{2.5}$  for three mineral dust and five anthropogenic particle modes are calculated. Currently, only few meso-scale models provide capabilities to calculate mineral dust and anthropogenic gases and particles in an online coupled way. COSMO-ART is a comprehensive model system which can be used to run such simulations. In previous studies COSMO-ART was used for Europe and the North African Deserts and showed its high reliability [Vogel *et al.*, 2006; Stanelle *et al.*, 2010; Bangert *et al.*, 2012]. In the framework of the present study the model results are also calibrated and validated using data from ground-based and satellite data, such as AOD,  $PM_x$  and meteorological parameters. However, it is important to keep in mind that ground-based measurement networks have a strongly limited capability for model calibration and validation, as they provide only information for single measurement points and sometimes have low temporal resolutions or many missing data. For this reason, additionally data from three passive satellite sensors and one active sensor is used. The passive sensors MODIS, OMI and MISR provide almost full coverage and daily information about horizontal aerosol distributions over China by means of AOD. However, as passive sensors only capture AOD over the whole column of the atmosphere they lack of information about the amount of aerosols near the ground. For the quantification of the vertical spatial distribution of aerosols, the space-borne lidar CALIOP aboard the CALIPSO satellite, which provides data of the 1064 nm and 532 nm backscatter intensity signal of the atmosphere, is used. The polarized components give additional information about particle types. Vertical profiles of these extinction coefficients show the vertical location and AOD of different types of aerosols in the atmosphere and provide the missing link between total column AOD of passive sensors and the amount of aerosol located near the ground. However, these systems are limited to some extent, as they provide information about atmospheric aerosol amounts due to their optical properties, but provide no data about aerosol mass or number concentrations. The combination of model, satellite and ground-based data is a promising way to get a detailed insight into the distribution, amount and vertical location of anthropogenic aerosols and mineral dust and facilitates the assessment of the health relevant amount of aerosol near the ground. The approach of combining passive and active sensor data is also a valuable tool to validate model performance on a broad spatial scale, which is not possible by the exclusive use of punctual ground-based measurement data.

There are new topics and features, which are raised up in this work. In the framework of this study COSMO-ART was set up for North Asia for the first time and the achieved results show, that the model system is applicable for this region and can be used for further studies in this region. Several model adaptations and sensitivity studies for calibration were undertaken to define the best fitting set-up of the dust module for the investigation domain. Model validation was performed within the framework of two

in-depth case studies. These case studies focus on the study of the impact of mineral dust on the urban atmosphere of Beijing during spring and summer. Several studies have been published during recent years pursuing this issue by means of geochemical analysis of PM<sub>10</sub> and PM<sub>2.5</sub> filter samples. However, these samples are only point measurements and provide no information about the spatio-temporal distribution and dynamics of mineral dust. The linkage of model, passive and active satellites and ground-based measurements assembled in this study is a unique approach. It offers the possibility to gain a detailed look into Asian mineral dust distribution and allows the verification of the reliability of the different instrumentations. Moreover, up to now simulations of Asian mineral dust dispersion mainly focused on spring, but less information is available for the summer season. One task of this study was to quantify the amount of mineral dust on the urban atmosphere of Beijing not only during spring but also during summer.

The main objectives of this work shall give more information to the existing open scientific questions about the spatio-temporal variability of airborne dust, dust source identification, dust emission strengths, atmospheric dynamics during dust transport, mixing with anthropogenic aerosols and its impact on air quality. Therefore, the main objectives are defined as following:

#### Thematic objectives:

- Characterization of the spatio-temporal variability of dust and anthropogenic aerosols in Northern China under varying meteorological conditions
- Definition of active mineral dust source regions and emission strengths
- Analysis of the dynamics of mid-range transport of dust towards Beijing
- Determination of the vertical distribution of dust in the atmosphere in the source regions and the downwind located area of Beijing
- Assessment of the impact of mineral dust on local air quality in the desert areas and in Beijing
- Estimation of the impact of anthropogenic emission reductions on air quality in Beijing during the Olympic Summer Games

#### Technical objectives:

- Adaptation of the COSMO-ART model for aerosol simulations in East Asia
- Estimation of the accuracy of COSMO-ART model results by validation with measurement data
- Analysis of the application of four different passive and active satellite-based sensor data for assessment of mineral dust loads and air quality

## 2 Methodology

### 2.1 Methodological approach

In the framework of the present work ground-based, satellite-based and model data were used in conjunction for two case studies in August 2008 and April 2011. A schematic overview of the methodological approach, relevant parameters, processes and methodologies is shown in Figure 2.

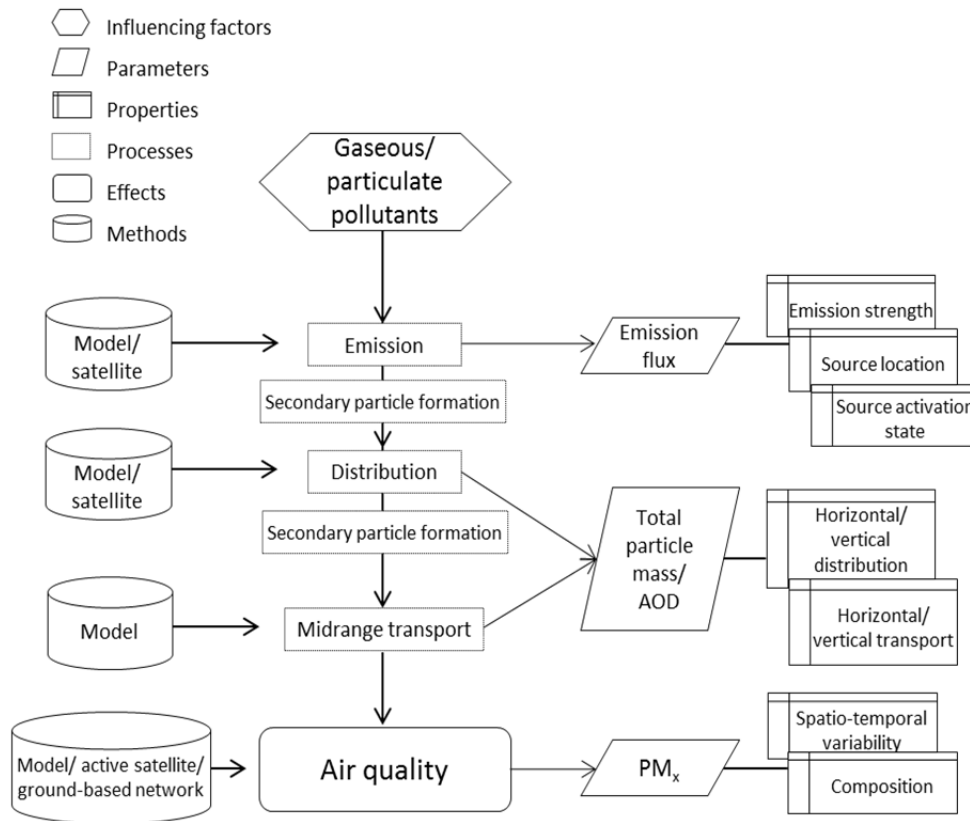


Figure 2: Schematic overview of the relevant impact factors, parameters, properties, processes, effects and methodological approaches used within the framework of the present work. The impact of primary and secondary geogenic and anthropogenic aerosols are studied over their whole lifetime from emission to transport and their formation during transport, to their impact on air quality. Relevant parameters are emission fluxes, total particle mass concentrations, AOD and near-ground PM<sub>x</sub>. Emission strengths, source locations and their activation state are identified by using COSMO-ART and satellite data. The horizontal and vertical distribution and transport of aerosols are also analyzed by using COSMO-ART and satellite data, whereas the transport and impact of aerosols on urban air quality are mainly studied by using COSMO-ART in conjunction with ground-based measurement data to get information about spatio-temporal variability and aerosol composition.

For the first part of the springtime case study (chapter 4) COSMO-ART model data was used in conjunction with passive and active satellite data for investigating dust variability inside Asian dust source regions. Passive and active satellite data were used for qualitative analysis of horizontal and vertical dust distribution. COSMO-ART was used to model corresponding particle emission fluxes to study emission strengths and identification of active source regions.

In the following part (chapter 5), the COSMO-ART model was used to study the horizontal and vertical spatio-temporal distribution and the mid-range transport of dust downwind of Beijing. In addition, active satellite data and ground-based measurement data were studied for assessing the impact of dust on air quality. Satellite data were not used for studying the mid-range dust transport process itself, as this procedure is characterized by fast moving air masses and dust plumes, which can hardly be captured by satellite data. However, CALIPSO satellite data and ground-based measurements were analyzed to characterize the mixing of dust with local pollutants and estimate the impact of dust on near-ground PM<sub>10</sub> and PM<sub>2.5</sub> concentrations.

The summertime case study (chapter 6) focuses on air quality in Beijing during the Olympic Summer Games in 2008 by using mainly data from COSMO-ART model and ground-based measurements. Additionally, MODIS satellite data were used to characterize the spatio-temporal variability of AOD.

## 2.2 Data

### 2.2.1 Ground-based measurement data

In this study, data of six ground-based meteorological and 12 air quality measurement stations in the region of Beijing were used. In Figure 3 the two model domains D1 and D2 and the location of the measurement sites are shown. Model set-ups are described in following chapters.

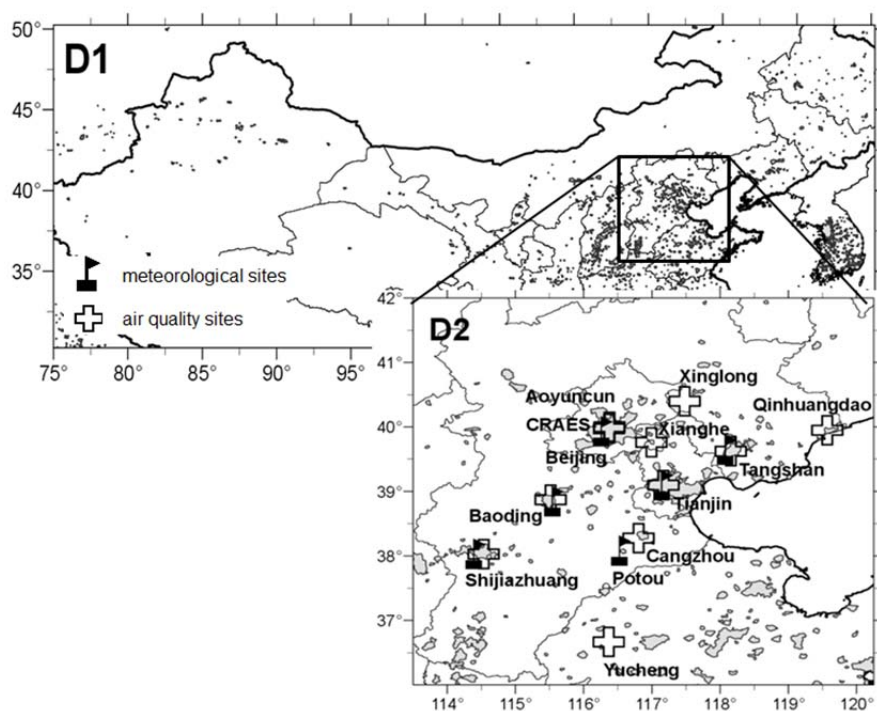


Figure 3: Location of all available ground-based measurement sites. Black flags mark meteorological sites, crosses mark air quality sites. Names of sites are abbreviated (see Table 1 and Table 2 for site names). D1 refers to model domain 1 located between 75°-130° E and 30.25°-50.25° N, D2 refers to model domain 2 located between 113.5°-120.25° E and 35°-42° N.

The measurement data was pre-processed with Microsoft Excel 2007. Missing values were counted and basic statistic values as daily mean average, minimum, maximum and standard deviations were calculated. For further analysis and comparison with model results the data was post-processed with NCAR Command Language (NCL) version 6.1.1 (<http://dx.doi.org/10.5065/D6WD3XH5>).

### 2.2.1.1 Meteorological data

Meteorological data is available for six stations which are part of the ground based measurement network of the World Meteorological Organization (WMO). Data is taken from the website [www.ncdc.noaa.gov](http://www.ncdc.noaa.gov) provided by the National Climatic Data Center (NCDC) of the National Oceanic and Atmospheric Administration (NOAA). The dataset is described at <http://gis.ncdc.noaa.gov/geoportal/catalog/search/viewMetadataDetails.page>. The data has two temporal resolutions of one or three hours. At all sites air temperature is measured in °C, relative humidity in %, sea level pressure in hPa, wind speed in  $\text{m s}^{-1}$  and wind direction in degree, visibility in km, and precipitation in mm. Meteorological conditions, such as dust events, thunderstorms or haze are recorded, too. A summary of all data is shown in Table 1.

Table 1: Summary of data availability and temporal resolution of selected meteorological parameters from the WMO official measurement network for both case studies in August 2008 (abbreviated as '08') and April 2011 (abbreviated as '11'). T = Temperature, RH = Relative humidity, U = Wind speed, V = Wind direction, PR = Precipitation, Vis = Visibility, Con = Conditions.

Site	Parameters														Temporal resolution (hours)	
	T		Con		SLP		U		V		PR		Vis		08	11
	08	11	08	11	08	11	08	11	08	11	08	11	08	11		
Baoding	•	•	•	•	•	•	•	•	•	•	•	•	•	•	3	3
Beijing	•	•	•	•	•	•	•	•	•	•	•	•	•	•	1	1
Potou	•		•		•		•		•		•		•		3	
Shijiazhuang	•		•		•		•		•		•		•		3	
Tangshan	•	•	•	•	•	•	•	•	•	•	•	•	•	•	3	3
Tianjin		•		•		•		•		•		•		•		3

### 2.2.1.2 PM<sub>10</sub>, PM<sub>2.5</sub> and anthropogenic trace gas data

PM<sub>10</sub>, PM<sub>2.5</sub> and anthropogenic trace gas data is available at 12 sites in the Beijing area. Measurement data from 11 sites is taken from the Beijing-Tianjin-Hebei Atmospheric Environment Monitoring Network established by the Institute of Atmospheric Physics (IAP) at the Chinese Academy of Sciences (CAS) [Xin *et al.*, 2012]. Data is provided by the State Key Laboratory of Atmospheric Boundary Layer Physics and Atmospheric Chemistry of IAP. In addition, measurement data from one site in Beijing (Beijing-CRAES) operated by S. Norra and N. Schleicher is analyzed.

PM<sub>10</sub> and PM<sub>2.5</sub> measurements by CAS-IAP are carried out in 8 m height at the Beijing measurement tower and 2 m height at all other stations. PM<sub>x</sub> in  $\mu\text{g m}^{-3}$  is sampled hourly with TEOM instruments with a measurement resolution of  $0.1 \mu\text{g m}^{-3}$  and a precision of  $1.5 \mu\text{g m}^{-3}$ . TSP and PM<sub>2.5</sub> measurements by

S. Norra and N. Schleicher were conducted at the Beijing-CRAES site using Mini-Volume samplers (Leckel, Berlin) with quartz fibre filters. The temporal resolution of these data is hourly for the Olympic Games case study in 2008. Network, equipment and chemical analysis are presented in *Norra et al.* [2010] and *Schleicher et al.* [2010b]. Additionally, hourly NO<sub>x</sub> and ozone concentrations, which are continuously measured at the Beijing measurement tower near the IAP building by CAS-IAP, were analyzed. Measurements are conducted in 2 m height. Network and equipment are described and discussed in *Xin et al.* [2012].

Table 2 shows the data availability for both case studies. The Beijing site provides least data, whereas all other stations have higher data availability of > 62%.

Table 2: Summary of the availability of trace gas, PM<sub>10</sub> and PM<sub>2.5</sub> data for the Beijing-CRAES measurement site and the Beijing-Tianjin-Hebei-Measurement Network, for both case studies in August 2008 and April 2011.

Site	Species								Availability in percent				
	NO <sub>x</sub>		O <sub>3</sub>		PM <sub>10</sub>		PM <sub>2.5</sub>		PM <sub>10</sub>		PM <sub>2.5</sub>		
	2008	2011	2008	2011	2008	2011	2008	2011	2008	2011	2008	2011	
Beijing-CRAES					•		•			100%		100%	
Aoyuncun					•		•			92%		95%	
Baoding					•	•	•	•		73%	97%	80%	97%
Beijing	•		•			•		•			47%		47%
Cangzhou							•					91%	
Qinhuangdao							•					98%	
Shijiazhuang					•		•			100%		100%	
Tangshan						•	•	•			91%	100%	90%
Tianjin						•		•			62%		62%
Xianghe					•	•	•	•		89%	96%	100%	96%
Xinglong							•	•				77%	97%
Yucheng							•					92%	

### 2.2.2 Satellite data

In this study, AOD at the 500 to 555 nm wavelength from three passive satellite sensors and one active satellite sensor were used. Moderate Resolution Imaging Spectroradiometer (MODIS) and Ozone Monitoring Instrument (OMI) provide almost full spatial coverage of the study area of Northern China for every day, whereas the Multi-angle Imaging SpectroRadiometer (MISR) offers data of two to three separate paths per day. The active sensor Cloud-Aerosol Lidar with Orthogonal Polarization (CALIOP) provides information about vertical profiles of clouds and aerosols in the atmosphere. MODIS on AQUA, OMI on AURA and CALIOP aboard CALIPSO (Cloud-Aerosol Lidar and Infrared Pathfinder Satellite Observations) are part of the A-Train constellation, a group of satellites flying in formation with a temporal offset of a few minutes between each other. AURA follows AQUA by 15 minutes. All satellites fly in an orbit of 705 km above the earth's surface.

For this investigation only cloud screened and quality controlled data are used. MODIS raw data are available in geotiff format and OMI images in netcdf format. MISR raw data were converted from hdf4 to

geotiff format using the HDF-EOS to GeoTIFF Conversion Tool (HEG) of version 2.12 from NASA (<http://newsroom.gsfc.nasa.gov/sdptoolkit/HEG/HEGHome.html>). All three datasets are further processed using ArcGIS Desktop 10.0 from ESRI (<http://esri.de/products/arcgis/>). CALIOP data were processed using Microsoft Excel, NCL and the Interactive Data Language (IDL) software version 7.9 distributed by EXELIS (<http://www.exelisvis.com/ProductsServices/IDL.aspx>).

### 2.2.2.1 AOD

AOD is the common metric to estimate the total aerosol loading over the whole column of the atmosphere. AOD describes the quantity of light which is attenuated during its path through the atmosphere by absorption and scattering (extinction). Though, AOD is defined as the integrated extinction coefficient over a certain vertical atmospheric column. The extinction coefficient describes the fractional attenuation of radiance per unit path length. As AOD is defined as integral, it has no unit. AOD ( $\tau$ ) can be derived according to  $e^{-\tau} = \frac{I}{I_0}$ , whereas  $I_0$  describes the intensity of radiation at the source and  $I$  denotes the intensity of radiation after a given path.

The radiative source can be natural, as solar radiation, or artificial, as a laser beam. Passive sensors, like the spectrometers aboard MODIS, OMI and MISR capture the attenuation of solar radiation, whereas the spaceborne lidar aboard CALISPO produces actively its own radiative source.

The detection of mineral dust aerosol over bright desert areas is fairly difficult for spaceborne spectrometers, as the in general high reflectance of the surface hampers the detection of overlaying aerosol layers at visible wavelengths. For this reason only passive satellite sensors which have already shown their capability to provide reasonably AOD data over bright desert areas were chosen for this study [Martonchik *et al.*, 2004; Hsu *et al.*, 2006; Huang *et al.*, 2007; Torres *et al.*, 2007].

### 2.2.2.2 Passive sensors

#### **MODIS-AQUA**

MODIS (Moderate Resolution Imaging Spectroradiometer) aboard AQUA is a passive sensor which measures the Earth's reflectivity at multiple channels. AQUA passes the equator from south to north during the afternoon at 1:30 pm (local time). The satellite overpass over Northern China lasts from approximately 3:00 am to 8:00 am (UTC). The cross track swath of MODIS covers 2330 km. The Earth's surface and atmosphere are viewed within 36 spectral bands ranging from 400 to 1440 nm.

For this study the most recent Collection 5.1 of MODIS Level 2 data with a nominal spatial resolution of 10 x 10 km<sup>2</sup> was used. It is distributed by NASA's Level 1 and Atmosphere and Distribution System (LAADS) (<http://ladsweb.nascom.nasa.gov/>). For the analysis of dust over bright areas like deserts the MODIS Deep Blue AOD product at 550 nm wavelength is the most reliable product [Hsu *et al.*, 2006].

The Deep Blue algorithm was specially developed to enhance the detection of aerosols over bright surfaces as snow or deserts. AOD values usually range from 0 to 5 with values greater 1 captured during dust or biomass burning events. More information about the instrument and the Deep Blue algorithm can be found in *Remer et al.* [2005] and *Hsu et al.* [2004].

### **OMI-AURA**

OMI (Ozone Monitoring Instrument) aboard Aura is a nadir-viewing imaging spectrometer designed to measure gases and aerosols in the near UV. Its wavelengths range from 270 nm in the UV to 500 nm in the visible spectrum. Nadir-viewing means that the sensor observes the earth directly located below itself. OMI provides daily global coverage. It has a horizontal resolution of 13 x 24 km<sup>2</sup> and its swath covers 2600 km in full cross-track direction.

For this investigation the cloud screened OMI Level 3 aerosol product OMAERUVd was used. These data were processed using the Near-UV algorithm for AOD and single scattering albedo detection providing AOD data at a wavelength of 500 nm. The AOD values at 500 nm are obtained by conversion of the retrieved AOD at 388 nm and therefore less reliable than the 388 nm AOD. The near-UV retrieval algorithm is especially sensitive to the presence of mineral dust and carbonaceous aerosol. The horizontal resolution of this dataset is 1° x 1° latitude/longitude grid. The data were obtained from the Goddard Earth Sciences Data and Information Services Center (GES-DISC) of NASA (<http://disc.sci.gsfc.nasa.gov/Aura/data-holdings/OMI>). More information is available in *Torres et al.* [2007].

### **MISR-TERRA**

MISR (Multi-angle Imaging Spectroradiometer) aboard TERRA measures the reflectivity of the Earth and atmosphere simultaneously using nine different cameras installed at different angles. The differences in reflection among viewing angles allow the distinguishing between particle types, cloud types and ground surface types. This multi-angle view also improves MISRs capability to detect aerosols over bright desert surfaces as radiances of the overlaying aerosol layers can be captured more easily [*Martonchik et al.*, 2004]. MISR-TERRA flies in 705 km height and provides a global coverage. Equator crossing is around 10:30 local time on its descending path. The swath in cross track direction is 360 km with a horizontal resolution of 0.15°. The nine angles range between 26.1° and 95°. One camera views the nadir (vertical direction) and four on both sides view the afterward and forward direction along the track. Each camera has four spectral bands with central wavelengths of 443 nm, 555 nm, 670 nm and 865 nm.

The MISR Level 2 aerosol product MIL2ASAE of Collection 11 was used for this work. For the comparison with the MODIS Deep Blue product at 550 nm and the OMI AOD product at 500 nm the MISR green band with a central wavelength of 555 nm was used. The data was obtained from the Atmospheric Sciences Data Center (ASDC) website (<https://eosweb.larc.nasa.gov/project/misr>).

Detailed explanations about the instrument and used algorithms are described in *Diner et al.* [1998] and [2001]. A validation of MISR data with ground-based sunphotometer AOD obtained from AERONET in desert areas is presented in *Martonchik et al.* [2004].

### 2.2.2.3 Active sensor – CALIOP-CALIPSO

CALIPSO carries the CALIOP (Cloud-Aerosol Lidar with Orthogonal Polarization) two wavelength polarization sensitive lidar. CALIOP provides information about the vertical distribution of cloud and aerosol layers, as well as cloud and aerosol properties. The CALIOP lidar measures directly the backscatter intensity at 1064 nm and orthogonally polarized components at 532 nm. CALIOP's polarization measurement enables differentiation between spherical and non-spherical particles which can be used for the detection and characterization of dust. CALIPSO provides global coverage with two overpasses over Northern China during 1:00 am to 5:00 am and 1:00 pm to 5:00 pm (UTC). CALIPSO follows AQUA by one to two minutes. Each orbit path of CALIPSO is separated by 24.7° longitude that leads to a 16-day repeat of the same orbit.

For this study CALIPSO lidar Level 2 validated aerosol products (data version 3.01) were used. These products comprise data of aerosol layers and profiles, a vertical feature mask for the differentiation of aerosol types, the aerosol extinction profile, and AOD. The aerosol layer and profile data have a horizontal resolution of 5 km and the vertical feature mask has a resolution of 333 m. The data for this study were obtained from the Atmospheric Science Data Center (ASDC) website (<https://eosweb.larc.nasa.gov/project/calipso>). More information about CALIPSO is available in *Winker et al.* [2009], *Young and Vaughan* [2009]. A study about the detection of dust plumes by CALIPSO can be found in *Huang et al.* [2007].

### 2.2.3 The model system COSMO-ART

The modeling data used in the present study were produced by conducting simulations with the model system COSMO-ART (Consortium of Small scale Modeling – Aerosols and Reactive Trace Gases). The system was developed at the Institute of Meteorology and Climate Research (IMK) at the Karlsruhe Institute of Technology (KIT) [*Vogel et al.*, 2009]. The model system consists of the operational weather forecast model COSMO (Consortium for Small-scale Modeling) of the German Weather Service (DWD) and the aerosol model ART (Aerosol and Reactive Trace gases) developed at IMK. ART consists of comprehensive modules for the treatment of gas phase chemistry and aerosol dynamics which are online coupled with the COSMO model [*Vogel et al.*, 2009; *Bangert et al.*, 2012]. COSMO-ART was designed to model emission, dispersion and deposition of gases and aerosols at each time step as function of the meteorological fields.

### 2.2.3.1 The weather forecasting model COSMO

The COSMO model is based on the Lokalmodel (LM) and is operationally used by the DWD. COSMO is a non-hydrostatic, non-unfiltered Euler equations based model for regional to local applications down to 10 km horizontal resolution. As it is a non-hydrostatic model, convection and the convective transport of gases and aerosols can be considered even for simulations with horizontal resolutions coarser than 7 km. *Doms and Schättler* [2002] present a detailed description of model properties.

### 2.2.3.2 Aerosols in COSMO-ART

The MADEsoot (Modal Aerosol Dynamics Model for Europe extended by soot) module is used for the treatment of aerosols within COSMO-ART [*Riemer et al.*, 2003]. The aerosol population is represented by eleven overlapping modes with lognormal distributions [*Vogel et al.*, 2009]. An overview of the existing modes, their chemical composition, mixing state and initial diameters are given in Table 3.

Table 3: Overview presenting the specific aerosol modes (row 1), their chemical compositions (row 2-5), mixing states (row 6), initial diameters in  $\mu\text{m}$  (row 7) and standard deviations (last row).

Mode	Chemical composition				Mixing state	Initial diameter ( $\mu\text{m}$ )	Standard deviation
	Inorganics	Organics	Soot	Dust			
if	•	•			internally	0.01	1.7
ic	•	•	•		internally	0.08	2.0
jf	•	•			internally	0.07	1.7
jc	•	•	•		internally	0.08	2.0
s			•		uniform	0.08	1.4
c	•				uniform	10.0	2.5
sa	•				uniform	0.2	1.9
sb	•				uniform	1.0	2.0
Sc	•				uniform	12.0	1.7
da				•	uniform	1.5	1.7
db				•	uniform	6.7	1.6
dc				•	uniform	14.2	1.5

The mode if represents Aitken mode particles, jc represents accumulation mode particles. Both modes are internally mixed, and consist of sulfate, ammonium, nitrate, water and organic compounds. The two internally mixed modes ic and jc represent aged secondary particles formed due to aging processes of soot in the atmosphere. They contain sulfate, ammonium, nitrate, water, organic species and soot. Pure soot is represented by mode s, which is directly emitted into the atmosphere. The mode c represents directly emitted Aitken mode particles, which are composed of inorganic species. Direct emissions of if, jf, ic and jc are not taken into account.

The five modes are subject to gas phase processes as nucleation, condensation and coagulation. The inorganic species sulfate, ammonium and nitrate are formed by nucleation of water and sulfuric acid. The

condensable organic compounds are built up by oxidation of organic species following an approach of *Odum et al.* [1996]. The condensation of organic species and sulfuric acid on the soot particle surfaces is the first considered mechanism transferring particles of mode if and jf into the internally mixed modes ic and jc. Within MADEsoot all available soot is transferred into these two modes, if the soluble portion of the available soot exceeds a threshold value of 5%. This assumption follows the approach of *Weingartner et al.* [1997]. The condensational growth rate of the particles depends on the size distribution of the particles and the available mass of the inorganic and organic condensable gaseous species, following the attempt of *Binkowski and Shankar* [1995]. The second approach of the formation of aged particles is the coagulation of soot particles with the modes if and jf. The mass of the soot particles is transferred into the aged modes ic and jc. The coagulation process follows an approach of *Whitby et al.* [1991]. Particles which are formed by intramodal coagulation stay in their original mode, whereas particles formed by intermodal coagulation switch towards the larger mode.

Six modes are represented by three modes of sea salt particles and three modes of mineral dust. Sea salt emissions are determined as a function of the sea surface temperature and 10-m wind speed [*Lundgren, 2010*]. The mineral dust emissions are calculated online as a function of friction velocity, surface roughness and soil water content [*Vogel et al., 2006*]. Chemical reactions between secondary formed particles and mineral dust are not considered.

The modal approach of MADEsoot determines that all particle modes have initial diameters which are changing during diffusion, transport and due to chemical reactions. Therefore,  $PM_{10}$  and  $PM_{2.5}$  have to be calculated offline according to the modelled diameters of all particles. For this task first of all, the median diameters of the modelled particle modes are calculated depending on their mass and number concentration. This step is done for every grid cell and time step. In the next step all particle modes with diameters smaller  $10\ \mu\text{m}$  and  $2.5\ \mu\text{m}$  are summarized up to receive  $PM_{10}$  and  $PM_{2.5}$  mass and number concentrations. The extraction of the median diameters of all particle modes is done using a shell script with climate data operators (cdo) (<https://code.zmaw.de/projects/cdo>). The summation of all particle modes with diameters smaller  $10\ \mu\text{m}$  and  $2.5\ \mu\text{m}$  is done with NCL.

All aerosols are subject to interactions with meteorological parameters such as radiation and temperature, humidity, precipitation and clouds (see Figure 4). There are effects of the aerosol on the meteorological parameters and vice versa. The most direct effect of aerosol causes changes of the air temperature by altering radiative fluxes in the atmosphere. This is followed by changes of turbulence, wind patterns and clouds. Moreover, humidity and precipitation can be altered. These changes have an impact on the composition and distribution of gases and aerosols. Cloud microphysics interactions are not considered in this work, as the study of climatic effects of aerosols are not the focus. The overview of all feedback processes is described in *Vogel et al.* [2009].

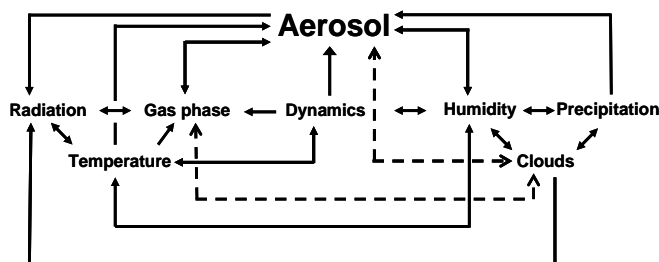


Figure 4: Feedback processes between aerosol and meteorological parameters included in the current COSMO-ART version. The dashed lines indicate cloud feedback processes which are newly included in the upcoming model version.

### 2.2.3.3 Treatment of mineral dust in COSMO-ART

The mineral dust module of COSMO-ART allows the online coupled calculation of three modes of mineral dust mass and number concentrations. For calculating the total dust emission flux into the atmosphere two different fluxes have to be considered, (1) the surface parallel saltation flux  $F_h$  (in  $\text{kg m}^{-1} \text{s}^{-1}$ ) and (2) the vertical flux of smaller particles  $F_v$  (in  $\text{kg m}^{-2} \text{s}^{-1}$ ) (see Figure 5). For this approach the threshold friction velocity parameterization by *Shao and Lu* [2000] and the saltation process parameterization by *Alfaro and Gomes* [1995] are combined. The mineral dust scheme is described in detail in *Vogel et al.* [2006].

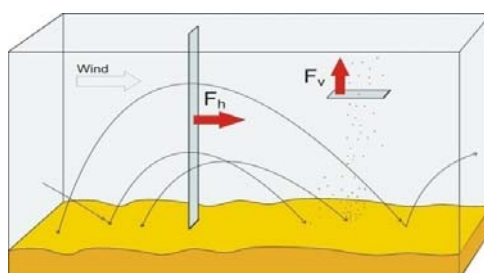


Figure 5: Schematic overview of mineral dust emission fluxes in COSMO-ART.  $F_h$  represents the horizontal saltation flux and  $F_v$  describes the vertical emission flux [Vogel et al., 2006].

#### Horizontal flux

The saltation process starts with the exceedance of the size-dependent threshold value  $u_{*t}(d_p)$  of the friction velocity  $u_*$ . The friction velocity is a parameter describing the impact of the turbulent impulse energy onto the soil surface. It can be defined as following:

$$u_* = \sqrt{-\overline{u' \omega'}} \quad [2.1]$$

The parameter  $u'$  stands for the temporal deviation of the horizontal wind component and  $\omega'$  for the deviation from the vertical wind component.

For ideal conditions with a smooth and dry surface *Shao and Lu* [2000] gained the following parameterization for the threshold friction velocity:

$$u_{*ts}(d_p) = \sqrt{A_n \cdot \left( \frac{\rho_p}{\rho_a} g d_p + \frac{\gamma}{\rho_a \cdot d_p} \right)} \quad [2. 2]$$

$A_n = 0.0123$  and  $\gamma = 3 \cdot 10^{-4} \text{kg s}^{-2}$  are empirical parameters. The factors  $\rho_p$  describe the bulk density of the soil and  $\rho_a$  the air density.

This equation has to be modified for non-ideal conditions with additional parameters for varying soil roughness  $f_{z0}$  and soil humidity  $f_n$ :

$$u_{*t}(d_p) = \frac{f_n \cdot u_{*ts}(d_p)}{f_{z0}} \quad [2. 3]$$

Threshold values of the friction velocity increase with increasing soil roughness and soil moisture and stronger wind velocities are needed to mobilize soil particles for the saltation process.

The influence of soil roughness on the threshold friction velocity is given by an empirically derived equation of *Alfaro and Gomes* [1995]:

$$f_{z0} = 1 - 0.55 \cdot (z_0)^{0.4} \cdot \ln \left( \frac{z_0}{z_{0s}} \right) \quad [2. 4]$$

The term  $z_0$  describes the roughness length of the soil in mm.  $z_{0s}$  denotes the roughness length for smooth surfaces and is estimated to be 1/30 of the diameter of the biggest existing soil particle. Roughness lengths are taken from the soil dataset of *Laurent et al.* [2005]. The dataset is described in section 1.4.2.

Soil moisture is considered according to the following expression of *Fécan et al.* [1998]:

$$f_n = \sqrt{1 + 1.21 \cdot (\eta - \eta')^{0.68}} \quad [2. 5]$$

The relationship is only valid for  $\eta > \eta'$  and 1. The factor  $\eta$  describes the gravimetric soil water content in %, whereas  $\eta'$  denotes the minimal value  $\eta$  can reach.  $\eta'$  depends on the clay content of the soil according to:  $\eta' = 0.0014 \cdot (\% \text{ clay})^2 + 0.17 \cdot (\% \text{ clay})$ .

After the implementation of soil roughness and soil moisture into the equation for smooth and dry conditions from *Shao and Lu* [2000] the following parameterization of the horizontal flux of particles of diameter  $d_p$  can be described according to *White* [1979]:

$$F_h(d_p) = C \cdot \frac{\rho_a}{g} \cdot u_*^3 \cdot \left( 1 + \frac{u_{*t}(d_p)}{u_*} \right) \cdot \left( 1 - \frac{u_{*t}^2(d_p)}{u_*^2} \right) \quad [2. 6]$$

The saltation flux  $F_h(d_p)$  in  $\text{kg m}^{-1} \text{s}^{-1}$  should be seen as a vertically integrated flux, as all particles lifted into the atmosphere by saltation will return to the surface after a while.

Factor  $C$  describes how much soil material is available for erosion and uplift into the atmosphere due to soil crusting [Gomes et al., 2003]. Wind tunnel measurements showed that under ideal and smooth conditions this parameter can be set to a value of 2.61 [White, 1979]. Gomes et al. [2003] showed during a field campaign in Spain that this value is unrealistically high. Studies in the Sahara showed a best fit of model and measurements at a factor of 0.8 [Stanelle et al., 2010]. The factor  $C$  is consistent over time and space and cannot be changed for different dust source regions in the model or during the simulation to consider rain events or the loss of erodible material.

The total horizontal saltation flux  $F_{th}$  is calculated after the integration of flux  $F_h(d_p)$  over all saltation particle sizes:

$$F_{th} = \int_{-\infty}^{\infty} F_{th}(d_p) \cdot \frac{\frac{\pi}{4} d_p^2 n_s^*(\ln d_p)}{\int_{-\infty}^{\infty} \frac{\pi}{4} d_p^2 n_s^*(\ln d_p) d \ln d_p} d \ln d_p \quad [2.7]$$

Parameter  $n_s^*(\ln d_p)$  describes the soil size distribution, representing the sum of different log-normal distributions [Chatenet et al., 1996]. The size distribution of soil particles has a broad range and varies among different locations. Information from measurements is rare, so the parameter carries a huge uncertainty into the parameterization of the mineral dust emissions.

Finally, the size distribution of the soil particle number density  $n_s^*(\ln d_p)$  is replaced by mass density size distribution  $m_s^*(\ln d_p)$  under the assumption that the mass density size distribution is the sum of the three log-normal distributions:

$$n_s^*(\ln d_p) = m_s^*(\ln d_p) \cdot \frac{6}{\pi \cdot \rho_p \cdot d_p^3} \quad [2.8]$$

$$m_s^*(\ln d_p) = \sum_{j=1}^3 m_{s,j}^*(\ln d_p) \quad [2.9]$$

### **Vertical flux**

The calculation of the vertical dust flux  $F_v$  follows an approach of Alfaro and Gomes [2001], which is based on the partitioning of available kinetic energy into the three dust modes. This theoretical concept allows the use of modal distributions of the mineral dust but prevents the determination of a fixed distribution of the particle mass flux under changing conditions. The three log-normal distributed mineral dust modes have fixed median diameters and standard deviations. These properties are defined independent from the underlying soil. The total vertical flux is partitioned over the three modes according to the kinetic energy which is used for mobilization of inactive soil particles by saltation. The kinetic energy depends on size and speed of the saltation particles. The speed is determined by  $u_*$ . Fine soil particles are only released into the

air, when the kinetic energy of the impacting saltation particles exceeds the binding energy of the fine soil particles. The kinetic energy flux  $E(d_p)$  of saltation particles with diameter  $d_p$  is almost proportional to the horizontal saltation flux  $F_h(d_p)$  and is calculated using the following equation with  $\beta = 163 \text{ m s}^{-2}$ :

$$E(d_p) = \beta \cdot F_h(d_p) \quad [2.10]$$

For the vertical mass flux of mode  $i$  which is emitted by saltation particles of diameter  $d_p$  the following equation can be determined:

$$F_{v,i}(d_p) = \frac{\pi}{6} \cdot \rho_p \cdot d_{d,i}^3 \cdot \frac{p_i(d_p) \cdot E(d_p)}{e_i} \quad [2.11]$$

The binding energy of mode  $i$  is represented by  $e_i$ ,  $d_p$  is its corresponding mass median diameter and  $p_i(d_p)$  is the fraction of the kinetic energy  $E(d_p)$  which is available for activation of particles of mode  $i$ . Binding energies are assumed to have constant values for each mode, and show an increasing trend towards the smallest mode (Table 4).

Table 4: Properties of the three mineral dust modes following *Alfaro and Gomes* [2001]

	Mode 1	Mode 2	Mode 3
$d_{g3}$ in $\mu\text{m}$	1.5	6.7	14.2
$\sigma$	1.7	1.6	1.5
$e_i$ in $\text{g cm}^{-2} \text{s}^{-2}$	3.61	3.52	3.46

To receive the total vertical mass flux all vertical mass fluxes of the three dust modes have to be integrated over all saltation particle sizes. The soil size distribution  $n_s^*(\ln d_p)$  is taken into account:

$$F_{tv,i} = \int_{-\infty}^{\infty} F_{v,i}(d_p) \cdot \frac{\frac{\pi}{4} d_p^2 \cdot n_s^*(\ln d_p)}{\int_{-\infty}^{\infty} \frac{\pi}{4} d_p^2 \cdot n_s^*(\ln d_p) d \ln d_p} d \ln d_p \quad [2.12]$$

After replacement of the size distribution of the soil particle number density by mass density the following equation can be expressed:

$$F_{tv,i} = \int_{-\infty}^{\infty} F_{v,i}(d_p) \cdot \frac{1}{d_p} \cdot \frac{m_s^*(\ln d_p)}{\int_{-\infty}^{\infty} \frac{1}{d_p} m_s^*(\ln d_p) d \ln d_p} d \ln d_p \quad ; i=1,3 \quad [2.13]$$

The final vertical dust flux equation reads as:

$$F_{tv,i} = \int_{-\infty}^{\infty} F_{v,i}(d_p) \cdot \frac{1}{d_p} \cdot \frac{\sum_{j=1}^3 \frac{\alpha_j}{\ln \sigma_{s j}} \cdot \exp\left(-\frac{(\ln d_p - \ln d_{gms j})^2}{2 \cdot \ln^2 \sigma_{s j}}\right)}{\int_{-\infty}^{\infty} \frac{1}{d_p} \cdot \sum_{j=1}^3 \frac{\alpha_j}{\ln \sigma_{s j}} \cdot \exp\left(-\frac{(\ln d_p - \ln d_{gms j})^2}{2 \cdot \ln^2 \sigma_{s j}}\right) d \ln d_p} d \ln d_p \quad [2.14]$$

### 2.2.3.4 Aerosol distribution – transport and deposition

The emission of mineral dust particles represents bottom boundary conditions in the model. After diffusion into the lowest model layer the particles are subject to distribution, transport and sedimentation. During these processes the initial particle diameters, mass- and number distributions change.

To calculate changes of the mineral dust total size distribution additional aerosol dynamics equations have to be solved. These equations treat processes which deal with changes of physical and chemical properties of aerosols. Advection, turbulence and sedimentation are taken into account. Dry and wet deposition of the mineral dust particles is included in COSMO-ART. Dry deposition considers sedimentation processes and Brown diffusion following an approach of *Slinn and Slinn* [1980]. The dominant process for mineral dust is sedimentation, due to the in general big sizes of mineral dust particles. The wet deposition of particles by precipitation is treated following *Rinke* [2008]. Coagulation, condensation and evaporation are not considered for mineral dust particles in COSMO-ART. They are also not subject to chemical reactions with gaseous species or photochemical reactions.

For the transport of mineral dust particles, aerosol dynamics equations are solved for two moments of particle size distribution, which are defined by characteristic particle properties. These properties are represented by log normal distributions of three modes with median diameter of the number size distribution and mass size distribution, total number and mass distribution and constant standard deviations. Moment zero is proportional to total number distribution and the third moment is proportional to total mass density. The number distribution of dust particles with a diameter  $d_p$  per volume is given as:

$$n_i^*(\ln d_p) = \frac{N_i}{\sqrt{2\pi \cdot \ln \sigma_i}} \cdot \exp\left(-\frac{(\ln d_p - \ln d_{g,i})^2}{2 \cdot \ln^2 \sigma_i}\right); i=1,3 \quad [2.15]$$

The mass distribution is given as:

$$m_i^*(\ln d_p) = \frac{m_i}{\sqrt{2\pi \cdot \ln \sigma_i}} \cdot \exp\left(-\frac{(\ln d_p - \ln d_{g3,i})^2}{2 \cdot \ln^2 \sigma_i}\right); i=1,3 \quad [2.16]$$

Index  $i$  denotes the three different mineral dust modes,  $d_{g,i}$  and  $d_{g3,i}$  are the number and mass median diameters and  $\sigma_i$  describes the constant standard deviation. Number and mass distribution median diameters are determined by  $d_{g,i} = d_{g3,i} \exp(-3 \ln^2 \sigma_i)$ .

The median diameter of the log-normal distribution is variable in time and space and can be expressed as following:

$$d_{g,i} = \sqrt[3]{\frac{m_i}{\frac{\pi}{6} \rho_s \cdot \exp\left(\frac{9}{2} \ln^2 \sigma_i\right) \cdot N_i}}; i=1,3 \quad [2.17]$$

The following equations describe the diffusion and transport of the dust particles in the air. The equations are averaged with the Reynolds formula. The normalized zeroth moment (mass density) and the third moment (number density) are described as:

$$\frac{\partial \widehat{q}^{M_{0,i}}}{\partial t} = -\widehat{v} \cdot \vec{\nabla} \widehat{q}^{M_{0,i}} - \overline{v_{s,M_{0,i}}} \frac{\partial \widehat{q}^{M_{0,i}}}{\partial z} + \vec{v} \cdot A^{M_{0,i}} \quad [2.18]$$

$$\frac{\partial \widehat{q}^{M_{3,i}}}{\partial t} = -\widehat{v} \cdot \vec{\nabla} \widehat{q}^{M_{3,i}} - \overline{v_{s,M_{3,i}}} \frac{\partial \widehat{q}^{M_{3,i}}}{\partial z} + \vec{v} \cdot A^{M_{3,i}} \quad [2.19]$$

The first terms  $\widehat{v} \cdot \vec{\nabla} \widehat{q}^{M_{0,i}}$  and  $\widehat{v} \cdot \vec{\nabla} \widehat{q}^{M_{3,i}}$  of both equations describe the diffusion of dust particles for both moments. The terms  $\overline{v_{s,M_{0,i}}}$  and  $\overline{v_{s,M_{3,i}}}$  are the sedimentation velocities;  $A^{M_{0,i}}$  and  $A^{M_{3,i}}$  describe the varying dust emissions from the soil. The mass and number concentration of dust in the air is described by diffusion of particles, sedimentation and emission changes.

The sedimentation velocities of number and mass densities are integrated over the log-normal distribution and can be expressed as following:

$$v_{s,M_{0,i}} = \frac{g \cdot \rho_p}{18 \cdot \nu \cdot \rho_a} \cdot \left[ \exp(2 \cdot \ln^2 \sigma_i) + 1.246 \cdot \frac{2 \cdot \lambda}{d_{g,i}} \cdot \exp\left(\frac{1}{2} \cdot \ln^2 \sigma_i\right) \right] \quad [2.20]$$

$$v_{s,M_{3,i}} = \frac{g \cdot \rho_p}{18 \cdot \nu \cdot \rho_a} \cdot \left[ \exp(8 \cdot \ln^2 \sigma_i) + 1.246 \cdot \frac{2 \cdot \lambda}{d_{g,i}} \cdot \exp\left(\frac{7}{2} \cdot \ln^2 \sigma_i\right) \right] \quad [2.21]$$

The factor  $\nu$  stands for the kinetic viscosity of air,  $\rho_p$  is the bulk particle density,  $\rho_a$  the air density,  $g$  describes the acceleration of gravity and  $\nu$  the kinematical viscosity of air.

The source term  $A^{M_{0,i}}$  of equation 2.18 is described by the vertical dust mass flux determined in equation 2.14 and adapted to the numerical grid according to the following assumption:

$$A^{M_{0,i}} = -\frac{\partial F_{tv,i}}{\partial z} \approx \frac{F_{tv,i}}{\Delta z,s} \quad ; i=1,3 \quad [2.22]$$

Term  $\Delta z, s$  is the thickness of the lowest model layer in which the dust is emitted. The source term  $A^{M_{3,i}}$  (equation 2.19) for the particle number concentrations is described by the following equation:

$$A^{M_{3,i}} = \frac{6}{\pi \cdot \rho_p \cdot d_{a,i}^3} \cdot \exp\left(-\frac{9}{2} \cdot \ln^2 \sigma_i\right) \cdot A^{M_{0,i}} \quad ; i=1,3 \quad [2.23]$$

### 2.2.3.5 Radiation in COSMO-ART

For the calculation of short- and long-wave radiative fluxes the General Radiative Algorithm Adapted to Linear-type Solutions radiation scheme (GRAALS) is implemented in COSMO. It is based on parameterizations by *Ritter and Geleyn* [1992]. The radiative transfer is determined by the  $\delta$ -two-stream method, which considers only vertical upward and downward fluxes in both hemispheres. Further information about the  $\delta$ -two-stream method is available in *Ritter and Geleyn* [1992].

As this scheme assumes, that AOD and asymmetry parameters are temporally constant for specific aerosol types, and that aerosol distribution is exponentially decreasing with height, the modified radiation scheme of *Stanelle et al.* [2010] was used. The modified scheme accounts for the high spatio-temporal variability of different kind of aerosols in the atmosphere as optical properties are calculated online.

The total extinction AOD  $\tau_d$  (scattering and absorption) is calculated online for each time step and model level as a function of the specific extinction coefficient  $b$ , single scattering albedo  $\omega$  and asymmetry factor  $g$ . The extinction coefficient, the single scattering albedo and the asymmetry factor depend on particle size and number concentrations and refractive indices and are derived a priori using Mie theory. According to the Mie theory all particles are assumed to be spherical. The refractive index of a particle is determined by its mineralogical composition and the wavelength of incoming radiation. In the model refractive indices are assumed to be similar for all dust particles and to be consistent in time and space. The specific extinction coefficients, single scattering albedo and asymmetry factors are provided offline in a table for the three initial dust modes distributions and eight spectral bands from 250 nm to 1045 nm.

The total AOD is calculated according to the following equation:

$$\tau_d(x, y, z) = b_{ges}(x, y, z) \cdot (h(x, y, z) - h(x, y, z - 1)) \quad [2. 24]$$

The index  $h(x, y, z)$  represents the height of the upper border of the lowest model layer. The index  $b_{ges}$  describes the extinction coefficient for a specific volume with the actual mass concentration  $m_i(x, y, z)$  of mode  $i$  and is calculated as follows:

$$b_{ges}(x, y, z) = \sum_{i=1}^3 b_i \cdot m_i(x, y, z) \quad [2. 25]$$

For this study AOD is calculated for the 555 nm wavelength. The specific extinction coefficients for the three dust modes at a wavelength of 555 nm are  $0.486 \text{ m}^2 \text{ g}^{-1}$  for mode 1,  $0.251 \text{ m}^2 \text{ g}^{-1}$  for mode 2 and  $0.225 \text{ m}^2 \text{ g}^{-1}$  for mode 3. The coefficients are constant in time and space.

A detailed description of the radiation scheme and the calculation of AOD is given in *Stanelle et al.* [2010]. For comparison with satellite data, AOD of all model levels were summarized to receive total AOD values for the whole atmospheric column. This is done using NCL.

### 2.2.3.6 Model handling

The model simulations were conducted on the KIT high-performance computer HP XC3000 (hc3) operated by Steinbuch Centre for Computing (SCC) (<http://www.scc.kit.edu/dienste/hc3.php>).

The model can be controlled directly by using command-line commands forwarded to the computer with the secure shell (ssh) software. The up- and download of input data, all changes of model parameters and files were carried out by using the command-line capabilities offered within ssh. The model has no graphical interface. The model results are available in netcdf format and are post-processed using NCL 6.1.1 and ArcGIS Desktop 10.0.

Main properties of the model runs are controlled by using an executable file, which contains all the necessary information about model domain size, date of simulation period and time steps, several fixed parameters and further necessary input parameters. This file also offers the possibility to turn requested modules on or off, like e.g. the dust module. The executable file is also used to start model runs by using ssh commands.

### 2.2.4 External input datasets for COSMO-ART

To run simulations external input data of meteorological boundary conditions for initialization and update are necessary. For the simulation of anthropogenic aerosols and mineral dust the implementation of a soil dataset and an anthropogenic emission inventory is needed.

The soil dataset and the anthropogenic emission inventory are originally stored in text files which cannot be read into COSMO-ART directly. The pre-processing of these datasets and the meteorological data was done by Heike Vogel of KIT/IMK-TRO. The pre-processing is done using the official COSMO pre-processor INT2COSMO (formerly known as INT2LM) [Knote *et al.*, 2011]. It was also used to interpolate the meteorological initial and boundary conditions, the soil dataset and emission inventory to the COSMO grid.

#### 2.2.4.1 Meteorological data and background pollution data

Initial and boundary meteorological data are taken from the Integrated Forecast System (IFS) model of the European Centre for Medium-Range Weather Forecasts (ECMWF). More information and technical reports of the IFS model are available at the website <http://www.ecmwf.int/research>.

Initial and background concentrations of anthropogenic trace gases and aerosols are taken from the Model for Ozone and Related chemical Tracers version 4 (MOZART-4). MOZART is an offline global chemical transport model providing background concentrations of several trace gases and aerosols on a global grid of  $2.5 \times 2.5^\circ$  [Emmons *et al.*, 2010].

### 2.2.4.2 Soil dataset

The calculation of mineral dust within COSMO-ART is based on modelled wind friction velocity in the lowest model level and soil properties. Soil properties are represented by a soil dataset created by *Laurent et al.* [2005]. The dataset contains information about soil type, particle size distribution, smooth and total roughness length, residual soil moisture and the fraction of the erodible material for each grid cell.

The dataset comprises 12 different soil type areas. The distribution is shown in Figure 6. The erodible fraction is represented by values between 0 and 1, and describes the fraction of material which is available for wind mobilization. The soil roughness length is derived from POLDER-1 (POLarization and Directionality of the Earth's Reflectances) reflectances [*Laurent et al.*, 2005] and data about soil characteristics are determined by analysis of a series of single soil samples collected in the Northeastern Chinese Deserts [*Mei et al.*, 2004; *Laurent et al.*, 2006].

The soil inventory for Northeastern Asia has a spatial resolution of  $0.25 \times 0.25^\circ$  and its domain stretches from  $35.5$  to  $47^\circ$  N and  $73$  to  $125^\circ$  E.

A detailed description of the soil data set is given in *Laurent et al.* [2005] and *Laurent et al.* [2006]. To the authors knowledge this dataset is the most developed soil dataset for mineral dust simulations which is currently available.

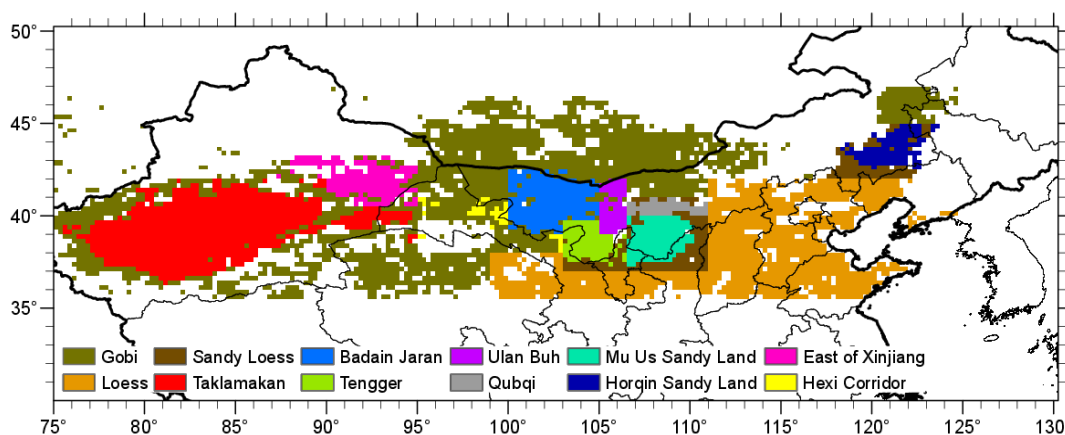


Figure 6: Map of regions comprising similar soil types and soil properties according to the soil dataset of *Laurent et al.* [2005]. 12 Regions are defined: Gobi Desert, loess areas, sandy Loess areas, Taklimakan Desert, Badain Jaran Desert, Tengger Desert, Ulan Buh Desert, Qubqi Desert, Mu Us Sandy Land, Hoqin Sandy Land, desert areas east of Xinjiang, and Hexi Corridor.

### 2.2.4.3 Anthropogenic emission inventory

The anthropogenic emission inventory used in this study was developed by G. Tang from CAS-IAP. It is based on the inventory developed for Asia during the Intercontinental Chemical Transport Experiment-Phase B (INTEX-B) campaign in 2006 [*Singh et al.*, 2009]. The INTEX-B inventory is described in detail in *Zhang et al.* [2009], whereas the inventory adapted by G. Tang is described in *Tang* [2010].

The INTEX-B inventory comprehends 22 countries in Asia and has a horizontal grid size of  $0.5 \times 0.5^\circ$ . Emissions are assigned to four source sectors comprising mobile sources, industrial emissions, emissions from residential areas and emissions from power generation. Every sector comprises carbonmonoxid (CO), nitrogen oxides ( $\text{NO}_x$ ), sulfur dioxide ( $\text{SO}_2$ ), non-methane volatile organic compounds (NMVOC) and particulate pollutants comprised within  $\text{PM}_{10}$  and  $\text{PM}_{2.5}$ . Emissions from biomass burning are not included. General information about the development of regional anthropogenic emission inventories for Asia is given among others in *Streets and Waldhoff* [2000]; *Hao et al.* [2002]; *Cao et al.* [2006]; *Ohara et al.* [2007]; *Klimont et al.* [2009]. The INTEX-B inventory developed by *Zhang et al.* [2009] is very well evaluated within several studies over the past years. INTEX-B was coupled with further national inventories, such as for Korea, leading to convincing results of the estimation of anthropogenic emission strengths in Asia in 2006. The inventory was also compared with bottom-up estimates by *Zhao and Wang* [2009] showing a slight underestimation of some species. An overview about the methodological approach and uncertainties of these bottom-up emission inventories created for China are given in *Zhao et al.* [2011]. There are also several modeling studies using the INTEX-B inventory. *Zhang et al.* [2008a] and *Donkelaar et al.* [2008] used the inventory for studies of the trans-pacific transport of polluted Asian air masses and found a good reproduction of  $\text{SO}_2$ , sulfate, ozone and  $\text{NO}_x$ . *Zhao et al.* [2009] used a regional chemical transport for simulating ozone concentrations with good results, whereas *Chen et al.* [2009] and *Matsui et al.* [2009] reported inconsistencies within the emission inventory by simulating CO concentrations in Beijing.

*Tang* [2010] made four modifications to adapt the inventory for model use. First of all, the extent of the inventory was limited to China and Korea. Secondly, emissions of  $\text{SO}_2$ ,  $\text{NO}_x$ , CO, NMVOC,  $\text{PM}_{10}$ ,  $\text{PM}_{2.5}$  were multiplied with factors of 36%, 55%, 18%, 29%, 13%, and 14%, reconsidering the increasing trend of Asian emission strengths from the years 2006 to 2008. The third modification comprised the interpolation of the inventory from  $0.5^\circ$  resolution to a grid cell size of  $0.25^\circ$  to achieve a better resolution for regional air quality modeling. Interpolation and assembling techniques are described in *Tang* [2010]. The last modification was made to change the temporal resolution of emissions. Within the inventory all species are defined as yearly emissions in  $\text{g s}^{-1}$  for every grid cell. Adapting the inventory for model purposes requested the transformation of yearly emissions to hourly emissions. As emissions stay the same over the whole year and seasonally changes of emissions were not reconsidered, a simple mathematical division of yearly emissions by time was done to achieve hourly emission strengths. G. Tang also transformed the inventory to a lambertian coordinate system with a grid cell size of  $0.25 \times 0.25^\circ$ . The type of projection and grid size were changed back to a kartesian coordinate system with regular grid cell size of  $28 \times 28 \text{ km}^2$  to fulfill requirements of the COSMO-ART model system. The transformation was done using ArcGIS 10.0 [*Sibson, 1981*]. This working step was done for the whole inventory.

The testing and adaption of the inventory is presented in chapter 3.

## 2.3 Methodological constraints on data comparability

### 2.3.1 Comparison of model, ground-based and satellite-based data with different temporal and spatial scales

The comparison of model results to ground-based and satellite-based data imply problems and uncertainties caused by the fact that these data have different temporal and spatial scales. Single point measurements are compared to raster data sets with varying pixel sizes and temporal resolutions. The horizontal resolution of the satellite and model data, used in this study, range from 5 km to 111 km. The data of these raster sets is a spatial average for a certain area, whereas the point measurements reflect the conditions of a specific place within this area. Especially trace gases and aerosols are highly variable in space and time and make it impossible that single measurements reflect the conditions of a wide area. A comparison of ground-based and satellite-based data introduce additional problems as clouds can hamper the capturing of AOD values in one pixel but not in the neighboring cells. Moreover the location of ground-based sites within a specific grid cell is not always clear, especially when sites are located very close at the border of two cells. The same task appears for comparison of model and ground-based measurement data.

The low resolution of COSMO-ART with a grid cell size of 28 x 28 km<sup>2</sup> makes it difficult to follow common approaches of *Gupta and Christopher* [2008] and *Ichoku et al.* [2002] who suggest to take in account surrounding grid cells for comparison of point measurements with raster data. *Ichoku et al.* [2002] mention that the maximum raster size for comparison with point data should not exceed 50 x 50 km<sup>2</sup>. The high trace gas and aerosol variability can introduce ambiguous errors for pixel sizes beyond 50 x 50 km<sup>2</sup> [*Ichoku et al.*, 2002]. For this reasons point measurement data from ground-based stations used within the present work are compared directly to the data of the grid cell they are located in.

For most of the comparisons of satellite derived raster data with model raster data the original grid cell size is kept constant to preserve all the information from the satellite data. The grid cell sizes of the used satellite products are 1.0 ° for OMI, 0.15 ° for MISR, 10 km for MODIS and 5 km for CALIPSO. OMI and MISR do not have equal grid cell sizes in latitude and longitude direction, which explain why data unit is degree. For some comparisons the satellite data is interpolated to a grid size of 0.25 ° to fit to the model data and allow direct raster comparison. These interpolations are done using the nearest neighbor interpolation tool of ArcGIS 10.0.

The mentioned inconsistencies of point and raster data comparison can be reduced to certain extents but should be kept in mind.

### 2.3.2 Effects of comparison of satellite derived and modelled AOD at different wavelengths

In the framework of this study satellite data of wavelengths between 500 nm and 555 nm are analyzed. AOD modelled with COSMO-ART is always calculated for 550 nm.

All AOD wavelengths are within the green band of the visible spectrum of the solar light, which comprises wavelengths from 490 to 575 nm. Aerosols are generally studied in the green band, as scattering and attenuation of radiation by gases is negligible in this band. Therefore, the major part of extinction has to be caused by aerosols. Furthermore, according to Mie theory, the scattering efficiency of aerosols is highest when aerosol diameters are similar to the wavelength of the radiation. As the average worldwide atmospheric aerosol loading contains mainly particles with diameters between 0.5-0.6  $\mu\text{m}$ , the green band is most efficient in scattering this aerosol.

In the present study, AOD data of different wavelengths were compared without using any interpolation methods to create a similar wavelength. It is assumed that possible differences among AOD values which are caused by differing wavelengths are negligible as all wavelengths are still within the same band. This assumption follows findings of *Chin et al.* [2009] who found that effects of small wavelength changes on measured extinction coefficients and AOD values are very small. However, studies of *Eck et al.* [1999] and *Kaskaoutis and Kambezidis* [2006] showed that there are significant differences in extinction efficiency of particles between wavelengths of 440, 675, 870 and 1020 nm.

### **3 Calibration and validation of the COSMO-ART mineral dust module and anthropogenic emission inventory**

Prior to the present study dust simulations with COSMO-ART were conducted for mineral dust of the Sahara Desert in the Dead Sea region [Vogel *et al.*, 2006] and North Africa [Stanelle *et al.*, 2010; Bangert *et al.*, 2012]. However, the dust module has never been used before for the dust sources in Northern China and Southern Mongolia. Therefore a calibration and validation of the dust module was necessary. In addition, the anthropogenic emission inventory was tested and effects of emission changes analyzed. Results of these tests are presented in this chapter.

#### **3.1 Testing and calibration of the mineral dust module**

The dust module was calibrated and validated conducting 1D and 2D sensitivity studies of parameter changes on dust emission fluxes.

##### **3.1.1 Impact of parameter variations on dust emission fluxes – 1D-studies**

To check the functionality of the dust module and the accuracy of the soil dataset, 1D-simulations of dust emission fluxes with the standalone version of the module were conducted [Vogel *et al.*, 2006]. Within the standalone version only dust emissions are calculated without activation of particle distribution and transportation. These simulations give the possibility to determine dust emissions and the ratio of vertical to horizontal dust flux near to the surface under varying conditions. Several parameters such as soil type, C factor, aerodynamic roughness length, the fraction of erodible soil and the wind friction velocity  $u_*$  can be modified manually. See chapter 2 for further explanations of these parameters.

During all simulations soil particle binding energies and soil moisture are kept constant. Soil moisture is set to 0% and binding energies of the three dust modes are  $e_1 = 3.61 \cdot 10^{-7} \text{ g cm}^{-2} \text{ s}^{-2}$ ,  $e_2 = 3.25 \cdot 10^{-7} \text{ g cm}^{-2} \text{ s}^{-2}$  and  $e_3 = 3.46 \cdot 10^{-7} \text{ g cm}^{-2} \text{ s}^{-2}$ . These settings showed best results in previous studies of mineral dust fluxes in sandy and stony deserts of North and West Africa [Vogel *et al.*, 2006; Stanelle *et al.*, 2010]. Binding energies are set according to findings of Alfaro and Gomes [2001].

In the first 1D-simulations the vertical dust fluxes for the 12 different soil types in the study domain and the ratio of the different dust modes were modelled under varying threshold friction velocity values. A map with the distribution and location of all soil types is shown in chapter 2. Factor C is set to 0.02, the erodible fraction and aerodynamic roughness lengths are set to the mean average values typical for the different soil types ranging between 0.25 and 1, as well as  $2.2 \cdot 10^{-4}$  and  $1.05 \cdot 10^{-3}$  mm, respectively. Factor C describes the crusting of the top soil layer, which affects the intensity of modelled dust fluxes.

It can be seen that there are significant differences of the total vertical dust flux among the soil types (Figure 7a). The highest total vertical dust flux is modelled in the sandy desert Badain Jaran in Central China with a maximum of  $85.4 \mu\text{g m}^{-2} \text{s}^{-1}$  for  $u_* = 1 \text{ m s}^{-1}$ . For  $u_* < 0.6 \text{ m s}^{-1}$  the area East of Xinjiang shows higher total dust fluxes. Lowest fluxes are reached in the Loess area. These results seem to be reasonable as the soil types loess and sandy loess consist totally of fine mode soil particles with median diameters smaller than  $74 \mu\text{m}$  and an erodible fraction  $< 0.75$  [Yang *et al.*, 2001]. The soils of the deserts Badain Jaran, Ulan Buh, Mu Us, East of Xinjiang and the Hexi Corridor have in general a higher ratio of coarse particles and erodible mass fraction [Mei *et al.*, 2004]. It takes much higher threshold wind friction velocities for activation of saltation of finer soil particles than coarser ones, due to the higher binding energies of small particles. Therefore, wind friction threshold values play an important role, as an overestimation of the threshold would lead to a suppression of dust fluxes and vice versa.

This simulation shows that the vertical dust fluxes of the different soil types are calculated properly. It can also be seen that the threshold wind friction velocities have a strong effect on dust flux intensities with an increasing trend of intensities towards higher thresholds. It becomes obvious how crucial a correct representation of the specific soil properties for these flux calculations is.

The ratio of the single vertical dust fluxes to the total dust flux for the soil type Gobi is presented in Figure 7b. The C factor is set to 0.02, the erodible fraction is 0.75 and an aerodynamic roughness length of  $1.5^{-3} \text{ mm}$  is assumed. The biggest mode 3 has the highest ratio of all modes, which is increasing with  $u_*$ . The ratio of the smallest mode 1 with a median diameter of  $1.5 \mu\text{m}$  is the lowest of all three modes. The simulation shows that the specific threshold friction velocity for this case is between  $0.4$  and  $0.5 \text{ m s}^{-1}$ . This threshold must be exceeded for the initiation of the saltation flux and the vertical dust flux. As the smallest particles have the highest binding energies the flux is dominated mainly by particles in mode 3.

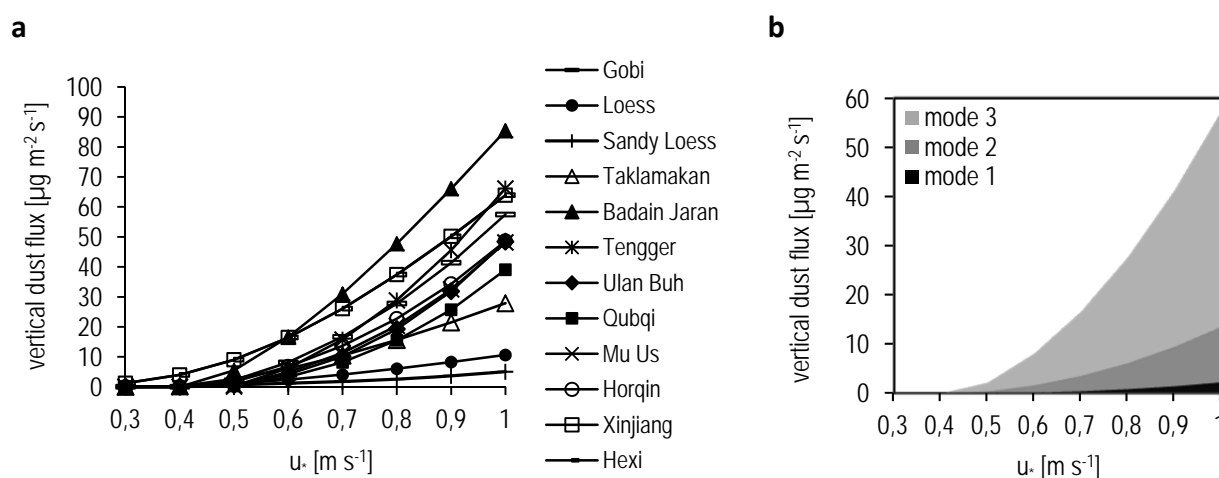


Figure 7: Differences of vertical dust flux intensities of the different soil types in the study domain (soil dataset of Laurent *et al.* [2005]) under changing wind friction velocities between  $0.3$  and  $1.0 \text{ m s}^{-1}$  (Figure 7a) and changes of vertical dust flux intensity of dust modes 1, 2 and 3 for different wind friction velocities between  $0.3$  and  $1.0 \text{ m s}^{-1}$  (Figure 7b).

An additional 1D-study was conducted to show the dependency of the vertical dust flux  $F_{tv}$  towards the horizontal saltation flux  $F_{th}$ , represented by dimension  $\alpha$ .  $\alpha$  is a varying factor representing intensity changes of the vertical flux due to changing friction velocities. If  $\alpha$  would be set to a constant value, the vertical dust flux would just be determined by the saltation flux without influence of the friction velocity. Therefore,  $\alpha$  shows up as a function of soil properties and wind friction velocity, describing changes of the ratio between saltation flux and vertical flux according to wind friction velocity variations.

Figure 8 shows the variability of  $\alpha$  for the two different soil types Gobi and Loess as function of  $u_*$ . In these simulations the mean value of the erodible fraction of all pixels belonging to the specific soil type were taken into account, namely 0.75 for Gobi and 0.07 for Loess. The constant C has no impact on the calculation of  $\alpha$  and is set to 0.02. For soil type Gobi the vertical dust flux starts when  $u_*$  exceeds  $0.4 \text{ m s}^{-1}$  and reaches its maximum at  $u_* = 0.85 \text{ m s}^{-1}$  and is then slightly decreasing (Figure 8a). For the soil type Loess  $\alpha$  exceeds 0 at lower values of  $u_*$  and reaches its maximum at  $0.5 \text{ m s}^{-1}$  and is decreasing towards higher values of the friction velocity (Figure 8b).

It is shown that the vertical dust flux of Loess is decreasing with increasing friction velocities, favoring the importance of the saltation flux. This study also points out the importance of a precise calculation of wind friction velocities. Furthermore, uncertainties are introduced by the missing information and measurement data of soil water contents for the area of Northern China. Studies of *Vogel et al.* [2006] pointed out that an increase of soil water content from 0 to 6 % leads to a total suppression of the vertical dust flux as  $\alpha$  becomes 0.

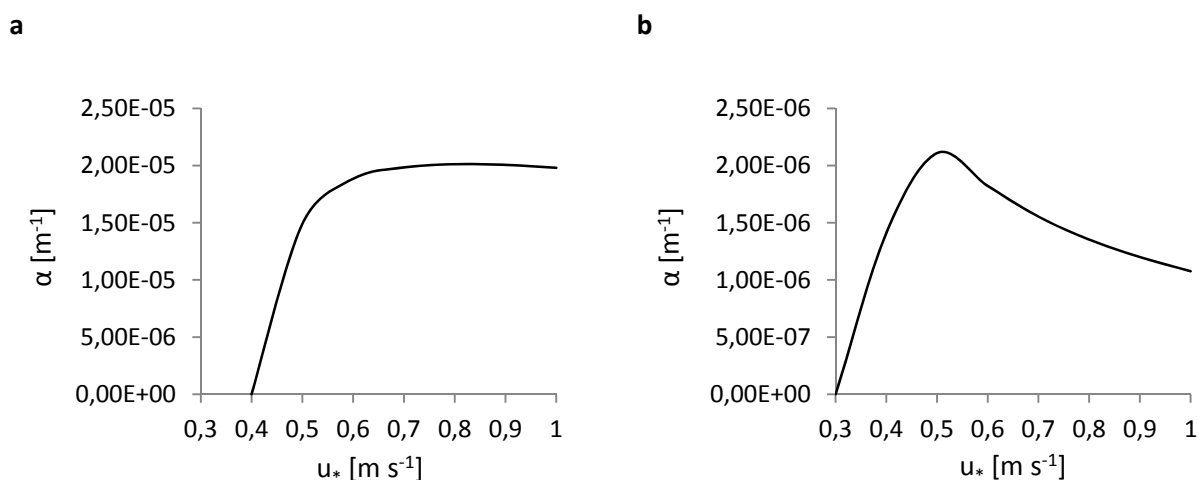


Figure 8: Dimension  $\alpha$  as function of  $u_*$  for soil type Gobi (Figure 8a) and soil type Loess (Figure 8b) with erodible fractions of 0.75, and 0.07, respectively.

Further simulations of the total vertical dust flux for the soil type Gobi showed significant differences between varying values for factor C.  $C = 0.02$  and  $C = 2.5$ , as determined by *Gomes et al.* [2003] and *White* [1979], were chosen for the present analysis.

The study showed that the total dust flux increases tremendously with increasing C and wind friction velocity  $u_*$  (Figure 9). The vertical dust flux at  $C = 0.02$  increases from 2.2 to  $57.4 \mu\text{g m}^{-2} \text{s}^{-1}$  for  $u_* = 0.5$  to  $1 \text{ m s}^{-1}$ . The dust flux with  $C = 2.5$  is increasing by a factor of 26.5 from  $270.2 \mu\text{g m}^{-2} \text{s}^{-1}$  to  $7179.9 \mu\text{g m}^{-2} \text{s}^{-1}$  between wind friction velocities of 0.5 and 1. The dust flux of  $C = 2.5$  is 122.8 times higher for  $u_* = 0.5$  than for  $C = 0.02$ . For a wind friction velocity value of 1 the dust flux of  $C = 2.5$  is even 125.1 times higher. This observation is similar for all soil types in the soil dataset.

The differences of the modelled vertical dust fluxes due to changes of the erodible fraction from 0.75 to 0.9 are very small compared to the impact of a changing C factor (Figure 9a and 9b). The dust flux of soil type Gobi with an erodible fraction of 0.95 is about 1.2 times higher than emissions from the same soil with a fraction of 0.75. The soil type Gobi shows variations of the erodible fraction between 0.6 and 0.92.

Both simulations show that the choice of C has a crucial impact on the modelled vertical dust flux intensity. The resulting dust fluxes for  $C = 0.02$  and 2.5 can differ by a factor of 122.8 for an erodible fraction of 0.75 for  $u_* = 0.5$ . This factor is much lower for calculations with an erodible factor of 0.9 with a value of about 33.1 between fluxes of  $C = 0.02$  and 2.5. For a wind friction velocity of 1 a factor of 125.1 can be assumed for the fluxes of  $C = 0.02$  and 2.5 with erodible fractions of 0.75 and 0.9. These simulations clearly show that the erodible fraction has a rather small impact on the vertical dust flux calculations. However, the choice of the constant C and correct simulation of  $u_*$  are highly critical factors for correct dust flux simulations. These findings coincide with published studies about dust simulation [*Vogel et al.*, 2006; *Darmenova et al.*, 2009; *Pasqui et al.*, 2013].

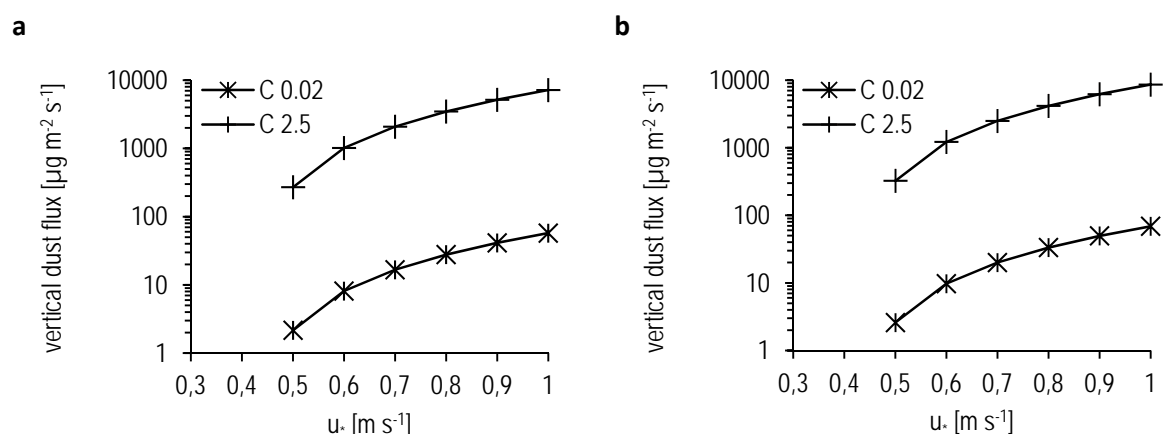


Figure 9: Total dust emission fluxes of the Gobi Desert soils (soil type 'Gobi') with  $C = 0.02$  and  $C = 2.5$  and an erodible fraction of 0.75 (Figure 9a) and 0.9 (Figure 9b) for varying wind friction velocities between 0.3 and 1.0. Vertical dust flux in  $\mu\text{g m}^{-2} \text{s}^{-1}$  (y-axis) is presented in logarithmic scale.

### 3.1.2 Variability of dust emissions – 2D-sensitivity studies

2D-simulations of the mineral dust module of COSMO-ART were conducted to test the reliability of the soil dataset on a regional scale and effects of different C factors on total dust emission fluxes.

1D-simulations already showed that small changes of constant C lead to strong variations of modelled dust emissions. For this reason, C can also be considered as a tuning factor for dust emission simulations. For these 2D-studies C were set to 0.1 and 0.25. These values are much lower than used for studies in Sahara Desert ( $C = 0.8$ ) and Spain ( $C = 2.5$ ) by *Stanelle et al.* [2010] and *Gomes et al.* [2003]. However, previous tests with those two values led huge overestimation of dust emission fluxes for the Asian Deserts (see also the previous section 3.1.1).

In Figure 10 results of varying C values on total dust emissions fluxes are shown. It can be seen that the emission flux for a  $C = 0.25$  is much higher as for  $C = 0.1$ . On August 29 emissions with  $C = 0.25$  are almost double compared to modelled values with  $C = 0.1$  for one specific grid cell in the Gobi Desert in South Mongolia. It showed up that  $C = 0.1$  lead to most reliable emission strengths.

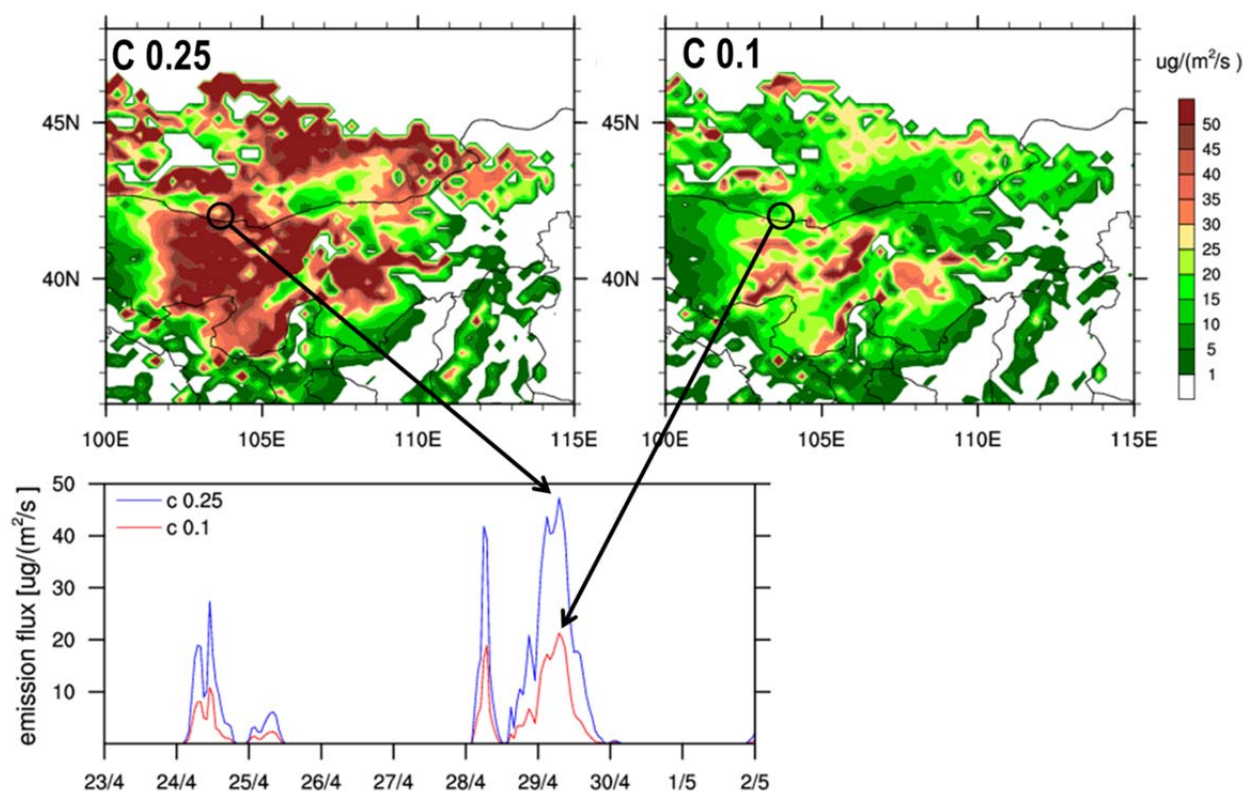


Figure 10: Total dust emissions (in  $\mu\text{g m}^{-2} \text{s}^{-1}$ ) on April 29, 06:00 h (UTC) modelled with COSMO-ART. The left plot shows emissions modelled with  $C = 0.25$  and the right plot shows emissions modelled with  $C = 0.1$ . The bottom plot shows emission changes for both runs from April 23 to May 2 in one grid cell at  $41.875^\circ \text{ N} / 103.875^\circ \text{ E}$  (black circles). The blue line indicates total dust emissions modelled with  $C = 0.25$  and the red line denotes emissions modelled with  $C = 0.1$ .

## 3.2 Testing and adaption of the anthropogenic emission inventory

The anthropogenic emission inventory of G. Tang [Tang, 2010] was used for simulating anthropogenic gaseous and particulate pollutants during the Olympic Summer Games in Beijing in 2008. Before simulating the whole case study episode, the functionality of the anthropogenic trace gas and aerosol module of COSMO-ART and the emission inventory was tested and compared to ground-based measurements. Measurement data was taken from the CAS-IAP network. Afterwards, the reduction factors applied to the inventory were compared with published values and effects of factor variations were studied. See chapter 2 for further explanations about the emission inventory of G. Tang and the CAS-IAP measurement data.

In this analysis only the gaseous pollutants NO, NO<sub>2</sub> and ozone were chosen, as these pollutants show clear diurnal concentration profiles and variations are directly dominated by emission changes. Moreover, these pollutants act as gaseous precursors for secondary aerosol formation. As a huge amount of the urban aerosol load in Beijing consists of such secondary formed particulates [He *et al.*, 2001; Schleicher *et al.*, 2010b], the correct simulation of gaseous precursors is highly important. The analysis of modelled secondary formed particulate concentrations in this section would give no information about the accuracy of the emission inventory. Further analysis of other gaseous precursors is just not possible due to missing measurement data.

For analysis of primary elemental carbon (BC) only daily measurement data is available, which makes it very difficult to study emission changes on a fine temporal scale. See chapter 6 for a comparative study about modelled and measure BC and secondary formed particulates.

### 3.2.1 Diurnal variations of gaseous pollutants

A small study was conducted choosing NO and ozone as test parameters, as both species show a clear diurnal trend close to their sources. Highest NO concentrations are mainly defined by peak emissions during vehicular rush-hours in the morning and afternoon, and maximum ozone concentrations mainly relate to solar radiation and air temperature.

The analysis showed that diurnal variations of NO and ozone in Beijing can be very well reproduced by using COSMO-ART for August 4-8, 2008 (Figure 11, left plot). The temporal course of morning and afternoon NO peaks are very well modelled, whereas the range of NO concentrations show some discrepancies which are determined by emission strength uncertainties. This issue also occurs for ozone and will be discussed in the next section. However, the temporal course of ozone concentrations with their daily maximum peak during noon is also very well modelled (Figure 11, right plot).

The results clearly show that COSMO-ART is working properly simulating the diurnal variations of major gaseous pollutants, even with a coarse model grid of 28 x 28 km<sup>2</sup>.

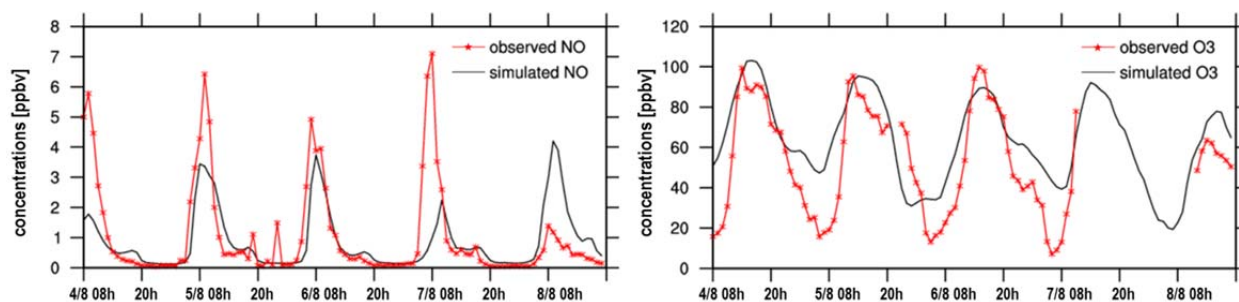


Figure 11: Daily variations of modelled and measured NO (left plot) and ozone (right plot) concentrations (both in ppbv) in Beijing for August 4 at 08:00 h up to August 8 at 19:00 h (local time).

### 3.2.2 Adaption of the anthropogenic emission inventory for the Olympic Summer Games case study

During the Olympic Summer Games from August 8 till 24 in 2008 several reduction measures were undertaken to reduce anthropogenic trace gas and direct aerosol emissions. Reduction measures comprised the closing and dislocation of heavy industry and power plants, traffic reductions, improvement of public transportation, and greening of areas [Wang *et al.*, 2010b; Schleicher *et al.*, 2012; Xin *et al.*, 2012]. Also technical improvements, such as industrial and automotive filter systems were introduced. Moreover, construction sites were closed during the Olympics and an odd-even day traffic control scheme was implemented [Fang *et al.*, 2009; Zhou *et al.*, 2010].

There are two principle approaches of estimating emission reductions: (1) measuring gaseous and particulate pollutant concentrations during the Olympic Summer Games and comparing them to measurements of previous time periods (days to years) and (2) simulating gaseous and particulate pollutant concentrations and adapting implemented emission inventories for estimation of emission reduction factors. In the present study emissions in the emission inventory were reduced according to factors found by Tang [2010]. Afterwards, modelled gaseous and particulate pollutant concentrations were validated using measurement data.

In the emission inventory  $\text{NO}_x$  in Beijing was reduced by a total of 43% for all sectors with a maximum reduction of 65% in the industrial sector (Table 5). In the provinces directly surrounding Beijing,  $\text{NO}_x$  was mainly reduced in the mobile sector by about 40%.  $\text{SO}_2$  in Beijing was only reduced for the power and industrial sector by 15%, and 60%, respectively. Outside of Beijing a stronger reduction was achieved for both sectors.  $\text{SO}_2$  in the mobile sector in the surrounding provinces showed a decrease of 40%.  $\text{PM}_{10}$  had its strongest reduction by 86% in the industrial sector in Beijing. In the surrounding areas  $\text{PM}_{10}$  was reduced less in all sectors with a maximum decrease of 40% in the mobile sector. NMVOCs in Beijing were reduced in the industrial and mobile sector by 65%, and 41%, respectively. For  $\text{NH}_3$  no significant emission reduction was reconsidered.

Table 5: Overview of emission sectors and available reduction factors of NO<sub>x</sub>, SO<sub>2</sub>, PM<sub>10</sub>, NMVOCs and NH<sub>3</sub> (in %) in Beijing and its direct surrounding, being valid for August 2008. In addition the total reductions are summarized for every species.

	Beijing	Species				
		NO <sub>x</sub>	SO <sub>2</sub>	PM <sub>10</sub>	NMVOC	NH <sub>3</sub>
Sector	Total	43	19	34	26	0
	Power	58	15	0	0	0
	Industry	65	60	86	65	0
	Residential	0	0	0	0	0
	Mobile	51	0	51	41	0
	Surrounding					
Sector	Total	21	22	22	10	0
	Power	29	28	23	0	0
	Industry	15	20	20	0	0
	Residential	0	0	0	0	0
	Mobile	40	40	40	40	0

A comparison to further published studies showed that these reduction factors are not always in accordance. However, these differences mainly depend on the method, how emission reduction factors were estimated, the classification of sectors, the area for which reduction measures are taken into account and the strength of emissions before the Olympic Summer Games period. *Gao et al.* [2011] estimated a reduction of total anthropogenic emissions by 50% for Beijing, 35% for the directly surrounding province Hebei and 10% for other provinces. *Guo et al.* [2013] found a reduction of total vehicle emissions by 30% in urban areas and 24% on a regional scale. Furthermore, they estimated a reduction of coal combustion emissions by 57% in urban areas and 7% on a regional scale. *Su et al.* [2011] studied NMVOC in Beijing in August 2008 and found total NMVOC emissions were 45% lower than during June. They estimated a reduction of NMVOC emissions by vehicles and industry by 66% and 15%. A study of *Wang et al.* [2009b] showed that SO<sub>2</sub>, CO, NO<sub>x</sub> and VOC emissions in Beijing were reduced by 60%, 32%, 36%, and 59%, respectively during the Olympic Summer Games compared to August 2006 and 2007. *Wang et al.* [2010b] conducted a more detailed study about emission reductions and found reductions of SO<sub>2</sub>, NO<sub>x</sub>, PM<sub>10</sub> and NMVOC by 41%, 47%, 55%, and 57%, respectively, for August 2008 compared to June 2008. Mobile sources accounted for 65% of the total NO<sub>x</sub> and 42% of the total NMVOC decrease, whereas industry and construction site closing accounted for 34% and 35% of the total PM<sub>10</sub> reduction.

### 3.2.3 Effects of emission factor variations on gaseous pollutant concentrations

A further analysis was conducted to test sensitivities of gaseous pollutant concentrations towards changing emission reduction factors. Three runs were performed for NO and NO<sub>x</sub> and compared to measurements for August 4 till 8. In run A, the specific NO<sub>x</sub> emission factors for the different sectors in Beijing and its surrounding provinces, as shown in Table 5, were reconsidered. In run B, NO<sub>x</sub> emissions were set to a total reduction factor of 50%. In run C, no emission reductions were applied, so it can be used as control run to show concentration levels without reduced emissions.

NO simulations showed that NO concentrations are strongly overestimated without emission reduction (Figure 12, left plot). NO concentrations reach maxima of up to 50 ppbv, whereas concentrations of run A and B are in good agreement with observed NO levels in Beijing. The correlation between run C and observed NO concentrations is very low compared to run A and B. It can also be seen that the correlation between run B and observed NO concentrations is better than for run A (Table 6). However, as average concentrations of run A fit much better with the observational data, emission data with reduction factors of run A were chosen as final input set-up. The comparisons of NO<sub>2</sub> simulations with observational data also showed that concentrations are strongly overestimated without emission reductions. However, minimum values fit very well with observations. It can also be seen that correlation coefficients for measured and modelled NO<sub>2</sub> are overall very low (Table 6), which is mainly determined by a general problem of NO<sub>2</sub> simulation due to its complex chemical nature. For NO<sub>2</sub> the emission data of run A were chosen again as final set-up because the average concentrations are very similar (Table 6). Ozone was also tested and it showed up that correlation coefficients are very good for all runs, but best for run A (Table 6).

Further effects of emission reductions are described and discussed in chapter 6.

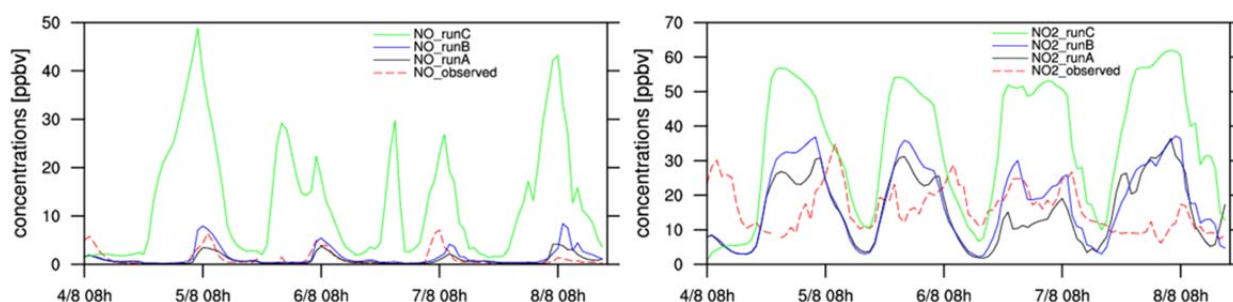


Figure 12: Comparison of observed NO and NO<sub>2</sub> concentrations with three different simulation runs of NO and NO<sub>2</sub> (both in ppbv) in Beijing for August 4, 08:00 h to August 8, 19:00 h (local time). The green lines (NO\_runC and NO<sub>2</sub>\_runC) denote the control runs without emissions reductions, the blue lines (NO\_runB and NO<sub>2</sub>\_runB) represent total NO<sub>x</sub> emission reductions of 50%, the black lines (NO\_runA and NO<sub>2</sub>\_runA) show NO<sub>x</sub> emission reductions according to G. Tang [Tang, 2010], and the red lines denote observed NO and NO<sub>2</sub> concentrations at the measurement site Beijing.

Table 6: Performance statistics of modelled NO, NO<sub>2</sub> and ozone concentrations in Beijing, for August 4, 08:00 h to August 8, 19:00 h (local time) in 2008. The following statistical parameters are calculated: mean average of modelled parameters (ave\_mod), mean average of observed parameters (ave\_obs), number of data points used for calculations (npt) and the Spearman correlation coefficient (r).

statistics	NO			NO <sub>2</sub>			O <sub>3</sub>		
	run C	run B	run A	run C	run B	run A	run C	run B	run A
ave_mod	13.2	1.5	0.9	34.7	17.9	15.4	21.2	40.4	65.9
ave_obs	1.1	1.1	1.1	16.2	16.2	16.2	52.7	52.7	52.7
npt	1.6	106	106	105	105	105	80	80	80
r	0.12	0.82	0.79	-0.17	-0.00	-0.12	0.58	0.73	0.82

## 4 Qualitative analysis of airborne mineral dust dynamics in Northern Chinese dust source regions using COSMO-ART in conjunction with satellite data

### 4.1 Introduction

For estimation of the impact of mineral dust on air quality in Northern China, it is crucial to gain information about dust sources and emission strengths in Asian dust source regions. China and Mongolia are covered by widespread sandy and stony deserts, which emit high amounts of airborne dust during dust events [Sun *et al.*, 2001]. These emissions can have a strong impact on the aerosol burden in Northern China, leading to an increase of AOD of the whole column of the atmosphere and also near-ground PM<sub>10</sub> and PM<sub>2.5</sub> levels.

Defining active dust source regions and estimating dust emission strengths is important for the characterization of dust dynamics in Northern China. However, there are three main challenges to be addressed. First of all, there is little information about the atmospheric amount of mineral dust within the source regions, mainly due to the low spatial coverage of ground-based measurement network sites. The limited number of existing sites renders dust monitoring difficult. The second reason is that continuous measurements of dust emissions in the source regions do not exist. The amount of dust lifted into the air by a dust event can only be estimated by its impact on visibility or PM<sub>10</sub> and PM<sub>2.5</sub> loads. Moreover, air quality sites most often report PM<sub>10</sub> and PM<sub>2.5</sub> mass concentration, which makes it difficult to distinguish the contribution of mineral dust from other natural or anthropogenic sources. This determination is only possible by a chemical analysis of PM composition or particle size measurements, but these methods are expensive and have even lower spatial coverage compared to mass concentration measurements.

Chemistry-transport models and satellite observations can help to fill data gaps of ground based networks by providing a regional perspective at higher spatial resolutions [Laurent *et al.*, 2006]. They also allow a characterization of mineral dust sources, emission strengths and the amount of dust transported towards the Chinese East Coast [Gong *et al.*, 2003; Laurent *et al.*, 2005].

In this chapter, AOD retrieved by passive and active satellite sensors and a weather-chemistry model are qualitatively analyzed for the area of Northern China for nine days in spring 2011. As for health and air quality studies only near ground dust concentrations are important, information about vertical layering and location of dust in the atmosphere is needed. This information can be obtained from the spaceborne lidar CALIOP aboard CALIPSO satellite. A relation of AOD to near-surface PM<sub>10</sub> and PM<sub>2.5</sub> concentrations can be established by combining satellite data with simulations. In this study, the meso-scale fully-coupled weather and chemistry model system COSMO-ART is used. The satellite data can also be used for model validation.

The goals of this study are (1) characterizing the spatio-temporal variability of dust in Northern China using AOD derived by passive satellite sensors and modelled with COSMO-ART, (2) validating COSMO-ART by satellite derived AOD, (3) defining active dust source regions and estimating dust emissions, (4) determine the health relevant amount of dust located near the ground by analyzing vertical CALIPSO profiles in conjunction with COSMO-ART, and (5) assessing air quality degradation due to dust in the North Chinese dust source regions by simulating  $PM_{10}$  and  $PM_{2.5}$  concentrations.

## 4.2 Case study, study domain, model set-up and data

The investigation period for this study is from April 28 to May 2 in 2011. On April 29 and 30 meteorological stations in Taklimakan Desert, Tengger Desert and Gobi Desert in South Mongolia reported widespread dust and blowing sand conditions.

The model domain covers whole Northern China, Southern Mongolia, and Korea from  $30^{\circ}$  to  $50.25^{\circ}$  N and  $75^{\circ}$  to  $130.25^{\circ}$  E (Figure 13). The horizontal resolution of the COSMO-ART simulations is set to  $28 \times 28 \text{ km}^2$ , with 40 vertical layers up to an altitude of 22 km. The model levels are terrain following with varying heights and become flat towards the uppermost level. Layer thicknesses are varying between 20 m for the lowest layer and 2000 m for the uppermost layer. The meteorological initial and boundary conditions for the model are updated every three hours. The calculation of mineral dust starts after one hour of model initialization, reconsidering a spin-off time of the meteorological driver. Boundary dust concentrations are set to zero. Anthropogenic trace gases and aerosols are not calculated in this case study. Model output of meteorological parameters, three initial dust modes,  $PM_{10}$ ,  $PM_{2.5}$ , AOD and dust emissions are available for every hour.  $PM_{10}$  and  $PM_{2.5}$  are only modelled for the lowest model layer (up to 20 m above ground). Meteorological parameters, AOD and initial dust modes are modelled for all layers.

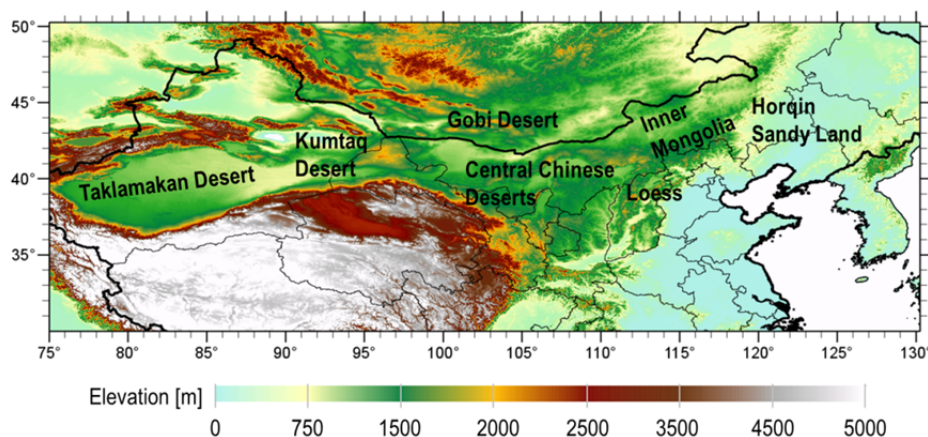


Figure 13: Map of the geo-location of the model domain ( $30\text{-}50.25^{\circ}$  N,  $75\text{-}130.25^{\circ}$  E), country and province boundaries and main desert areas superimposed with a surface elevation map. Elevation in the study domain ranges between 0 and 8848 m. Topographic data is taken from the global digital elevation model provided by the Earth Resources Observation and Science Center (EROS) ([www.eros.usgs.gov](http://www.eros.usgs.gov)).

### 4.3 Methodological approach for satellite and model image processing

A specific image processing approach was created to enhance qualitative comparison and statistical analysis of satellite and model data. Image post processing is done with the ArcGIS 10.0 spatial analyst toolbox.

Daily MODIS data consist of 5-minute-granules, which cover different geographical locations of the study domain at different times (Figure 14). For the analysis of AOD variability and comparison with other data, composite images are created for every day. This procedure was only undertaken for MODIS data, as OMI and MISR products are already provided as daily mosaic images.

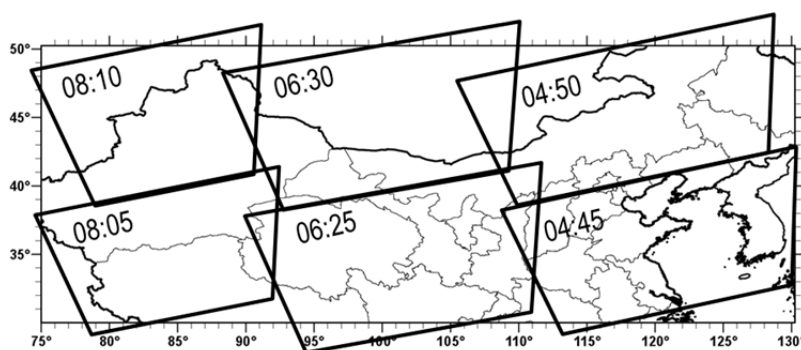


Figure 14: Example of MODIS 5-minute-granules available over the study domain during one day and their times of recording.

For composition of daily MODIS images up to five different granules, with specific times of recording for different locations, have to be combined into one image. Granules which have a temporal gap of more than 10 minutes are cut at their edges to prevent overlapping and are then combined to one image. The specific original spatial resolution of all satellite data is kept in the analysis. This method reduces inaccuracies of AOD values, which would be caused by simple averaging of AOD in the areas where the single images overlap. The same procedure is undertaken for MODIS cloud mask images. An overlapping of the satellite images would lead to a strong increase of biases, as a simple averaging of cloud cover would create totally incorrect data.

The same method is used to generate suitable COSMO-ART AOD images. Before assembling COSMO-ART data, AOD of all model levels is summarized. This step is necessary for comparison with MODIS AOD, as AOD quantifies the aerosol loading over the whole atmospheric column. Next, up to three COSMO-ART images are assembled for specific times which are in temporal accordance with MODIS images.

For an easier comparison with MODIS images, the MODIS cloud mask is overlaid above the composited COSMO-ART AOD images. This means, that all pixels in which cloud cover exceeds 90% (100% are total cloud cover) are colored white to create images comparable towards the MODIS images.

## 4.4 Results

### 4.4.1 Characterization of the spatio-temporal variability of AOD in Northern China

#### 4.4.1.1 Characterization of dust distribution by passive satellite AOD

AOD from MODIS, OMI and MISR is analyzed in detail to characterize the spatio-temporal distribution of airborne mineral dust over Northern China and to identify the active dust source regions. All data are cloud screened and determined to be free of cloud contamination.

Between April 23 and 27 the overall aerosol loading is relatively low with AOD values  $> 1.5$  for almost whole China. MODIS data of April 24 are missing. On April 27 AOD values in the eastern part of Taklimakan Desert start increasing. Between April 28 and May 1 AOD values over the Taklimakan Desert are increased. On April 29 and 30 there are higher AOD values over Southern Mongolia and Inner Mongolia. According to these findings, the following detailed analysis of the spatio-temporal distribution of airborne dust and dust source regions focuses on April 28 to 30.

Figure 15 shows MODIS Deep Blue AOD at 550 nm, OMI AOD at 500 nm, and MISR AOD at 555 nm for the study episode from April 28 to 30. The comparability of AOD at different wavelengths was shown in chapter 2. MODIS and OMI AOD values range between 0.1 and 5.5 and MISR AOD ranges between 0.1 and 1.5.

On April 28 MODIS and OMI AOD is available for parts of the Taklimakan Desert, Kumtaq Desert, the Central Chinese Deserts and some areas in Inner Mongolia (Figure 15a and 3b). OMI and MISR provide less data for this day. MISR provides AOD data for the western edge of the Taklimakan Desert and Central China (Figure 15c). MODIS and OMI detect highest values (4.1 and 5.1) in the Kumtaq Desert, a plain sand desert at the northeastern edge of the Taklimakan Desert. All three satellites also provide data for the southwestern areas of Taklimakan Desert with similar values below 1.1. OMI also shows AOD up to 2.6 for South Taklimakan Desert. Over Central China, MODIS, OMI, and MISR capture low AOD with some individual hot spots of AOD around 1 to 1.5 over Southern Mongolia.

On April 29, MODIS provides most AOD data, showing strong AOD signals in Taklimakan Desert and Gobi in Southern Mongolia and Inner Mongolia (Figure 15d). OMI captures both hot spots (Figure 15e). MISR captures the AOD signal at the eastern edge of the Taklimakan Desert (Figure 15f). MODIS AOD in Taklimakan Desert shows values around 4.1 within a large area and a maximum of 5.3. OMI AOD in this region exceeds 5.5 and MISR captures AOD values of 1.5 at the eastern rim of the Taklimakan. The second AOD hot spot is noted in Gobi Desert in South Mongolia and Inner Mongolia with a mean AOD of 1.0 to 2.8 for MODIS and 2.0 to 4.5 for OMI. However, MISR give some information about aerosol loading in the region south of Beijing. AOD is between 0.5 and 1.2 for all three sensors.

On April 30 high AOD values are captured in Taklimakan Desert (Figure 15g, 15h and 15i). MODIS and OMI AOD have maxima of 4.4, and 4.6, respectively in the south of the desert. MISR AOD shows a peak of 1.3 in the same region. MODIS, OMI and MISR also provide some AOD information for the Central Chinese region. MODIS AOD is below 1.1, whereas OMI captures single spots of higher AOD up to 4.1. MISR AOD for Gobi in Southern Mongolia is mainly lower 0.5. MODIS detects an additional strong AOD signal over Inner Mongolia, Horqin Sandy Land and east of it, with values between 2.0 and 4.2. This signal is not captured by OMI and MISR.

The range of captured AOD values by MODIS and MISR are in agreement with former studies of *Hsu et al.* [2006]. Dust plumes can clearly be distinguished from other aerosols as AOD during such events always exceeds values of 2.0 [*Han et al.*, 2012a].

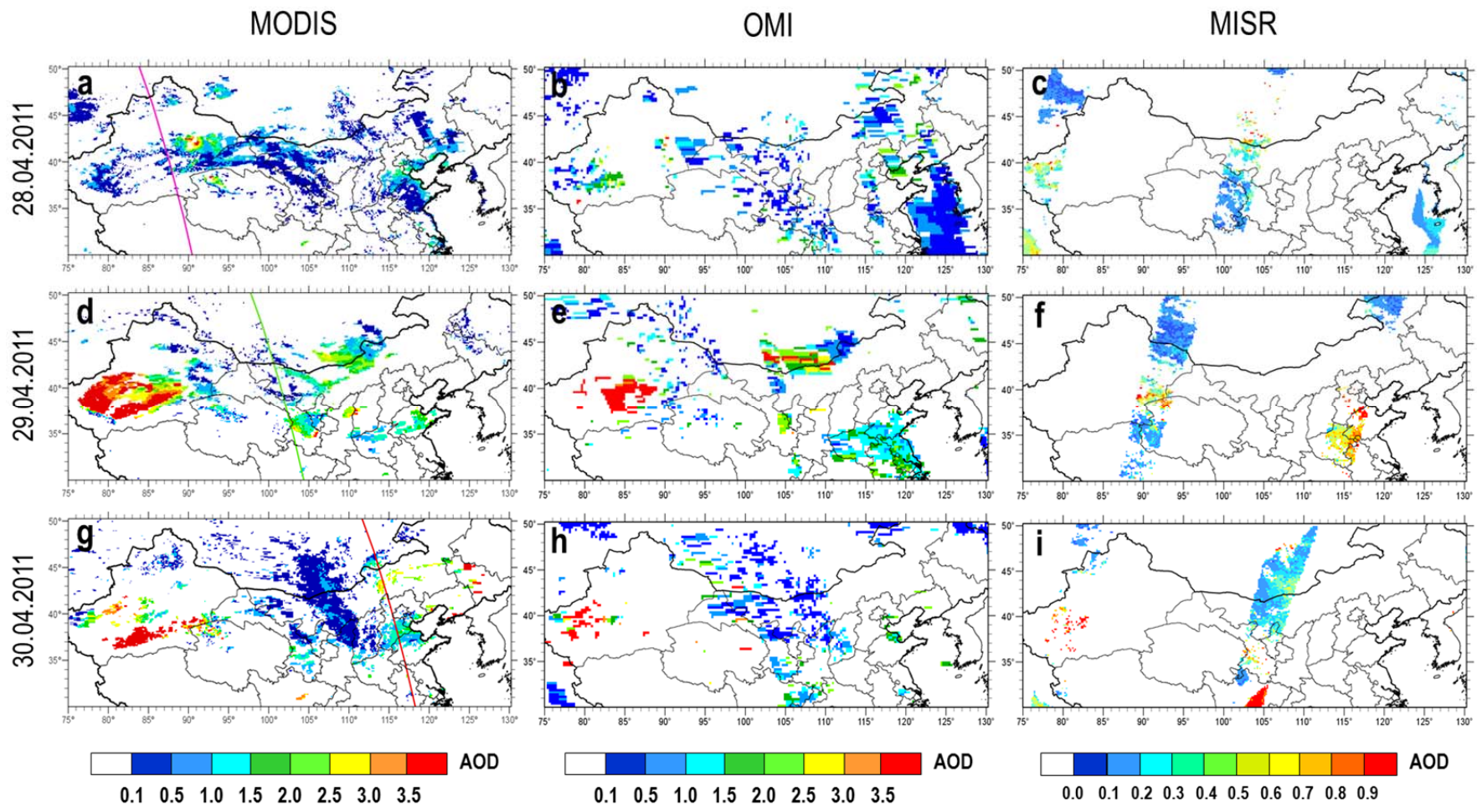


Figure 15: Multi-sensor AOD data for April 28, 29 and 30, 2011 (date is shown on the left hand side of the plot). Color indicates retrieved AOD values; the white color denotes missing or negligible ( $< 0.1$ ) low AOD data due to clouds or snow/ ice cover. The first column shows MODIS Deep Blue AOD for April 28 (a), April 29 (d), and April 30 (g). The second column shows OMI 500 nm AOD for April 28 (b), April 29 (e), and April 30 (h). The third column shows MISR 555 nm AOD for April 28 (c), April 29 (f), and April 30 (i). The colored lines in images (a), (d) and (g) represent CALIPSO overpass paths for each day; the pink line for April 28, the green line for April 29 and the red line for April 30 (data is analyzed in section 4.4.2 and 4.4.3). The AOD range of MODIS and OMI is 0.1 to 3.5; and 0 to 0.9 for MISR.

#### **4.4.1.2 Identification of active dust source regions**

The analysis of MODIS, OMI, and MISR passive satellite data shows that aerosols are present over most of the dust source regions of Northern China during this episode (Figure 15).

On April 28 MODIS and OMI capture a strong AOD signal of 4.1 and 5.1 in the Kumtaq Desert at the eastern rim of the Taklimakan Desert indicating high atmospheric aerosol loading. On April 29 MODIS and OMI capture high AOD up to 5.3, and 5.5, respectively in Taklimakan Desert. Even MISR shows values up to 1.5. As such high values can only be caused by mineral dust, wildfires or volcanic eruptions, these regions can clearly be identified as active source regions during the study episode [Hsu *et al.*, 2006]. Despite of this, the captured aerosol can hardly be mistaken to be anthropogenic aerosol, as these regions are only sparsely populated and urbanized.

A second strong AOD signal can be seen for the Gobi Desert in Southern Mongolia on April 29. Again this AOD can be considered to be mineral dust from this source region. On April 30 high MODIS AOD values are captured for the region of Inner Mongolia, Horqin Sandy Land and east of it. This signal is not detected by OMI and MISR and could be related to the dust source regions of Inner Mongolia and Horqin Sandy Land or it might be a moving dust plume, which was initiated one day earlier in Gobi Desert in South Mongolia. More information about dust transport can be gained from model simulations (see chapter 5.).

#### **4.4.1.3 Simulation of dust distribution by COSMO-ART AOD**

Passive satellites provide high spatial information about the aerosol loading in Northern China, but only for areas where no clouds are present. This circumstance can lead to high amounts of missing AOD data. Models represent a valuable instrument to provide AOD data also for these areas, as aerosol is also calculated when clouds are present.

For that reason COSMO-ART is applied for a three-day episode of April 28 to 30, 2011. The results of the AOD simulations using COSMO-ART are presented in this section (Figure 16).

On April 28 highest AOD is modelled in the Kumtaq Desert at the eastern rim of Taklimakan Desert, in Gobi Desert in Southern Mongolia and North China (Figure 16a). Maximum AOD of 4.6 is modelled for Kumtaq Desert. In Gobi Desert in Southern Mongolia AOD reaches 1.1. AODs below 0.5 are calculated for the region southeast of the Central Chinese Deserts.

On April 29 highest AOD values are modelled for Taklimakan and Kumtaq Desert, Southern Gobi Desert and the Central Chinese Deserts (Figure 16b). AOD of up to 1.2 can be seen for the western rim of Taklimakan Desert and an AOD of up to 2.4 is still present in Kumtaq Desert. AOD in Gobi Desert reaches maxima of 1.4, and 2.1 in Mu Us Sandy Land.

On April 30 simulations reproduce AOD in Taklimakan Desert, Hexi Corridor, the Central Chinese Deserts except of Badain Jaran, Inner Mongolia, Horqin Sandy Land and the region of Beijing (Figure 16c). Highest AOD is modelled for the region south of Beijing with maximum values of 3.1. AOD reaches 1.0 and 1.2 in Taklimakan Desert, and the Central Chinese Deserts, respectively. AOD in Inner Mongolia and Horqin Sandy Land reaches highest AODs of 2.6, and 1.1, respectively.

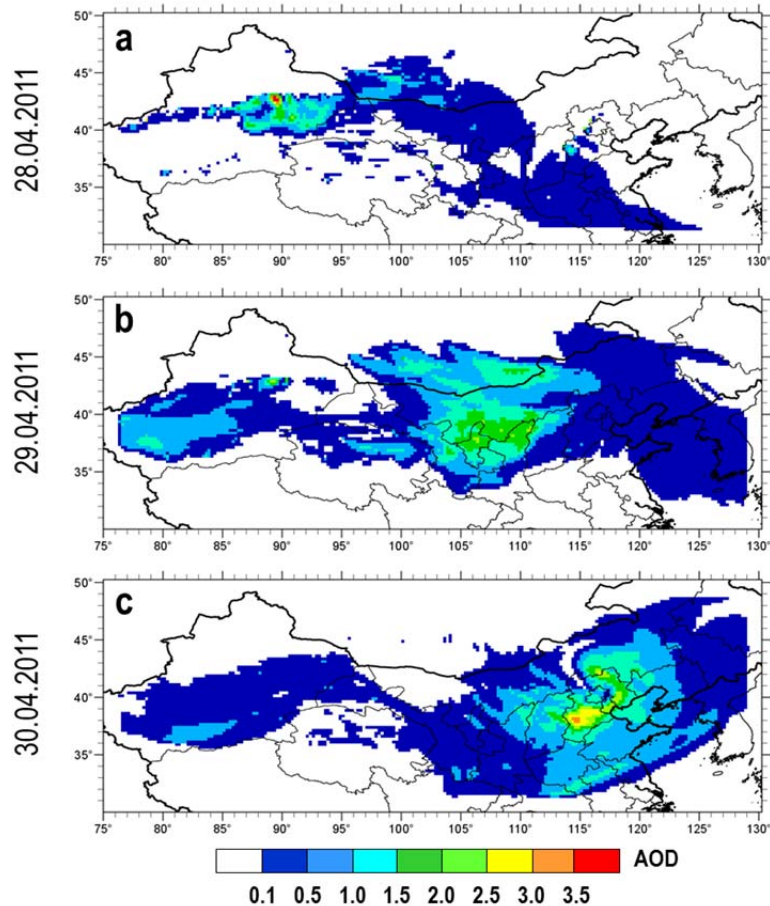


Figure 16: Horizontal distribution of AOD modelled using COSMO-ART for April 28 to 30, 2011. The date is displayed on the left hand side of the plots. AOD range is 0.1 to 3.5. The white color denotes missing or negligible low ( $< 0.1$ ) AOD data due to low aerosol loadings, clouds or snow/ ice cover. Images are composited of up to three single images to fit temporally towards the MODIS composite images. April 28 is composed of images from 06:00 and 08:00 UTC (first plot); April 29 05:00, 07:00 and 08:00 UTC (second plot) and April 30 06:00 and 07:00 UTC (third plot).

#### 4.4.2 Application of satellite derived AOD for model validation

Satellite data from passive sensors can help to improve model performance by providing information about horizontal AOD distribution and the amount of airborne aerosol. In this section model results are verified and validated using satellite data.

For comparison of MODIS and COSMO-ART AOD the MODIS cloud mask is overlaid on COSMO-ART images. The method is described in section 4.3.

To assess the extent of agreement between MODIS derived AOD and modelled AOD, the difference of AOD is calculated for every grid cell. Negative AOD values (blue color) denote an underestimation of modelled COSMO-ART AOD compared to MODIS and positive values (red color) show an overestimation of modelled AOD compared to MODIS AOD (Figure 17c, 17f, 17i).

The qualitative comparison of modelled and measured AOD shows a good agreement of model and satellite regarding AOD spatial distribution on April 28 (Figure 17a and 17b). The main hot spot of atmospheric mineral dust captured by MODIS, namely Kumtaq Desert, is also modelled using COSMO-ART. However, the calculation of AOD differences between COSMO-ART and MODIS shows that COSMO-ART AOD is overestimated by values up to 3.1 for some areas in the southern part of Kumtaq Desert (Figure 17c). In the northeastern part of the desert modelled AOD is underestimated up to 3.0. The increased AOD in Gobi in Southern Mongolia and Northern China is captured by the model. AOD differences in parts of Taklimakan Desert, Inner Mongolia, West Mongolia and Kazakhstan are low with a range of -0.5 to +0.5.

For April 29 the spatial distribution of modeled AOD is in good agreement with the satellite derived AOD of MODIS (Figure 17d and 17e). It should be noted, that AOD modelled for the Yellow Sea is not derived by MODIS, as the Deep Blue AOD algorithm does not capture aerosol over water. AODs in the western edge of the Taklimakan Desert are reproduced by the model; however, AOD values are lower than MODIS AODs with a maximum difference of 3.9 (Figure 17f). The second hot spot in Gobi Desert in Southern Mongolia is also captured by the model, with AOD underestimation up to 1.9. The deviations between satellite and model in the Central Chinese region go up to 1.2 for some single grid cells.

On April 30 the model reproduces the two main aerosol hot spots in South Taklimakan and in the Beijing region (Figure 17g and 17h). However, highest AODs in Beijing are modelled for the area south of Beijing. MODIS captures highest values in Inner Mongolia, north of Beijing. Therefore, the strongest deviations are received for these areas, with a maximum overestimation of modelled AOD of 2.5 in the region south of Beijing and an AOD underestimation of up to 2.8 for the area north of Beijing (Figure 17i). The AOD difference in Taklimakan Desert reaches a maximum of 3.9. AODs in the Central Chinese region and Gobi Desert are in good agreement between 0 to +0.8, and 0 to -0.5, respectively.

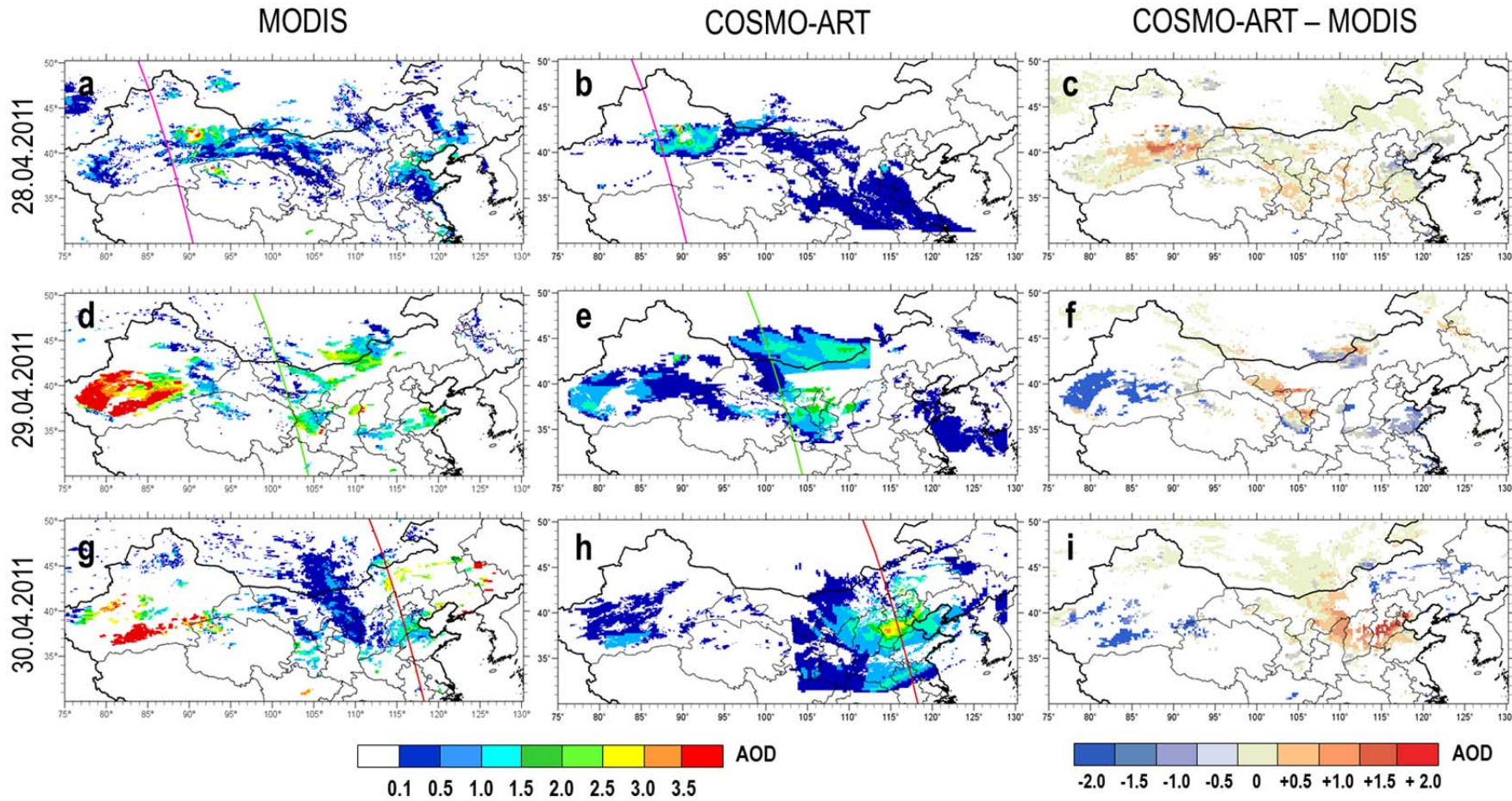


Figure 17: MODIS Deep Blue AOD (left column) and modelled COSMO-ART AOD (center column) for April 28, 06:00 and 08:00 UTC (first row); April 29, 05:00, 07:00 and 08:00 UTC (second row) and April 30, 06:00 and 07:00 UTC (third row). Increasing values of AOD are color coded from blue to red. AOD range is 0 to 4. The white color denotes missing or negligible low (< 0.1) AOD due to clouds or snow/ ice cover. CALIPSO overpass paths are shown by colored lines for April 28 (pink line), April 29 (green line) and April 30 (red line). Differences between modelled and satellite derived AOD for April 28 to 30 are shown in the right column. Blue colors denote AOD < 0.1 which occur when MODIS AOD is higher than COSMO-ART AOD and red colors are AOD > 0.0 representing higher values of COSMO-ART than derived by MODIS; the light beige color shows AOD similar for MODIS and COSMO-ART

To get a better insight into the capability of COSMO-ART to produce reasonable whole column AOD in the three selected source regions, namely Taklimakan Desert, Central China and Inner Mongolia, model results are compared with MODIS and CALIPSO total AOD along the three CALIPSO paths. For this purpose MODIS and CALIPSO AOD are averaged to a grid cell size of  $0.25^\circ$  to fit the horizontal resolution of the simulations. For comparison AOD of MODIS and COSMO-ART is taken of grid cells, which are located closest to the CALIPSO path.

In Taklimakan Desert the model and both satellites capture AOD over the basin on April 28 (Figure 18, first plot). Maximum AODs of COSMO-ART are modelled for  $40.2^\circ$  and  $41.9^\circ$  N with values of 1.6 and 1.1, respectively. AOD of MODIS and CALIPSO reaches 1.4 and 0.6 at the southern edge of the basin at  $39^\circ$  and  $38.4^\circ$  N, respectively. There is not any AOD modelled for the area south of  $39^\circ$  N and north of  $42.2^\circ$  N. There is a huge discrepancy between model and satellites regarding the location of maximum AOD. There seems to be a spatial shift of AOD maximum towards the north in the model.

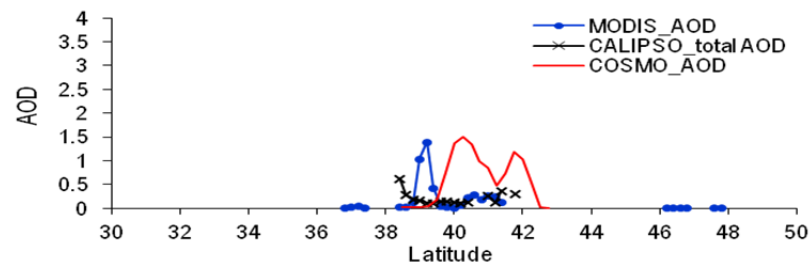
For April 29 the model models AOD between  $32.1^\circ$  and  $46.5^\circ$  N (Figure 18, second plot). There are four major AOD peaks at  $36^\circ$ ,  $38^\circ$ ,  $43.7^\circ$  and  $45^\circ$  N. Model and satellites are in good agreement regarding the location of these AOD peaks. However, modelled AOD values are slightly underestimated for the peaks at  $36^\circ$ ,  $43.7^\circ$  and  $45^\circ$ . The maximum COSMO-ART AOD is 1.4 at  $45^\circ$  N. Modelled AOD between  $39^\circ$  and  $43^\circ$  fits very well with CALIPSO AOD.

On April 30 AOD is modelled for the region between  $31.8^\circ$  and  $47^\circ$  N (Figure 18, third plot). Modelled AOD shows a maximum value of 3.0 at  $38.5^\circ$  N and a minimum of 0.01 at  $41^\circ$  N. Modelled AODs in Inner Mongolia between  $42^\circ$  and  $47^\circ$  N are below 0.31. There are only negligible values of AOD modelled for this region. The model results fit best with the CALIPSO AOD between  $32^\circ$  and  $35.5^\circ$ .

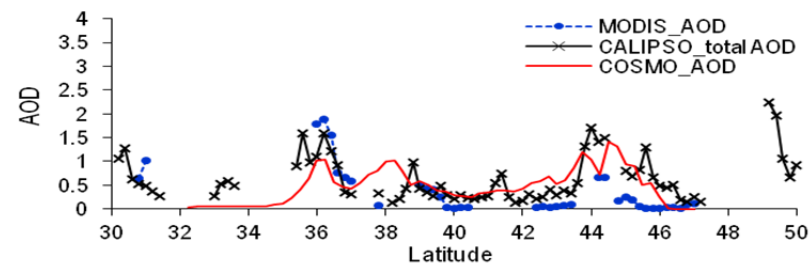
Statistical indicators (mean, median, minimum, maximum, standard deviation, data counts) for modelled COSMO-ART and satellite derived AOD of CALIPSO and MODIS for the three paths are shown in Table 7.

The model is able to reproduce the spatial distribution of total AOD very well for all three paths, whereas significant differences in AOD levels can be found. For all paths minimum AODs of satellites and the model are below 0.1 and maximum AODs are between 1.42 and 3.04. On April 29 the mean AODs of all instruments show lowest variations of all paths of 0.43 to 0.47. Highest biases can be seen for mean AOD of CALIPSO and COSMO-ART for April 28 and for MODIS and COSMO-ART for April 30. Maximum AOD of MODIS and COSMO-ART is in good agreement for Taklimakan Desert on April 28. However, CALIPSO shows a very low maximum of 0.19. The high number of missing AOD seems to lead to a strong underestimation of AOD in this case.

28.04.2011\_07:30 UTC\_Taklamakan Desert



29.04.2011\_06:30 UTC\_Central China



30.04.2011\_05:30 UTC\_Inner Mongolia/ Beijing

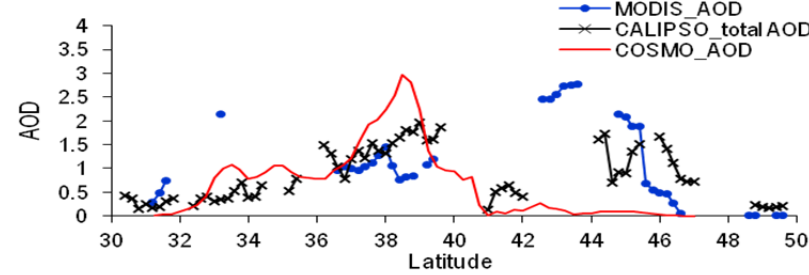


Figure 18: Modelled COSMO-ART AOD (red line), MODIS Deep Blue AOD (blue line with dots) and CALIPSO total AOD (black line with asterisk) captured along the three selected CALIPSO overpass paths from south (30° N) to north (50° N). The overpass regions are Taklimakan Desert on April 28 07:30 UTC (first plot), Central China on April 29 06:30 UTC (second plot) and Inner Mongolia/ Beijing on April 30, 05:30 UTC (third plot).

Table 7: Statistical indicators of CALIPSO and MODIS total AOD for the three CALIPSO cross tracks over Taklimakan Desert on April 28, Central China on April 29 and Inner Mongolia/ Beijing on April 30, 2011. AOD mean (aod\_ave), median (aod\_med), minimum (aod\_min), maximum (aod\_max), standard deviation (aod\_dev) and number of data values (npt) are shown.

		aod_ave	aod_med	aod_min	aod_max	aod_dev	Npt
April 28	MODIS	0.19	0.03	0.02	1.73	0.37	37
	CALIPSO	0.11	0.12	0.03	0.19	0.11	57
	COSMO-ART	0.62	0.63	0.00	1.5	0.54	18
April 29	MODIS	0.43	0.10	0.02	2.71	0.64	47
	CALIPSO	0.45	0.20	0.00	3.04	0.60	265
	COSMO-ART	0.47	0.43	0.00	1.42	0.37	60
April 30	MODIS	1.12	0.96	0.02	2.77	0.84	46
	CALIPSO	0.76	0.40	0.00	3.00	0.77	193
	COSMO-ART	0.68	0.34	0.00	2.96	0.75	64

#### 4.4.3 Simulation of dust emissions inside the source regions using COSMO-ART

MODIS, OMI, MISR and COSMO-ART AOD clearly show aerosol distribution in Northern China and provide information about the activation state of dust source regions. However, dust emissions cannot easily be estimated by means of AOD. COSMO-ART, however, has the capability to model these dust emissions.

Figure 19 shows modelled emissions of all dust modes for April 28 to 30. On April 28 dust emissions reach  $182 \mu\text{g m}^{-2} \text{s}^{-1}$  and  $82 \mu\text{g m}^{-2} \text{s}^{-1}$  in Kumtaq Desert, and Gobi Desert in South Mongolia, respectively (Figure 19). There are no emissions calculated for the Tarim Basin in Central Taklimakan and in general low emissions  $< 5 \mu\text{g m}^{-2} \text{s}^{-1}$  for the Central Chinese Deserts.

On April 29 Taklimakan Desert, the Southern Mongolian Gobi Desert and the Central Chinese Desert are active (Figure 19). Even in Horqin Sandy Land emissions are modelled. In Taklimakan Desert, the Loess Plateau and Horqin Sandy Land emissions are mainly lower than  $10 \mu\text{g m}^{-2} \text{s}^{-1}$ . High emissions up to  $100 \mu\text{g m}^{-2} \text{s}^{-1}$  are modelled for some spots in Gobi Desert and the Central Chinese Deserts east of Badain Jaran.

On April 30, no emissions are modelled in Tarim Basin and Badain Jaran Desert (Figure 19). Emissions in the Central Chinese Deserts are  $< 11 \mu\text{g m}^{-2} \text{s}^{-1}$ . Emissions in Gobi Desert in Southeast Mongolia go up to  $28 \mu\text{g m}^{-2} \text{s}^{-1}$  for single grid cells. Highest emissions of up to  $140 \mu\text{g m}^{-2} \text{s}^{-1}$  are calculated in the Loess Plateau.

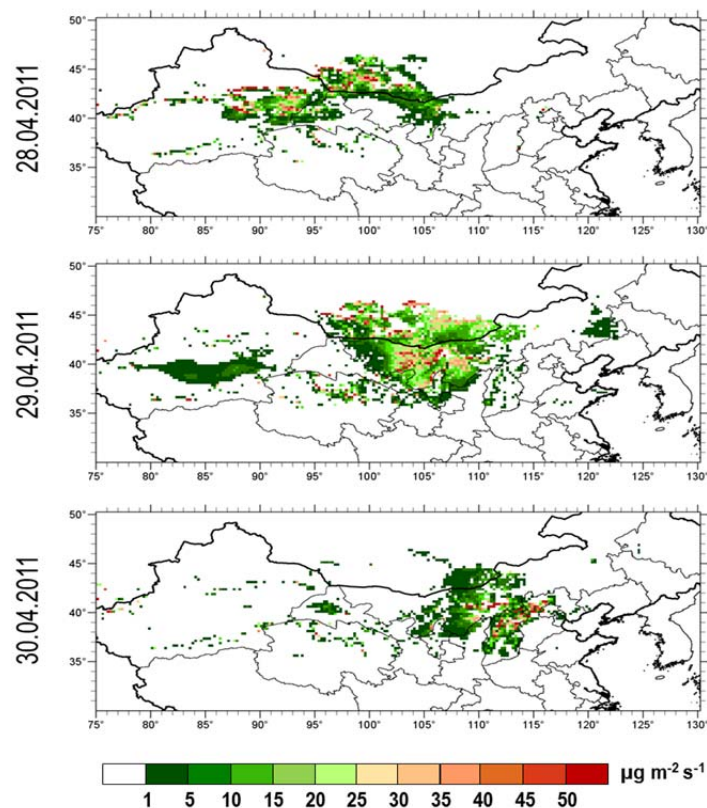


Figure 19: Modelled COSMO-ART total mineral dust emissions summarized of all dust modes in  $\mu\text{g m}^{-2} \text{s}^{-1}$  for April 28, 06:00 and 08:00 UTC (first plot); April 29, 05:00, 07:00 and 08:00 UTC (second plot) and April 30, 06:00 and 07:00 UTC (third plot). White color denotes negligible emissions  $< 1 \mu\text{g m}^{-2} \text{s}^{-1}$ . Date is shown on left hand side of the plot. The bottom scale is valid for all plots.

#### **4.4.4 Analysis of the vertical distribution of dust in the major dust source regions using COSMO-ART and CALIPSO spaceborne lidar data**

Aerosol products of MODIS, OMI and MISR provide information about the spatio-temporal variability of the aerosol loading of the whole atmospheric column. However, these products provide no information about vertical aerosol distributions. Knowledge of vertical aerosol profiles, which show the amount of aerosol located near the ground, is very important for air quality studies.

Moreover, vertical profiles show aerosol plumes aloft, which might have no influence on local air pollution but could be transported over long distances affecting air quality in remote regions, including mid-range transport to the Chinese East Coast or long-range transport to Korea, Japan, or the U.S. Besides the vertical information, clouds and aerosol types can be identified by analyzing CALIPSO cloud and aerosol feature mask data.

To provide a better understanding of the linkage between total column AOD and near-ground air quality, vertical CALIPSO AOD profiles are analyzed. The CALIPSO paths for April 28, 29 and 30 crossing the three main source regions Taklimakan Desert, Central China and Gobi Desert in Southern Mongolia and Inner Mongolia are shown in Figure 15 and Figure 17 (colored lines). In addition, CALIPSO feature AOD and COSMO-ART layer AOD are depicted in comparative way. CALIPSO feature AOD shows AOD values for all features which are classified to be aerosol. The COSMO-ART layer AOD shows modelled AOD values for every grid cell, in which aerosol was modelled. Feature AOD and layer AOD are not directly comparable, as CALIPSO grid cell sizes vary with height.

Studying CALIPSO feature mask data for April 28 aerosol layers all over Taklimakan basin between 38° to 42° up to a height of 6 km can be seen (Figure 20, first column). All aerosol features captured by CALIPSO are classified to be pure dust. There is no other aerosol type identified. One feature in the middle of the dust layer is classified as cloud, which seems to be a misclassification (see discussion section in this chapter). There are several separated dust layers located at different heights. At the southern rim of the basin dust layers are uplifted up to 5.9 km. In the center of the basin most dust is located near the ground. Single feature AOD values detected by the feature mask algorithm are shown in Figure 20, second row, first plot. AOD values range between 0.01 and 0.12. Maximum AODs up to 0.1 can be found in the basin center and the uplifted layer at the southern rim of Taklimakan Desert. Highest layer AOD modelled with COSMO-ART can be seen for the same region (Figure 20, first column, third plot). Most modelled AOD is also located near the ground, which is in agreement with CALIPSO. In the northern rim of the basin uplifted layers can be seen, which are not captured by CALIPSO. However, the spatial shift that occurs in the comparative analysis of MODIS, CALIPSO and COSMO-ART total AOD, is present again.

On April 29 the CALIPSO lidar measures a flat but widely stretched dust layer near the ground for the area of the Central Chinese Deserts and Southern Mongolia between 38° and 47° N. There are some

further dust layers in the southern direction of the path (Figure 20, second column). There is also a small spot of polluted dust at the southern border of the study area. There are some single features between and under the continuous dust layer which are classified as clouds. This seems to be a misclassification and will be discussed later in this chapter. The maximum CALIPSO feature AOD is 2.8 and is located at 44° N. A lot of feature AOD is missing due to different reasons, which is an issue in the discussion section.

The horizontal and vertical location of modelled layer AOD is in good accordance with CALIPSO. All modelled dust is located near the ground and no uplifted layers are present. Highest layer AOD of 0.11 can be seen in the area close to 36° N, which is in accordance with the CALIPSO feature AOD. Higher values are also modelled for the area between 42° and 46° N.

On April 30, a clear near ground dust signal can be seen along the CALIPSO path south of Beijing (Figure 20, third column, first plot). There is no lidar backscatter signal from the surface below the dust layer due to total attenuation of the signal. There are additional smaller spots of dust and polluted dust south and north along the path over Inner Mongolia between 42° to 47° N. However, the signal is not clear, as cloudiness is very high. Feature AOD values of the continuous dust layer between 37° and 40° N show strong variations ranging from 0.4 to 2.8. Feature AOD in Inner Mongolia is between 0.6 and 2.0. Modelled layer AOD shows a maximum of 0.28 close to 38° and 39° N. Most dust is located near the ground, which is in accordance with CALIPSO. There are also some uplifted dust layers between 4 and 11 km height at 33° to 36° N. These layers can also be seen in the CALIPSO feature mask. However, the highest located feature is classified as cloud and the lower located features are classified as polluted dust. The 11 km feature seems to be misclassified, whereas the lower feature seems to be influenced by mixing of dust with local pollutants. There was no dust modelled for Inner Mongolia.

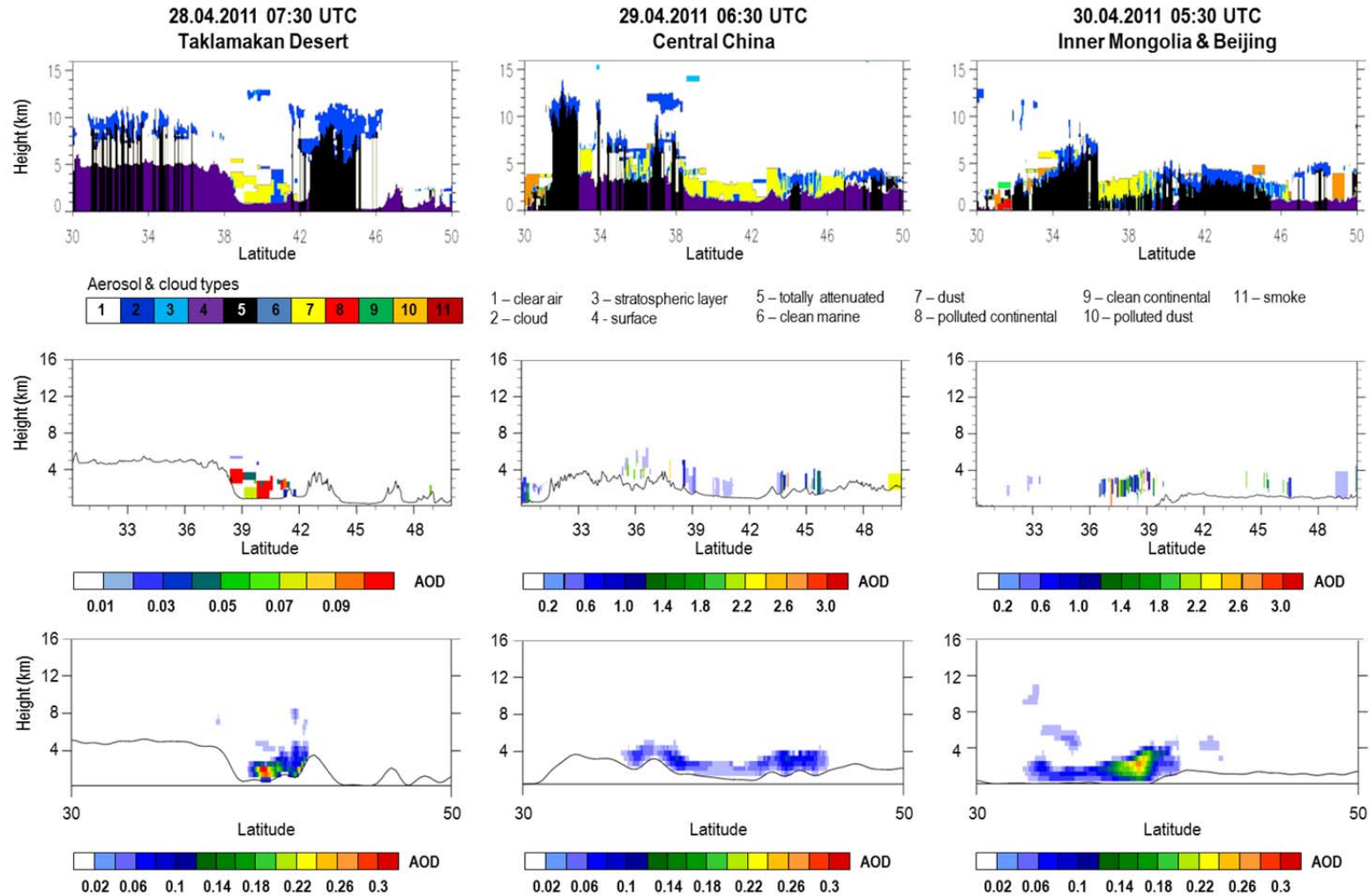


Figure 20: The first three plots of the first row show the vertical location of aerosol and cloud types found by the CALIPSO feature mask algorithm for the three paths over Taklimakan Desert on April 28, 07:30 UTC, Central China on April 29, 06:30 UTC, and Inner Mongolia/Beijing on April 30, 05:30 UTC. The second row represents vertical profiles of CALIPSO feature AOD for each transect. The scale for the first plot is 0.01 to 1.0, scales of the second and third plot are 0.1 to 3.0. The white color donates missing AOD due to inexistence of aerosol, clouds or algorithm failures. The third row shows COSMO-ART layer AOD for the three paths with an AOD range of 0.02 to 0.3.

#### 4.4.5 Assessment of the impact of dust on air quality in the major source regions and dust storm type definition

The use of satellite derived total AOD for air quality assessment without any additional information from ground-based measurement stations is limited, as it does not provide any direct information about PM<sub>10</sub> and PM<sub>2.5</sub> concentrations near the ground. However, PM<sub>10</sub> and PM<sub>2.5</sub> are still the common metrics in assessing air quality. COSMO-ART offers the possibility to provide this missing information by computing total AOD, feature AOD, PM<sub>10</sub> and PM<sub>2.5</sub>.

Near-surface PM<sub>10</sub> and PM<sub>2.5</sub> mass concentrations for the main dust emission source regions on April 28, 29 and 30 are modelled to quantify the impact of mineral dust on air quality within the source regions.

On April 28, PM<sub>2.5</sub> and PM<sub>10</sub> concentrations in Kumtaq Desert reach values of 350-1100  $\mu\text{g m}^{-3}$  and 1000-7000  $\mu\text{g m}^{-3}$  with higher concentrations in some single grid cells up to 1814  $\mu\text{g m}^{-3}$  and 15895  $\mu\text{g m}^{-3}$  (Figure 21a, 21b). PM<sub>10</sub> concentrations in the northeastern part of Badain Jaran Desert and Ulan Buh Desert reach a maximum of 3852  $\mu\text{g m}^{-3}$  in the central area of the region. PM<sub>2.5</sub> in these regions reaches maximum values of 372  $\mu\text{g m}^{-3}$ . PM<sub>2.5</sub> and PM<sub>10</sub> concentrations in Gobi Desert in South Mongolia go up to maximum values of 810  $\mu\text{g m}^{-3}$ , and 7819  $\mu\text{g m}^{-3}$ , respectively.

On April 29 highest PM<sub>2.5</sub> concentrations are modelled for the southwestern rim of Taklimakan Desert, the Central Chinese Deserts and small spots in Gobi Desert in Southern Mongolia (Figure 21c). Highest modelled PM<sub>2.5</sub> concentrations are 611  $\mu\text{g m}^{-3}$  in Taklimakan Desert, 1361  $\mu\text{g m}^{-3}$  in Tengger Desert, and 710  $\mu\text{g m}^{-3}$  in Gobi Desert in South Mongolia. PM<sub>10</sub> concentrations in these regions reach highest values of 2851  $\mu\text{g m}^{-3}$  in Southwest Taklimakan Desert, 6266  $\mu\text{g m}^{-3}$  in Tengger Desert and 6749  $\mu\text{g m}^{-3}$  in single grid cells in the South Mongolian Gobi Desert (Figure 21d).

One day later, on April 30, PM<sub>2.5</sub> levels in South Taklimakan drop to a maximum of 25-338  $\mu\text{g m}^{-3}$  and PM<sub>10</sub> to 100-1394  $\mu\text{g m}^{-3}$  (Figure 21e, 21f). The highest concentrations are calculated for the region between Mu Us Sandy Land and Beijing with maxima of 895  $\mu\text{g m}^{-3}$  for PM<sub>2.5</sub> and 10947  $\mu\text{g m}^{-3}$  for PM<sub>10</sub>.

The modelled concentrations also show that PM<sub>10</sub> and PM<sub>2.5</sub> in all active source regions exceed the Chinese national air quality standard Grade III (> 250  $\mu\text{g m}^{-3}$ ).

It is also important to mention that modelled PM<sub>10</sub> and PM<sub>2.5</sub> concentrations can be very high for some single grid cells inside the source regions. These high values should not be considered as totally wrong, as the validation of AOD values showed that modelled and measured AOD are in similar ranges. According to PM<sub>10</sub> measurements of *Jugder et al.* [2011] in the Asian Deserts and modeling studies of *Ge et al.* [2011] and *Han et al.* [2012a], such high concentrations are possible for short times during dust storms. However, the spatial average of PM<sub>10</sub> and PM<sub>2.5</sub> concentrations over whole regions is much lower. This issue will also be discussed in section 4.5.6 in this chapter.

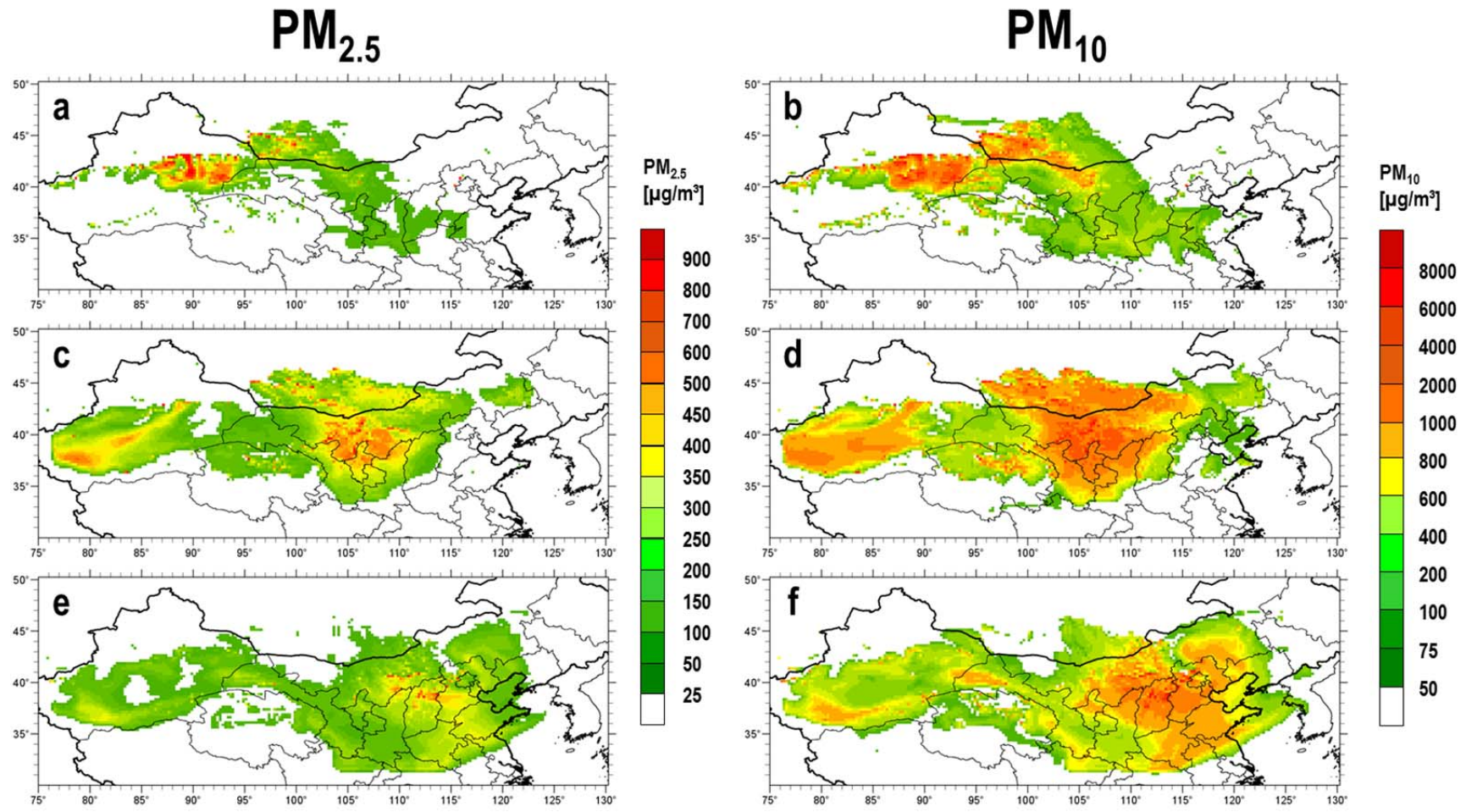


Figure 21: PM<sub>2.5</sub> (left column) and PM<sub>10</sub> (right column) mass concentrations (in  $\mu\text{g m}^{-3}$ ) modelled for the lowest model layer for April 28, 06:00 and 08:00 UTC (first row); April 29, 05:00, 07:00 and 08:00 UTC (second row) and April 30, 06:00 and 07:00 UTC (third row) in the study domain modelled with COSMO-ART. Study time is shown on the left hand side of the plot.

## 4.5 Discussion

### 4.5.1 AOD variations of passive satellite sensors

The intercomparison of MODIS, OMI and MISR AOD in section 1.3 shows that all three sensors capture AOD distribution in Northern China, even in bright desert areas as Taklimakan Desert or the Central Chinese Deserts. Detecting dust particles over bright surfaces is still highly challenging, as the reflectance of the ground is very high, especially in the visible range. Therefore, separating the ground signal from the atmospheric dust signal can be difficult [Hsu *et al.*, 2004]. However, the study showed that the sensors are in good agreement regarding the spatio-temporal aerosol distribution for many areas. However, there can be high differences of AOD values among the sensors. These differences are mainly caused by three constraints, the strong reflectivity of bright surfaces as deserts, cloud contamination of image pixels and technical reasons.

It can be seen, that in the presented study MISR captures often lower AOD values with maximum values of 1.6 even in active source regions. This finding is in accordance with past studies, which showed that MISR tends to underestimate AOD above 1.0 over bright reflecting surfaces up to a factor of 2 [Hsu *et al.*, 2006; Xiao *et al.*, 2009; Wong *et al.*, 2013].

The second reason is often related to cloud contamination of optical satellite images. The study in this chapter showed that OMI AOD values are sometimes biased high with respect to MODIS and MISR. This could often be related to sub-pixel cloud contamination errors [Ahn *et al.*, 2008]. The possibility of cloud contamination is given due to the coarse resolution of OMI images. Moreover, cloudiness is generally very high during Asian dust events, as many of them are triggered by cyclonic systems. Studies of Remer *et al.* [2005] and Ichoku *et al.* [2002] showed, that even MODIS AOD retrieval accuracy is less reliable during cloud cover of 80% and higher within a grid cell. For this reason, only 100% cloud free pixels are considered for the Deep Blue AOD retrieval [Hsu *et al.*, 2004].

The third main reason for differences can be related to different spatial resolutions, retrieval algorithms and calibration methods [Ahn *et al.*, 2008].

A significant difference of satellite derived AOD in this study can be seen for Taklimakan Desert on April 29. OMI only captures AOD in the eastern part of the desert, whereas MODIS captures high values also in the western part. According to the two main constraints on AOD retrieval two explanations are possible. One explanation is that MODIS AOD is strongly overestimated for the western area due to clouds, which are not captured by OMI. The second explanation is that OMI does not capture any AOD in this region because of high reflectivity of the surface. A study of Chen *et al.* [2012] showed that about 15% of atmospheric aerosol is not captured by OMI. These considerations should be kept in mind for model validation.

The study revealed, that AOD is often missing, not only due to clouds but often due to high reflecting surfaces. The high amount of missing data renders also problems to satellite-based validation of modelled data. Further analysis would be needed to obtain more information about systematic discrepancies between the three satellites in dust loaded environments on regional and continental scales [Xiao *et al.*, 2009]. However, to the author's knowledge such detailed studies have not been undertaken yet.

#### **4.5.2 Analysis of modelled and satellite derived total AOD variations**

A comparative study with MODIS, CALIPSO and COSMO-ART data was carried out to validate the capability of the model to reproduce reliable AOD values and spatial distribution.

It showed up that modelled AOD matches with MODIS derived AOD for many regions, regarding the spatial distribution of AOD. AOD could be modelled for Taklimakan Desert, Kumtaq Desert, Gobi Desert and the Central Chinese Deserts, Horqin Sandy Land and the loess area southwest of Beijing. However, modelled AOD is totally missing for Kazakhstan, Southwest Mongolia and some areas of Inner Mongolia. AOD in these regions cannot be reproduced by the model, because they are not included in the soil dataset. The soil dataset is based on POLDER satellite data from 1996 to 1997 [Laurent *et al.*, 2005]. It seems that the ongoing desertification processes, especially in Inner Mongolia increased the extent of some of the existing desert areas [Zhang *et al.*, 2003b]. As Inner Mongolia is still affected by desertification processes, it is a growing dust source and should be reconsidered in future dust simulations.

However, the analysis showed that there are some significant differences between modelled and satellite derived AOD values. Therefore, the conformity of satellite derived and modelled AOD loadings were also studied. It showed up that AOD in Gobi Desert in Southern Mongolia and in the Central Chinese Deserts is reproduced very well by the modeled results with maximum deviations of -0.5 and +1.2 (Figure 22). The strongest underestimation of modelled AOD can be found in Taklimakan Desert, Inner Mongolia and Horqin Sandy Land, with maximum AOD differences of 3.9, 2.9, and 2.8, respectively. The strongest overestimation of modelled AOD in Greater Beijing is 2.5.

It showed up that especially in the Tarim Basin not enough dust is lifted into the air. There are two main reasons possible. One reason can be related to inaccurate values for soil properties in the soil dataset. The threshold friction velocity could be determined to be too high or the erodible soil fraction too low. However, studies of Laurent *et al.* [2005] and Laurent *et al.* [2006] showed, that this issue does not occur during simulations of dust event frequency in Taklimakan Desert. The accuracy of the soil dataset was also tested by own sensitivity analysis presented in chapter 3, without showing any distinctive features. The second reason can be caused by inaccuracies of the dust parameterization. However, this issue was also addressed during the sensitivity studies, which showed that the module is working fine. The third, most likely reason, seems to be an underestimation of dust emissions because of underestimated wind speeds.

This problem occurred also in a study of *Darmenova et al.* [2009] using WRF-Chem model for dust simulation. It seems that the specific basin topography induces a great challenge towards accurate wind simulation. This problem does not exist for Gobi Desert and the Central Chinese Desert, which are located on plateaus. There is also evidence that an inaccurate simulation of wind conditions leads to a southern shift of the dust plume center in the region of Beijing on April 30 which causes an AOD overestimation. This discrepancy between MODIS and COSMO-ART is further analyzed in the following chapter 5.

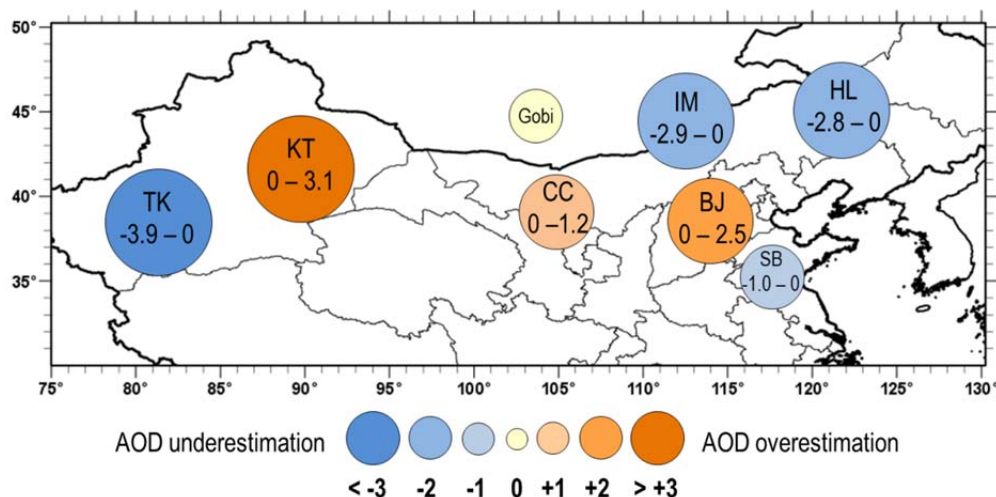


Figure 22: Ranges of differences (expressed as AOD values) of satellite derived and modelled AOD during April 28 to 30, 2011. The blue colored dots denote an underestimation of modelled AOD; orange colored dots denote an overestimation of modelled AOD. The central beige dot denotes no significant difference between COSMO-ART and MODIS (-0.5 – 0.5). The size of the dots is increasing with increasing difference.

The comparison of total AOD of MODIS, CALIPSO and COSMO-ART support the findings of the spatial analysis of MODIS and COSMO-ART AOD distribution. The results showed less agreement for the Taklimakan path on April 28, AOD overestimation at Beijing on April 30 and missing AOD in Inner Mongolia. Explaining this, first of all, it is important to point out that all three instruments use different AOD retrievals and have varying spatial resolutions. The CALIPSO lidar footprint is 90 m at the ground, whereas MODIS's best resolution is 10 x 10 km<sup>2</sup>. COSMO-ART AOD is modelled for 0.25° x 0.25°. It is obvious that a better fit of AOD cannot be achieved. Even regridding of MODIS and CALIPSO to fit the COSMO-ART resolution does not solve the problem. Such issues were also addressed by *Chen et al.* [2012].

However, the comparison also showed a good fitting of modelled results towards the satellites, especially for the Central Chinese path on April 29. The comparison of all paths showed, that modelled data fits better with CALIPSO AOD than MODIS AOD. A study of *Wong et al.* [2013] showed that CALIPSO mainly underestimates AOD. Correlation coefficients are low with maxima of 0.2. However, this finding is not that obvious for this study. Only during the Taklimakan overpass CALIPSO underestimates AOD compared to MODIS and COSMO-ART.

For the comparison of satellite derived and modelled AOD it is also important to mention, that there are main differences of AOD retrieval by these two different instruments. COSMO-ART AOD is calculated using constant wavelength dependent extinction coefficients for the three initial dust modes. AOD variations are strongly connected to changing dust concentrations. Therefore, AOD is mainly triggered by atmospheric dust concentrations determined by emission and transport. Satellite AOD is retrieved by measuring the reflection of solar light in the atmosphere. Extinction coefficients can show strong variations due to aerosol types; the vertical location of aerosol layers and the amount of clouds, which can cause cloud contamination problems (see section 4.5.1). These different approaches can lead to discrepancies between satellite and model AOD. However, as the main aerosol type in desert areas can be assumed to be mineral dust, effects by the different AOD retrievals of satellite and model can be assumed to be negligible. Differences can also be caused by the refractive indices, which describe the mineral structure of the dust particles. They are specific for the different global dust source regions. However, as measurements are rare, refractive indices used in this study are adapted to Saharan dust particles. However, a study of *Darmenova et al.* [2009] showed, that this circumstance only leads to extremely small variations. Further studies about Asian dust particles are needed to provide better information about dust particle and soil properties.

### **4.5.3 Analysis of modelled dust emissions during the case study**

Estimation of dust emissions is a challenging task, as emission strengths are highly variable depending on external constraints like atmospheric conditions and soil properties. Internal constraints on emission parameterization are presented in chapter 2 and chapter 3. As there are no continuous measurements of dust emissions in the Asian Deserts, a quantification of modelled emissions is difficult. However, according to the results of the comparison of AOD derived by satellites and COSMO-ART it can be assumed that the location and amount of modelled emissions can be considered to be overall reliable for the case study.

The study about dust emissions for April 28 to 30 showed that most emissions are modelled for Kumtaq Desert, Gobi and the Central Chinese Deserts and in the loess area between Mu Us Sandy Land and Beijing. The emissions in Kumtaq Desert on April 28 seem to be significantly overestimated as there is a positive bias of the modelled AOD for this regions compared to MODIS. Modelled wind speeds in 10-m height for this region are very strong exceeding  $10 \text{ m s}^{-1}$ , which explains high emissions. As AOD is in good accordance for Gobi Desert for all days during the case study, emissions seem to be in the right order of magnitude. The study clearly shows again that AOD modelled for Inner Mongolia is brought there by transport, as emissions are almost totally missing. This problem is caused by the soil dataset. The high emissions in the loess area on April 30 seem to be overestimated and therefore less reliable. They are as high as in Gobi or the Central Chinese Deserts. This assumption is also supported by the findings of the satellite and model

AOD comparison. This discrepancy could be caused by overestimation of wind speed in the lowest model layer or missing precipitation which can depress dust emission. As modelled wind speeds are very high exceeding  $12 \text{ m s}^{-1}$ , emission overestimation really seems to be caused by incorrect wind simulation. Studies showed that wind speed and soil moisture play in general an important role for correct dust emission calculation [Vogel *et al.*, 2006; Darmenova *et al.*, 2009]. However, the exact simulation of both parameters depends on the capability of the meteorological model. The impact of wind and precipitation on dust transport on April 30 will be discussed in detail in the following chapter.

#### **4.5.4 Analysis of the combined use of CALIPSO and COSMO-ART data for determination of aerosol types and vertical profiles**

The spaceborne lidar aboard CALIPSO is a novel instrument to measure vertical atmospheric profiles of clouds and aerosols. Unlike passive satellite sensors, the CALIPSO lidar can directly observe aerosol over bright areas or beneath thin clouds [Huang *et al.*, 2007; Winker *et al.*, 2009]. However, as desert and snow surfaces have high reflectivity, it is still a challenging task to detect dust particles even by an active sensor. Up to now, studies using CALIPSO data mainly focused on analysis of extinction profiles for biomass burning events [Amiridis *et al.*, 2010], clouds [Grenier *et al.*, 2009], global AOD retrieval [Yu *et al.*, 2010] or dust events [Eguchi *et al.*, 2009]. Up to now, there is only a small number publications about the possibilities of the synergetic use of CALIPSO with models like COSMO-ART to study Asian dust distribution, activation states of dust sources or its impact on air quality [Huang *et al.*, 2007; Amiridis *et al.*, 2013].

The presented study shows that almost all aerosols detected in Taklimakan Desert, the Central Chinese Deserts, Inner Mongolia and Beijing consist of mineral dust. The comparison of vertical CALIPSO and COSMO-ART profiles shows that most of these dust layers are located near the ground with a strong impact on air quality. Both instruments also capture some small elevated layers in different heights. This is indicating that strong wind speeds lifted some amounts of dust up to higher altitudes. The comparison of both datasets also showed that the horizontal location of dust is in mainly good accordance. The main discrepancy between CALIPSO and COSMO-ART is calculated for the Taklimakan case. There is a horizontal spatial shift of the dust plume, which has already occurred in the comparison of MODIS and COSMO-ART total AOD distribution. On April 30 modelled AOD for the area between  $45^\circ$  and  $50^\circ$  N is totally missing, which can be related to missing emissions in this region.

This analysis shows that CALIPSO has the potential to be used for studies about dust distribution, source identification and for air quality studies. However, limitations of CALIPSO became obvious. Misclassification of features, missing feature AOD and algorithm characteristics are the three main challenges for using CALIPSO vertical feature mask data [Young *et al.*, 2013].

Misclassifications can be seen for the Taklimakan case on April 28 and the Central Chinese path on April 29. On April 28 the feature in the middle of the dust layer is classified as cloud but with low confidence

level in the CALIPSO raw dataset offered by NASA. It seems to be a clear misclassification error because of the stretched vertical shape of the feature and its location between and under the surrounding dust layers. In this case, the feature mask algorithm obviously fails a correct classification. For April 29 this problem occurs at 39.5° and 41° N. There are two features between and beneath the dust which are classified as clouds. A further misclassified cloud is located between 42° and 41° N. Between 43° and 45° N, the dust is mixed with near-ground clouds, which can be a potential indicator of possible misclassification problems. This issue is a known problem of the CALIPSO feature mask algorithm tending to classify very dense aerosol layers as cloud. *Chen et al.* [2012] compared OMI towards CALIPSO and showed that up to 11% of aerosol features are misclassified clouds. Another study of *Omar et al.* [2013] shows that CALIPSO tends to detect 45% more clouds in scenes, which are classified by AERONET to be cloud-free. These findings are in correspondence with findings of further studies about the use of the CALIPSO feature mask algorithm [*Huang et al.*, 2007; *Young and Vaughan*, 2009]. This error is induced by uncertainties in the lidar polarization ratio, which characterizes clouds, aerosols and their subtypes. Lidar ratios are determined according to typical aerosol types with similar properties [*Young et al.*, 2013]. However, limited information about these aerosol properties affects the accuracy of the CALIPSO feature mask algorithm [*Burton et al.*, 2013].

These misclassifications and the high amount of data with low confidence level can lead to a significant decrease of feature AOD data. This issue causes the third mentioned challenge. The reduction of feature AOD can clearly be seen for the Central Chinese path on April 29. Several feature AODs are missing for the continuous dust layer between 39°-43° N. This seems to be mainly caused by misclassifications. The high amount of missing data makes it difficult to use it for data comparison or detailed studies.

The third challenge of CALIPSO feature detection is related to technical characteristics. A study of *Omar et al.* [2013] shows that CALIPSO tends to detect only up to 80% of the existing atmospheric aerosol features during day. This circumstance is mainly caused by high interferences of the solar background noise during day, especially over bright desert areas.

#### **4.5.5 Alternative methods of near-ground PM<sub>x</sub> concentration determination by combined use of passive sensor and mixing layer height data**

The study of the vertical location of aerosol in the atmosphere by use of CALIPSO profiles clearly shows that only a certain amount of dust is located near the ground and that several uplifted layers can exist, especially in the case of mineral dust events. These uplifted layers lead to high uncertainties in satellite derived air quality studies, which focus on the establishment of empirical linear relationships between total AOD derived by passive satellite sensors and near-ground PM<sub>10</sub> and PM<sub>2.5</sub> concentrations. Such studies were conducted e.g. by *Guo et al.* [2009a]; *Liu et al.* [2009]; *van Donkelaar et al.* [2010]; *Filip and Stefan* [2011]; *Li et al.* [2011]. Most of these studies take into account relative humidity to consider particle

growth and the effect of mixing layer height (MLH), as it is assumed that 90% of all atmospheric aerosol is within the planetary boundary layer (PBL). This method showed reasonable results for studies of anthropogenic aerosol pollution [Wiegner *et al.*, 2006; Schäfer *et al.*, 2012a; Schäfer *et al.*, 2012b]. However, this approach is difficult to use for analysis of dust storms, biomass burning or volcanic eruptions as these events are often accompanied by the presence of uplifted layers located above the mixing layer height.

#### 4.5.6 Air quality in Northeast Asian desert areas

Only few studies about the impact of dust on air quality in desert regions exist, as only a minor part of the whole Chinese population lives in the Chinese desert regions. This fact renders comparison of results gained in this study difficult.

Jugder *et al.* [2011] analyzed PM<sub>10</sub> and PM<sub>2.5</sub> concentrations from four measurement stations in Gobi and found maximum concentrations of 6626 µg m<sup>-3</sup>, and 2899 µg m<sup>-3</sup>, respectively, during a dust storm in 2010. A modeling study of Ge *et al.* [2011] used RAMS-CMAQ for simulation of PM<sub>10</sub> concentrations for a dust storm in March 2002 and found values exceeding 9000 µg m<sup>-3</sup> in Gobi Desert. Han *et al.* [2012a] used the same model for simulation of a dust storm event in 2010 and found PM<sub>10</sub> concentrations exceeding 5000 µg m<sup>-3</sup> in Gobi in Southern Mongolia and Inner Mongolia and up to 1000 µg m<sup>-3</sup> for the downwind regions. AOD values in these source regions exceeded 2.0. A modeling study of Huang *et al.* [2013] using WRF-Chem found highest PM<sub>10</sub> values of 3900 µg m<sup>-3</sup> in the Hexi Corridor during a dust storm event in May 2011, which was initiated in Gobi Desert in Southern Mongolia. These results indicate that the modelled PM<sub>10</sub> mass concentrations of the study presented in this chapter are in a reliable range. However, for some areas inside the source regions PM<sub>10</sub> seem to be overestimated. This happens in Kumtaq Desert and some areas of the Central Chinese Deserts.

However, as modelled AOD fits well towards four different satellite sensor systems, the real extent of uncertainty remains unsecure. PM<sub>10</sub> and PM<sub>2.5</sub> measurement data is not available for validation in the source regions. However, the impact of dust on air quality will be analyzed in detail for Beijing in the following chapter.

## 4.6 Summary and conclusions

In this chapter an in-depth study about the spatio-temporal variability of dust in Asian dust source regions for a three day episode in April 2011 was presented.

The goals of this study were (1) characterizing the spatio-temporal variability of dust in Northern China using AOD derived by passive satellite sensors and modelled with COSMO-ART, (2) validating COSMO-ART by satellite derived AOD, (3) defining active dust source regions and estimating dust emissions, (4)

determining the health relevant amount of dust located near the ground by analyzing vertical CALIPSO profiles in combination with COSMO-ART, and (5) assessing air quality degradation due to dust in the Northern Chinese dust source regions by simulating PM<sub>10</sub> and PM<sub>2.5</sub> concentrations.

The characterization of dust distribution by passive satellite AOD and modelled COSMO-ART AOD showed that highest AOD can be found in Taklimakan Desert, Kumtaq Desert, Gobi Desert in Southern Mongolia, the Central Chinese Deserts and Inner Mongolia during the study episode. AOD reaches maximum values of 5.3 in Taklimakan Desert. These values are extremely high compared to studies of *Hsu et al.* [2006] and are a clear signal of atmospheric dust. The comparison of the MODIS, OMI and MISR showed that all satellites are in overall good agreement regarding the spatial distribution of dust. Main AOD differences can be caused by algorithm specifications and cloud contamination. As Asian source regions are only sparsely populated and urbanized and are not situated downwind of dense urban areas, the AOD distribution clearly shows the activation state of the source regions. Kumtaq Desert, Taklimakan Desert and Gobi Desert are the main active regions during the study time.

The comparison of modelled AOD with satellite derived AOD showed that the overall spatial distribution of AOD can be reproduced by using COSMO-ART. However, it seems that the activation state of Taklimakan Desert cannot be modelled very well by using COSMO-ART. A similar issue can be seen for Inner Mongolia and Horqin Sandy Land. However, as Inner Mongolia is not included in the soil dataset as own desert source, this problem will remain until an improved version of the dataset is available. These problems lead to an underestimation of AOD for some areas in Taklimakan Desert, Inner Mongolia and Horqin Sandy Land with AOD differences of up to 3.9, 2.9, and 2.8, respectively. There is also an overestimation of modelled AOD for the area near Beijing on April 30 which can be related to incorrect dust emission simulation.

The study showed that dust emissions are increased for Kumtaq Desert and Gobi Desert on April 28, Gobi Desert and Central China on April 29 and the loess area on April 30. Emissions are very low for the Tarim Basin in Taklimakan, causing the underestimation of AOD in this region on April 29 and 30. The high emissions in the loess region seem to be overestimated due to overestimation of 10-m wind speeds. The high emissions in this region and the missing emissions in Inner Mongolia seem to correspond with the southern shift of the dust plume on April 30. This assumption will be analyzed in detail in the following chapter.

Knowledge about the amount of dust located near the ground is very important for air quality studies since these particles mainly affect human health. To determine this amount CALIPSO vertical feature profiles were studied in conjunction with modelled AOD profiles. First of all, CALIPSO clearly showed that almost all AOD captured by the passive satellite sensors is mineral dust. Secondly, almost all of this dust is located near the ground and can reach altitudes of 6 km in the Tarim Basin, Badain Jaran Desert in Central

China, Inner Mongolia and the Beijing plain. The feature mask also shows some uplifted dust layers in Tarim Basin and Beijing. These layers were also modelled for Beijing by using COSMO-ART. However, this study also revealed CALIPSOs limitations for such studies. Data availability, especially feature AOD, can be drastically reduced due to missing data. Reasons are mainly feature misclassifications because of a low lidar signal-noise-ratio due to solar radiation or cloud contamination. Despite of these reasons, CALIPSO has the potential to capture the vertical location of aerosol layers and identify aerosol types. CALIPSO can be used for the improvement of air quality and dust modeling, as it is the only possibility to validate modelled results for dust particle uplifting and vertical distribution.

It can be concluded that the combined use of passive and active satellite data offers a valuable tool for gaining an insight into the spatio-temporal distribution and variability of mineral dust in Northern China for air quality assessment and model validation. An active instrument like the CALIPSO lidar has the potential to provide the missing link between column AOD and the vertical location of aerosol layers.

## 5 In-depth study of airborne mineral dust mid-range transport in Northeast China and its impact on Beijing's air quality using COSMO-ART and ground-based network data

### 5.1 Introduction

Beijing, the capital of China, is frequently hit by dust storms [Han *et al.*, 2007]. During strong storm events long-lasting westerly winds carry high amounts of mineral dust from Asian dust source regions into the city area and its surrounding [Wang *et al.*, 2013]. The arrival time and amount of this dust highly depend on its dynamical distribution and its transport pathway [Zhang *et al.*, 2003a]. Airborne mineral dust can cause a significant degradation of air quality in Beijing and its surrounding by increasing near-ground PM<sub>10</sub> and PM<sub>2.5</sub> mass concentrations [Han *et al.*, 2007]. The health of the city residents is strongly affected by this air quality degradation [Breitner *et al.*, 2011].

Understanding the spatio-temporal dynamics and transport patterns of dust is important for quantification of the impact of dust on air quality in regions located downwind of the widespread Asian dust source regions. However, dust dynamics and transport are still not fully understood, which renders also problems towards the assessment of the impact of dust on Beijing's air quality.

Up to now, studies about Asian airborne dust focused on the investigation about the horizontal distribution of mineral dust [Gong *et al.*, 2003; Uno *et al.*, 2004; Sugimoto *et al.*, 2013], dust storm frequencies and seasonal occurrence statistics [Sun *et al.*, 2001; Ding *et al.*, 2005; Laurent *et al.*, 2005; Shao and Dong, 2006], dust source identification [Xuan and Sokolik, 2002; Wang *et al.*, 2008b; Taramelli *et al.*, 2013], and the estimation of the atmospheric dust loading [Tegen and Fung, 1995; Zender *et al.*, 2004; Tanaka and Chiba, 2006]. Only few studies were conducted analyzing the spatio-temporal dynamics of vertical and horizontal structure of dust storms, and its linkage between wind conditions, orography and transport pathway. Xuan *et al.* [2004] classified two systems of Asian dust events, namely moving dust events and stationary dust events. Transport pathways for moving dust events were studied by Sun *et al.* [2001] and Zhang *et al.* [2003a], who found four to five main routes for dust transport from the main dust source regions to the Chinese Northeast Coast. However, the linkage between transport route and 3D-structure of the dust plume has not yet been studied. A study of Uno *et al.* [2008] focused on 3D-structures of an Asian dust event originating in Gobi Desert by using CALIPSO data and the 4DVAR dust model. However, further detailed 3D-studies about the structure of specific dust events, including horizontal and vertical dust distribution and the temporal movement of dust plumes are rare. Su and Toon [2011] found that Asian dust is distributed in two different vertical layers. Uno *et al.* [2003] pointed out that more detailed studies about dust transport are needed to reduce existing uncertainties. Furthermore, the linkage between orography and dust event structure are not fully understood. There are some studies

about topographic influences and dynamic processes in the atmosphere of the Sahara Desert [Cuesta *et al.*, 2009; Ansmann *et al.*, 2011; Knippertz and Todd, 2012], but not for China.

As there are still open questions about dust dynamics and transport patterns, it is highly challenging to estimate the impact of mineral dust on Beijing's urban air quality. The ground-based monitoring of PM<sub>10</sub> and PM<sub>2.5</sub> mass concentrations is still the common metric used for assessing particulate impact upon air quality. However, ground-based monitoring of mineral dust is difficult due to low spatial coverage of measurement networks and missing international standards for dust event definition. While the Chinese Meteorological Administration classifies dust events in different types according to the impact of dust on visibility [Shao and Dong, 2006], the typical spatial characteristics of these dust event types and their impact on near-ground PM<sub>10</sub> and PM<sub>2.5</sub> concentrations still remain unclear [Wang *et al.*, 2006]. In addition, PM<sub>10</sub> and PM<sub>2.5</sub> concentration measurements do not provide any information about particle types or their sources and source regions. Chemical analysis of particle filters is the common way to determine particle composition and to carry out source apportionment studies as done by Norra *et al.* [2010]; Schleicher *et al.* [2010b]; 2010a]; Schleicher *et al.* [2011b]. However, this method renders difficulties due to high costs and low spatio-temporal coverage of ground-based measurements. Moreover, as hourly Chinese PM<sub>10</sub> and PM<sub>2.5</sub> measurement data are hardly available for scientific studies, most researchers focus on the comparison of modelled data towards API (air pollution index) [Bian *et al.*, 2011; Ge *et al.*, 2011]. However, API data has limitations which render its use for dust impact studies difficult. First of all, API index values describe the air quality in total and not only PM<sub>10</sub> pollution [Bian *et al.*, 2011]. Secondly, the API index is limited to a value of 500. Strong air quality degradation with PM<sub>10</sub> values higher 500, which often occur during dust events, cannot be described by it.

To gain more information about airborne mineral dust dynamics, 3D-mid-range transport patterns and the impact of dust on air quality in Greater Beijing, the model system COSMO-ART was used in conjunction with ground-based measurement and CALIPSO satellite data.

Using COSMO-ART for a specific dust storm episode in April 2011, offers high resolved spatio-temporal information about airborne dust dynamics in Northern China and characteristics of mid-range dust transport from source regions to Beijing. The analysis focuses on a three day episode from April 28 to 30 in 2011. In addition, COSMO-ART was used to model dust emissions and 10-m height wind speeds to investigate dust mobilization in the main dust source regions. Studying mid-range transport patterns of airborne dust gives also information about the characteristics of its horizontal and vertical distribution. Furthermore, the qualitative analysis of modelled PM<sub>10</sub> and PM<sub>2.5</sub> concentrations in conjunction with ground-based measurements offers the possibility to identify the impact of dust on air quality. In addition, information about potential mixing processes of dust with local anthropogenic aerosols can be gained by analyzing CALIPSO vertical feature mask data, which provides information about aerosol types.

The goals of this work are (1) characterizing spatio-temporal dynamics of mineral dust in Northern China, (2) analyzing characteristics of dust mobilization in the dust source region of this dust event, (3) understanding the mid-range transport pattern of the dust moving towards Eastern China, (4) assessing the impact of airborne mineral dust on air quality in the metropolitan area of Beijing, and (5) studying the mixing of mineral dust with local pollutants by analyzing CALIPSO aerosol type information.

## **5.2 Case study**

For the case study about the impact of mineral dust on air quality in Beijing the same model set-up is used as for the study of mineral dust in the dust source regions presented in chapter 4.

Again, only mineral dust is modelled. Simulations of anthropogenic aerosol are not conducted as the main focus of this chapter is set on the spatio-temporal distribution of mineral dust in Northern China, the dust emission process and dust transport during a severe dust event towards Beijing. It is also assumed that strong wind speeds accompanying the dust storm event lead to a blowing out of the main amount of local anthropogenic aerosols in Beijing before arrival of the dust front. Moreover, a transport of anthropogenic aerosol from the dust source regions to Beijing should be negligible, as there are only few significant anthropogenic sources in these remote areas.

The study period is from April 24 to May 2 in 2011, which is also the same period as for the study presented in chapter 4. The study presented in the current chapter focuses especially on the period of April 28 to 30, as on April 30 meteorological stations in Beijing, Baoding and Tianjin reported a strong dust event with blowing sand conditions.

## **5.3 Results**

### **5.3.1 Mineral dust dynamics in Northern China**

Modelled total dust concentrations and 10-m height wind speeds show the high variability of airborne dust due to meteorological conditions and can give information about dust source regions. For this reason, the spatio-temporal dynamics of airborne dust in Northern China are analyzed for April 28 at 06:00 h to April 30, 18:00 h. This time is chosen, as the study about dust variability in the source regions presented in chapter 4, showed that there is no stronger dust event initiated in the source regions before April 28, 06:00 UTC, and that negligible amounts of dust are transported to Beijing. According to the distribution of airborne dust, dust emissions and 10-m height wind speeds are analyzed in detail for active dust source regions during this time period.

### 5.3.1.1 Simulation of mineral dust dynamics in Northern China

In this section the horizontal spatio-temporal dynamics of modelled airborne mineral dust are analyzed. Therefore, total mineral dust mass concentrations, which are summed up of all three dust modes, are studied for the lowest model layer in the study domain. It should be noted that the lowest model layer has a vertical thickness of 20 m.

The change of airborne dust mass concentrations in the lowest model layer from April 28 at 12:00 h to April 30, 18:00 h is shown in Figure 23. The first plot in the top left corner shows the onset of dust distribution in Gobi Desert in Southwest Mongolia and Kumtaq Desert. 12 hours later, on April 29, 00:00 h, dust from Kumtaq Desert covers whole Taklimakan Desert with concentrations exceeding  $4 \text{ mg m}^{-3}$ . At the same time dust originating in Gobi Desert moved southeastwards covering the Central Chinese Deserts. At the same time dust concentrations in Eastern Gobi Desert start to increase to  $2.5 \text{ mg m}^{-3}$ . On April 29 around 06:00 h dust concentrations reach their maximum in Gobi Desert, the Central Chinese Deserts and Inner Mongolia. At the same time, dust concentrations in Kumtaq Desert and Taklimakan Desert start decreasing. On the same day, around 12:00 h dust concentrations in the Central Chinese Deserts and Inner Mongolia show a decrease. Six hours later, mass concentrations in Gobi Desert in Southeast Mongolia are still high ( $> 4 \text{ mg m}^{-3}$ ). However, concentrations over the Loess area between Beijing and the Central Chinese Deserts still show a decreasing trend. On April 30 at 00:00 h highest mineral dust concentrations can be found in the area between the Chinese-Mongolian border and Beijing. Six hours later dust concentrations in Beijing and south of it still exceed  $4 \text{ mg m}^{-3}$ . On April 30 around 12:00 h and 18:00 h dust concentrations decrease to  $2.5 \text{ mg m}^{-3}$  in the area south of Beijing and the Yellow Sea

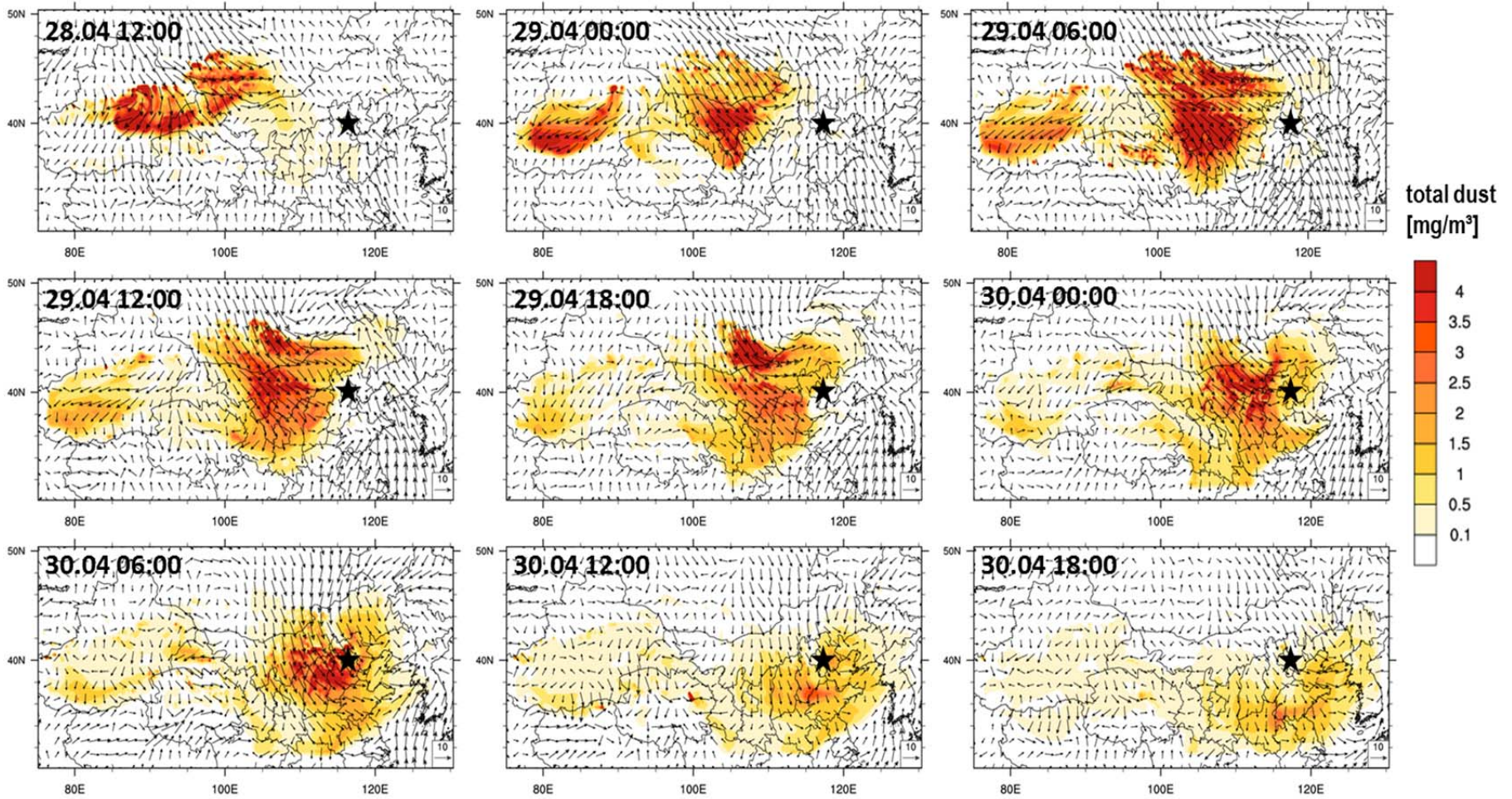


Figure 23: Horizontal distribution of total dust mass concentrations (sum of all dust modes) (in  $\text{mg m}^{-3}$ ) in the lowest model layer and 10-m height wind vectors (meridional and zonal wind vectors in  $\text{m s}^{-1}$ ) from April 28 to 30, 2011 (from top left to bottom right) modelled using COSMO-ART. The reference wind speed vector is shown in the bottom right corner of each plot and is set to  $10 \text{ m s}^{-1}$ . Beijing is marked by a black asterisk. The scale on the right hand side refers to dust concentrations and is valid for all plots. Time is always UTC. Day and time of the plots (from top left to bottom right): 28.04 12:00 h, 29.04 00:00 h, 29.04 06:00 h, 29.04 12:00 h, 29.04 18:00 h, 30.04 00:00 h, 30.04 06:00 h, 30.04 12:00 h, and 30.04 18:00 h.

### 5.3.1.2 Analysis of dust mobilization in the source regions

The analysis of airborne dust dynamics in Northern China from April 28 to 30 shows two main dust events occurring during this period, one in Taklimakan Desert and one in Gobi Desert and the Central Chinese Deserts. As there is no evidence for long-range transport of dust from Taklimakan Desert to the Chinese East Coast, the analysis of dust mobilization characteristics focuses on Gobi Desert. This analysis helps understanding the specific conditions which are necessary for dust uplift.

In this study dust mobilization is characterized by analyzing total mineral dust emissions, near-surface wind speeds and wind directions, as well as the connection of wind speeds and surface roughness in the dust source regions. Dust emissions and wind conditions are modelled with COSMO-ART. Total dust emissions are summed up of all three dust modes. Information about surface roughness is taken from the soil data of *Laurent et al.* [2005], which is also used as input data for dust simulation in this study.

On April 28 around 12:00 h emissions are initiated in West Gobi Desert by strong northwesterly and westerly winds up to  $15.8 \text{ m s}^{-1}$  (see Figure 25 for dust emissions and wind directions and Figure 26 for wind speeds). In a small area up to  $47 \mu\text{g}$  of dust particles are emitted per  $\text{m}^2$  and second. On April 29 between 00:00 h and 06:00 h there are two main areas with high dust emission fluxes (up to  $50 \mu\text{g m}^{-2} \text{ s}^{-1}$ ), one in the Southeast Mongolian Gobi Desert and the second in the Central Chinese Deserts. Wind speeds in Gobi and the Central Chinese Deserts reach  $17 \text{ m s}^{-1}$ , and  $14 \text{ m s}^{-1}$ , respectively. The strong northwesterly wind and the low roughness lengths (Figure 24), favor uplifting of high amounts of dust particles. Between 06:00 h and 18:00 h wind speeds in Central China slowly decrease to  $12 \text{ m s}^{-1}$ , whereas wind speeds in Gobi Desert stay strong. The main wind direction is still northwest. However, due to the low roughness lengths in the Central Chinese Deserts, low amounts of dust are still emitted even under weak wind conditions. At 12:00 h and 18:00 h dust emissions are still high in Gobi Desert. On April 30 between 00:00 h and 06:00 h wind speeds in Gobi Desert are still strong ( $8\text{-}14 \text{ m s}^{-1}$ ) with wind directions from northwest. There are still small amounts of dust emissions in this area, due to low surface roughness. At the same time, wind speeds in the loess area between Beijing and the Central Chinese Deserts start increasing to  $17 \text{ m s}^{-1}$ . This leads to a strong increase of dust emissions ( $> 50 \mu\text{g m}^{-2} \text{ s}^{-1}$ ) in some areas west and southwest of Beijing, despite of the high surface roughness lengths considered for this area. At 06:00 h the wind direction in the Gobi Desert changes to north and wind speed decreases to  $2\text{-}8 \text{ m s}^{-1}$ . On April 30 at 12:00 h only low dust emissions for some small patches are modelled as wind speeds fall below the threshold friction velocity determined by the surface roughness length.

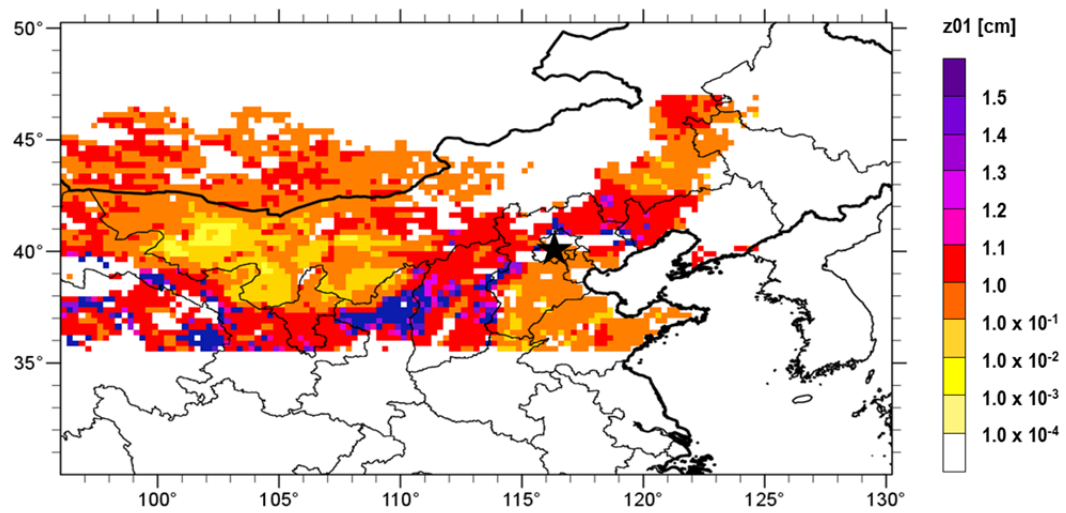


Figure 24: Total soil roughness length  $z_{01}$  (in cm) for the Chinese and South Mongolian Deserts included in the soil dataset of *Laurent et al.* [2005] and taken as input dataset for COSMO-ART simulations. Beijing is marked by a black asterisk.

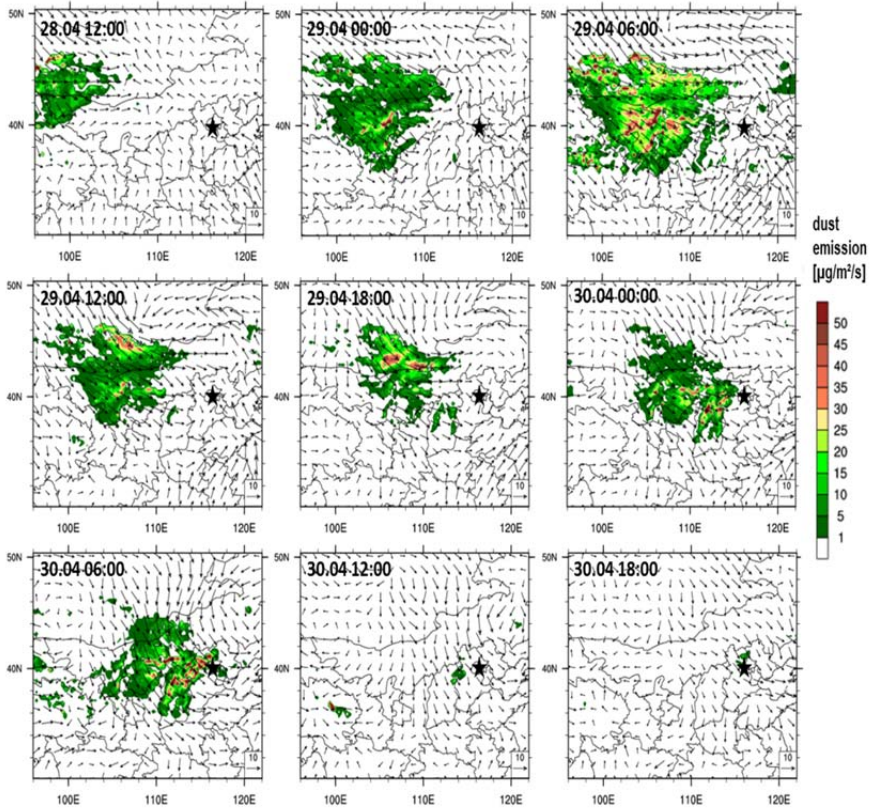


Figure 25: Total dust emissions (sum of all dust modes) (in  $\mu\text{g m}^{-2} \text{s}^{-1}$ ) and 10-m height wind vectors (meridional and zonal wind vectors in  $\text{m s}^{-1}$ ) for Northeast China for April 28 to 30 in 2011, modelled with COSMO-ART. Reference wind speed vector is shown in the bottom right corner of each plot and set to  $10 \text{ m s}^{-1}$ . Beijing is marked by a black asterisk. The scale on the right hand side refers to dust emissions and is valid for all plots. Time is UTC. Day and time of the plots (from top left to bottom right): 28.04 12:00 h, 29.04 00:00 h, 29.04 06:00 h, 29.04 12:00 h, 29.04 18:00 h, 30.04 00:00 h, 30.04 06:00 h, 30.04 12:00 h and 30.04 18:00 h.

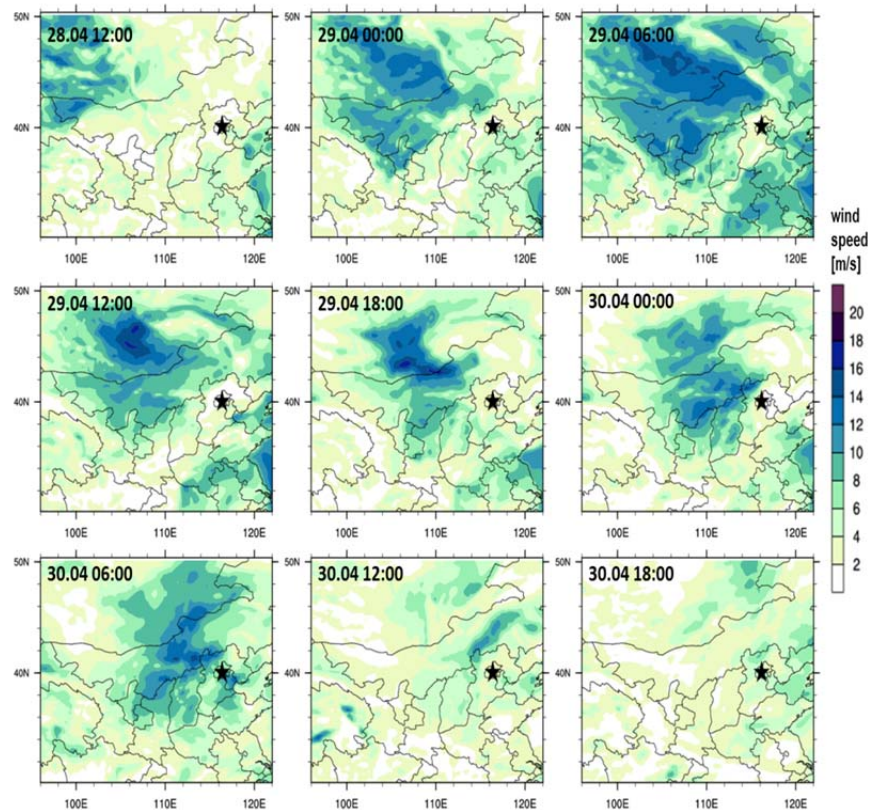


Figure 26: Wind speed (in  $\text{m s}^{-1}$ ) in 10 m above ground for Northeast China from April 28 to 30 in 2011, modelled with COSMO-ART. Beijing is marked by a black asterisk. The scale on the right hand side refers to wind speed and is valid for all plots. Time is UTC. Day and time of the plots (from top left to bottom right): 28.04 12:00 h, 29.04 00:00 h, 29.04 06:00 h, 29.04 12:00 h, 29.04 18:00 h, 30.04 00:00 h, 30.04 06:00 h, 30.04 12:00 h and 30.04 18:00 h

### 5.3.2 Mid-range transport of mineral dust towards Beijing

After mobilization, airborne dust particles stay in the source region or they are transported to areas located downwind. The analysis of dust dynamics already indicated that dust is mobilized in Gobi Desert, the Central Chinese Deserts and the loess area and then transported to the east and southeast of China. The transport pattern and pathway is analyzed in this section. Therefore, the horizontal dust plume transport is studied in combination with two vertical dust profiles for two selected cross-sections.

#### 5.3.2.1 Synoptic weather conditions

The mid-range dust transport is triggered by a Mongolian cyclone with frontal system [Fu *et al.*, 2013]. This low-pressure system causes strong wind speeds (up to  $17 \text{ m s}^{-1}$ ) in Gobi Desert (see previous section).

The synoptic weather situation in Beijing is shown in Figure 27. The Beijing weather station recorded an increase of wind speed up to  $15.2 \text{ m s}^{-1}$  and a change of wind direction from east to west-northwest on April 30 around 03:00 h, showing the arrival of the cyclone and the starting point of the dust event. At the same time, sea level pressure is increasing from 999.4 hPa to 1001.5 hPa. Air temperature is also increasing up to  $20 \text{ }^\circ\text{C}$ . There is not any significant amount of precipitation reported for this period in Beijing and its surrounding.

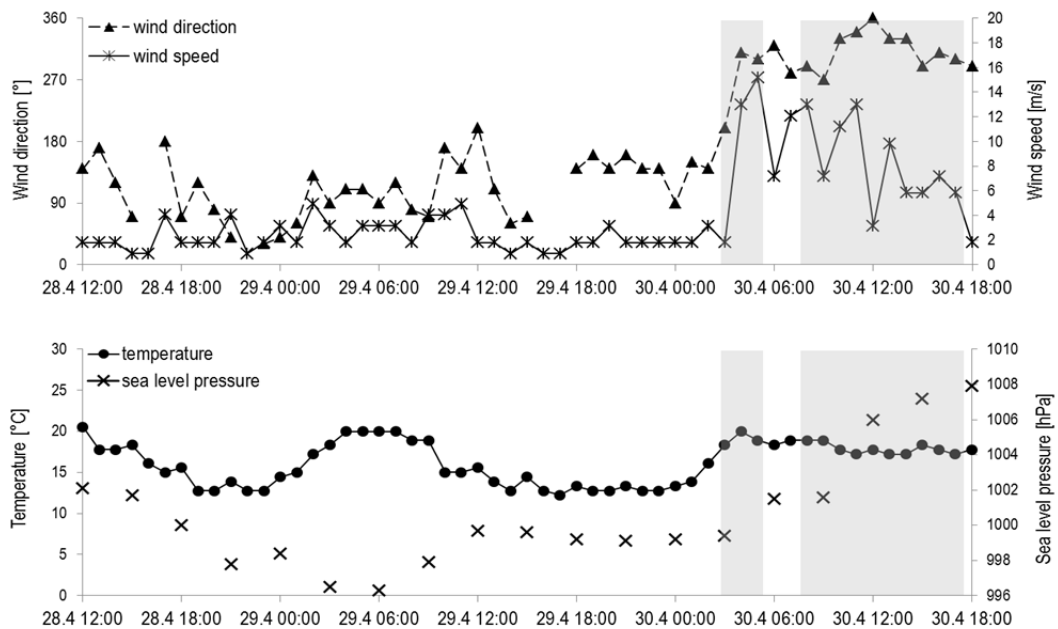


Figure 27: The first plot shows wind direction (in  $^\circ$ ) (black dashed line with triangles) and wind speed (in  $\text{m s}^{-1}$ ) (black line with asterisk) in 10 m height from April 29 at 12:00 h to April 30 at 18:00 h in 2011 measured in Beijing. The second plot shows air temperature (in  $^\circ\text{C}$ ) (black line with dots) and sea level pressure (in hPa) (black stars) in 2 m height from April 28 at 12:00 h to April 30 at 18:00 h in 2011 measured in Beijing. Reported dust events are shown in grey. Time is UTC.

### 5.3.2.2 Horizontal movement of dust plumes

In this section the horizontal movement of mineral dust between April 28 and 30 is shown. For this task the contours of total dust mass concentrations summarized over all model layers are plotted in a schematic illustration (Figure 28). The shaded areas of the plumes enfold total dust mass concentrations  $> 2 \text{ mg m}^{-3}$ . The movement patterns of the dust plumes are shown in 12-hour intervals between April 28, 12:00 h and April 29, 18:00 h and in 6-hour intervals between April 29, 18:00 h and April 30, 12:00 h.

There are two initial dust plumes originating in east and west of South Mongolia. The first plume in Gobi Desert is initiated on April 28 around 12:00 h (black line). Main average wind direction for this area is west, pushing the dust plume towards southeast. On April 29 around 00:00 h the plume is located over the Central Chinese Deserts and Gobi Desert (purple line). On the same day around 12:00 h a second plume is initiated in Gobi Desert in Southeast Mongolia by strong winds from north-northwest (blue line). At the same time the first plume is moving further towards southeast covering a large area over the Central Chinese Deserts and the loess area (blue line in the south). On April 29 around 18:00 h the first plume moved further on towards the region south of Beijing, whereas the second plume is still located in Gobi Desert (green lines). The main wind direction is northwest. On April 30 at 00:00 h both dust plumes merge together and arrive at Beijing (red lines). The arrival of the dust front is accompanied by a strong increase of wind speeds and the change of the main wind direction in Beijing and its surrounding (see section 5.3.2.1). Six hours later on April 30 at 06:00 h a single dust plume covers the whole area of Beijing, Tianjin, and their surrounding provinces (orange line). On April 30, 12:00 h and 18:00 h, the dust moves further on towards the East Coast governed by northern winds (yellow line).

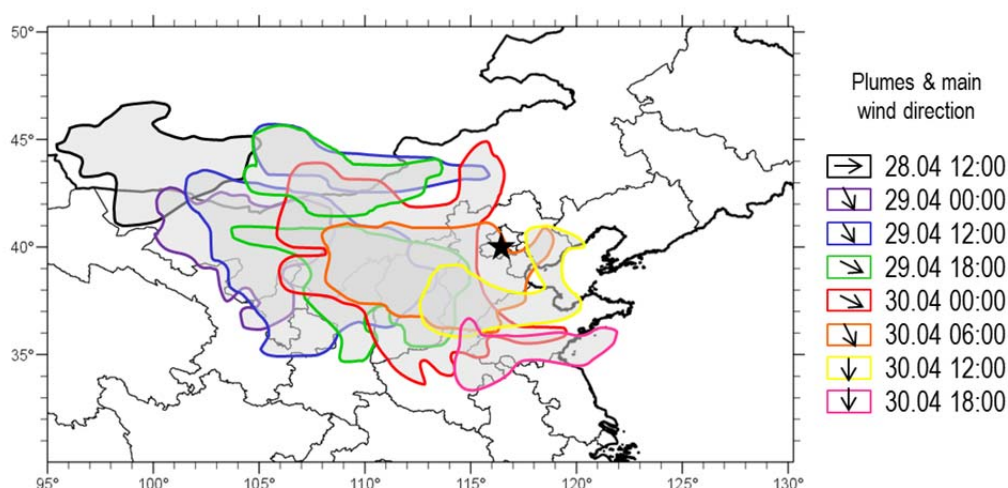


Figure 28: Horizontal movement of dust plumes from Gobi Desert to the Chinese East Coast from April 28 to 30 in 2011 modelled using COSMO-ART. The grey shaded areas show the area covered by modelled total dust mass concentrations  $> 2 \text{ mg m}^{-3}$  summarized over all model layers. The colored lines show the dust plumes at different times (in UTC). The black line shows the initial dust plume on 28.04 12:00 h, purple stands for 29.04 00:00 h, blue for 29.04 12:00 h, green for 29.04 18:00 h, red for 30.04.

### 5.3.2.3 Vertical distribution of airborne dust

To improve the understanding of the vertical dust transport pattern, vertical profiles of total dust mass concentrations are modelled with COSMO-ART. 18 profiles are analyzed for two different cross-sections. Each cross-section comprises nine profiles. The profiles are in temporal accordance with the dust plume study presented in the previous section. Cross-section A is located between 44° N/ 100° E and 34° N/ 120° E, following the transport pathway of the first dust plume, which was initiated in Southwest Gobi (Figure 29, black solid line). Cross-section B is located between 44° N/ 108° E and 37° N/ 122° E and follows the pathway of the second dust plume which originated in Southeast Gobi (Figure 29, black dashed line).

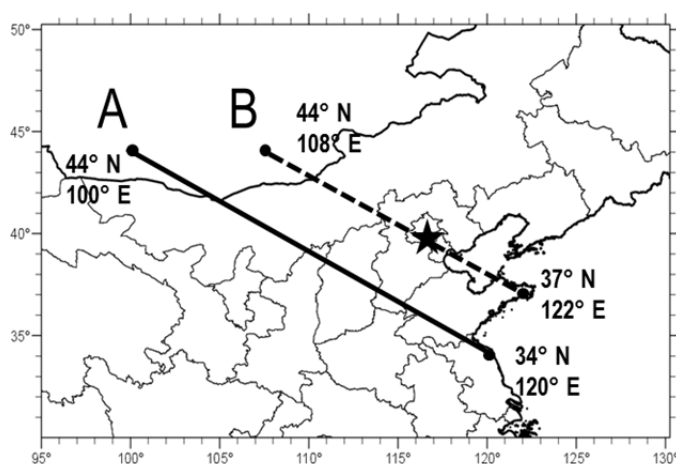


Figure 29: Location of cross-section paths A and B. Cross-section A is located between 44° N/ 100° E and 34° N/ 120° E (solid line); cross-section B is located between 44° N/ 108° E and 37° N/ 122° E (dashed line). Beijing is marked by a black asterisk.

The nine profiles of the first cross-section A are presented in Figure 30. It can be seen that on April 28 at 12:00 h dust is lifted into the air in Gobi Desert between 41° and 44° N. Most dust is lifted up to 5 km, but small amounts of dust are also lifted up to 8 km height due to strong near-surface wind speeds  $> 12 \text{ m s}^{-1}$  and vertical wind velocities. Highest concentrations ( $< 2.5 \text{ mg m}^{-3}$ ) are located near the ground. 12 hours later near-surface dust concentrations between 40° and 41° N increased to  $3.5 \text{ mg m}^{-3}$ . Strong wind speeds carry dust towards Southeast. On April 29 around 06:00 h the main dust plume moved forward towards the southeast. A continuous 3 to 4 km high dust layer covers the area between 38° and 44° N. However, dust concentrations of the main plume decreased, whereas concentrations between 40° and 44° N increased due to the dust emissions in this area. On the same day at 12:00 h near-surface dust concentrations between 39° and 44° N increased up to  $3.5 \text{ mg m}^{-3}$ . At 18:00 h only small amounts of dust are left between 41° and 44° N, whereas dust is now present in the area of the Northeast Chinese plain between 35° and 37°. Strong descending winds push the dust from the mountains down towards the plain, whereas ascending winds lift dust up to higher altitudes at 36° N. On April 30 at 00:00 h a continuous but flat dust layer is present between 34.5° and 41° N. Strong descending wind distribute the dust further

towards the southeast. Dust concentrations exceed  $4 \text{ mg m}^{-3}$  between  $38^\circ$  and  $38.5^\circ$  N. At 06:00 h the spatial extent of the dust plume with concentrations exceeding  $4 \text{ mg m}^{-3}$  extended towards  $37^\circ$  N. Low wind speeds between  $40^\circ$  and  $44^\circ$  hamper re-initialization of dust emissions in this source region. However, higher wind speeds in the southern part of the cross-section push the dust further to the south. At 18:00 h maximum dust concentrations can be found in higher altitudes, indicating dust uplift and long-range transport.

The nine profiles of the second cross-section B are shown in Figure 31. On April 28 at 12:00 h only small amounts of airborne dust are in the atmosphere of the cross-section and near-surface wind speeds are lower  $6 \text{ m s}^{-1}$ . On April 29 at 00:00 h near-surface wind speeds increased and dust emission is initiated between  $42^\circ$  and  $44^\circ$  N. Small amounts of dust have already been lifted towards high altitudes of 10 km by strong vertical velocities. At 06:00 h a continuous dust plume has formed between  $41^\circ$  and  $44^\circ$  N extending up to 4 km. The transport of small amounts of dust towards the southeast still exists. At 12:00 h the near-surface dust plume can still be found in the same area. In addition, a second cut-off plume in 4 to 5 km height can be seen. An uplifted dust plume with low concentrations up to  $1 \text{ mg m}^{-3}$  is transported in heights of 3 to 5 km towards the southeast by turbulent winds. At 18:00 h two dust plumes with dust concentrations exceeding  $4 \text{ mg m}^{-3}$  are present in the area between  $42.5^\circ$  and  $44^\circ$  N. One of these dust plumes is located near the ground and a second one between 2 and 3 km. There are also two dust plumes in two different heights transported towards the Beijing region. One plume is transported near the ground by descending winds and the second one is distributed in 2 to 4 km height by strong horizontal winds. On April 30 at 00:00 h a dense dust plume with concentrations exceeding  $4 \text{ mg m}^{-3}$  is located at  $41^\circ$  N. In addition, a continuous dust near-surface dust layer is present in the Beijing region. At 06:00 h the dense dust plume passed Beijing and moved forward to the southeast. Only small amounts of dust are emitted in the source region between  $41^\circ$  and  $44^\circ$  N. At 12:00 the dust is transported further to the southeast and concentrations are decreasing.

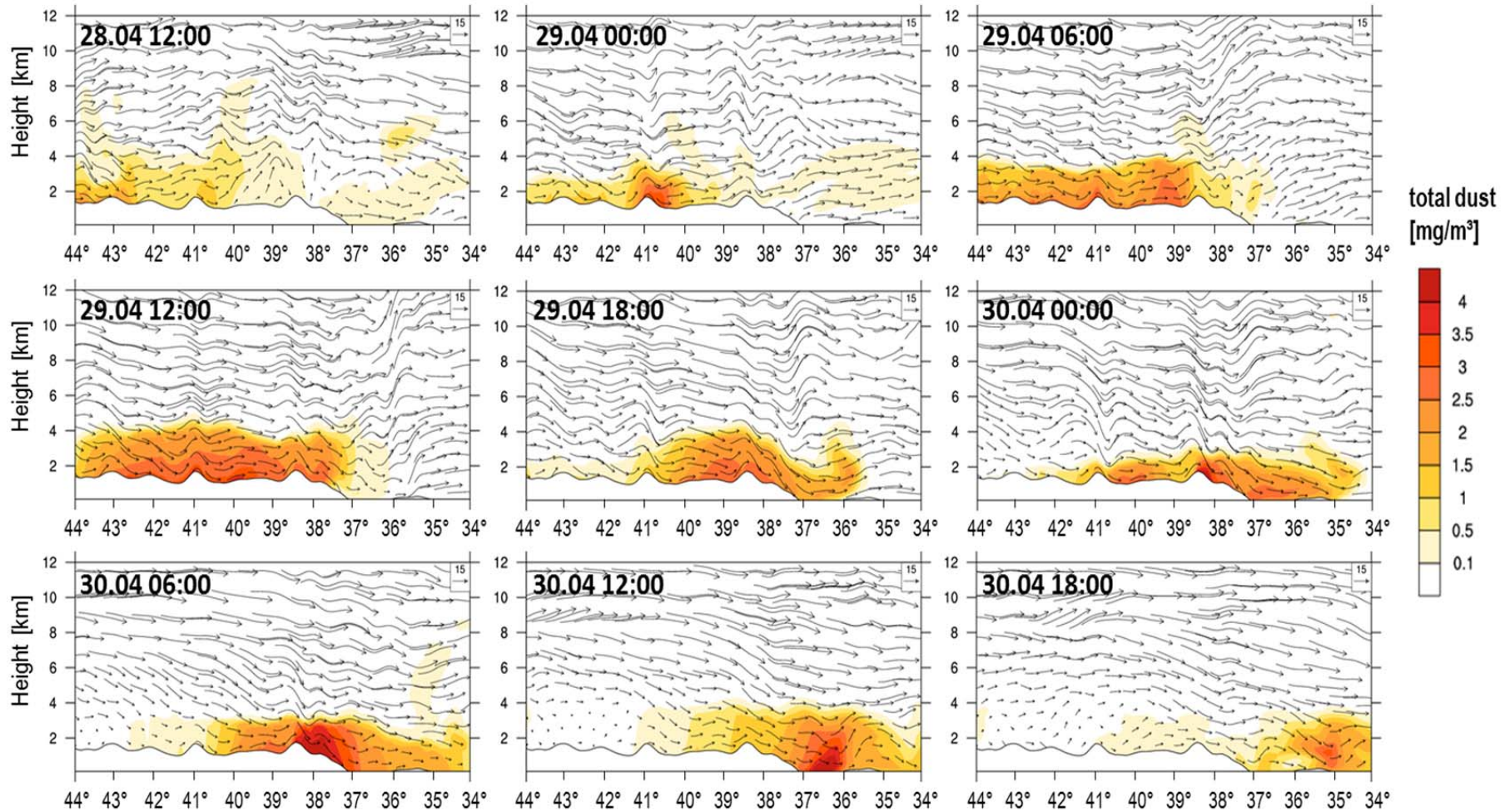


Figure 30: Profiles of total dust mass concentrations (in  $\text{mg m}^{-3}$ ) and wind vectors (wind speed and vertical wind velocity in  $\text{m s}^{-1}$ ) for cross-section A ( $44^\circ \text{ N} / 100^\circ \text{ E}$  to  $34^\circ \text{ N} / 120^\circ \text{ E}$ ) from April 28 to 30, 2011. The vertical wind velocity is multiplied by a factor of 20 to make vertical movement visible. The reference vector is shown in the top right corner of the plots and set to  $15 \text{ m s}^{-1}$ . The scale on the right hand side refers to total dust mass concentrations and is valid for all plots. Time is UTC. Day and time of the plots from the top left to the bottom right: 28.04 12:00 h, 29.04 00:00 h, 29.04 06:00 h, 29.04 12:00 h, 29.04 18:00 h, 30.04 00:00 h, 30.04 06:00 h, 30.04 12:00 h and 30.04 18:00 h.

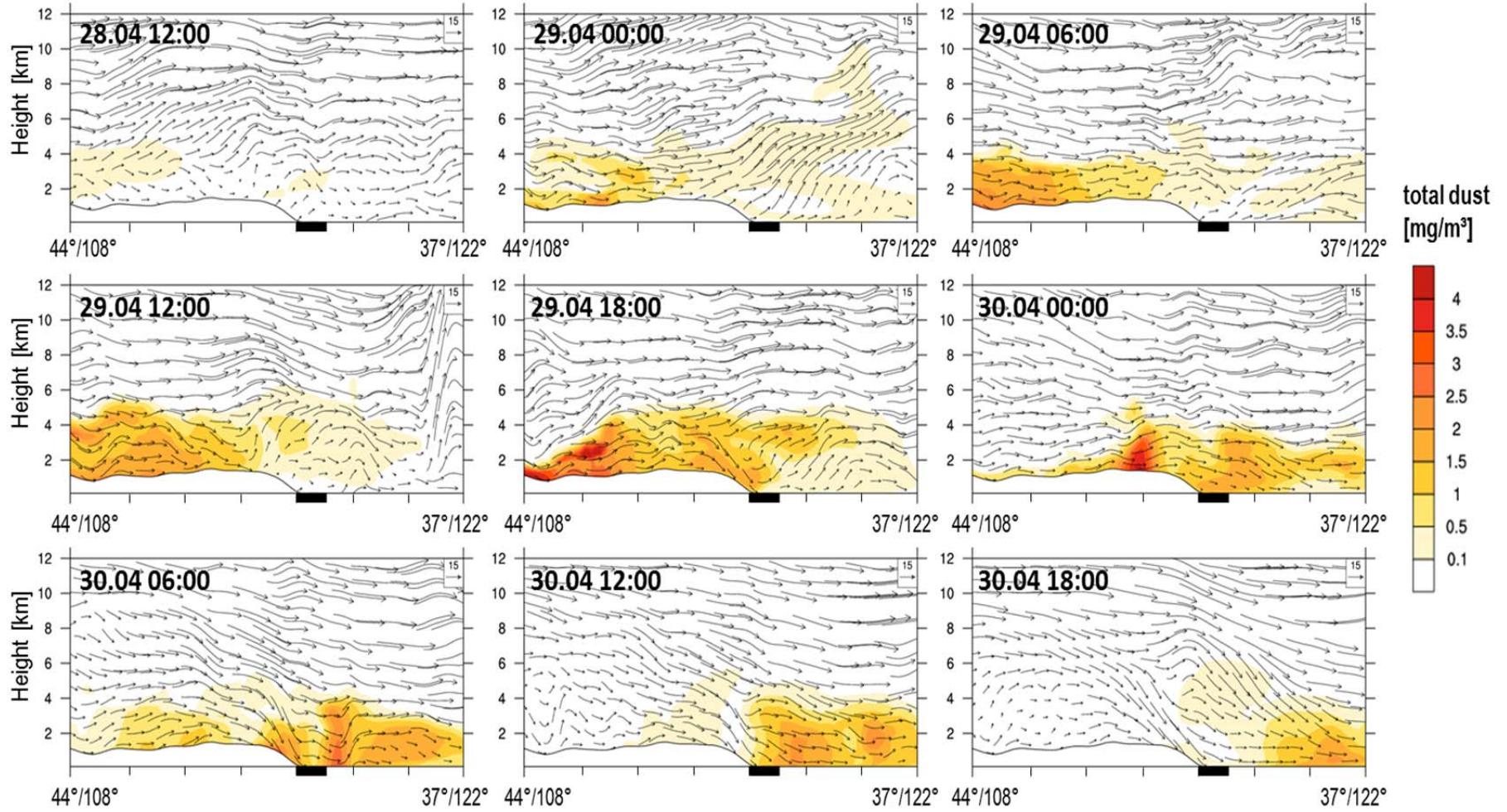


Figure 31: Profiles of total dust mass concentrations (in  $\text{mg m}^{-3}$ ) and wind vectors (wind speed and vertical wind velocity in  $\text{m s}^{-1}$ ) for cross-section B ( $44^\circ \text{ N} / 108^\circ \text{ E}$  to  $37^\circ \text{ N} / 122^\circ \text{ E}$ ) from April 28 to 30, 2011. The vertical wind velocity is multiplied by a factor of 20 to make vertical movement visible. The reference vector is shown in the top right corner of the plots and set to  $15 \text{ m s}^{-1}$ . The scale on the right hand side refers to total dust mass concentrations and is valid for all plots. The location of Beijing is marked by the thick black bar. Time is UTC. Day and time of the plots from the top left to the bottom right: 28.04 12:00 h, 29.04 00:00 h, 29.04 06:00 h, 29.04 12:00 h, 29.04 18:00 h, 30.04 00:00 h, 30.04 06:00 h, 30.04 12:00 h and 30.04 18:00 h

### 5.3.3 Assessment of the impact of mineral dust on air quality in Beijing

Airborne dust can be assumed to have a strong impact on air quality in terms of  $PM_{10}$  and  $PM_{2.5}$  levels, when dust is located near the ground. However, ground-based  $PM_{10}$  and  $PM_{2.5}$  measurements on their own give information about general aerosol air quality but do not show the ratio of different aerosol types or their sources. Therefore, quantifying the impact of dust on  $PM_{10}$  and  $PM_{2.5}$  levels can be highly challenging, especially in cities like Beijing, as Beijing's air quality is affected by various aerosol types from various sources. For this reason, complementary to ground-based measurements, models can be used to assess the impact of airborne dust on  $PM_{10}$  and  $PM_{2.5}$ .

The analysis of mineral dust dynamics presented in chapter 5.3.1 showed that most of the dust transported to Beijing and its surrounding is located near to the ground. The dust can be supposed to have an impact on Beijing's air quality due to its vertical location and the high total dust concentrations. However, the simulations do not indicate how strong  $PM_{10}$  and  $PM_{2.5}$  levels are affected by this dust.

Quantifying the amount of mineral dust brought by mid-range transport from the source regions towards metropolitan Beijing, local  $PM_{10}$  and  $PM_{2.5}$  mass concentrations are modelled and also compared to measurements from the CAS-IAP ground-based network. Therefore,  $PM_{10}$  and  $PM_{2.5}$  were modelled for the lowest model layer for Beijing and its surrounding between  $37^\circ$  to  $43^\circ$  N and  $113^\circ$  to  $120^\circ$  E.

#### 5.3.3.1 Mixing of dust with local particulate pollutants

In the analysis about dust inside source regions in chapter 4, it was shown that CALIPSO feature mask data can be used for the classification of aerosol types. In this section it is used to analyze possible mixing of the mid-range transported dust with local anthropogenic pollutants in Beijing and to assess the amount of anthropogenic pollutants remaining in the urban atmosphere during this dust storm. Measurements of anthropogenic trace element concentrations at one site in Beijing by N. Schleicher already showed that the amount of anthropogenic particulates was small compared to previous days.

There are three CALIPSO profiles available for April 29, 30 and May 1, passing the area near Beijing.

A pure near-surface dust layer is captured by CALIPSO for the area close to  $36^\circ$  and  $40^\circ$  N on April 29 around 18:30 h (Figure 32, first cross-sectional plot). It seems that there is no mixing with anthropogenic pollutants in the area of Beijing and south of it during the arrival of the first dust front. Between  $40^\circ$  and  $45^\circ$  N a near-surface layer is classified as cloud. There is not any signal from the surface below the dust and cloud layer due to total attenuation of the lidar beam.

On April 30 around 05:30 h a near-surface pure dust layer is captured in the area south of Beijing between  $36.5^\circ$  and  $40^\circ$  N (Figure 32, second cross-sectional plot).

At this time the second dust front hit Beijing and its surrounding. The CALIPSO data show that there is no mixing of dust with other aerosol types during this time.

On May 1, 18:30 h there are still pure dust layers present in the area between 36° and 43° N (Figure 32, third cross-sectional plot). A widely stretched cloud in 5-13 km height is captured between 35° and 41° N.

In all three cases there is no evidence of mixing of dust with local pollutants. These results also show that anthropogenic aerosols are not playing a significant role in the urban atmosphere covered by the dust plumes during this dust event. Even on May 1, after the passage of the main dust plumes, only mineral dust is captured in the atmosphere east of Beijing.

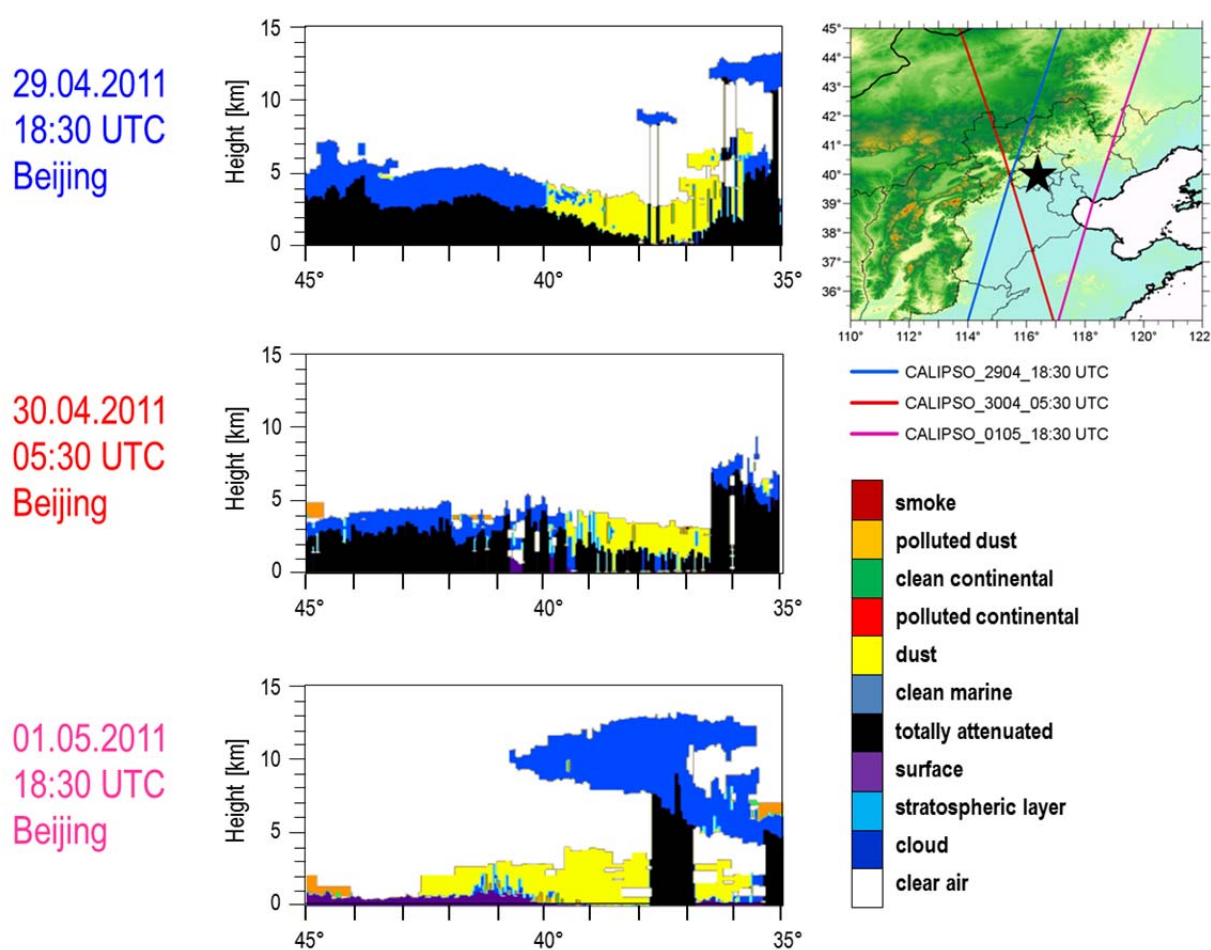


Figure 32: CALIPSO vertical feature mask profiles for three cross-sections passing Beijing on April 29 at 18:30 h (blue line on map, first cross-sectional plot), April 30 at 05:30 h (red line on map, second cross-sectional plot), and May 1 at 18:30 h (pink line on map, third cross-sectional plot). Time is in UTC. The locations of the cross-sections are shown in the map at the top on the right hand side. Beijing is marked by a black asterisk. The cross-sectional plots are located between 35° and 45° N. The legend of CALIPSO features are shown on the right hand side.

### 5.3.3.2 Simulation of the spatial variability of PM<sub>10</sub> and PM<sub>2.5</sub> concentrations using COSMO-ART

The CALIPSO lidar showed that there is only mineral dust present in the area of Beijing and its surrounding between April 28 and May 1. This finding is also in accordance with measurements by N. Schleicher. It can be assumed that the regional particulate loading is mainly dominated by mineral dust. For this reason, only mineral dust is modelled using COSMO-ART to characterize the spatio-temporal distribution of modelled PM<sub>10</sub> and PM<sub>2.5</sub> in Greater Beijing from April 29, 12:00 h to April 30 at 18:00 h.

PM<sub>2.5</sub> concentrations are very low in the whole region on April 29 before 12:00 h (Figure 33, top panel plots). Between April 29 at 12:00 h and 18:00 h PM<sub>2.5</sub> concentrations strongly increase up to 400 µg m<sup>-3</sup> in the northwestern and southwestern part of the region due to the arriving of the first dust front southwest of Beijing. On April 30 at 00:00 h the second dust front with high PM<sub>2.5</sub> concentrations > 450 µg m<sup>-3</sup> can be seen in the western part of the region. PM<sub>2.5</sub> concentrations in Beijing city reach their maximum of 274 µg m<sup>-3</sup> between 00:00 h and 06:00 h, after the second front passed the city area. At 12:00 h PM<sub>2.5</sub> concentrations already start decreasing. There are still two areas south and east of Beijing, where concentrations are still between 250 µg m<sup>-3</sup> and 400 µg m<sup>-3</sup>.

PM<sub>10</sub> concentrations are already high on April 29 at 12:00 h northwest and southwest of Beijing (Figure 33, bottom panel plots). The arrival of the first dust front at 18:00 h in the southwest of Beijing is accompanied by a strong increase of PM<sub>10</sub> concentrations up to 2750 µg m<sup>-3</sup>. PM<sub>10</sub> concentrations in Beijing city and the close surrounding are slightly influenced by the dust. Six hours later on April 30 at 00:00 h the second dust front causes a strong increase of PM<sub>10</sub> concentrations west of Beijing. At the same time PM<sub>10</sub> in the southwestern part of the region is still increased. Both dust fronts lead to high PM<sub>10</sub> loads in the whole area on April 30 at 06:00 h. PM<sub>10</sub> concentrations decrease slowly during the following six hours.

The time series of changing PM<sub>10</sub> and PM<sub>2.5</sub> concentrations in Beijing and its surrounding clearly show the arrival of the two dust plumes which hit Beijing on April 30 between 00:00 h and 06:00 h. The PM<sub>2.5</sub> distribution is much more homogeneous over the whole area; with highest values during arrival of the second dust front. After the arrival of the second front the PM<sub>2.5</sub> level is decreasing quiet fast, whereas PM<sub>10</sub> reaches extremely high values on April 30 around 06:00 h.

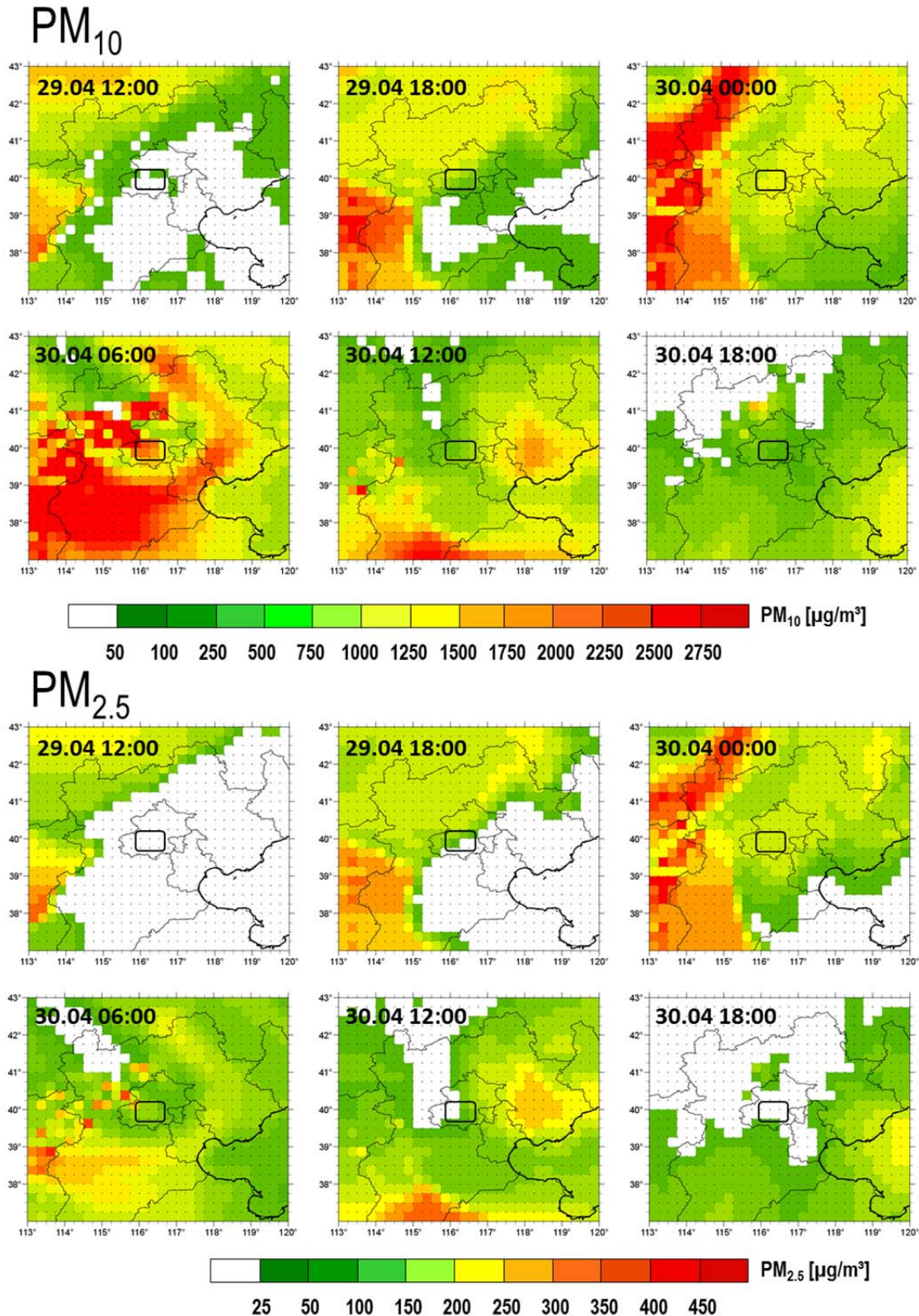


Figure 33: PM<sub>2.5</sub> (top panel plot) and PM<sub>10</sub> (bottom panel plot) mass concentrations (in  $\mu\text{g m}^{-3}$ ) from April 29 at 12:00 h to April 30 at 18:00 h in the lowest model layer modelled with COSMO-ART. Date and time is shown in the top left of the plots and all times are in UTC. Beijing city is marked by a black cuboid. Small black dots show the horizontal COSMO-ART grid cell raster.

### 5.3.3.3 Quantifying the impact of mineral dust on air quality

For quantification of the impact of airborne dust on Beijing's air quality,  $PM_{10}$  and  $PM_{2.5}$  from the CAS-IAP ground-based network are compared to modelled  $PM_{10}$  and  $PM_{2.5}$  concentrations for April 24 at 00:00 h to May 2 at 00:00 h. Time of data is UTC. In addition, measured visibility and dust event reports are analyzed. A discussion about dust event type definition is presented in this chapter in section 5.4.2. According to the findings of section 5.3.3.1 and 5.3.3.2 anthropogenic aerosol is not modelled for this case study. Therefore, it should be kept in mind, that observed  $PM_{10}$  and  $PM_{2.5}$  concentrations can contain all types of aerosol, whereas modelled  $PM_{10}$  and  $PM_{2.5}$  concentrations only comprise pure mineral dust.

The location of the measurement sites, used for this study, is shown in Figure 34. A general overview of the dataset is given in chapter 2.

For comparison, point-based data of ground-based measurement sites and raster-based data of simulations with COSMO-ART were paired. For this task, the grid cell sizes of the model simulations which fit with the geo-location of the measurement sites were matched.

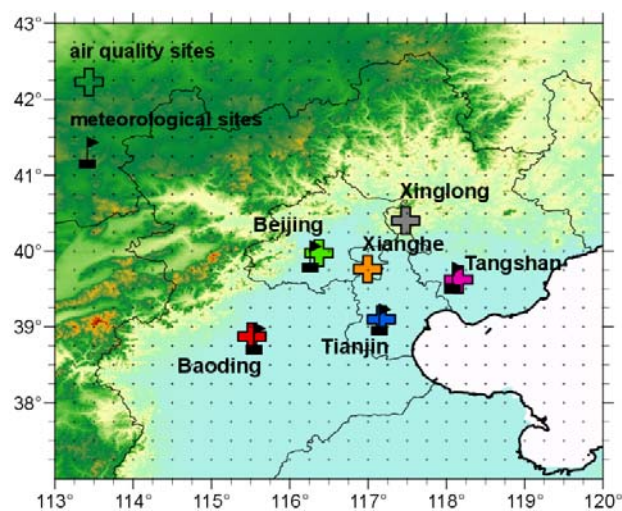


Figure 34: Locations of NOAA meteorological measurement sites and CAS-IAP air quality measurement sites providing  $PM_{10}$  and  $PM_{2.5}$  data for April 24 to May 2 in 2011. Air quality sites are marked with a colored cross, meteorological sites are marked with a black flag. Black lines show country and province boundaries, superimposed with a surface elevation map (data source: see chapter 4) and the grid cell raster of the COSMO-ART model setup.

The sites Xianghe, Tangshan and Baoding provide  $PM_{10}$  data for the whole time period of the case study, whereas data of the sites Beijing and Tianjin are only available from April 24 to 27, till 08:00 h UTC, and April 24 to 28, till 16:00 h UTC, respectively (see Figure 35 and Figure 36).  $PM_{2.5}$  data of Xianghe, Tangshan, Baoding and Xinglong is available for almost the whole study episode, whereas data of Beijing and Tianjin end on April 27, 07:00 and April 28, 14:00 h. Visibility and dust event reports are only available for the sites Beijing, Baoding, Tianjin and Tangshan. Therefore, information about visibility and dust events from the Beijing site is also used for Xianghe and Xinglong.

It can be seen that a dust event is modelled for all measurement sites for April 29 to April 30. The dust event has a single peak at Beijing, Baoding and Tianjin, whereas there is a double peak modelled for Xianghe, Tangshan and Xinglong. For April 24-29 only small amounts of dust are modelled for all sites.

At the Beijing site it can be seen that the modelled increase of dust is in well agreement with the measured decline of visibility and the first peak of the reported dust event (Figure 35, first row). The second and third reported events are not reproduced by the model. However, there is a small second peak of modelled  $PM_{10}$  and  $PM_{2.5}$  concentrations on April 30 around 22:00 h. Modelled  $PM_{2.5}$  and  $PM_{10}$  reach  $274 \mu\text{g m}^{-3}$ , and  $2700 \mu\text{g m}^{-3}$ , respectively, on April 30 at 03:00 h. Observed visibility decreases to 1.7 km on April 30 at 01:00 h. Two hours later a blowing dust event is reported at this site. There is a small gap between 06:00 h and 08:00 h before a second dust event is reported for 08:00 h to 17:00 h. A third event is reported for May 1 from 01:00 h to 03:00 h.

At Baoding highest  $PM_{2.5}$  concentrations are measured on April 25 and 29, whereas the peak on April 30 is not very distinctive (Figure 35, second row). Mean  $PM_{2.5}$  concentrations before and after the dust event are  $78 \mu\text{g m}^{-3}$ , and increase to  $148 \mu\text{g m}^{-3}$  during the dust event. The mean concentration value of  $78 \mu\text{g m}^{-3}$  can be considered to be the anthropogenic  $PM_{2.5}$  background for this station during non-dust periods. However, visibility shows its lowest value of 8.1 km on April 30 at 00:00 h and a blowing dust event is reported for 01:00 h to 06:00 h. During this time measured  $PM_{10}$  reaches its maximum of  $982 \mu\text{g m}^{-3}$ . Mean  $PM_{10}$  concentrations during the dust event are  $374 \mu\text{g m}^{-3}$  higher than during the time period before and after the event when mean concentrations are  $182 \mu\text{g m}^{-3}$ . The timing of the modelled dust dominated  $PM_{10}$  and  $PM_{2.5}$  increases are in good accordance with the reported dust event and the measured peaks. However, the modelled  $PM_{10}$  and  $PM_{2.5}$  concentrations are overestimated by a factor of 2.5, and 2, respectively.

At Tianjin site a dust event is reported for April 30 between 03:00 h and 19:00 h (Figure 35, third row). Six hours earlier observed visibility has already dropped to 5.7 km. During the dust event, visibility reaches a minimum of 8.1 km. The modelled dust-induced increase of  $PM_{10}$  and  $PM_{2.5}$  fits well with the decrease of reported visibility and dust event occurrence.

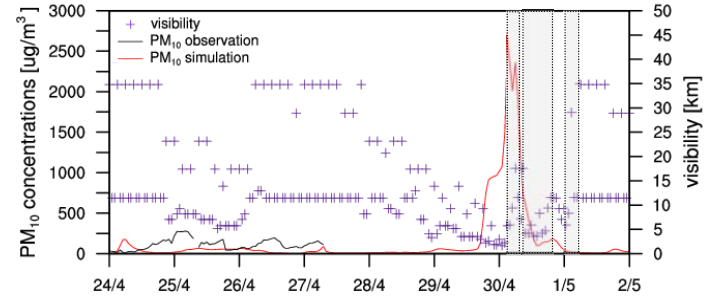
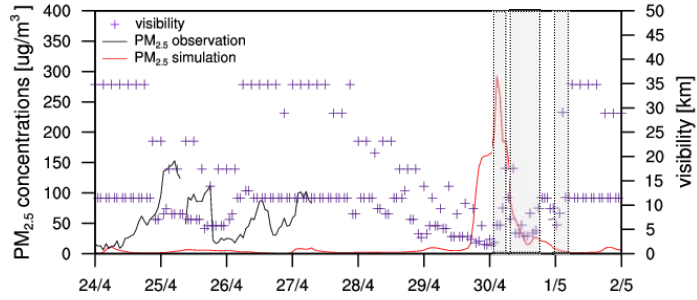
At Xianghe observed  $PM_{2.5}$  concentrations reach  $337 \mu\text{g m}^{-3}$  on April 30 around 18:00 h (Figure 36, first row). Mean  $PM_{2.5}$  concentrations increase from an anthropogenic dominated background concentration of around  $65 \mu\text{g m}^{-3}$  up to  $197 \mu\text{g m}^{-3}$  during the dust event. The timing of the  $PM_{2.5}$  increase can be reproduced very well with COSMO-ART. However, modelled  $PM_{2.5}$  concentrations are underestimated by a factor of around 2. This peak is also modelled for  $PM_{10}$  but with a slight underestimation. Mean anthropogenic background concentrations before and after the event are  $153 \mu\text{g m}^{-3}$ , and increase to a mean value of  $631 \mu\text{g m}^{-3}$  during the dust event.

Measured  $PM_{10}$  concentrations reach maximum values of  $1000 \mu\text{g m}^{-3}$  during the dust event. There is also an earlier  $PM_{2.5}$  peak of  $141 \mu\text{g m}^{-3}$  measured at 04:00 h. This peak is also modelled but with higher values up to  $260 \mu\text{g m}^{-3}$ . Modelled  $PM_{10}$  concentrations during this peak reach almost  $2400 \mu\text{g m}^{-3}$ , whereas measurements do not capture it at all. During both peaks, dust events are reported at the Beijing site and visibility drops to a minimum of 1.7 km at 01:00 h on April 30.

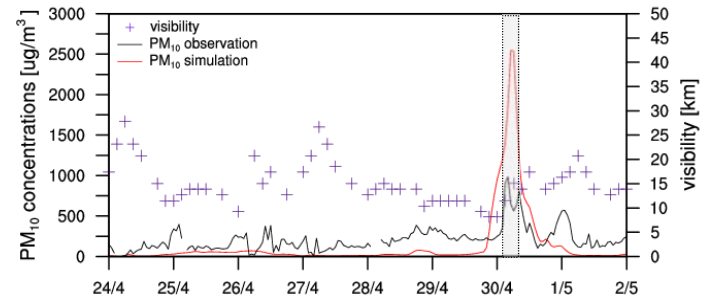
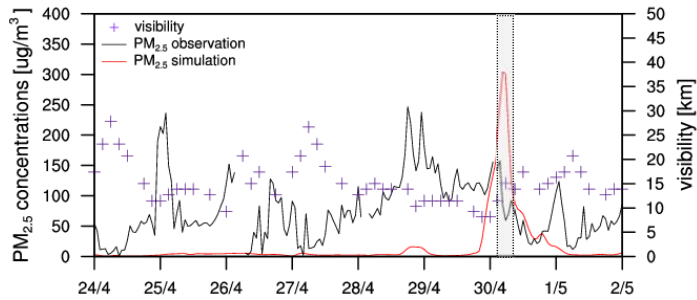
At Tangshan site measured  $PM_{2.5}$  and  $PM_{10}$  concentrations reach maxima of  $319 \mu\text{g m}^{-3}$ , and  $981 \mu\text{g m}^{-3}$ , respectively on April 30 around 18:00 h (Figure 36, second row). There is also a second smaller peak observed a few hours earlier. Both peaks are also reproduced by the model.  $PM_{2.5}$  of the first peak is overestimated by a factor of 2 and slightly underestimated for the second peak by a factor of 1.1. Regarding  $PM_{10}$ , the modelled concentrations are slightly overestimated for both peaks and there is a temporal shift of the increase of concentrations. Visibility drops to a minimum of 9.2 km on April 29 around 21:00 h. There is not any dust event reported at this site.

At Xinglong two  $PM_{2.5}$  peaks of  $161 \mu\text{g m}^{-3}$  and  $198 \mu\text{g m}^{-3}$  are observed for April 30 at 02:00 h as well as 16:00 h (Figure 36, third row). The mean  $PM_{2.5}$  background concentration increases from  $37.7 \mu\text{g m}^{-3}$  to  $130.4 \mu\text{g m}^{-3}$  during the dust event. The timing and the scale of the first peak is reproduced by the model very well, whereas the timing of the second peak is modelled a few hours too early. The modelled  $PM_{2.5}$  concentration peaks are very well correlated with the drop of visibility and the dust event report at the Beijing site. This accordance can also be seen for the modelled  $PM_{10}$  concentrations.

Beijing



Baoding



Tianjin

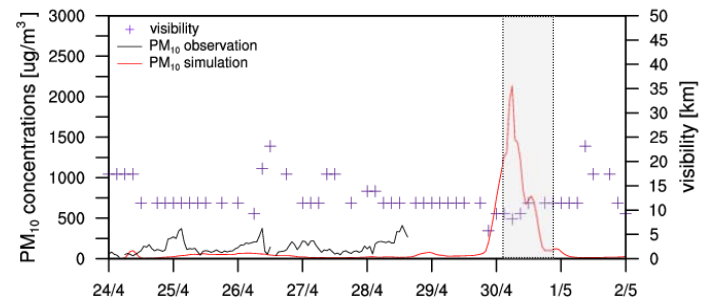
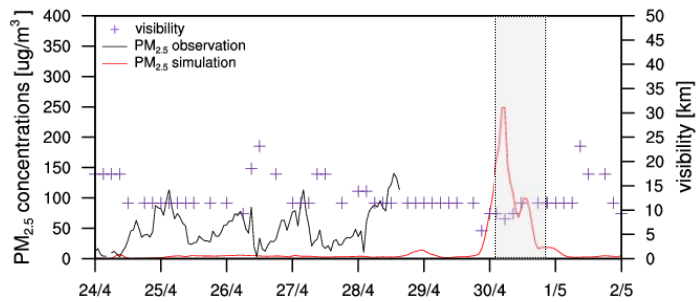
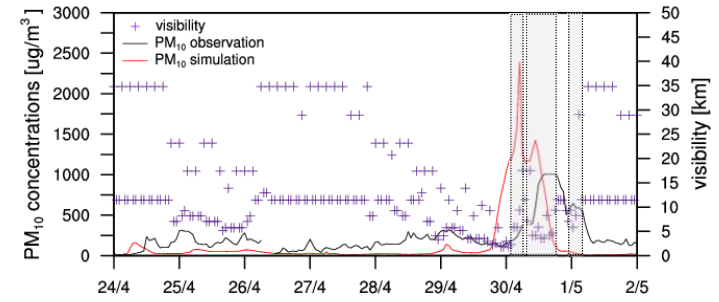
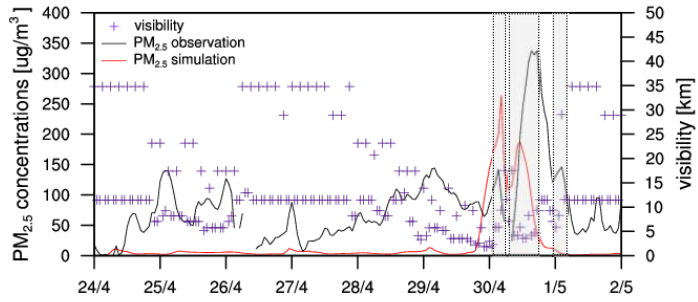
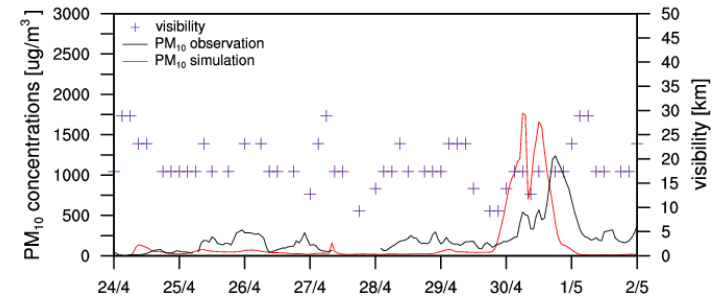
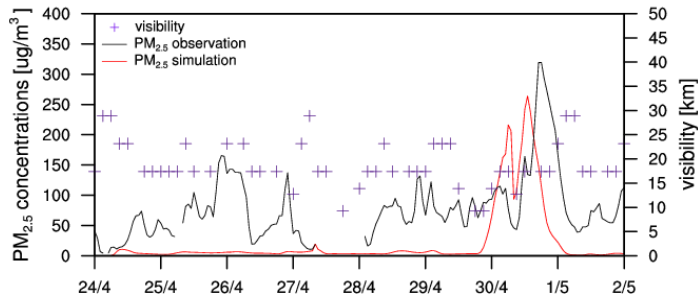


Figure 35: Comparison of  $PM_{10}$  and  $PM_{2.5}$  (in  $\mu g m^{-3}$ ) measured at sites in Beijing, Baoding and Tianjin with  $PM_{10}$  and  $PM_{2.5}$  (in  $\mu g m^{-3}$ ) modelled for the according locations with COSMO-ART for April 24 at 00:00 h to May 2 at 00:00 h in 2011. Time is in UTC. In addition observed visibility (in km) and dust events are shown. The comparison of modelled and observed  $PM_{2.5}$  is shown on the left hand side of the plot, and the comparison of  $PM_{10}$  on the right hand side. The red line denotes modelled  $PM_{10}$  and  $PM_{2.5}$ , the black line denotes observed  $PM_{10}$  and  $PM_{2.5}$ . The purple crosses show observed visibility and reported dust events are shaded in light grey.

Xianghe



Tangshan



Xinglong

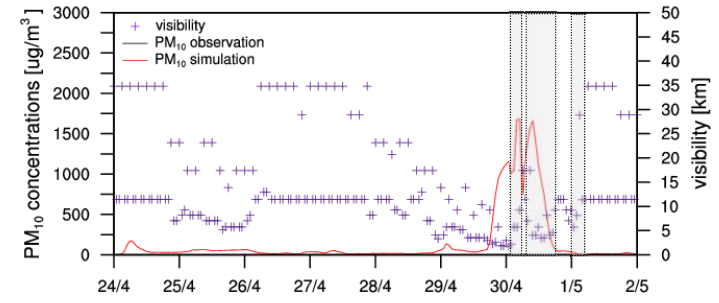
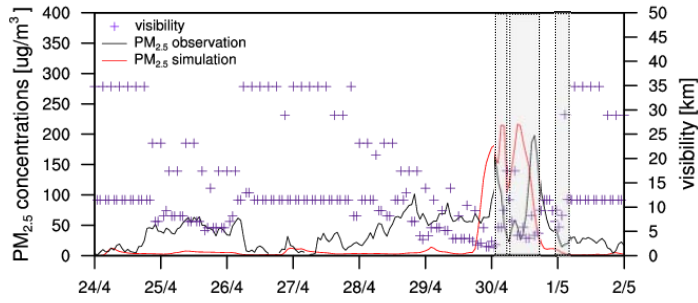


Figure 36: Same figure as Figure 34 but for the measurement sites Xianghe, Tangshan and Xinglong. Meteorological data for Xianghe and Xinglong are taken from the site Beijing as there are no active NOAA meteorological sites near Xinglong and Xianghe for this time period.

## 5.4 Discussion

### 5.4.1 Relating dust mobilization in Gobi Desert and wind conditions

The study about dust mobilization in section 5.3.2.1 gave an insight into dust emission mobilization in Gobi Desert, the Central Chinese Deserts and the loess area west of Beijing from April 28 to 30 in 2011.

There are two main issues which still hamper regional dust emission modeling in Asian. On the one hand side, soil properties of dust source regions are described insufficiently or information is totally missing. Particle size distributions, surface roughness and soil crusting are the major unknown properties. On the other hand, meteorological processes are sometimes insufficiently reproduced by the model due to the coarse model grid and the steep topography of China. Especially, small-scale convection, turbulence and soil moisture conditions are sometimes difficult to reproduce by the models. Since in-situ measurement data of dust emission fluxes is not available for most Chinese desert regions, the estimation of the accuracy of modelled emissions is highly challenging for dust model studies.

The analysis of dust mobilization presented in section 5.3.1.2 showed that on April 30 between 00:00 h and 06:00 h relatively strong emissions are modelled for the loess area. This finding is somehow confusing as the loess area is generally not considered to be a strong dust source region. Moreover, the analysis showed that modelled wind speeds are high ( $> 14 \text{ m s}^{-1}$ ) in this area. Maybe wind speeds are overestimated due to the grid resolution of 28 km of the COSMO-ART model. This could lead to an overestimation of wind speeds in areas with steep mountains and small-scale topographic changes. However, also roughness length in this area is high with maximum values above 1.5 cm. Therefore, it could also be assumed that the defined threshold friction velocity might be underestimated, which could lead to an over-prediction of  $\text{PM}_{10}$  in the Beijing region. This assumption is supported by comparing results to the findings of *Fu et al.* [2013]. They used CMAQ 5.0 model coupled with a dust model to model  $\text{PM}_{10}$  emissions for April 28 to 30. They predicted emissions only in Gobi Desert. *Lee et al.* [2013] modelled the same time period and found emissions up to  $10 \mu\text{g m}^{-2} \text{ s}^{-1}$  in the loess area west of Beijing. Modelled wind speeds are between 12 to  $16 \text{ m s}^{-1}$  and therefore comparable to the study conducted in this thesis. They also claim that the loess area can be considered as a significant dust source in winter (December – February) and spring (March – May) with seasonal emission strengths of 5-10  $\text{t km}^{-2}$ , and 2-5  $\text{t km}^{-2}$ , respectively for the two seasons.

*Tegen et al.* [2013] found in their study about dust source activation mechanisms in the Sahara that a model grid resolution of 28 km could lead to a overestimation of the surface roughness length in a steep topography which could lead to a suppression of dust emissions. This finding is somehow contradictory to the findings of the study presented in this work.

The difficulty of correct threshold friction velocity estimation was shown by *Park and Park* [2013]. They pointed out that the threshold value for the Chinese loess area is mainly underestimated in existing models. They also pointed out that soil moisture plays a key role for threshold friction velocity simulations. Including an average soil moisture value for the loess area would increase the threshold friction velocity value up to a factor of 2. This threshold increase would decelerate dust emission initialization, as binding energies between soil particles would increase. *Darmenova et al.* [2009] found in sensitivity studies of different dust emission schemes that the horizontal dust flux, which triggers the vertical flux, is most sensitive to friction velocity, whereas soil parameters are mainly important for low wind speed dust event. Therefore, insufficient simulations of meteorological fields lead to highest uncertainties of model results [*Knippertz and Todd*, 2012].

#### 5.4.2 Analyzing dust event definitions

The analysis of modelled and measured PM<sub>10</sub> and PM<sub>2.5</sub>, as well as measured visibility and reported dust events in section 5.3.3.2 showed that Beijing, Tianjin and Baoding report dust events, but not Tangshan. This circumstance is somehow confusing, as Tangshan is located only around 100 km northeast of Tianjin.

In China dust events are defined by the Chinese Meteorological Administration according to the dust's impact on visibility. Dust is classified in four categories, (1) dust-in-suspension or widespread dust conditions describe dust which stays near the ground or source and visibility falls below 10 km; (2) during blowing dust conditions sand or dust is lifted up to higher altitudes than during widespread dust conditions and visibility is reduced to 1-10 km; (3) dust storms lift large amounts of particles in the air and reduce visibility to 200-1000 m; and (4) severe dust storms, when heavy wind raises extreme large amounts of particles and reduce visibility to less than 200 m [*Shao and Dong*, 2006]. Dust observations are conducted manually by an observer. Furthermore a dust event is only reported when it is also recognized at the same time at five different measurements sites.

According to this classification scheme, all reported dust event in Beijing, Tianjin and Baoding are classified as blowing dust event. The missing dust event report in Tangshan can be explained by the observed visibility which is below 10 km on April 29, but increases to 12-17 km on April 30, when the dust event is reported at the other sites. Visibility records are often reported every three hours and there is always a temporal shift between visibility reduction and the initialization of a dust event, as it takes some time for the particles to accumulate in the air and reduce visibility to 10 km and less. This leads to the observed temporal shift of the occurrence of minimum visibility and the report of a dust event. So, maybe airborne dust is observed on April 30, but measured visibility is above 10 km and prevents dust event reporting. This temporal shift makes it also difficult to define the exact source region, as particles are subject to mid- and long-range transport right after their uplift. Moreover, directly inside the desert

regions, only a few measurement sites exist which could be used for the study of active sources regions. As this analysis showed, the presented classification scheme of dust events can contain some shortcomings.

*Song et al.* [2007] introduced an alternative dust type classification scheme in their study analyzing dust and PM<sub>10</sub> concentrations in Northeast China in spring from 2000 to 2005. Dust types are classified according to measured PM<sub>10</sub> concentrations. Hourly PM<sub>10</sub> concentrations < 200 µg m<sup>-3</sup> are classified as suspended dust, 200-5500 µg m<sup>-3</sup> as blowing dust, 5500-15000 µg m<sup>-3</sup> for sand and dust storm and concentrations > 15000 µg m<sup>-3</sup> for severe sand and dust storms. *Song et al.* [2007] did not define further characteristics of dust events. They also did not define a distinction of dust, haze and fog, which could lead to possible misclassifications of days as dust day instead of haze day. During hazy days, high amounts of anthropogenic pollutants are dominant, whereas foggy days are dominated by high amounts of atmospheric humidity. Following the approach of *Song et al.* [2007] the reported dust events of this case study can be classified as blowing dust event at Beijing, Tangshan, Tianjin and Baoding.

#### **5.4.3 Assessing the uncertainty of simulating meteorological fields**

Analyzing the accuracy of modelled dust dynamics and dust impact on PM<sub>10</sub> and PM<sub>2.5</sub> concentrations, it is important to estimate model performance of main modelled meteorological parameters. For this reason performance statistics of the meteorological variables wind speed, wind direction and air temperature at the four sites Beijing, Baoding, Tianjin and Tangshan are calculated for the time period of April 24, 00:00 h, to May 2, 00:00 h. These calculations were conducted using NCL. The following attributes are calculated and shown in Table 8: mean average of modelled parameters (ave\_mod), mean average of observed parameters (ave\_obs), number of data points used for calculations (npt) and the Spearman correlation coefficient (r).

There is a general good fit of modelled and observed temperatures at all four sites with correlation coefficients between 0.6 and 0.9 (Table 8). Correlation coefficients between modelled and observed wind directions show stronger variations between 0.07 and 0.55. Beijing shows the best correlation of modelled and observed wind speeds. However, it should be noted that Beijing offers the highest total number of data points among all sites due to the hourly observation interval. The correlation coefficient for wind direction is also highest at Beijing with 0.55 and lowest at Tianjin with 0.12. However, it is important to note, that for this statistical analysis point-based measurement data is compared to raster-based data.

In-depth study of airborne mineral dust mid-range transport in Northeast China and its impact on Beijing's air quality using COSMO-ART and ground-based network data

---

Table 8: Performance statistics of modelled 10-m wind speed (WS), 10-m wind direction (WD) and 2-m temperature (T) at Beijing, Baoding, Tianjin and Tangshan from April 24 at 00:00 h to May 2 at 00:00 h in 2011. The following statistical parameters are calculated: mean average of modelled parameters (ave\_mod), mean average of observed parameters (ave\_obs), number of data points used for calculations (npt) and the Spearman correlation coefficient (r).

site	Statistics	WS	WD	T
Beijing	ave_mod	3.5	184	16.1
	ave_obs	3.2	185	16.3
	Npt	193	174	193
	R	0.41	0.55	0.86
Baoding	ave_mod	3.3	183	17.1
	ave_obs	3.6	139	17.7
	Npt	53	53	53
	R	0.44	0.19	0.9
Tianjin	ave_mod	4.2	197	16.8
	ave_obs	4.5	235	14.9
	Npt	53	53	53
	R	0.12	0.07	0.60
Tangshan	ave_mod	3.7	166	14.4
	ave_obs	4.4	190	14.9
	Npt	53	53	53
	R	0.32	0.45	0.78

The comparison of modelled and observed wind speeds and directions is visualized in Figure 37. It can be seen that the change of wind direction from east to north at the beginning of the first dust event at Beijing is modelled too early. During the dust event, modelled and observed wind directions are in good accordance, whereas the modelled increase of wind speed is lower than observed wind speeds. The early change of the modelled wind direction change to north could explain the early timing of the modelled dust arrival found at the study about the comparison of modelled and observed PM<sub>10</sub> and PM<sub>2.5</sub> concentrations in Xianghe and Xinglong. During the arrival of the dust event at Baoding modelled and observed wind speeds increase from almost calm conditions to 8-9 m<sup>-1</sup>. Also modelled and observed wind directions are in good agreement. In Tianjin the agreement of modelled and observed wind speeds and directions are lowest of all sites. However, during the dust event both curves fit very well. There is a change of wind direction to north and an increase of wind speeds. The change of modelled and observed wind direction on April 30 can also be seen at Tangshan. Also the steep increase of wind speeds to 12 m s<sup>-1</sup> is reproduced by the model. Furthermore, it can be assumed that the dust event also affected Tangshan, even a dust event is not reported by the Chinese Meteorological Administration.

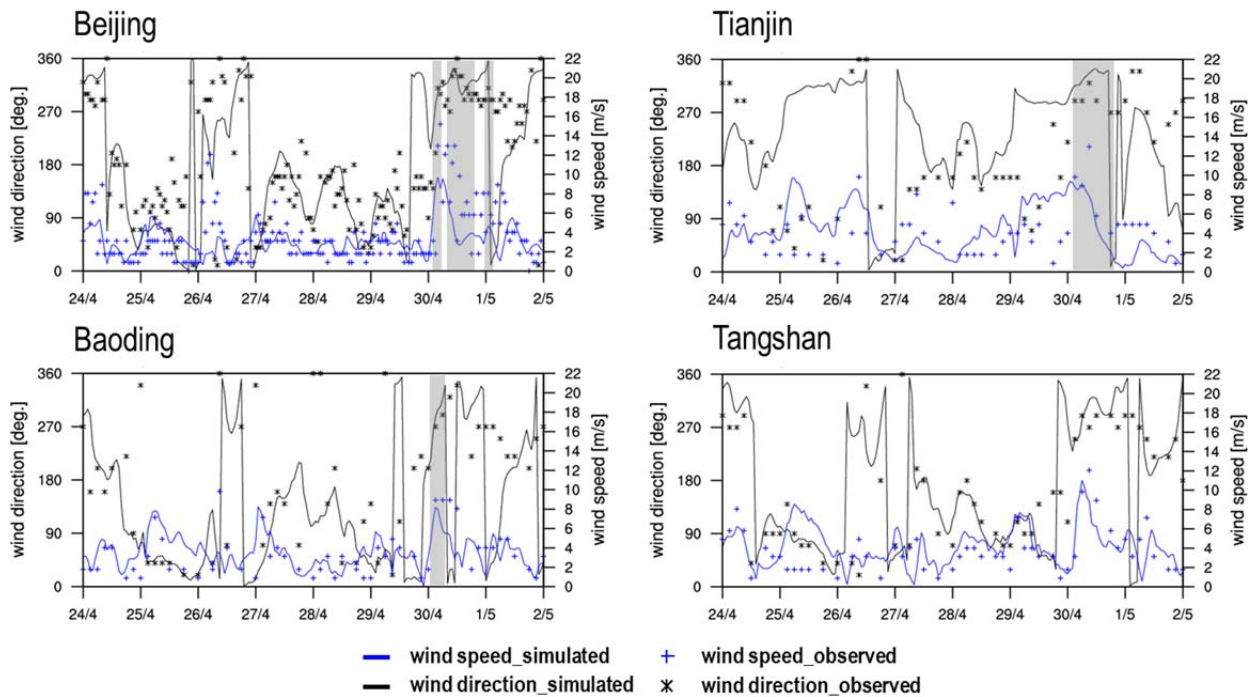


Figure 37: Modelled and observed wind speed (in  $\text{m s}^{-1}$ ) and wind direction (in  $^{\circ}$ ) for Beijing, Baoding, Tianjin and Tangshan between April 24 at 00:00 h and May 2 at 00:00 h in 2011. The blue line denotes modelled wind speeds; the blue cross denotes observed wind speeds, the black line shows modelled wind directions and the black asterisk shows observed wind directions. Reported dust events are shaded in grey.

#### 5.4.4 Relating the observed dust event transport route to existing classifications

As presented in chapter 1, there are different classification systems of transport routes of Asian dust.

Following the approach of *Xuan and Sokolik* [2002] the dust event detected in Northeast China during the case study between April 28 and 30 can be defined as moving dust storm type. Dust events in Taklimakan Desert are mostly stationary dust storm types, as dust is only transported outside the source region under specific weather conditions. However, modelled dust concentrations inside the Hexi corridor, which is the main transport pathway for dust events originating in Taklimakan Desert, are very low. Therefore, an influence of Taklimakan Desert dust on Beijing's air quality can be neglected.

As the modelled dust event in Northeast China moves towards the east and southeast, it follows the northerly Mongolian path and the northern desert path defined by *Zhang et al.* [2003a]. These two paths are the main dust routes which transport dust from Gobi Desert to Eastern China [*Zhang et al.*, 2003a].

#### 5.4.5 Analyzing the influence of orography on dust distribution

The study about vertical dust dynamics presented in section 5.3.2.2 showed some interesting features of dust distribution due to the specific wind conditions and the topographic situation. A detailed analysis of

the vertical dust distribution on April 30 between 00:00 h and 05:00 h is shown in Figure 38. The presented profiles are part of the cross-section B shown in section 5.3.2.2.

It can be seen that there is a strong dust plume close to 41° N modelled for April 30 at 00:00 h. One hour later the plume split into two different layers located between the ground and 2.5 km height and between 3 and 5.5 km height. There is also some dust located over the North China Plain between 37° and 40° N, with a gap over the small part which crosses the Yellow Sea. Beijing is located at 40° N. At 02:00 h highest concentrations can be found around 4 km height and the horizontal winds begin to change. At 02:00 h and 03:00 h the dust is pushed down the mountain ridge by strong descending winds and a vortex forms in the lee of the mountain ridge. It seems that dust is pushed down to the area of Beijing by the vertical winds. It is not clear if the high dust concentrations close to the ground at 03:00 h are caused by downdraft of dust from the uplifted plume at 4 km height or originate from newly emitted particles from the ground between 39° and 40° N. The analysis of dust emissions in section 5.3.1.2 showed that there are some emissions predicted for this area. This circumstance is also discussed in section 5.4.1. At 03:00 h and 04:00 h a long vertical dust cloud, which stretches from the ground to 5 km height is located over Beijing. This tall dust plume also causes the high modelled AOD values presented in chapter 4, section 4.4.1.3. The vertical extent of the modelled dust is also captured by CALIPSO (section 5.4.3).

To date, the impact of steep orography on dust distribution has only been studied for Sahara Desert. *Cuesta et al.* [2009] found that mountains cause modifications of the dust flow in Sahara Desert. A wave in the lee of the obstacle causes a change of the planetary boundary layer height and therefore a change of dust distribution. A strong vertical mixing in the lee of the mountain was observed. A similar orographic effect can also be seen for the Asian dust event presented in this work.

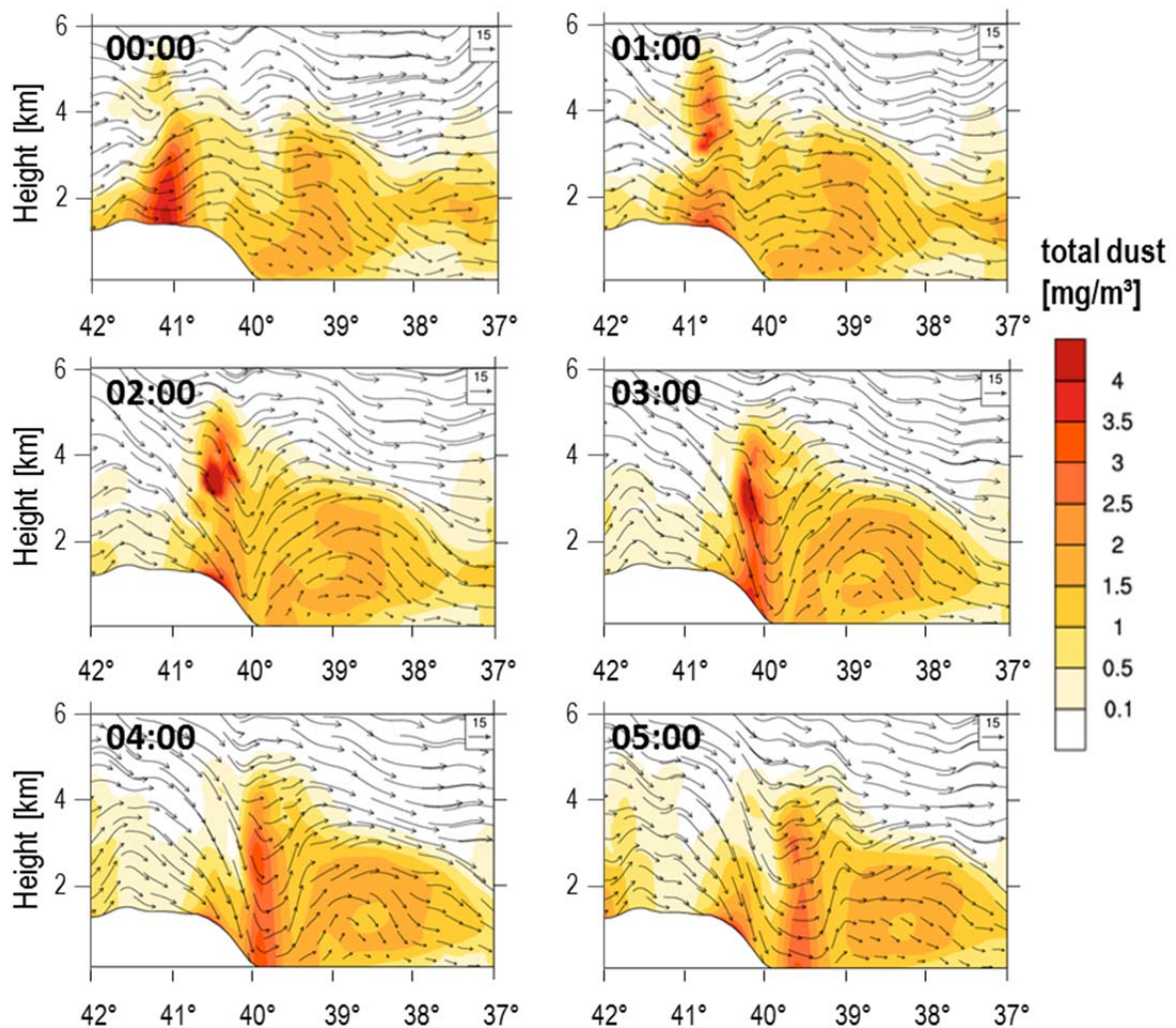


Figure 38: Vertical profiles of total dust concentrations (in  $\text{mg m}^{-3}$ ) up to 6 km height for a part of cross-section B between 37° and 42° N for April 30, 00:00 h to 05:00 h. Time is UTC. The vertical wind velocity is multiplied by a factor of 20 to make vertical movement visible. The reference vector is shown in the top right corner of the plots and set to  $15 \text{ m s}^{-1}$ . The scale on the right hand side refers to total dust mass concentrations and is valid for all plots. Beijing is located at 40° N.

#### 5.4.6 Estimating orographic effects on dust impact on $\text{PM}_{10}$ and $\text{PM}_{2.5}$

The locations of the measurement sites in the Beijing region and their locations in respect to the main dust transport pathway are expected to have an effect on the impact of dust on air quality.

The study about the impact of dust on air quality in Beijing and its surrounding (section 5.3.3) showed that the influence of dust on air quality shows strong variations even in a relatively narrow area. In addition, the study about vertical transport of dust (section 5.3.2.2) revealed that dust distribution is strongly influenced by topography. It showed up that dust which is transported from the eastern part of Gobi Desert and the loess area to Beijing (profile B) is distributed in two different vertical layers and two main dust plumes.

The steep slope of the mountains west of Beijing causes turbulences which lead to a strong vertical stretching of dust plumes. The study also showed that modelled dust concentrations are highest in Beijing and Baoding, which are located closest to the western mountain ridge. There are also differences of the timing and duration of reported dust events. The duration of events reported at Beijing and Baoding are shorter than the event reported at Tianjin. It can be assumed that the areas closer to the mountains are affected by higher dust concentrations during shorter time periods, whereas the areas closer to the Chinese East Coast are affected by a longer time period but with lower concentrations. However, this assumption can only be drawn during pure dust events with low influence of anthropogenic particles.

#### **5.4.7 Assessing constraints which cause discrepancies between modelled and measured PM<sub>10</sub> and PM<sub>2.5</sub> concentrations**

The results of the study of dust impact on PM<sub>10</sub> and PM<sub>2.5</sub> concentrations showed that mid-range transport of airborne dust, leads to a strong increase of PM<sub>10</sub> and PM<sub>2.5</sub> in the Beijing region between April 29 and 30. PM<sub>10</sub> concentrations start increasing a few hours earlier than PM<sub>2.5</sub> and also stay on a higher level for a longer time period than PM<sub>2.5</sub> does. This circumstance could be caused by the fact, that particles in the size range of PM<sub>2.5</sub> are smaller and can be transported in higher altitudes more easily. Moreover, these results clearly show the different source regions of the two dust plumes transported to the region of Beijing. During the arrival of the first plume, PM<sub>2.5</sub> and PM<sub>10</sub> concentrations increase in the area south of Beijing. However, the second dust plume is accompanied by a strong increase of PM<sub>10</sub> concentrations south of Beijing on April 30 around 06:00 h, whereas PM<sub>2.5</sub> concentrations are already decreasing in this area. This discrepancy could be caused by different particle size distributions. The amount of bigger particles of the size range up to 10 µm is higher during the second dust plume than during the first one. This result supports the earlier finding that the source of the second plume has to be located closer to the Beijing region than the source region of the first plume.

To quantify the accuracy of modelled PM<sub>10</sub> and PM<sub>2.5</sub> concentrations and to investigate the impact of dust on air quality, a comparison of measured and modelled PM<sub>10</sub> and PM<sub>2.5</sub> with reported visibility and dust event occurrence was conducted. The possible underestimation of the threshold friction velocity for the loess area in combination with high wind speeds, could lead to the overestimation of PM<sub>10</sub> at Baoding, Xianghe and Tangshan by 1650 µg m<sup>-3</sup>, 1350 µg m<sup>-3</sup>, and 1000 µg m<sup>-3</sup>. As there is no PM<sub>10</sub> data available for the time period of the dust event at Beijing, Tianjin and Xinglong, a closer analysis for these sites is not possible. The comparison also showed that there is a temporal lack of the beginning and ending of the dust peaks of measured and modelled PM<sub>10</sub> at Xianghe and Tangshan, whereas the arrival time of dust at Baoding fits very well. At Tianjin one can see an almost perfect fit of the beginning and ending of the modelled dust peak with reported dust event occurrence. As the arrival time fits well for the southern sites Baoding and Tianjin, one can assume that there are some constraints on correct simulation of wind

direction and speed in this region. The discrepancy of the modelled and observed timing of the dust event at Beijing and Tangshan could be explained by the early change of modelled wind directions to north (see section 5.4.3).

The temporal shift of the beginning and ending point of modelled dust induced  $PM_{10}$  peaks can also be seen for the second peak of modelled  $PM_{2.5}$  concentrations at Xinglong. Start and ending points of the first  $PM_{2.5}$  peaks fits almost perfectly for Xianghe, Tangshan, Xinglong and Baoding. There are also some discrepancies between modelled and measured  $PM_{2.5}$  concentrations. However, model and measurements are in better agreement for  $PM_{2.5}$  than  $PM_{10}$ . There is an overestimation of modelled  $PM_{2.5}$  concentrations for the first peak on April 30.  $PM_{2.5}$  is overestimated by  $120 \mu\text{g m}^{-3}$  at Xianghe,  $100 \mu\text{g m}^{-3}$  at Tangshan, and  $25 \mu\text{g m}^{-3}$  at Xinglong. As some data points are missing at Baoding during the dust event, the real extent of modelled  $PM_{2.5}$  overestimation remains unclear. The second  $PM_{2.5}$  peak is underestimated at Xianghe and Tangshan by  $150 \mu\text{g m}^{-3}$ , and  $60 \mu\text{g m}^{-3}$ , respectively and slightly overestimated at Xinglong by  $10 \mu\text{g m}^{-3}$ . The underestimation at Xianghe and Tangshan could be related to the presence of anthropogenic aerosols which are not reconsidered within the model simulations but captured in the ground-based measurements. As Xianghe and Tangshan are located downwind of Beijing,  $PM_{2.5}$  concentrations could also be affected by additional anthropogenic  $PM_{2.5}$  sources. As anthropogenic particles mainly consist of small particles, mainly  $PM_{2.5}$  concentrations are affected by these particles.  $PM_{2.5}$  is also strongly overestimated at the most southern located site Baoding. This overestimation could also be related to high dust emissions modelled for the loess area, as strong wind speeds also release high amounts of small particles. Another reason already appeared in findings of chapter 4, which showed that there seems to be a slight shift of the location of the cyclone which triggers the dust transport. The comparison of modelled AOD and AOD captured by MODIS showed that highest AOD of MODIS is located slightly further in the north than the modelled AOD. This leads to a loss of agreement between modelled and satellite derived AOD in the south and north of Beijing (see section 4.5.2). This circumstance could also be the reason for the temporal lack of the beginning and ending of the dust induced  $PM_{10}$  and  $PM_{2.5}$  peaks.

Besides meteorological constraints and model uncertainties, it should be kept in mind that in this analysis raster-based  $PM_{10}$  and  $PM_{2.5}$  concentration data is compared to point-based data. Moreover, the point-based  $PM_{10}$  and  $PM_{2.5}$  concentrations are measured in 2-m height, whereas the modelled raster-based concentrations are valid for the lowest model layer, which is approximately 20 m thick. The comparison of these totally different data can lead to a certain extent of disagreement which should not be related to 'wrong' model results. Despite of these discrepancies, it is important to note, that the temporal variability of measured and modelled concentrations are in really good agreement.

## 5.5 Summary and conclusions

In this chapter an in-depth study about dust dynamics and mid-range transport in Northeastern China for a three day episode in April 2011 was presented.

The goals of this study were (1) characterizing the spatio-temporal dynamics of mineral dust in Northern China by simulating total dust concentrations with COSMO-ART, (2) analyzing the characteristics of dust mobilization in the dust source region of this dust event by combined analysis of modelled dust emissions and wind conditions, (3) understanding the mid-range transport pattern of the dust transported towards Eastern China by studying the characteristics of horizontal and vertical dust distribution, (4) assessing the impact of the airborne mineral dust on air quality in the metropolitan area of Beijing analyzing modelled  $PM_{10}$  and  $PM_{2.5}$  concentrations in conjunction with  $PM_{10}$  and  $PM_{2.5}$  ground-based measurement data, and (5) studying the mixing of mineral dust with local pollutants by use of CALIPSO aerosol type data.

The analysis of dust dynamics and dust mobilization showed that Beijing and its surrounding are only affected by dust originating in the Northeastern Chinese desert regions. There is not any dust from Taklimakan Desert transported to Beijing. It showed up that there are three main regions in Northeastern China where mineral dust is emitted between April 28 and 30; namely Gobi Desert, the Central Chinese Deserts and the loess area west of Beijing. On April 29 around 06:00 h dust is emitted in a wide spread area, covering all three source regions. Dust emissions are initialized as soon as threshold friction velocity is exceeded by the 10-m wind speeds. This threshold strongly depends on the roughness of the surface. As surface roughness in many parts of the Central Chinese Deserts is lower than in Gobi Desert and the loess area, in the Central Chinese Deserts higher amounts of dust are emitted at lower wind speeds. Dust emission stops as soon as wind speeds fall below  $6 \text{ m s}^{-1}$ .

After dust particles are mobilized they are either deposited in the source region or transported to the downwind regions. Under certain atmospheric conditions with strong updrafts, airborne dust can also be transported to regions far away from the sources. The study about the transport of airborne dust mobilized in the source regions in Northeast China between April 28 and 30 showed that this dust event is transported on a mid-range scale to Beijing.

There are two dust fronts moving on southeastern paths towards Beijing. The plume on the more southern pathway arrives first in the Beijing region, followed by the second front in the north. West of Beijing, both plumes merge to one single dust front on April 30 between 00:00 h and 06:00 h. On April 30 06:00 h the dust cloud stretches from  $33^\circ$  to  $42^\circ$  N and  $107^\circ$  to  $120^\circ$  E, covering the whole region of Beijing, Tianjin, and their surrounding provinces Hebei Province, Shanxi Province, Shandong Province and most parts of Henan Province. At 12:00 h the front moves further on towards the Yellow Sea and Korea.

The vertical profiles of cross-sections A and B showed the spatio-temporal distribution of dust in the Gobi Plateau, the Central Chinese Deserts, loess area and Beijing and the dynamical dust transport towards Southeast China. In the Gobi area dust uplift is initiated by strong wind speeds. Then the airborne dust is transported by horizontal winds towards the southern rim of the plateau. At the beginning of dust emission in both cross-sections, dust is lifted to altitudes up to 10 km. After 18 hours a continuous dust layer in the Gobi Plateau in cross-section A has built up due to enduring dust emissions in this region. Approximately 12 hours later dust emissions in the northern part of the Gobi stopped and the remaining airborne dust is transported towards the southeast by descending winds. In cross-section B there are two dust plumes with two different vertical layers built up in the Gobi Plateau between April 29 at 12:00 h and 18:00 h. The first plume is transported towards Beijing in two different heights, one close to the ground triggered by descending winds and a second one in 2 to 4 km height lifted up by ascending winds. The second plume has two different layers which merge together on April 30 at 00:00 h. The second plume arrives at Beijing on April 30 around 06:00 h.

The results of this study clearly showed that there is a moving dust event originating in the Gobi Desert in South Mongolia, in the Central Chinese Deserts and the loess area west of Beijing. High amounts of airborne dust particles are transported towards Beijing. It can also be seen that most of the dust in Beijing and its surrounding is located near the ground. Total dust concentrations are always highest in the lowest model layer. The dust can be supposed to have an impact on Beijing's air quality due to its vertical location and the high total dust concentrations. However, the simulations do not indicate how strong Beijing's air quality, in terms of  $PM_{10}$  and  $PM_{2.5}$  levels, is affected by this dust.

To define the amount of airborne dust in terms of  $PM_{10}$  and  $PM_{2.5}$  in Beijing and its surrounding,  $PM_{10}$  and  $PM_{2.5}$  concentrations were modelled for this area and compared to ground-based measurements. The results showed that mid-range transport of airborne dust, lead to a strong increase of  $PM_{10}$  and  $PM_{2.5}$  in the Beijing region between April 29 and 30.  $PM_{10}$  concentrations start increasing a few hours earlier than  $PM_{2.5}$  and also stay on a higher level for a longer time period than  $PM_{2.5}$  does. This circumstance could be caused by the fact, that particles in the size range of  $PM_{2.5}$  are smaller and can be transported in higher altitudes more easily. Moreover, these results clearly show the different source regions of the two dust plumes transported to the region of Beijing. During the arrival of the first plume,  $PM_{2.5}$  and  $PM_{10}$  concentrations increase in the area south of Beijing. However, the second dust plume is accompanied by a strong increase of  $PM_{10}$  concentrations south of Beijing on April 30 around 06:00 h, whereas  $PM_{2.5}$  concentrations are already decreasing in this area. This discrepancy could be caused by different particle size distributions. The amount of bigger particles of the size range up to  $10\ \mu\text{m}$  is higher during the second dust plume than during the first one. This result supports the earlier finding that the source of the second plume has to be located closer to the Beijing region than the source region of the first plume.

To quantify the impact of airborne dust on  $PM_{10}$  and  $PM_{2.5}$  in Beijing and its surrounding, modelled  $PM_{10}$  and  $PM_{2.5}$  concentrations were compared to measurement data of the CAS-IAP ground-based network. The study showed that the measured  $PM_{2.5}$  peaks on April 30 in Baoding, Xianghe, Tangshan and Xinglong are dominated by dust particles. The dust caused also a strong increase of  $PM_{10}$  mass concentrations at Baoding, Xianghe and Tangshan. At the sites Beijing, Baoding and Tianjin only one  $PM_{10}$  and  $PM_{2.5}$  peak is measured and modelled on April 30. The timing of the  $PM_{10}$  and  $PM_{2.5}$  increase at the site Baoding is well modelled by the model. However, the  $PM_{10}$  and  $PM_{2.5}$  are overestimated by factors of 2.5 and 2. The modelled concentration peaks are well correlated with reported dust events and the drop of visibility. At the sites Xianghe, Tangshan and Xinglong two  $PM_{2.5}$  maxima are measured and modelled on April 30.  $PM_{10}$  simulations also show a clear double peak, whereas measured concentrations at Xianghe only show one clear peak and a small second peak at the Tangshan site. The timing of the two  $PM_{2.5}$  peaks at Xianghe and Tangshan is modelled very well, whereas the concentration increase of the second peak at the Xinglong site start slightly to early. The scale of modelled  $PM_{2.5}$  concentrations is in very good accordance with measurements at Xinglong. At Xianghe and Tangshan one can see an underestimation of the second  $PM_{2.5}$  peak in the late evening of April 30. This underestimation could be due to the presence of anthropogenic aerosols which are not reconsidered within the model simulations but captured in the measurements. As Xianghe and Tangshan are located downwind of Beijing,  $PM_{2.5}$  concentrations could also be affected by additional anthropogenic  $PM_{2.5}$  sources. As anthropogenic particles mainly consist of small particles,  $PM_{2.5}$  concentrations are affected much stronger by these particles. This influence cannot be seen for  $PM_{10}$  as modelled concentrations are slightly overestimated for both peaks at Tangshan and strongly overpredicted at Xianghe. The modelled dust peaks agree well with the observed visibility decline and reported dust events.

The comparison of modelled and measured  $PM_{10}$  and  $PM_{2.5}$  showed that the measured  $PM_{10}$  and  $PM_{2.5}$  peaks during the dust event seem to be dominated by the airborne dust. This result is in accordance with CALIPSO feature mask profiles for the Beijing region on April 29 to May 1. The CALIPSO data clearly showed that there are no significant amounts of anthropogenic particulates detected in the urban atmosphere. It can be concluded that particle modifications induced by mixing processes do not occur in this case of dust mid-range transport. Moreover, the CALIPSO feature mask product showed its high potential for use in air quality studies in dust loaded environments. It provides a strong information source about atmospheric aerosol composition and the vertical location and layering of aerosol layers.

The presented study about dynamics, mid-range transport and impact of airborne dust on air quality in Beijing showed that dust was activated in three different source regions between April 28 and 30 and then transported towards Beijing on a southeast transport pathway. Most of the dust is distributed near the ground but also in some uplifted layers due to turbulences in the lee of the mountains.

As most dust is located near the ground, it can be supposed to have an impact on air quality in terms of  $PM_{10}$  and  $PM_{2.5}$  in Beijing and its surrounding. It showed up that the strong increase of measured  $PM_{10}$  and  $PM_{2.5}$  concentrations on April 29 and 30 is dominated by the airborne dust. The study also showed that COSMO-ART is an appropriate model system for simulation of dust mobilization and transport and that CALIPSO satellite data give important information about atmospheric aerosol composition and its vertical location.

## 6 Assessment of air quality in Greater Beijing during the Olympic Summer Games in 2008 using COSMO-ART in conjunction with MODIS satellite data and ground-based measurements

### 6.1 Introduction

In addition to natural air pollutants, such as mineral dust, Beijing is also strongly affected by anthropogenic pollutants from emissions of local and regional sources, such as traffic, industry, domestic heating, and construction activities. Beijing's special air quality situation came into international focus in summer 2008, when Beijing hosted the 29. Olympic Summer Games [Streets *et al.*, 2007]. For this reason, the Beijing Municipality and the Chinese Government introduced several emission reduction measures to improve air quality and reduce the risk of high pollution levels on the athletes' health. Reduction measures comprised the closing and dislocation of heavy industry and power plants, traffic reductions, improvement of public transportation, and greening of public areas. Also technical improvements, such as industrial and automotive filter systems were introduced. Moreover, construction sites were closed during the Olympic period [Fang *et al.*, 2009; Wang *et al.*, 2010c; Zhou *et al.*, 2010; Schleicher *et al.*, 2012; Xin *et al.*, 2012].

To date several studies have been conducted, focusing on analysis of air quality during the Olympic Summer Games and the question if air quality changes were caused by the emission reduction measures. Noticeable reductions of gaseous pollutants were found for Beijing during the Olympic period. Mijling [2009] observed a reduction of NO<sub>2</sub> concentrations in Beijing by 60%, 30% in Tianjin, and 20% in Shijiazhuang by analyzing NO<sub>2</sub> column observations from GOME-2 and OMI satellites. Witte *et al.* [2009] analyzed OMI and MOPITT satellite data and found a smaller reduction of atmospheric column NO<sub>2</sub> up to 43%. Wang *et al.* [2010c] analyzed NO<sub>x</sub> and VOC concentrations in Beijing and found decreases by 25% and 20-45%, respectively. Sun *et al.* [2011] also detected a slight ozone decrease during the Olympic Summer Games, mainly due to reduction of local VOC and NO<sub>x</sub> emissions. Su *et al.* [2011] observed a reduction of NMVOC emissions by 45% in Beijing in August 2008, whereas Wang *et al.* [2009b] estimated an emission reduction of NO<sub>x</sub> by 36%. As ozone concentrations were only slightly decreased, both studies supposed a significant influence of regional pollutant sources and meteorological conditions on Beijing's air quality during the Olympic Summer Games. This assumption is also supported by Wang *et al.* [2010c], who even found ozone concentrations to be increased by 16% during the Olympic period at an urban measurement site in Beijing.

The reduction of gaseous pollutants also showed a significant effect on aerosol concentrations in Beijing. Cermak and Knutti [2009] studied the effect of reduction measures on the regional aerosol load by comparison of MODIS AOD data from the Olympic Summer Games period and from previous years,

estimating a decrease of AOD by 11% in Beijing. *Liu et al.* [2012] used MODIS satellite data in conjunction with a statistical model and found  $PM_{2.5}$  concentrations were lowered by 20-24  $\mu g m^{-3}$  (27-33%) during the Olympic Summer Games compared to a two-month period before and after August 2008. The analysis of  $PM_{2.5}$  measurement data in Beijing in summer 2008 by *Li et al.* [2013] reported that  $PM_{2.5}$  was reduced by 49% compared to the 27 day period prior to the Olympic period mainly due to reduction of secondary formed particles. A similar level of reduction was found by *Schleicher et al.* [2011a]; *Schleicher* [2012] who showed that daytime and nighttime  $PM_{2.5}$  concentrations were reduced by 48% and 46% during the Olympic Summer Games compared to the 24 day period prior to the Olympic Summer Games. Similar PM reductions were also estimated by *Gao et al.* [2011] using WRF-Chem model for summer 2008. *Schleicher et al.* [2012] also found that daily TSP was reduced by 63%; more efficiently than  $PM_{2.5}$ , which highlights the strong influence of inflowing polluted air masses from the surroundings on Beijing's particle pollution. *Wang et al.* [2009a] estimated that the specific weather conditions and mitigation measures accounted for 40% and 16% for the  $PM_{10}$  and  $PM_{2.5}$  variations in Beijing during the Olympic Summer Games, whereas *Xin et al.* [2012] reported a much stronger effect of the mitigation measures by 62-82%.

All studies showed that the urban atmosphere in Beijing is a heterogeneous mixture of different gaseous and particulate species. This circumstance makes an accurate simulation of urban air quality highly challenging. Up to now, detailed and high resolved information from modeling studies about the spatio-temporal variability of TSP,  $PM_{10}$  and  $PM_{2.5}$  in Beijing and its chemical composition variations are rare, especially during the Olympic Summer Games. Such simulations are still challenging, as they strongly depend on the accuracy of the emission inventory used as input data. For Asia, only two inventories are freely available to date, TRACE-P which is based on emissions from the year 2000 and INTEX-B, based on the year 2005. Moreover, the emission situation in Beijing and its surroundings has strongly changed during the Olympic Summer Games in 2008, when several emission reduction measures were undertaken. Several measurement studies were conducted using a bottom-down method to estimate the magnitude and impact of emission reductions on air quality. However, there is no linear correlation between emission reductions and atmospheric concentrations of gaseous and particulate air pollutants. Up to now, there is also no clear indication if these reduction measures dominated the observed air quality improvement during the Olympic Summer Games or if meteorological conditions played a more significant role. Moreover, besides the anthropogenic contribution to local air pollution, the influences of mid and long-range transported mineral dust on Beijing's air quality during summer is still an open question. Such particles could be a possible contributor to the observed slight reduction of  $PM_{2.5}$  which was measured by *Schleicher et al.* [2011a]; *Schleicher et al.* [2012].

To improve the understanding of air quality in Beijing during the Olympic Summer Games in 2008 the model system COSMO-ART was set up for a ten day period from August 4 to 14 in 2008, comprising four

days before the beginning of the Olympics and five days after the opening ceremony. In the framework of this study anthropogenic gases and aerosols, as well as mineral dust were modelled for Northeast China. In this chapter, first of all, modelled and observed meteorological conditions are defined and compared. Afterwards, modelled TSP, PM<sub>10</sub> and PM<sub>2.5</sub> concentration variations are analyzed and compared towards hourly and daily measurement data from ground-based sites in and around Beijing. To get more information about the composition of the urban aerosol during the Olympic Summer Games, the amount and ratio of secondary formed organic aerosols, SOA, carbonaceous species, and mineral dust are analyzed. In addition, the effect of the anthropogenic emission changes during the Olympic Summer Games are investigated by comparing NO<sub>3</sub><sup>-</sup> and SO<sub>4</sub><sup>2-</sup> concentrations modelled in three different runs with and without NO<sub>x</sub> and SO<sub>2</sub> emission reduction factors. Furthermore, the interactions between modelled pollutants and meteorological conditions are studied. Finally, the spatial distribution patterns of aerosols in Beijing and its surroundings and the influence of mineral dust on air quality are discussed.

The goals of this work focus on (1) analyzing the meteorological conditions during the Olympic Games, (2) characterizing the spatio-temporal distribution of TSP, PM<sub>10</sub> and PM<sub>2.5</sub> (3) defining the chemical composition of TSP, PM<sub>10</sub> and PM<sub>2.5</sub>, (4) assessing the interactions between particulate air pollutants and meteorological parameters, (5) defining the effects of emission reductions on air quality, and (6) estimating the impact of mineral dust on air quality in Beijing during the Olympic Summer Games.

## 6.2 Case study and model set-up

COSMO-ART is set up for the time period from August 4 at 00:00 h to August 14 at 00:00 h in 2008 (UTC). This time period is chosen as the Olympic Summer Games started in the evening of August 8 and lasted until August 24. As the model is set up in weather forecast mode, it is not reasonable to run the model for the whole period of the Olympic Summer Games or a longer time period.

For the simulation of this case study the mineral dust module, as well as the anthropogenic gas and aerosol module are switched on to reconsider anthropogenic emissions and natural mineral dust emissions. Mineral dust is modelled for model domain D1, whereas anthropogenic emissions are only modelled for the nested model domain D2. A map of both domains is shown in chapter 2. The grid cell size of both domains is set to 28 x 28 km<sup>2</sup>.

For simulation of mineral dust the same model set-up properties as chosen for the April 2011 case study (see chapter 4 and chapter 5) are used. Boundary data for gaseous species are updated every six hours. The release of emissions from the regional emission inventory and the calculation of atmospheric pollutant concentrations start after one hour of model initialization. As the inventory is already well validated, a detailed validation is not conducted within the framework of this study. However, results of

former modeling studies using this inventory are discussed together with results from the current study in section 6.4 of this chapter.

For comparison of modelled and measured data, point-based data of ground-based measurement sites and raster-based data of simulations with COSMO-ART are paired. For this task, the grid cell sizes of the model simulations which fit with the geo-location of the measurement sites were matched. The locations of the measurement sites are shown in Figure 39.

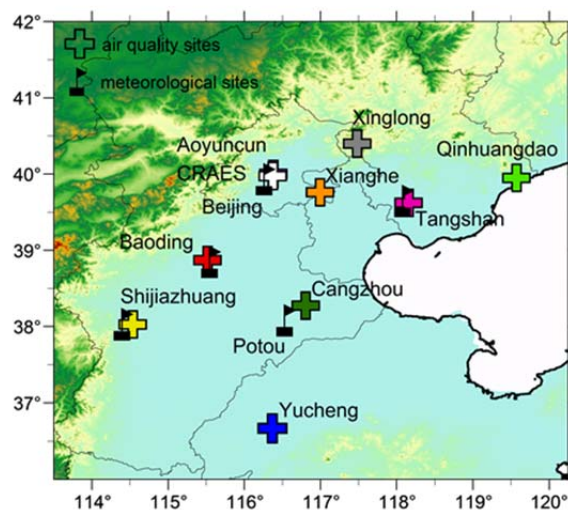


Figure 39: Map (36-42° N, 113.5-120.25° E) of location of NOAA meteorological measurement sites, CAS-IAP and CRAES air quality measurement sites providing data for August 4 to 14 in 2008 in model domain 2. Air quality sites are marked with colored crosses and meteorological sites are marked with a black flag. Black lines show country and province boundaries, superimposed with a surface elevation map (data source: see chapter 4).

## 6.3 Results

### 6.3.1 Meteorological conditions during the Olympic Summer Games

#### 6.3.1.1 Observed weather conditions

In this study meteorological parameters, such as temperature, wind speed, relative humidity, precipitation and visibility, measured at five sites in and near Beijing, are analyzed to give an overview of the meteorological conditions during the Olympic Summer Games case study from August 4 to 14 in 2008. Wind direction data is not included in this analysis, as wind directions measured in urban areas mainly represent local conditions but not the origin of air masses, which are a major factor for air quality conditions. Air mass origins are analyzed in detail in sections 6.3.2 and 6.4.

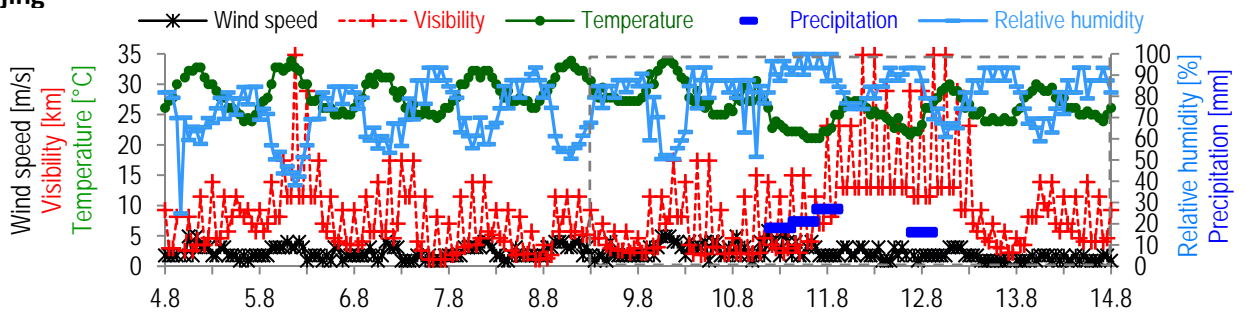
Time-series of wind speed, temperature, relative humidity and precipitation amounts are shown in Figure 40. In addition, visibility is presented, as it gives a first overview about local air quality [Bäumer *et al.*, 2008]. Visibility is strongly influenced by aerosol concentrations, air temperature, humidity and precipitation.

The data show that highest visibility records always occur during the temperature maximum at noon, as relative humidity is decreased by the high temperatures, mixing layer height and wind speeds are highest, which leads to mixing and dilution of aerosols in the urban atmosphere [Zhang *et al.*, 2010].

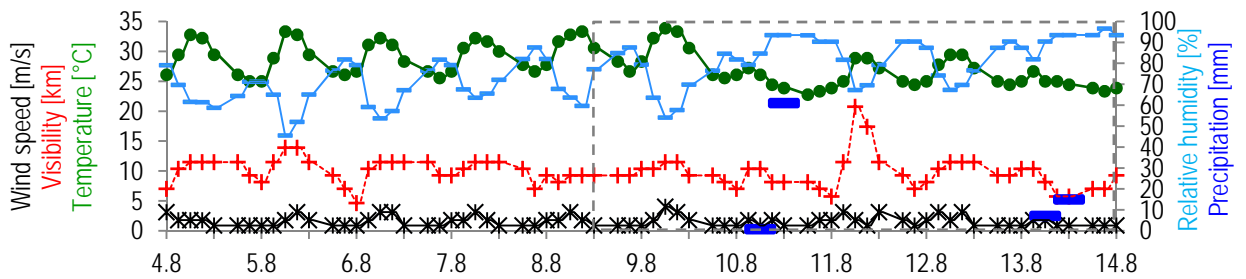
The presented time-series show that temperatures are very high during the whole period at all sites. However, there is a clear decrease of temperature from August 10 to 14 at all sites. During this period also several precipitation events were reported at all sites. Highest precipitation amounts (70 mm) were observed in Baoding on August 10. In Beijing four major precipitation events were measured on August 10 and 12 with maximum values of 27 mm. In general, relative humidity stayed on a high level during the whole period with minimum values of 40% and maxima of 100%. Whereas wind speeds were mainly low between 0 and 6 m s<sup>-1</sup> during the whole period. It can be seen that highest wind speeds (< 6 m s<sup>-1</sup>) were reported in Beijing and Tangshan (5.3 m s<sup>-1</sup>) on August 10, and 11, respectively. Maximum visibility < 35 km was measured in Beijing on August 5, 11 and the morning of August 12. Lowest visibility variations can be seen for Potou.

The simulation period can be divided into two parts according to similar meteorological conditions, the first part from August 4 to 9 and the second part between August 10 and 14. The weather conditions during the second part of the time-series indicate an increase of air quality in Beijing and its surroundings, as the lower temperatures can hamper ozone and secondary particle formation, and the precipitation events lead to a washout of atmospheric pollutants. The interactions between the specific meteorological situation and air quality during the Olympic Games period will be discussed in section 6.4.1.

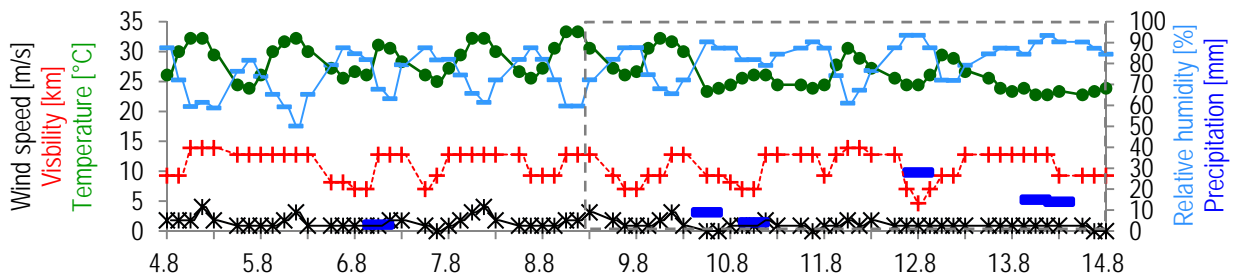
**Beijing**



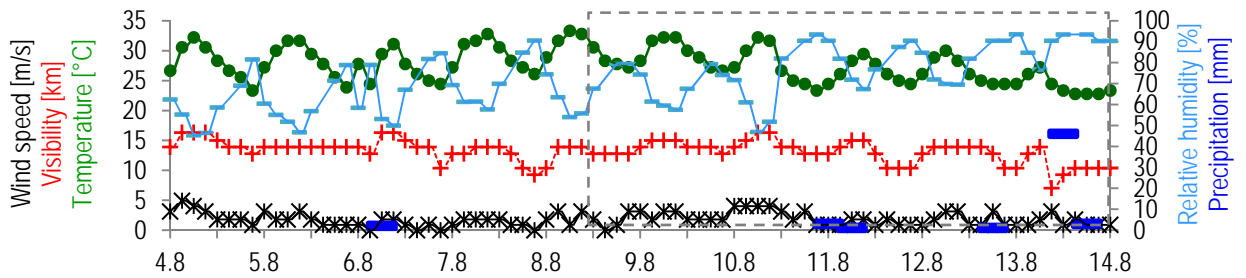
**Baoding**



**Shijiazhuang**



**Potou**



**Tangshan**

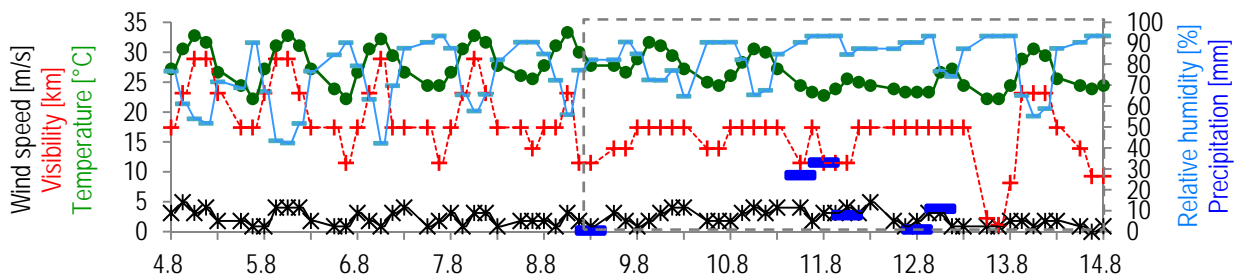


Figure 40: Time-series of wind speed (black line with asterisk), visibility (red line with cross), temperature (green line with dot), and precipitation (blue bulk) measured at NOAA sites in Beijing, Baoding, Shijiazhuang, Potou, and Tangshan from August 4 at 00:00 h to August 14 at 00:00 h in 2008. Wind speed in  $\text{m s}^{-1}$ , visibility in km, temperature in  $^{\circ}\text{C}$ , and precipitation in mm. The dashed grey boxes mark the Olympic period during the case study.

### 6.3.1.2 Comparison of modelled and observed weather conditions

As urban air quality critically depends on weather conditions, it is highly important to know how accurate meteorology is reproduced by the model. For this reason performance statistics of the major meteorological parameters wind speed, wind direction, temperature, relative humidity and precipitation at five sites in and around Beijing were calculated for the simulation period of August 4-14. The calculations were done using NCL software. The following statistical attributes were calculated and are shown in Table 9: mean average of modelled parameters (ave\_mod), mean average of observed parameters (ave\_obs), number of data points used for calculations (npt) and the Spearman correlation coefficient (r). For the comparison of precipitation, measured precipitation amounts in mm m<sup>-2</sup> and modelled precipitation amounts in kg m<sup>-2</sup> are summarized over the whole simulation period and shown by total sum (sum\_mod and sum\_obs). This is done, as the main precipitation variable in COSMO-ART is defined by sum over time and grid cell. The comparison of observed and modelled wind speed, temperature and relative humidity is visualized in Figure 41.

It shows up that especially air temperature and relative humidity are very well reproduced at all sites, with correlation coefficients of 0.76-0.9 and 0.52-0.74, respectively (Table 9). Major differences of modelled and measured relative humidity can be seen for minimum values at the sites Beijing on August 8-10, as well as at Baoding, Shijiazhuang, and Potou on August 13 (Figure 41). At all sites air temperature is underestimated between August 12 and 13. At the same time wind speeds are strongly overestimated, indicating a change of modelled air mass origin which causes a temperature decrease. Wind speeds are generally hard to evaluate, as observed wind speeds and wind directions are strongly influenced by local conditions, when measured inside the urban area. Modelled wind speeds show a best agreement at Potou and Tangshan site, and a lowest correlation for Baoding. However, wind directions are best modelled at Baoding site with a correlation coefficient of 0.37. Lowest agreement is achieved at Potou site. The comparison of precipitation amounts shows the lowest accordance for Beijing with highest discrepancies between total amounts and correlation coefficient. The total amount fits best for Potou and Tangshan with differences of 0.4 mm and 16.1 mm, whereas the correlation coefficient is best for Shijiazhuang and Baoding with 0.76 and 0.35. However, as six-hourly observational precipitation data was used, a low agreement with modelled data should be expected.

The resulting statistics of the conducted meteorological simulations and their effects on air quality are further analyzed in the discussion part of this chapter.

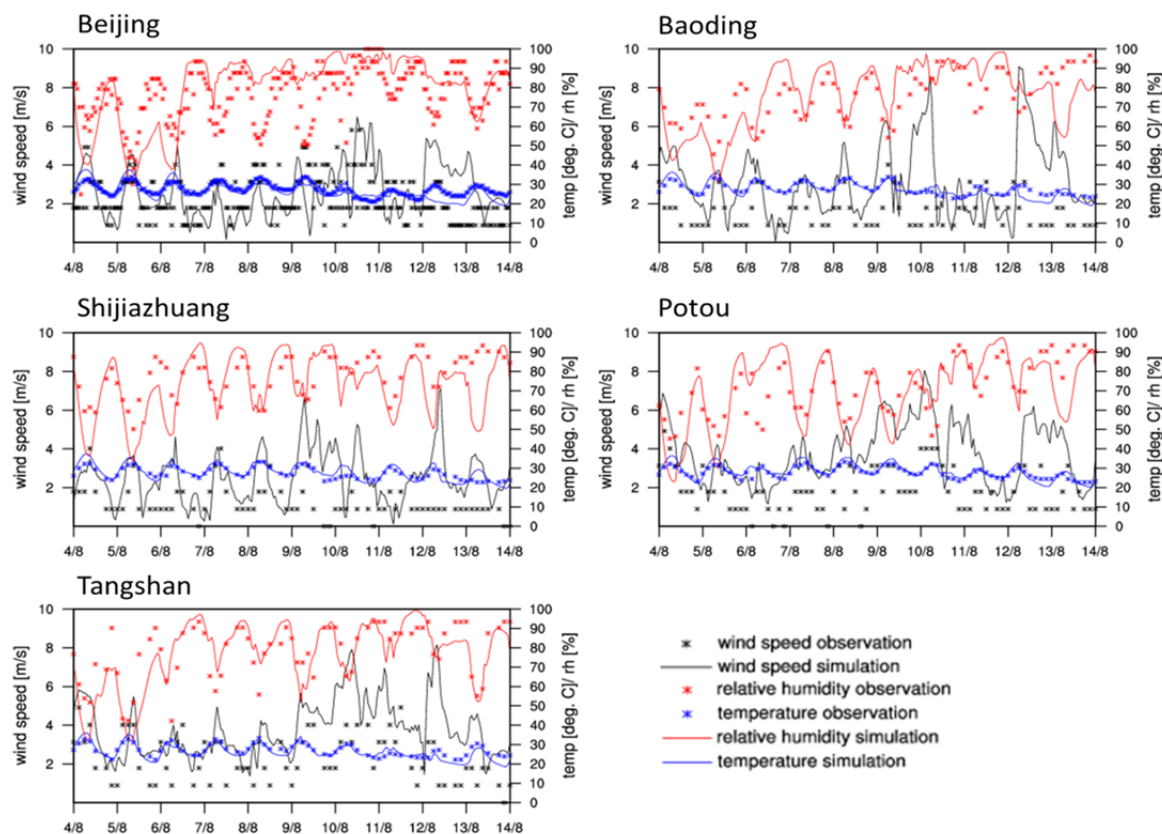


Figure 41: Comparison of observed and modelled meteorological parameters at sites Beijing, Baoding, Shijiazhuang, Potou, and Tangshan from August 4 to 14. Asterisk always describe measurement date and solid lines describe modelled data. Black denotes wind speeds (both in  $\text{m s}^{-1}$ ), red denotes relative humidity (both in %), and blue denotes temperature (both in  $^{\circ}\text{C}$ ). The scale of wind speed is on the left hand side of the plot, temperature and relative humidity on the right hand side of the plots.

Table 9: Performance statistics of the modelled 10-m wind speed (WS), 10-m wind direction (WD), 2-m temperature (T), 2-m relative humidity (RH), and precipitation (PRP) at Beijing, Baoding, Shijiazhuang, Potou, and Tangshan from August 4 at 00:00 h to August 14 at 00:00 h in 2008. Following statistical parameters are calculated: mean average of modelled parameters (ave\_mod), mean average of observed parameters (ave\_obs), data points used for calculations (npt) and Spearman correlation coefficient (r).

Site	statistics	WS	WD	RH	T	statistics	PRP
Beijing	ave_mod	2.6	160	79.8	26.5	sum_mod	395.6
	ave_obs	2.2	150	76.6	27.4	sum_obs	82.0
	npt	238	225	241	240	npt	4
	r	0.22	0.22	0.61	0.76	r	-0.2
Baoding	ave_mod	3.2	137	75.5	27.4	sum_mod	169.5
	ave_obs	1.6	157	76.0	27.8	sum_obs	83.8
	npt	71	71	71	71	npt	4
	r	0.19	0.37	0.52	0.79	r	0.35
Shijiazhuang	ave_mod	2.6	181	71.2	28.2	sum_mod	38.6
	ave_obs	1.2	180	78.0	27.3	sum_obs	72.9
	npt	71	65	71	71	npt	6
	r	0.21	0.19	0.53	0.81	r	0.76
Potou	ave_mod	3.8	168	69.9	28.4	sum_mod	55.7
	ave_obs	1.8	155	71.7	27.7	sum_obs	56.1
	npt	81	76	71	81	npt	6
	r	0.50	0.08	0.68	0.90	r	0.26
Tangshan	ave_mod	3.9	128	76.0	26.2	sum_mod	96.2
	ave_obs	2.3	158	78.0	27.2	sum_obs	80.3
	npt	71	70	71	71	npt	6
	r	0.48	0.41	0.74	0.85	r	0.09

### **6.3.2 Spatio-temporal distribution and variability of TSP, PM<sub>10</sub> and PM<sub>2.5</sub> concentrations**

#### **6.3.2.1 Spatio-temporal variability of AOD**

As AOD is a robust indicator of air quality, it was modelled for Beijing and its surroundings for the Olympic Summer Games case study. Modelled AOD reflects the total atmospheric loading consisting of anthropogenic aerosols and mineral dust. It was modelled for domain D2, for August 5-13 in 2008. Figure 42 shows the spatial distribution of AOD in Beijing and its surroundings for every day at 14:00 h (local Beijing time).

During the simulation period, AOD in domain D2 raised up to values  $> 1.5$ , representing a significant aerosol loading over the region of Beijing, Tianjin and Hebei Province. The simulations showed that on August 5, AOD over the whole region is lower 0.7 and main wind direction over the North Chinese Plain is east. One day later, on August 6, AOD increased up to 1.0 in Southern Hebei Province. AOD over Beijing is still lower than 0.4. Main wind direction changed to southeast. On August 7, AOD is still high in Hebei Province, but also increased in Tianjin and Beijing city. On the following day, on August 8, AOD over these areas is still high ( $< 1.3$ ). Main wind direction is south. On August 9, AOD further increased in Beijing and especially in the area between Baoding and Shijiazhuang, located south of Beijing. In addition, AOD in the region north of Beijing increased up to 1.2 in some areas. In general, AOD exceeds values of 0.8 over the whole region of Beijing, Tianjin, and Hebei Province. On August 10, 10-m wind speeds exceeded  $5 \text{ m s}^{-1}$  in the region of Tianjin and Hebei Province. AOD values are highest in the western parts of Beijing, Baoding, and Shijiazhuang. On August 11, northerly winds lead to a distribution of this aerosol towards the south, whereas easterly winds bring clean air from the ocean towards Tianjin and Beijing. However, one day later AOD over Tianjin and Southern Hebei Province strongly increased ( $> 1.6$ ) in Tianjin and south of Shijiazhuang. On August 13, the main wind direction over the whole area changed towards north-northeast. The figure shows that AOD are highest over North Shandong Province, the neighboring province of Hebei Province in the south.

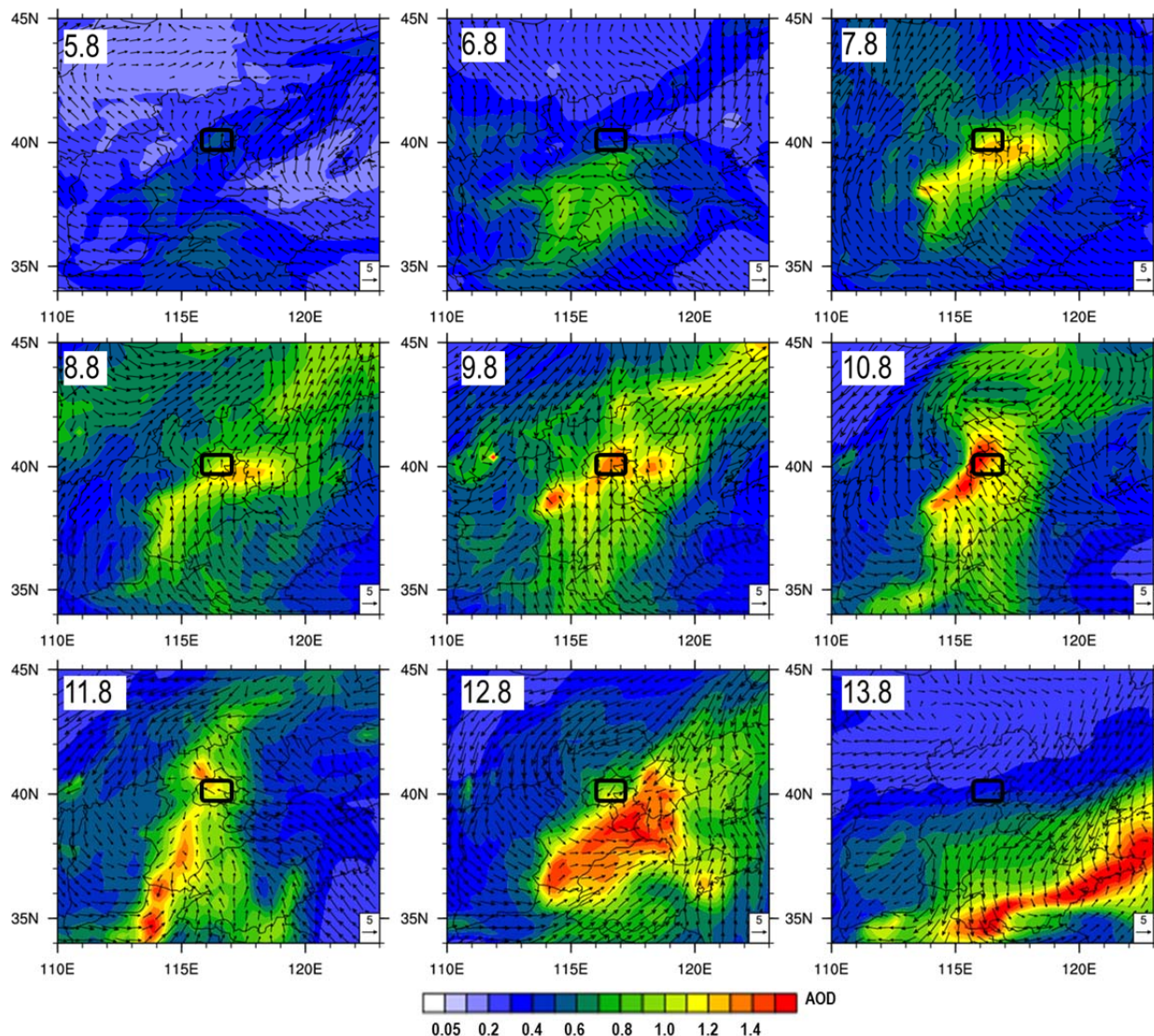


Figure 42: Spatio-temporal distribution of total AOD and 10-m wind vectors (meridional and zonal wind vectors in  $\text{m s}^{-1}$ ) in model domain D2 from August 5 to 13 in 2008 (from top left to bottom right) modelled by using COSMO-ART. AOD reflects the aerosol loading of the whole atmospheric column. White color denotes negligible ( $< 0.05$ ) or missing AOD values; red colors denote  $\text{AOD} > 1.5$ . Beijing is marked by a black box. The reference wind speed vector is shown in the bottom right corner of each plot and is set to  $5 \text{ m s}^{-1}$ . Time of every plot is 06:00 h (UTC) which corresponds with 14:00 h local Beijing time.

The modelled AOD values can be considered to be in a realistic range, as they are in accordance with findings by *Cermak and Knutti* [2009], who calculated daily spatial averages of MODIS AOD over Beijing and its surroundings for the period from August 1 to September 19. Observed AOD averaged over a region of 500 km radius, range between 0.5-1.5 for August 4-14. Further studies about AOD variability for the Olympic period are not published yet. Also a further comparison of modelled and satellite derived AOD is not meaningful, as MODIS-TERRA and MODIS-AQUA provide not enough data for the selected domain during the simulation period. However, a comparison of modelled and observed dust-only AOD was possible for the study of the mineral dust distribution in domain D1, which is presented in section 6.4.6.

### 6.3.2.2 Spatio-temporal distribution and variability of TSP, PM<sub>10</sub>, PM<sub>2.5</sub> concentrations and air mass origins

AOD is a first indicator about air quality in Beijing during the Olympic Summer Games regarding particulates. It showed that air quality in this region is significantly reduced compared to the region of Inner Mongolia and Shanxi Province, which is located west of Hebei Province. To quantify near-ground air quality, hourly and daily TSP, PM<sub>10</sub> and PM<sub>2.5</sub> concentrations were modelled with COSMO-ART for the lowest model layer in domain D2. In addition daily wind conditions in 10-m height were modelled.

The results of modelled near-ground wind conditions and TSP concentrations are shown in Figure 43. Modelled PM<sub>10</sub> concentrations are presented in Figure 44 and PM<sub>2.5</sub> concentrations in Figure 45.

It shows that on August 5, highest TSP ( $> 140 \mu\text{g m}^{-3}$ ) and PM<sub>10</sub> ( $25\text{-}35 \mu\text{g m}^{-3}$ ) concentrations are modelled for Baoding, Shijiazhuang and their surroundings. However, highest PM<sub>2.5</sub> concentrations are found north of Beijing, indicating atmospheric transport as there are no significant anthropogenic sources in this area. TSP, PM<sub>10</sub> and PM<sub>2.5</sub> concentrations in Beijing show maximum values of  $70 \mu\text{g m}^{-3}$ ,  $35 \mu\text{g m}^{-3}$ , and  $9 \mu\text{g m}^{-3}$ , respectively. Main wind direction in Beijing-Tianjin-Hebei region is southeast with relatively low wind speeds in the whole area. The high TSP concentrations in Shijiazhuang and Baoding correspond with almost calm wind conditions, whereas the wind pattern north of Beijing supports the assumption of the transport of smaller aerosols towards Inner Mongolia.

On August 6, wind speeds in the Baoding-Shijiazhuang region are still very low and the area of high TSP concentrations expands towards south and east. Highest PM<sub>10</sub> concentrations ( $30\text{-}40 \mu\text{g m}^{-3}$ ) are also found in this region. High PM<sub>2.5</sub> concentrations north and west of Beijing indicate mid-range transport of aerosols from Beijing-Hebei Province towards Inner Mongolia.

One day later, on August 7, TSP concentrations also increase in Southern Beijing and Tianjin. Main wind direction in this region is south with low wind speeds. It can also be seen, that a wind channeling effect leads to distribution of TSP from Beijing and Hebei Province towards Inner Mongolia. TSP concentrations in this area show elevated levels, even there are no significant anthropogenic sources located. PM<sub>10</sub> and PM<sub>2.5</sub> concentrations are also strongly increased in these regions.

On August 8, TSP distribution in Beijing, Tianjin, Baoding and Shijiazhuang is similar to August 7. In addition, a second TSP hot spot formed in Shandong Province, south of Beijing. However, highest PM<sub>10</sub> and PM<sub>2.5</sub> concentrations are still modelled for areas north of Beijing. Main wind direction is still south, but wind speeds slightly increase up to  $4 \text{ m s}^{-1}$ . The wind channeling effect is still visible.

On August 9, TSP concentrations in Beijing, Tianjin, South Hebei Province and West Shandong Province exceed  $150 \mu\text{g m}^{-3}$ . PM<sub>10</sub> in these areas also increase to  $40 \mu\text{g m}^{-3}$ , whereas PM<sub>2.5</sub> concentrations are very low ( $< 8 \mu\text{g m}^{-3}$ ). Still, an outflow of aerosols from Hebei and Beijing towards Inner Mongolia is visible.

On August 10, wind speeds in Beijing, Tianjin, Hebei and Shandong Province increase and wind directions change to east-southeast. These conditions lead to an inflow of clean marine air to Tianjin and North Hebei Province, but also cause the transport of TSP and PM<sub>10</sub> from the southern parts of the domain to the region of Beijing, Shijiazhuang and Baoding. However, a significant inflow of PM<sub>2.5</sub> is not modelled. The wind conditions in Inner Mongolia and Shanxi Province change towards a strong northerly pattern, carrying clean air towards Beijing-Tianjin-Hebei.

On August 11, wind conditions are almost calm in Southern Hebei Province which leads to an accumulation of aerosols with high TSP ( $> 160 \mu\text{g m}^{-3}$ ) and PM<sub>10</sub> ( $> 50 \mu\text{g m}^{-3}$ ) concentrations. Highest PM<sub>2.5</sub> concentrations are found north of Beijing and south of Tianjin. During this day and the next two days, TSP concentrations are strongly decreasing in Beijing, Baoding and Shijiazhuang, as the main wind direction changes towards north. PM<sub>10</sub> concentrations are also decreasing in this area but strongly increase in the southern parts of the domain, as aerosol is transported towards this region by northerly winds. This effect can also be seen for PM<sub>2.5</sub> on August 12.

The spatio-temporal distribution of TSP clearly shows the location of anthropogenic TSP sources in the Beijing-Tianjin-Hebei Province region, whereas PM<sub>10</sub> and PM<sub>2.5</sub> are more homogeneously distributed in the region. High amounts of PM<sub>2.5</sub> concentrations are continuously found in the regions downwind of source regions, but they are low within the source regions itself. This topic is further discussed in section 6.4.

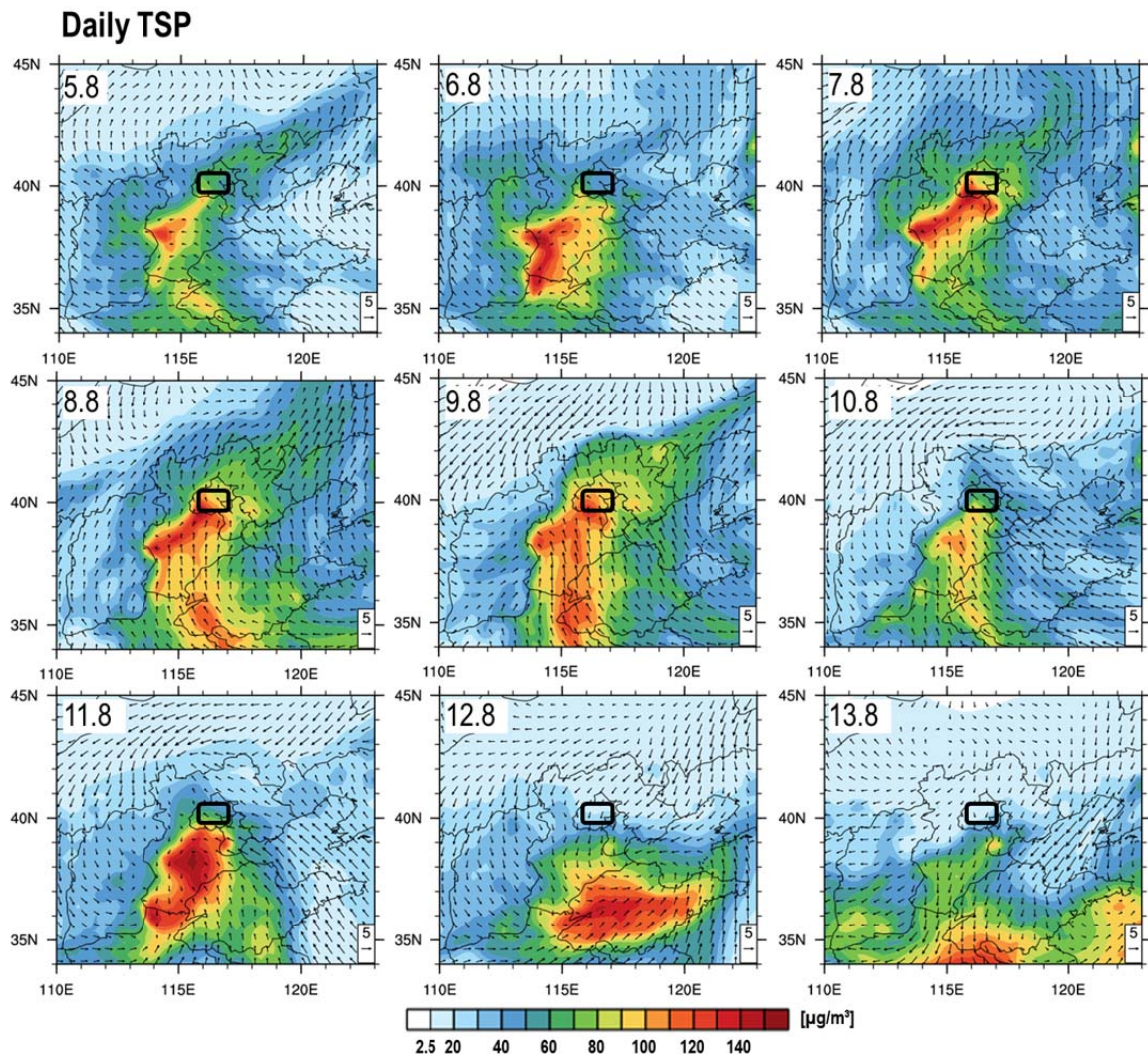


Figure 43: Spatio-temporal distribution of daily TSP concentrations (in  $\mu\text{g m}^{-3}$ ) and 10-m wind vectors (meridional and zonal wind vectors in  $\text{m s}^{-1}$ ) in model domain D2 from August 5 to 13 in 2008 (from top left to bottom right) modelled by using COSMO-ART. TSP comprises anthropogenic aerosols and mineral dust and is calculated for the lowest model layer. White color denotes negligible ( $< 2.5$ ) or missing TSP values; red colors denote TSP  $> 160 \mu\text{g m}^{-3}$ . Beijing is marked by a black box. The reference wind speed vector is shown in the bottom right corner of each plot and is set to  $5 \text{ m s}^{-1}$ . TSP is average over 24 hours for every day, beginning at 01:00 h UTC ( $\sim 09:00$  h Beijing time) for temporal accordance with daily measurement data from CRAES site (see section 6.3.2.3).

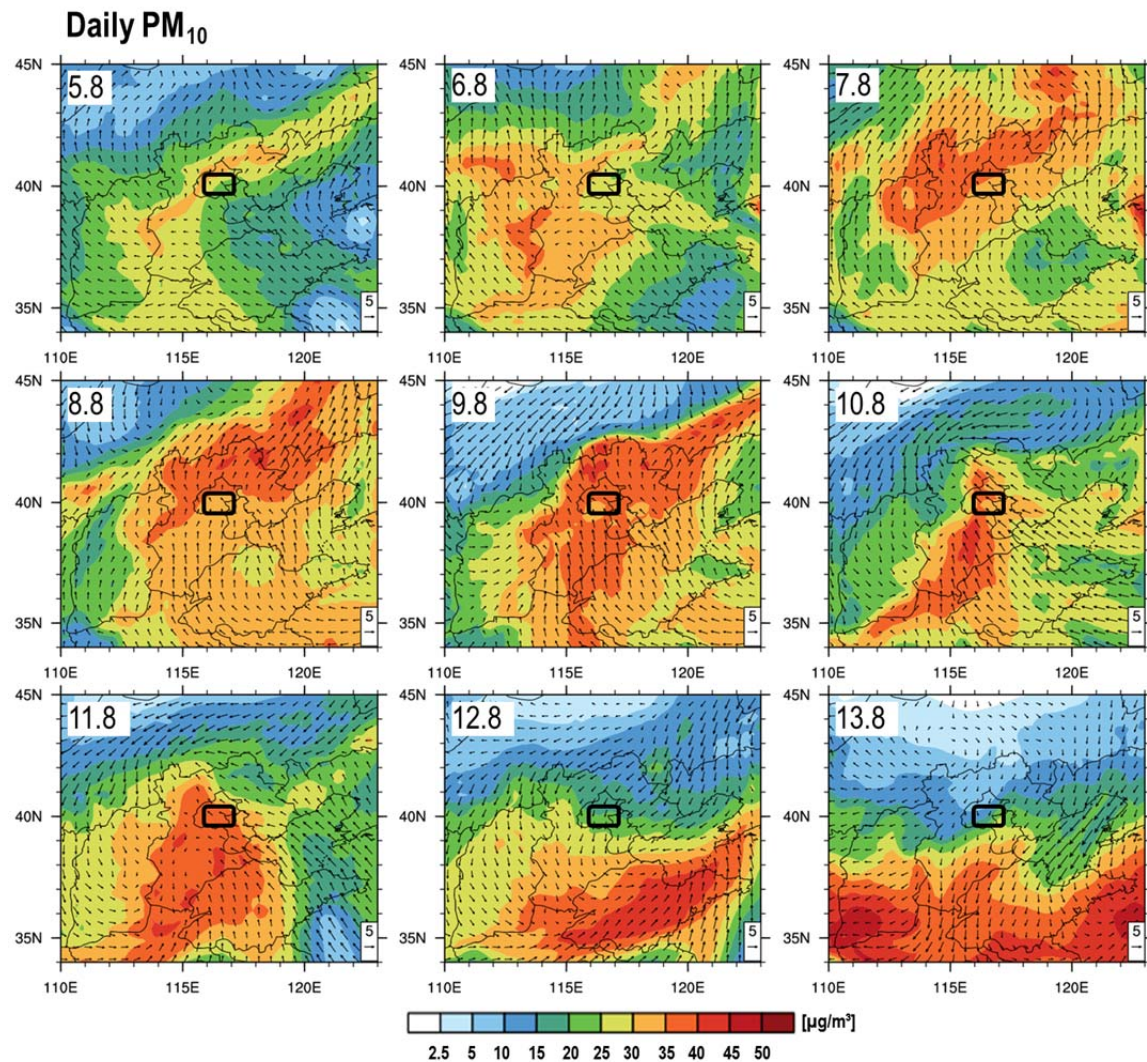


Figure 44: Spatio-temporal distribution of daily PM<sub>10</sub> concentrations (in  $\mu\text{g m}^{-3}$ ) and 10-m wind vectors (meridional and zonal wind vectors in  $\text{m s}^{-1}$ ) in model domain D2 from August 5 to 13 in 2008 (from top left to bottom right) modelled by using COSMO-ART. TSP comprises anthropogenic aerosols and mineral dust and is calculated for the lowest model layer. White color denotes negligible ( $< 2.5$ ) or missing PM<sub>10</sub> concentration values; red colors denote PM<sub>10</sub> concentrations  $> 50 \mu\text{g m}^{-3}$ . Beijing is marked by a black box. The reference wind speed vector is shown in the bottom right corner of each plot and is set to  $5 \text{ m s}^{-1}$ . PM<sub>10</sub> is averaged over 24 hours for every day, beginning at 01:00 h UTC ( $\sim 09:00$  h Beijing time) for temporal accordance with daily measurement data from CRAES site (see section 6.3.2.3).

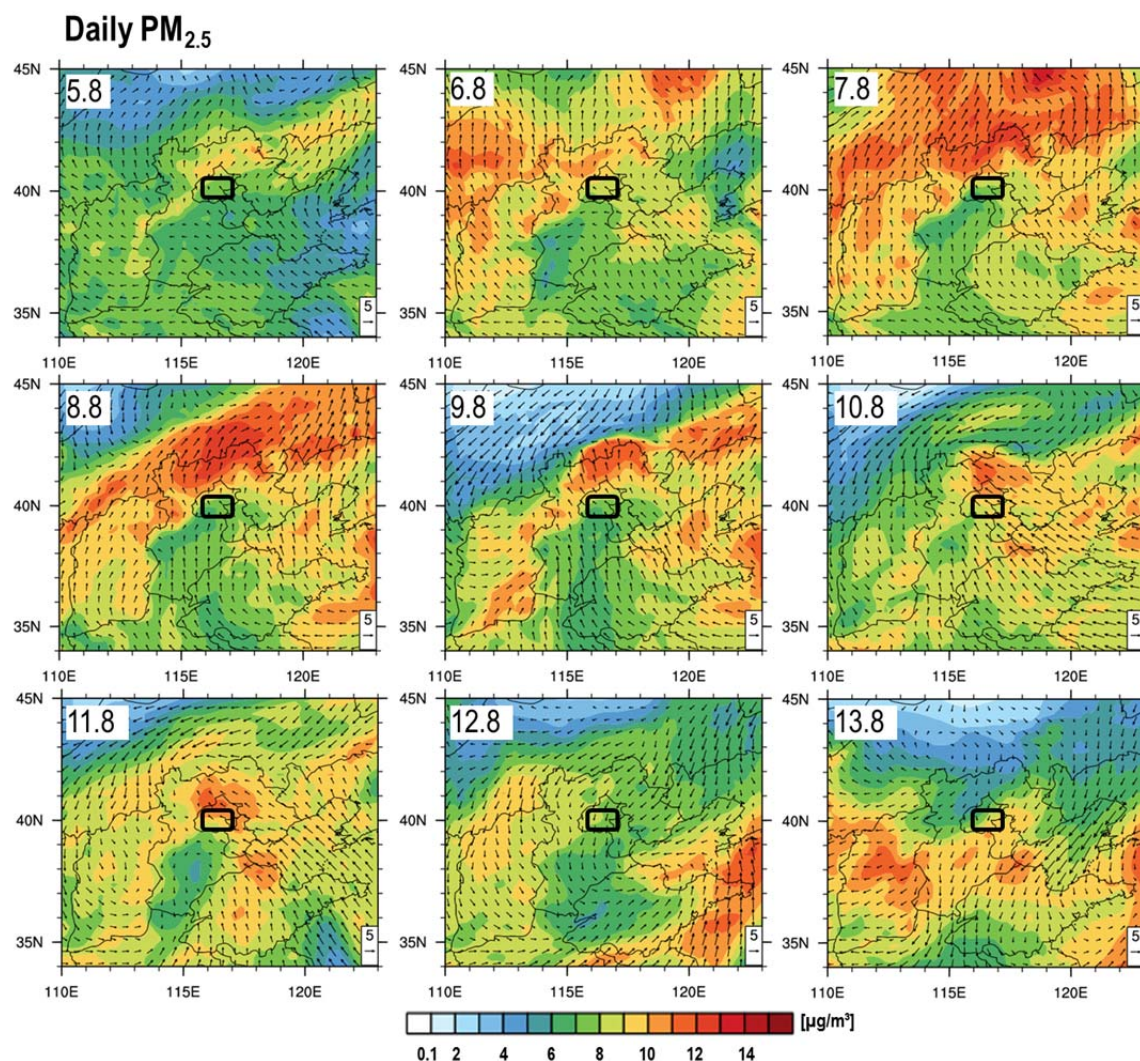


Figure 45: Spatio-temporal distribution of daily  $PM_{2.5}$  concentrations (in  $\mu g m^{-3}$ ) and 10-m wind vectors (meridional and zonal wind vectors in  $m s^{-1}$ ) in model domain D2 from August 5 to -13 in 2008 (from top left to bottom right) modelled using COSMO-ART. TSP comprises anthropogenic aerosols and mineral dust and is calculated for the lowest model layer. White color denotes negligible ( $< 0.1$ ) or missing  $PM_{2.5}$  concentration values; red colors denote  $PM_{2.5}$  concentrations  $> 16 \mu g m^{-3}$ . Beijing is marked by a black box. The reference wind speed vector is shown in the bottom right corner of each plot and is set to 5  $m s^{-1}$ .  $PM_{2.5}$  is average over 24 hours for every day, beginning at 01:00 h UTC ( $\sim 09:00$  h Beijing time) for temporal accordance with daily measurement data from CRAES site (see section 6.3.2.3).

### 6.3.2.3 Comparison of modelled and observed TSP, $PM_{10}$ and $PM_{2.5}$ in Beijing

Modelled hourly-mean  $PM_{10}$  and  $PM_{2.5}$  concentrations were compared to CAS-IAP measurement data in Beijing and its surroundings to check the level of accordance of predicted and measured concentrations. In addition, modelled daily TSP and  $PM_{2.5}$  concentrations in Beijing were also compared to daily TSP and  $PM_{2.5}$  data measured at Beijing-CRAES. For this analysis, modelled hourly TSP and  $PM_{2.5}$  concentrations were averaged over 24 hours. As the starting time of daily measurements is at 09:00 h (Beijing time), modelled data were averaged according to this time period.

The comparison of hourly modelled and measured PM<sub>10</sub> and PM<sub>2.5</sub> concentrations at Aoyuncun (Beijing) site shows that modelled values are strongly underestimated on August 4-9 and August 13 (Figure 46, left hand side). PM<sub>10</sub> is underestimated by a factor of 3-7, and PM<sub>2.5</sub> by a factor of 2.7-15 for these time periods. For PM<sub>10</sub> the agreement is much better on August 10 and 11. However, PM<sub>2.5</sub> is still most of the time underestimated for these two days.

The comparison of daily modelled and observed TSP and PM<sub>2.5</sub> concentrations also showed that modelled TSP concentrations are underestimated for August 4 to 9 and even slightly overestimated for August 10-12 (Figure 46, right hand side). In general, daily modelled and observed TSP fits much better than hourly values. However, the decreasing trend of measured TSP concentrations cannot be reproduced by the model, whereas modelled and observed daily TSP concentrations fit almost perfectly on August 10 and 12. Discrepancies between modelled and observed TSP levels are stronger during the period before the Olympic Summer Games started and lower afterwards. Regarding daily PM<sub>2.5</sub> concentrations, the strong overestimation of modelled PM<sub>2.5</sub> concentrations can also be seen within the comparison of daily PM<sub>2.5</sub> concentrations. PM<sub>2.5</sub> is underestimated by a factor of 2-13. The smallest discrepancy is found for August 11.

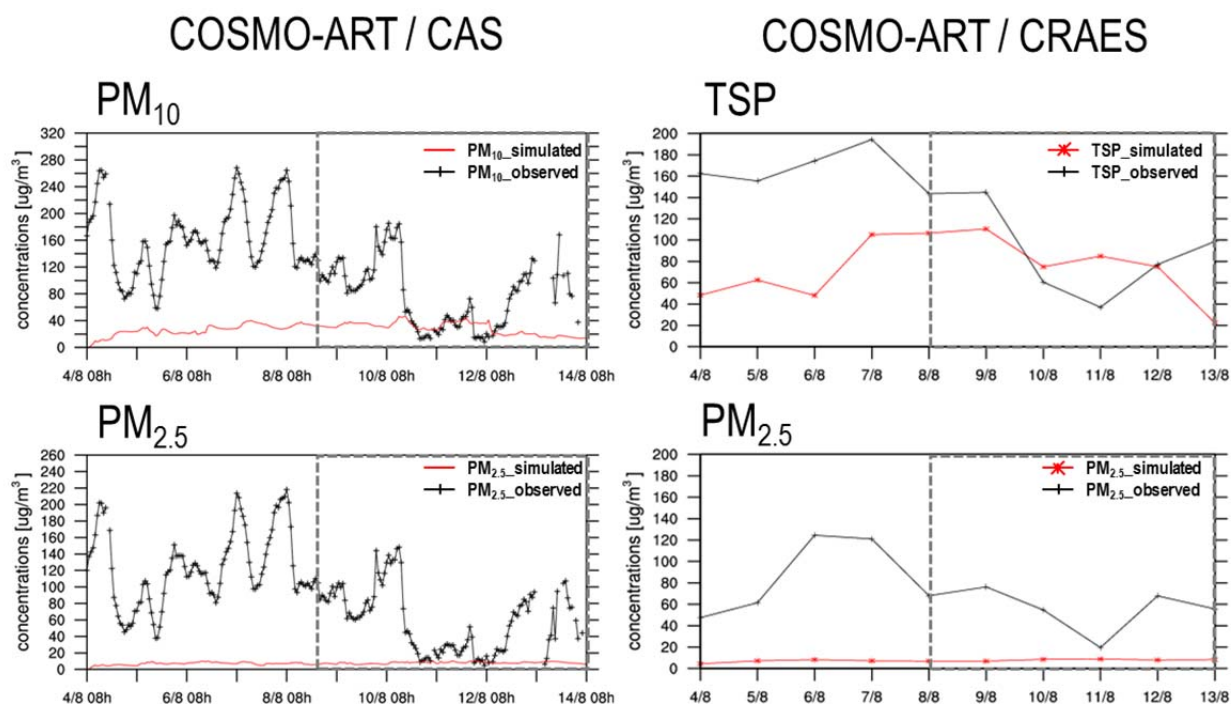


Figure 46: Comparison of hourly PM<sub>10</sub> (top plot, left column) and PM<sub>2.5</sub> concentrations (bottom plot, left column) and daily TSP (top plot, right column) and PM<sub>2.5</sub> (bottom plot, right column) concentrations (all in  $\mu\text{g m}^{-3}$ ) observed at CAS site Aoyuncun in Beijing and CRAES site in Beijing and modelled with COSMO-ART for August 4-13, 2008. Red lines denote modelled data and black lines define observed data. The grey box indicates the start of the Olympic period.

Visualizing modelled hourly  $PM_{10}$  and  $PM_{2.5}$  concentrations of all sites reveal that  $PM_{10}$  and  $PM_{2.5}$  concentrations show almost similar levels (Figure 47).  $PM_{10}$  goes up to  $45 \mu g m^{-3}$  on August 10 and 12. A diurnal cycle with peaks around noon is visible. Modelled  $PM_{2.5}$  concentrations go up to  $12 \mu g m^{-3}$  on August 7 and 11. A diurnal cycle is not that pronounced as for  $PM_{10}$ , as  $PM_{2.5}$  stronger reflects aerosol background conditions.

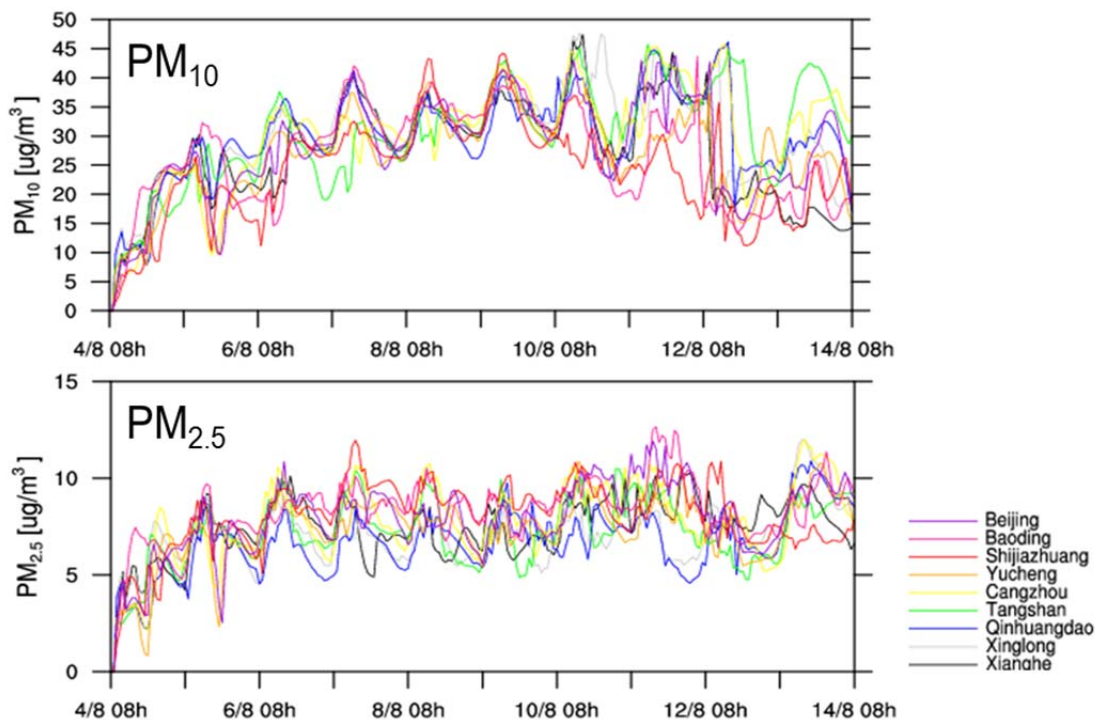


Figure 47: Temporal variability of  $PM_{10}$  and  $PM_{2.5}$  concentrations (in  $\mu g m^{-3}$ ) at site Aoyuncun (Beijing), Baoding, Shijiazhuang, Yucheng, Xianghe, Xinglong, Tangshan, Qinhuangdao, and Cangzhou for August 4-14 in 2008 modelled with COSMO-ART. Time is local Beijing Time. Purple lines define  $PM_{10}$  and  $PM_{2.5}$  concentrations at Aoyuncun (Beijing) site, pink lines stand for Baoding, red lines stand for Shijiazhuang, orange lines stand for Yucheng, yellow lines stand for Cangzhou, green lines stand for Tangshan, blue lines stand for Qinhuangdao, bright grey lines stand for Xinglong, and dark grey lines stand for Xianghe.

As all sites show similar concentration levels for hourly  $PM_{10}$  and  $PM_{2.5}$ , further visualization of modelled and observed concentrations are not presented. However, performance tests of  $PM_{10}$  and  $PM_{2.5}$  simulations were conducted and showed that a best fit of modelled and observed hourly  $PM_{10}$  variability is achieved for Baoding. The modelled  $PM_{10}$  average is  $28.0-29.7 \mu g m^{-3}$  and the observed average is  $120.6-136.3 \mu g m^{-3}$ . Modelled and observed  $PM_{2.5}$  concentrations also show strong discrepancies for all sites. The modelled  $PM_{2.5}$  average is  $6.7-8.3 \mu g m^{-3}$ , whereas the observed average is  $66.4-102.2 \mu g m^{-3}$ .

This issue will be further discussed in section 6.4.

Assessment of air quality in Greater Beijing during the Olympic Summer Games in 2008 using COSMO-ART  
in conjunction with MODIS satellite data and ground-based measurements

Table 10: Performance statistics of modelled PM<sub>10</sub> and PM<sub>2.5</sub> at Aoyuncun (Beijing), Baoding, Shijiazhuang, Yucheng, Xianghe, Xinglong, Tangshan, Qinhuangdao, and Cangzhou for August 4-14 in 2008, and comparison with measurement data. The following statistical parameters are calculated: mean average of modelled parameters (ave\_mod), mean average of observed parameters (ave\_obs), number of data points used for calculations (npt) and the Spearman correlation coefficient (r). – means that no observational data are available, preventing a further comparison.

Site	statistics	PM <sub>10</sub>	PM <sub>2.5</sub>
Aoyuncun (Beijing)	ave_mod	28.2	7.4
	ave_obs	120.6	90.3
	npt	222	228
	r	-0.18	-0.33
Baoding	ave_mod	27.9	7.0
	ave_obs	130.2	84.6
	npt	177	193
	r	0.1	-0.03
Shijiazhuang	ave_mod	29.7	6.7
	ave_obs	129.5	85.0
	npt	240	240
	r	-0.14	-0.3
Yucheng	ave_mod	-	7.3
	ave_obs	-	102.2
	npt	-	222
	r	-	-0.15
Xianghe	ave_mod	28.0	7.9
	ave_obs	136.3	87.8
	npt	214	240
	r	-0.04	-0.37
Xinglong	ave_mod	-	8.3
	ave_obs	-	66.4
	npt	-	185
	r	-	-0.22
Tangshan	ave_mod	-	7.3
	ave_obs	-	99.7
	npt	-	240
	r	-	-0.34
Qinhuangdao	ave_mod	-	8.1
	ave_obs	-	84.1
	npt	-	236
	r	-	-0.17
Cangzhou	ave_mod	-	7.8
	ave_obs	-	91.1
	npt	-	219
	r	-	-0.23

### 6.3.3 Composition of urban TSP, PM<sub>10</sub> and PM<sub>2.5</sub>

In this section the composition of urban aerosol in Beijing and its surrounding cities is analyzed. TSP, PM<sub>10</sub> and PM<sub>2.5</sub> comprise particles of different size ranges, which leads to a difference in chemical composition. Therefore, the composition of the urban aerosol also reflects the influence of major sources. To get an insight into the composition of urban TSP, PM<sub>10</sub> and PM<sub>2.5</sub>, the spatio-temporal variability of secondary particles (NH<sub>4</sub><sup>+</sup>, NO<sub>3</sub><sup>-</sup>, SO<sub>4</sub><sup>2-</sup>), soot (equal to BC), secondary organic aerosols (SOA), primary PM<sub>10</sub>, and mineral dust concentrations are modelled and analyzed for Beijing and its surrounding cities for August 4-14 in 2008. Moreover, the modelled chemical composition of TSP in Beijing city was compared to measurement data from the Beijing-CRAES site.

### 6.3.3.1 Relative chemical composition of urban aerosol in Beijing

The relative chemical composition of urban aerosol in Beijing and its surrounding during the Olympic Summer Games case study was modelled with COSMO-ART. Relative ratios of all species fractions were calculated. Following species were defined:  $\text{NH}_4^+$ ,  $\text{SO}_4^{2-}$ ,  $\text{NO}_3^-$ , SOA, soot, dust and primary  $\text{PM}_{10}$ . Soot comprises BC and primary  $\text{PM}_{2.5}$ , whereas dust comprises dust particles of all three modes. In addition, temporal variations of chemical species were analyzed for TSP,  $\text{PM}_{10}$  and  $\text{PM}_{2.5}$  for August 4-14.

Modelled relative chemical compositions showed significant variations among the different sites in the Beijing region. It also showed that there is a species ratio change among TSP,  $\text{PM}_{10}$  and  $\text{PM}_{2.5}$ .

Regarding TSP composition,  $\text{NO}_3^-$ , SOA and mineral dust are the most abundant species at all sites (Figure 48).  $\text{NO}_3^-$ , SOA and mineral dust vary between 21.6-30.1%, 18.0-32.9%, and 10.6-27.5%, respectively.  $\text{NO}_3^-$  is lowest in Tangshan and highest in Xinglong, whereas SOA is highest at Tangshan site and lowest in Qinhuangdao. Mineral dust, however, has its highest ratio in Qinhuangdao and is lowest in Beijing. Soot and  $\text{SO}_4^{2-}$  show low ratios at all sites. Primary  $\text{PM}_{10}$  varies between 5% in Xinglong and 14.8% in Tangshan.  $\text{NO}_3^-$  and SOA are the most abundant species in Beijing, accounting for > 60% of all species.

$\text{PM}_{10}$  at all sites mainly consists of the secondary formed species  $\text{NH}_4^+$ ,  $\text{NO}_3^-$  and  $\text{SO}_4^{2-}$  (Figure 49). They account for 61-66%.  $\text{NH}_4^+$  shows a maximum ratio at Shijiazhuang and a minimum in Qinhuangdao, whereas  $\text{NO}_3^-$  has its maximum in Qinhuangdao and its minimum in Baoding.  $\text{SO}_4^{2-}$  is also highest in Baoding and lowest in Qinhuangdao.  $\text{PM}_{10}$  accounts for 10% in Xinglong and 17.9% in Tangshan. Soot ranges between 3.9-5.3% among all sites. In Beijing around 64% of  $\text{PM}_{10}$  consists of  $\text{NH}_4^+$ ,  $\text{NO}_3^-$  and  $\text{SO}_4^{2-}$ , whereas  $\text{PM}_{10}$  accounts for 14%, and SOA, mineral dust and soot for around 22%.

For  $\text{PM}_{2.5}$  it can be seen that the secondary formed species  $\text{NH}_4^+$ ,  $\text{SO}_4^{2-}$  and  $\text{NO}_3^-$  have the highest ratio among all species for all sites (Figure 50). Ratios range between 61.7% in Beijing and 70.1% in Tangshan. Soot and primary  $\text{PM}_{10}$  are the following most abundant species with ratios of 11-17.4% and 61.-14.7%. Baoding, Shijiazhuang, Yucheng and Tangshan have a higher amount of soot aerosols than primary  $\text{PM}_{10}$ , whereas all other sites show slightly higher amounts of primary  $\text{PM}_{10}$ .  $\text{PM}_{10}$  ratios are highest in Qinhuangdao and lowest in Shijiazhuang and soot ratios are highest in Baoding and lowest in Qinhuangdao. Dust and SOA are the species with lowest ratios among all aerosol species, accounting for 2.9-7.7%, and 1.4-6.5%, respectively. Lowest amounts of dust are modelled for Qinhuangdao and highest for Beijing. The minimum and maximum ratios of SOA are 1.4% in Baoding and 6.5% in Qinhuangdao.

The change of the different aerosol species ratios between the different aerosol size classes can be seen, when comparing all three figures. Especially the ratios of  $\text{SO}_4^{2-}$ ,  $\text{NH}_4^+$  and soot significantly increase from TSP to  $\text{PM}_{2.5}$ , whereas  $\text{NO}_3^-$  and SOA show a clear decrease. Dust ratios are slightly higher at the sites located in the West of the region compared to the sites in the East.

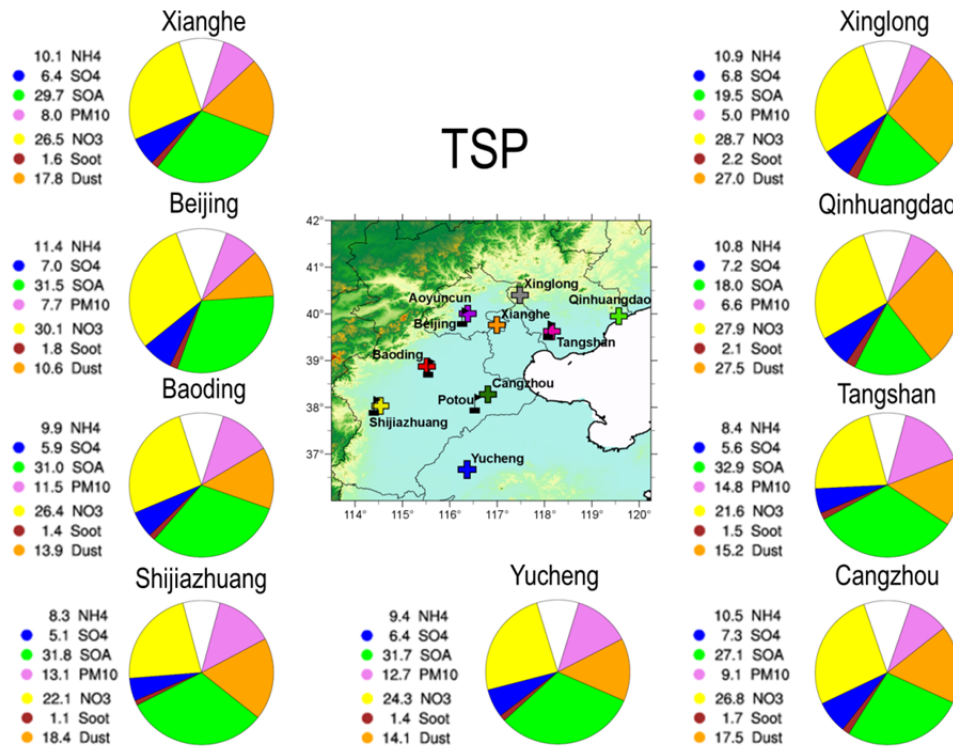


Figure 48: Modelled chemical compositions of TSP for all available sites averaged for August 4-14. White color denotes  $\text{NH}_4^+$ , blue denotes  $\text{SO}_4^{2-}$ , yellow denotes  $\text{NO}_3^-$ , green denotes SOA, brown denotes soot, purple denotes primary  $\text{PM}_{10}$ , and orange denotes mineral dust. All ratios are in % and refer to specific total mass concentrations. The location of all sites is shown in the central plot.

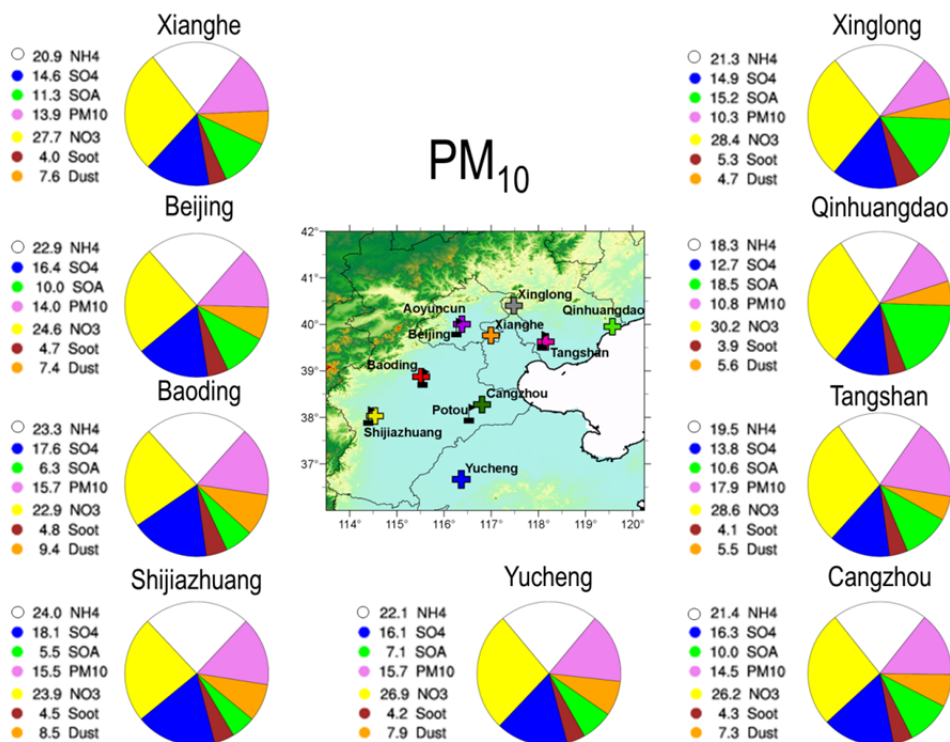


Figure 49: Same figure as Figure 48 but showing modelled chemical compositions of  $\text{PM}_{10}$  for all sites averaged for August 4-14.

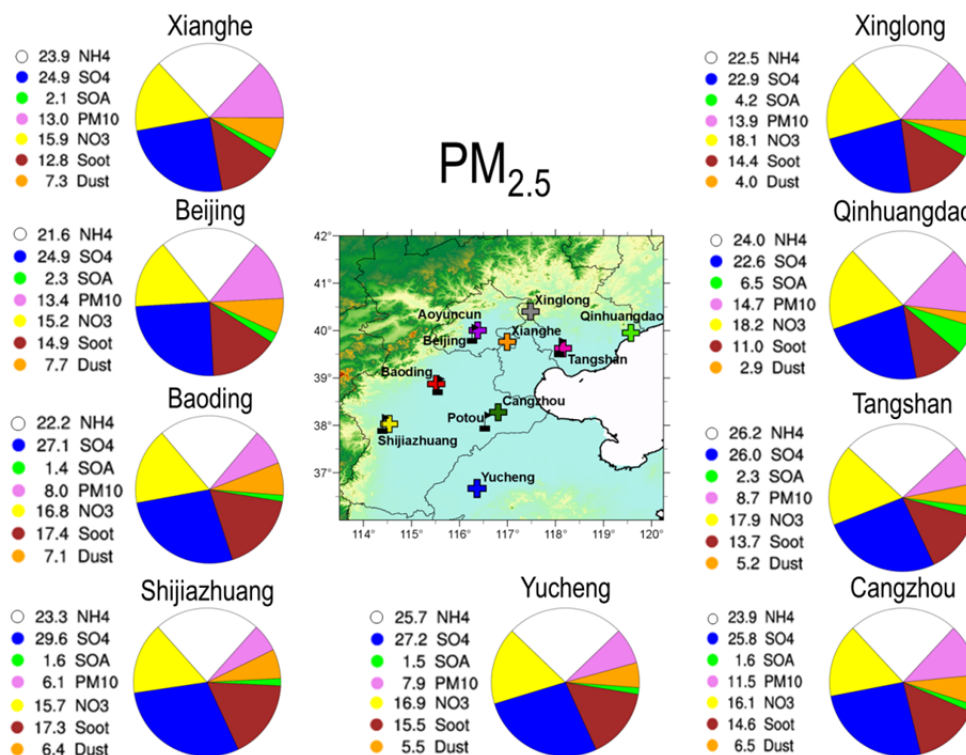


Figure 50: Same figure as figure 48 but showing modelled chemical compositions of  $PM_{10}$  for all sites averaged for August 4-14.

The study showed that TSP of all sites is mainly dominated by  $NO_3^-$  and SOA, whereas  $PM_{10}$  and  $PM_{2.5}$  mainly consist of  $NH_4^+$ ,  $NO_3^-$  and  $SO_4^{2-}$ . The ratio of soot is strongly increasing between TSP and  $PM_{2.5}$ , whereas SOA and dust ratios are decreasing. This behavior can also be seen in time-series of TSP,  $PM_{10}$  and  $PM_{2.5}$  compositions for August 4-14 (Figure 51 and Figure 52).

Moreover, it showed that the ratios of the different species significantly vary over time. It can be seen, that the most abundant species of TSP at all sites are  $NO_3^-$  and SOA. However, during August 10-14 the influence of mineral dust on TSP composition is strongly increasing. At all sites located in the east of the region, such as Tangshan, Xinglong, and Xianghe only a single mineral dust peak is modelled on August 12, whereas several dust peaks are modelled for Beijing, Baoding and Shijiazhuang. During this time the amount of  $NO_3^-$  and SOA are strongly lowered, whereas the ratio and amount of  $PM_{10}$  stays on a similar level during the whole simulation period.

Regarding the temporal variability of  $PM_{10}$  it can be seen that there is a significant decrease of total concentrations on August 12 at all sites. However, the species ratios show only small temporal variations.  $PM_{10}$  is dominated by  $NH_4^+$ ,  $NO_3^-$  and  $SO_4^{2-}$  during all the time. Soot and primary  $PM_{10}$  stay on a similar level during the whole period, whereas SOA shows stronger variations. In Beijing, SOA ratios are highest from August 12-14, whereas SOA ratios in Qinhuangdao, Xinglong and Xianghe show fewer changes.

For  $PM_{2.5}$  it can be seen that the ratio of soot increased, whereas SOA decreased. Soot levels start increasing two days after model initialization. From August 10-14 the influence of mineral dust is also

visible in  $PM_{2.5}$ . Primary  $PM_{10}$  particle amounts stay on a similar level during the whole period, whereas SOA concentrations are highest from August 10-13.

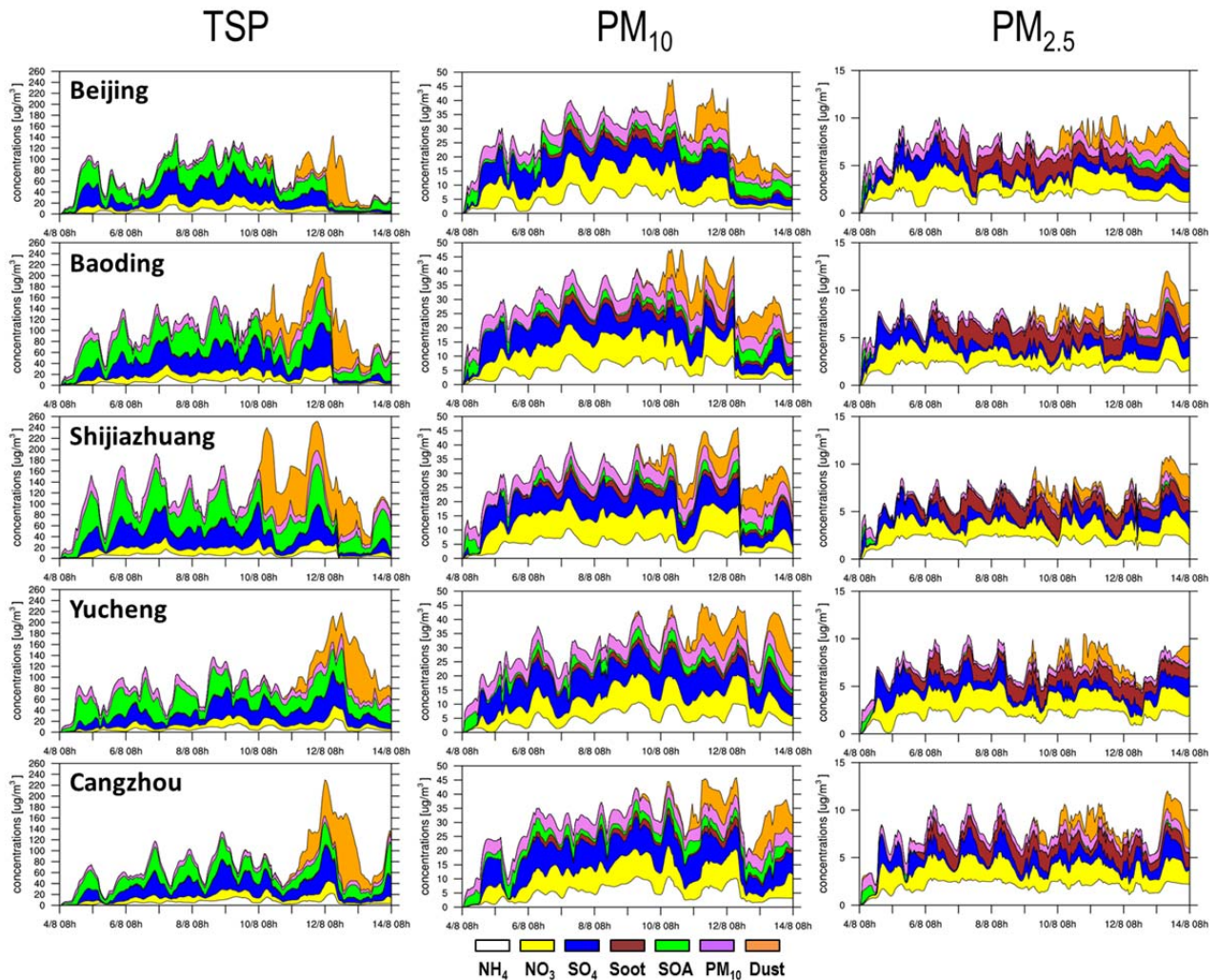


Figure 51: Temporal changes of TSP,  $PM_{10}$  and  $PM_{2.5}$  composition at Beijing (top row), Baoding (second row), Shijiazhuang (central row), Yucheng (forth row), and Cangzhou (bottom row) for August 4-14, 2008 modelled by using COSMO-ART. Time is always Beijing time (UTC + 8h). White defines  $NH_4^+$  concentrations, yellow defines  $NO_3^-$ , blue defines  $SO_4^{2-}$ , brown defines soot, green defines SOA, purple defines direct  $PM_{10}$ , and orange defines mineral dust. All species are described in  $\mu\text{g}/\text{m}^3$ .

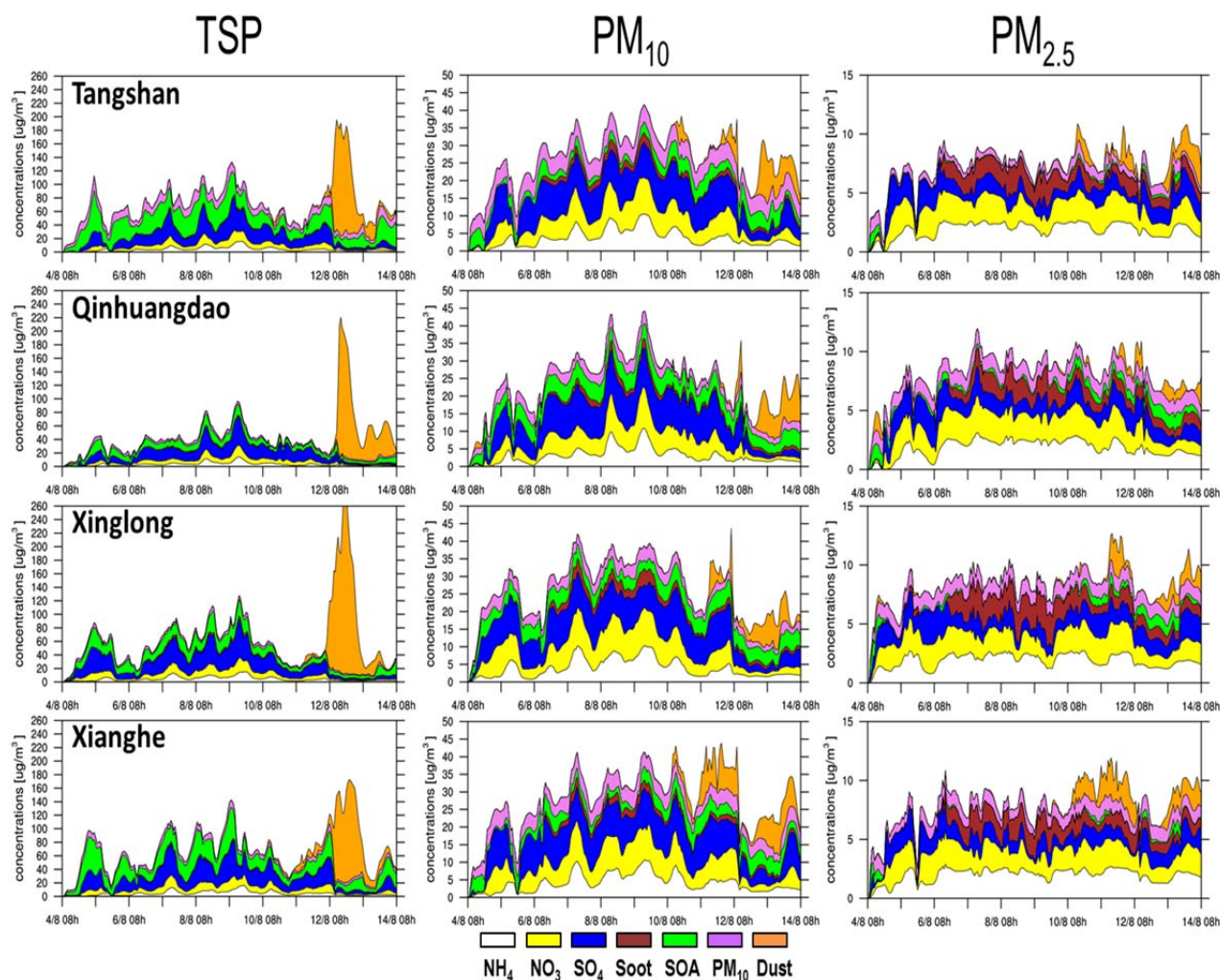


Figure 52: Same figure as figure 51 but showing temporal changes of TSP, PM<sub>10</sub> and PM<sub>2.5</sub> composition at Tangshan (top row), Qinhuangdao (second row), Xinglong (third row), and Xianghe (bottom row) for August 4-14, 2008 modelled by using COSMO-ART.

### 6.3.4 Comparison of modelled and observed daily-mean atmospheric nitrate and sulfate concentrations

In this section, NO<sub>3</sub><sup>-</sup>, SO<sub>4</sub><sup>2-</sup> and soot concentrations modelled for Beijing are compared to daily measurement data from Beijing-CRAES site [Schleicher *et al.*, 2011]. Modelled NO<sub>3</sub><sup>-</sup>, SO<sub>4</sub><sup>2-</sup> and soot concentrations are averaged to daily values, which are in temporal accordance with measurement data. The analyzed modelled and observed NO<sub>3</sub><sup>-</sup>, SO<sub>4</sub><sup>2-</sup> and soot concentrations are valid only for TSP.

The comparison showed that modelled and measured NO<sub>3</sub><sup>-</sup> concentrations of TSP are in an overall good accordance, with a slight underestimation of modelled values (Figure 53, top row). However, there is a strong underestimation of modelled NO<sub>3</sub><sup>-</sup> by a factor of 2 on August 6. On August 8, measurement data is missing.

Comparing modelled and observed  $\text{SO}_4^{2-}$  concentrations reveals a strong underestimation of modelled values for almost the whole period (Figure 53, central row). Only on August 11, concentrations fit well.

A similar behavior of modelled and observed soot concentrations can be seen for the comparison of observed BC and modelled soot concentrations (Figure 53, bottom row). Modelled values are strongly underestimated by a factor around 3.5 for August 4-10 and show a much better fit for August 11-13 with a slight underestimation of  $0.1\text{-}0.2 \mu\text{g m}^{-3}$ .

Reasons for the strong underestimation of modelled  $\text{SO}_4^{2-}$  and soot are discussed in section 6.4.4.

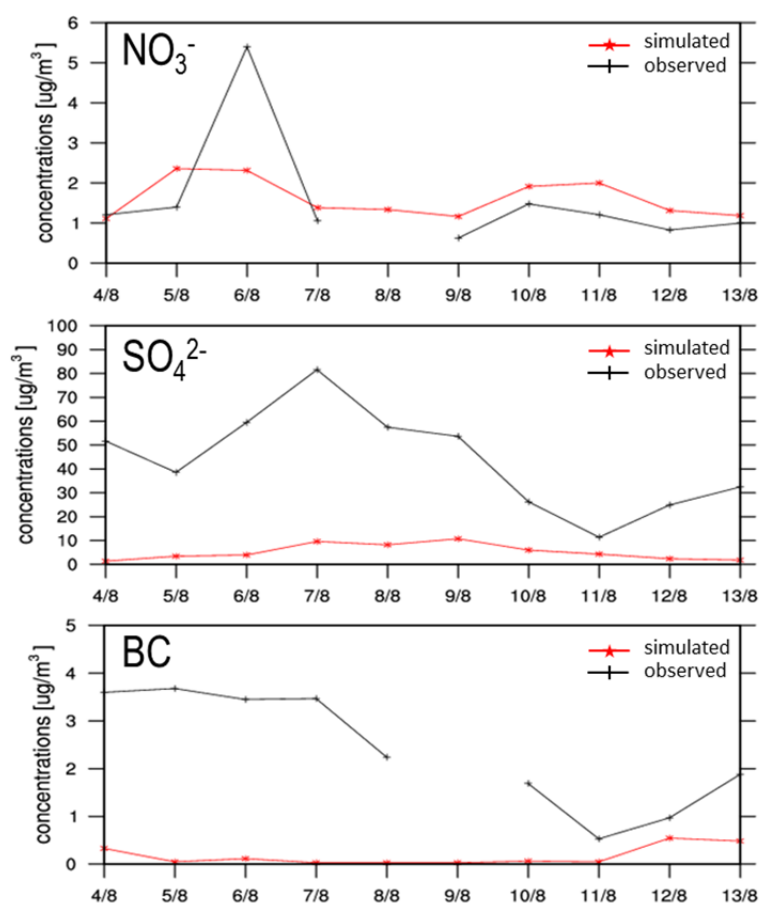


Figure 53: Comparison of daily averaged  $\text{NO}_3^-$  (top row),  $\text{SO}_4^{2-}$  (central row) and BC (bottom row) concentrations (in  $\mu\text{g m}^{-3}$ ) observed at CRAES-Beijing site and modelled with COSMO-ART for August 4-13, 2008. Red lines denote modelled data and black lines define observational data.

## 6.5 Discussion

### 6.5.1 Assessing the level of accuracy of modelled meteorological conditions and its impact on air quality

Meteorological conditions play a major role for aerosol air quality and its simulation, as temperature and relative humidity directly control secondary particle formation, precipitation events lead to a washout of particles and wind directions trigger in- or outflow of pollutant plumes.

The comparison of modelled and observed meteorological parameters (see section 6.3.1.2) showed that especially temperature and relative humidity are reproduced very well within the simulations. Wind speed and direction are always more difficult to reproduce, as both parameters mainly represent local conditions when measured in urbanized areas. This circumstance can cause deviations between modelled and observed values. However *Gao et al.* [2011] showed that even a model resolution of 4 x 4 km<sup>2</sup> would not significantly increase the accuracy of modelled wind conditions within a meso-scale model system.

Moreover, it can be noted that resulting correlation coefficients of major meteorological parameters in the present study are in accordance with published results of aerosol modeling studies in Beijing during the Olympic Games found by *Song et al.* [2006]; *Wang et al.* [2008a]; *Gao et al.* [2011]; *Jiang et al.* [2012]. Comparing meteorological conditions towards PM<sub>x</sub> levels in Beijing clearly shows that meteorology has a strong influence on air quality, especially during August 10-12, 2008 (Figure 54).

It can be seen that there is an episode of higher air pollution directly before the Olympic Summer Games episode, as observed TSP concentration in Beijing is high (150-200 µg m<sup>-3</sup>). Modelled TSP concentrations are lower as observed ones, especially on August 5-6. This difference seems to be partially caused by inaccuracies due to inflowing air masses and underestimation of relative humidity, which hampers secondary particle formation. On August 4-6 modelled air masses arriving Beijing mainly originate from southeast. Observed and modelled wind speeds and temperature fits very well for this period.

For August 8-14 observed and modelled TSP concentrations fit better than for August 4-8. On August 9 a decrease of temperatures and TSP can be seen for the observed and modelled data. On August 10 a one-day period with higher wind speeds, lower temperatures and precipitation events is observed. Air masses reach Beijing from southeast. During this time, all modelled TSP species show a strong concentration decline. In this case meteorological conditions can be considered as main trigger for the observed and modelled TSP decline. On August 12 there is another situation with a precipitation event. The precipitation seems to support the decline of observed TSP concentrations. In addition, a strong decline of anthropogenic TSP species is observed. Air masses originate from northeast, which leads to an increase of the ratio of dust in modelled total TSP concentrations. The influence of air mass origin and aerosol plume movement patterns are further described in the following section 6.4.5., whereas the impact of dust on local air quality is studied in section 6.4.8.

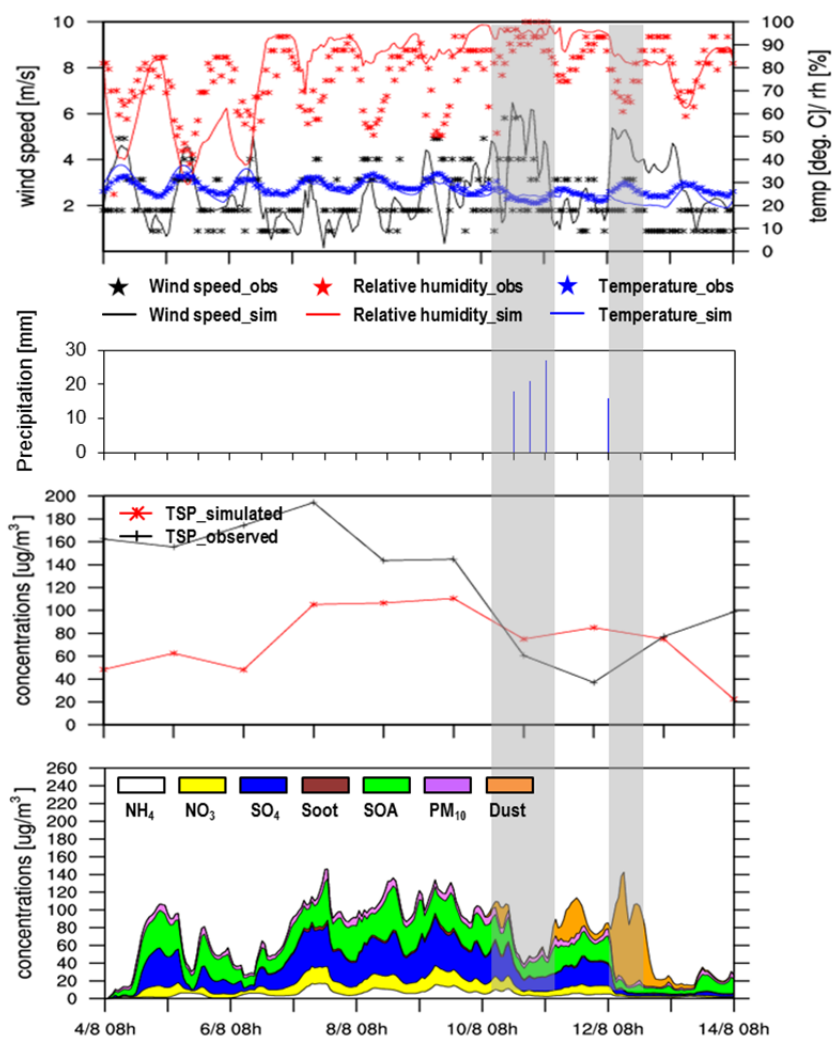


Figure 54: Demonstration of selected observed and modelled hourly and daily meteorological parameters, TSP concentrations and its chemical species in Beijing during August 4-14. Selected meteorological parameters are wind speed (in  $\text{m s}^{-1}$ ), relative humidity (in %), temperature (in  $^{\circ}\text{C}$ ) (all shown in top plot), and precipitation (in mm) (second plot). Observed wind speed, humidity and temperature are represented by asterisks, modelled values by closed lines. Modelled and observed TSP concentrations (in  $\mu\text{g m}^{-3}$ ) and chemical species concentrations (in  $\mu\text{g m}^{-3}$ ) of modelled TSP are shown in the third plot and the bottom plot. The black line with asterisk denotes observed TSP and the red line with asterisk denotes modelled TSP, whereas chemical species  $\text{NH}_4^+$ ,  $\text{NO}_3^-$ ,  $\text{SO}_4^{2-}$ , soot, SOA,  $\text{PM}_{10}$  and dust are represented by white, yellow, blue, brown, green, purple, and orange colors. The grey boxes show two specific meteorological conditions with low TSP concentrations.

### 6.5.2 Defining horizontal distribution patterns of TSP, $\text{PM}_{10}$ and $\text{PM}_{2.5}$ concentrations

The study about the spatial distribution of modelled daily TSP,  $\text{PM}_{10}$  and  $\text{PM}_{2.5}$  concentrations showed that TSP concentrations are always highest close to areas of major emission sources, whereas  $\text{PM}_{10}$  and  $\text{PM}_{2.5}$  concentrations are also increased in areas far away from major source regions. It showed up that this behavior is typical for modelled particulate matter with and without considering emission reduction factors. This difference only leads to a change of concentrations levels but not to a spatial shift of typical concentration hot spots.

During the simulation period, TSP concentrations are highest in the industrialized region south of Beijing, whereas PM<sub>10</sub> and PM<sub>2.5</sub> are distributed more homogeneously. Therefore, PM<sub>10</sub> and PM<sub>2.5</sub> distribution clearly highlights ongoing atmospheric transport. As PM<sub>10</sub> and PM<sub>2.5</sub> concentrations have higher amounts of secondary formed particles, their maxima show a spatial shift towards the location of the emission sources. The simulation results also showed that maxima PM<sub>2.5</sub> concentrations levels are always found in areas located downwind of the active source regions, whereas modelled PM<sub>2.5</sub> concentrations inside the source regions are much lower. This result, additionally, indicates the possible missing of primary anthropogenic PM<sub>2.5</sub> sources inside the source regions.

However, the resulting modelled spatial distribution pattern of TSP, PM<sub>10</sub> and PM<sub>2.5</sub> concentrations is typical and was also found within published modeling and measurement studies by *An et al.* [2007]; *Qu et al.* [2010]; *Wu et al.* [2011]; *Xin et al.* [2012].

### 6.5.3 Air mass movement, topographic effects and aerosol distribution

Besides the location of emission sources, the connection of origin and movement of air masses and regional topography are the major influence on spatio-temporal variability of aerosols. Pollution plumes are a typical sign of atmospheric transport processes. For the study of such pollutant transport processes, AOD variability and air mass movement were analyzed for two time periods on three selected days in August 2008. This study also highlights the influence of the surrounding on local air quality in Beijing. AOD is chosen as air quality indicator, as it is calculated on the basis of modelled TSP mass concentrations, which showed up to fit best with observed concentrations. Therefore modelled AOD can be expected to have good accuracy. Moreover, AOD gives information about the whole atmospheric column, which allows the reconsideration of uplifted layers.

On August 10 at 06:00 h and 12:00 h (UTC) highest AODs in the study region are modelled for the western parts of Beijing and the close surroundings north and west of it (Figure 55, left row). There is also a pronounced westerly border, where AOD values show a steep decline from > 1.5 to 0.2. Main wind directions are different for the areas west and east of the mountains. Air masses in the west mainly originate from northwest, whereas air masses in the east mainly arrive from southeast. Particle pollutants, originating from sources in Beijing and its southeastern surrounding, are pushed towards the mountains and accumulate in the western parts of Beijing. AOD west of the mountains is significantly lower. The mountain ridge west of Beijing prevents distribution of particle pollutants to areas located in the west. Visible pollutant movement only occurs to the north and south. A direct transport to the east cannot be seen in the modelled data. The study about mineral dust transport towards Beijing (see chapter 5) already showed that steep topography affects the transport patterns of airborne particles. Beijing is surrounded by high mountain ridges in the north, west and south which cause a topographic lee-effect on air masses.

On August 11 at 06:00 h and 12:00 h (UTC), highest AODs are modelled for Beijing and its surrounding south of it (Figure 55, central row). Major AOD hot spots are located over North Beijing, Shijiazhuang, and the highly industrialized belt south of Shijiazhuang. These pollutant plumes are pushed towards the south, whereas nearby air masses from the south cause a transport of aerosols towards Beijing. There seems to be a channeling effect of air masses in this area between the mountains and the regions near the coast.

On August 12 at 12:00 h (UTC) highest AODs are modelled for the region south of Beijing (Figure 55, right row). Pollutants are pushed towards the Chinese Sea by westerly air masses originating. A pollutant plume above the Chinese Sea is visible, which is also induced by air masses from south, transporting pollutants towards the region. However, at the same time clean air masses with wind speeds  $< 5 \text{ m s}^{-1}$  are modelled for the northern parts of the domain. At 00:00 h (UTC) these air masses lead to dilution of particulate pollutants in Beijing and the northern parts of its surrounding Hebei province. Remaining pollutants are transported towards the coast and the south.

The present study clearly shows two major aspects of aerosol air quality, first of all the dynamic movement of aerosol plumes and secondly the influence of air mass origin on air quality in Beijing.

The aerosol plume movement in the area of Greater Beijing was also studied by *Wang et al.* [2010a], who identified meso-scale low pressure systems in front of the mountains to be the main reason for the occurrence of convergence flow fields of high  $\text{PM}_{10}$  concentrations in the region of Beijing and south of it. This situation leads to a southwesterly flow of pollutants, as visualized for August 11 in Figure 55. They also identified a northeasterly transport pathway, which can be seen for August 12-13 in Figure 55. This typical synoptic situation leads to an increase of air quality in Beijing, as strong wind speeds and clear air masses cause a dilution of local air pollutants. This case was also seen in the present study for August 12-13.

The highly dynamic atmosphere of the Chinese Plain also renders problems for the study about the impact of local emission reductions on air quality in Beijing. *Chen et al.* [2007]; *Wang et al.* [2010c] and *Wang et al.* [2010a] found that the influence of surrounding provinces on the local Beijing air pollution is very high under certain meteorological conditions. *Cheng et al.* [2007] found that Hebei Province accounts for around 27% of mean  $\text{PM}_{10}$  concentration levels in Beijing in July (2002), whereas Shanxi Province southwest of Beijing and Tianjin City only account for around 4% and 9%. *Wang et al.* [2010c] tried to answer the question of defining the impact of reduction measures on air quality but could not clearly differentiate it, as meteorological conditions and air mass movement mask a clear emission reduction signal. This problem was also highlighted by *Schleicher et al.* [2012].

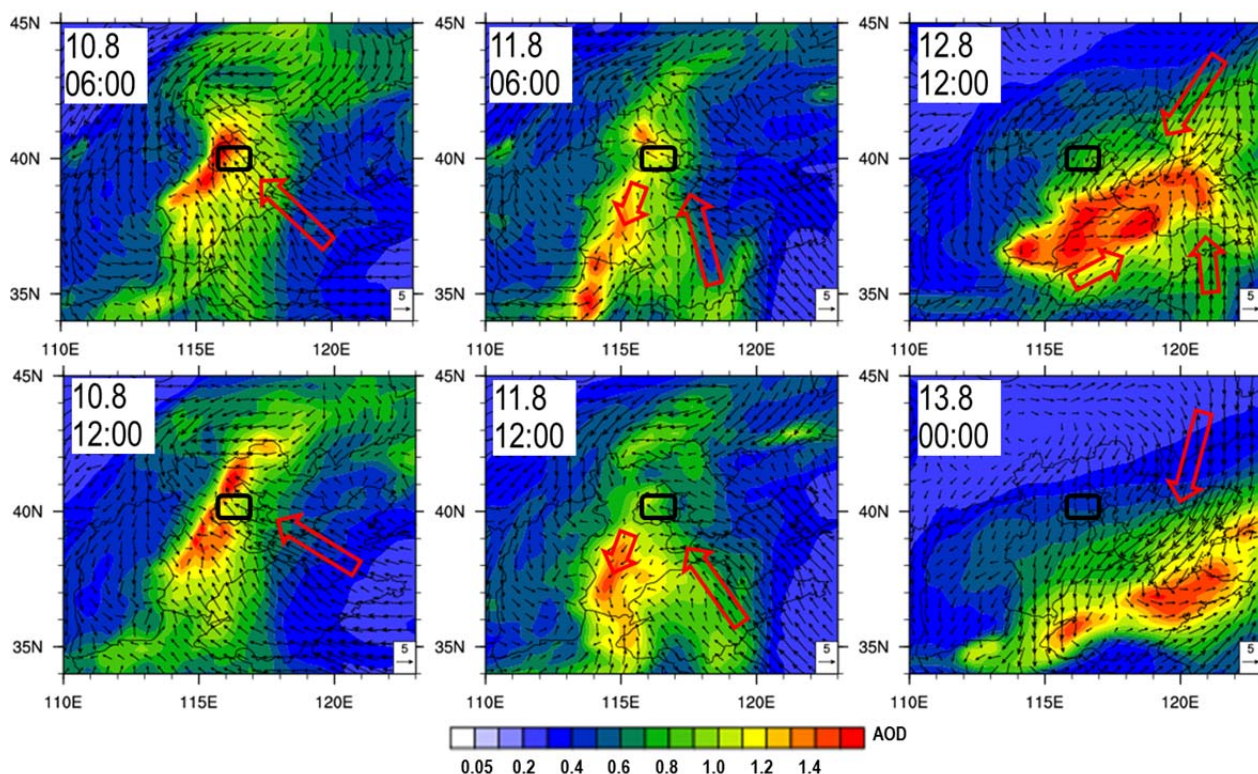


Figure 55: Spatio-temporal distribution of total AOD and 10-m wind vectors (meridional and zonal wind vectors in  $\text{m s}^{-1}$ ) in model domain D2 from August 10-13 in 2008 (from top left to bottom right) modelled by using COSMO-ART. White color denotes negligible or missing AOD, red colors denote  $\text{AOD} > 1.5$ . Beijing is marked by a black box. The reference wind speed vector is shown in the bottom right corner of each plot and is set to  $5 \text{ m s}^{-1}$ . Day and time of the plots (from top left to bottom right): 10.08 06:00 h, 11.08 06:00 h, 12.08 12:00 h, 10.08 12:00 h, 11.08 12:00 h, and 13.08 00:00 h. Time is UTC.

#### 6.5.4 Defining reasons for discrepancies of modelled and observed $\text{PM}_{10}$ and $\text{PM}_{2.5}$ concentration levels and its relative chemical compositions

The comparison of modelled and observed TSP,  $\text{PM}_{10}$  and  $\text{PM}_{2.5}$  concentrations showed good results for daily TSP concentrations and strong discrepancies for daily and hourly  $\text{PM}_{10}$  and  $\text{PM}_{2.5}$  concentrations.

Comparing modelled and observed daily TSP and  $\text{PM}_{2.5}$  concentrations in Beijing showed a relative good fit of concentration levels for TSP during the Olympic Summer Games (Figure 46), whereas there are huge discrepancies for  $\text{PM}_{2.5}$ . There are two explanations for that. There is either an important source of  $\text{PM}_{2.5}$  missing in the emission inventory which plays a less important role for TSP simulations than for  $\text{PM}_{2.5}$ , or the reduction factors for some species are overestimated which leads to a stronger reduction of modelled  $\text{PM}_{2.5}$  than observed.

The comparison of modelled and observed relative chemical compositions can be used for identification of inaccuracies. In this analysis the relative chemical composition of  $\text{PM}_{2.5}$  for Beijing during the study episode consists of secondary particles ( $\text{NH}_4^+$ ,  $\text{SO}_4^{2-}$ ,  $\text{NO}_3^-$ ), SOA, primary  $\text{PM}_{10}$ , soot and dust by ratios of 61%, 25%, 13%, 15%, and 8%, respectively.

*He et al.* [2001] identified yearly ratios of 38%, 32%, 7.5%, 1.5%, and 21.5% for secondary particles ( $\text{NH}_4^+$ ,  $\text{SO}_4^{2-}$ ,  $\text{NO}_3^-$ ), organic species, BC, crustal species and unidentified species for  $\text{PM}_{2.5}$  in Beijing during 1999-2000. A comparison of modelled ratios with ones defined by *He et al.* [2001] showed that the ratio of secondary formed particles is twice for the modelled concentrations than the observed ones. The ratio of secondary organics is in better agreement with 25% for modelled concentrations and 32% for observed ones. Modelled dust is higher than observed crustal species. *Guinot et al.* [2007] found similar ratios for 2003-2004 as *He et al.* [2001] for 2001-2002. However, *Guinot et al.* [2007] additionally defined the ratio of dust within aerosols  $< 2 \mu\text{m}$  (fine fraction) and  $> 2 \mu\text{m}$  (coarse fraction) and found a yearly average ratio of around 22% for the fine fraction and around 72% for the coarse fraction. However, as atmospheric dust concentrations show strong inter-annual variations, these results should be mainly seen as indicator for the importance of the influence of dust on urban air quality. *Han et al.* [2007] determined the ratio of dust on Beijing's TSP and  $\text{PM}_{2.5}$  to be around 20% in summer season during 2001-2004. This value fits very well with modelled ratios of the present study conducted for August 2008. Despite of all, it should be noted that the species ratios show diurnal to yearly variations which makes it difficult comparing ratios modelled in the present study with published data.

A further comparison of modelled ratios of the present study with ratios modelled with CMAQ model by *Fu et al.* [2009] showed a good agreement for secondary particles with a slight underestimation of COSMO-ART ratios by 4%. Modelled soot ratios using COSMO-ART are underestimated by only 2%. *Fu et al.* [2009] found ratios for  $\text{NH}_4^+$ ,  $\text{SO}_4^{2-}$ ,  $\text{NO}_3^-$ , and BC of 11%, 21%, 10% and 10% in monthly measurements of  $\text{PM}_{2.5}$  during July 2001 in Beijing. OC accounted for 17% and others for 31%. Ratios of crustal species were not defined. However, *Fu et al.* [2009] also found an underestimation of modelled  $\text{PM}_{2.5}$  concentrations with concentrations converted from API, indicating some inconsistencies within the TRACE-P emission inventory (the previous version of INTEX-B inventory).

Comparing modelled  $\text{NO}_3^-$ ,  $\text{SO}_4^{2-}$  and BC concentrations to daily time-series of TSP data obtained by *Schleicher et al.* [2011a] (section 6.4.2) showed a relatively good fit for  $\text{NO}_3^-$  concentrations and low agreement for  $\text{SO}_4^{2-}$  and BC. It showed that  $\text{NO}_x$  emissions and their reductions during the Olympic Summer Games are represented well. This finding also corresponds with results of the comparison of modelled and measured  $\text{NO}_x$  concentrations, found during the calibration and evaluation studies presented in chapter 3. The modeling study of *Gao et al.* [2011] showed that major uncertainties of  $\text{NH}_4^+$  simulation is due to partitioning of  $\text{HNO}_3$  into the aerosol phase.

The good fit of modelled and measured hourly ozone concentrations also indicates a well representation of VOC concentrations, which is important to know, as ozone formation highly depends on VOC concentrations levels.

As the comparison also showed a strong  $\text{SO}_4^{2-}$  concentration underestimation by the model results, modelled  $\text{SO}_2$  concentrations were compared to published measurement data [Wang *et al.*, 2010c]. The results of this comparison clearly showed that modelled  $\text{SO}_2$  concentrations are in a similar range as measured ones (5-100  $\mu\text{g m}^{-3}$ ).

During the Olympic Games  $\text{SO}_2$  concentrations strongly decreased which should also lead to a drastic decrease of  $\text{SO}_4^{2-}$  concentrations. However, such decrease is modelled with COSMO-ART but not observed within measurements [Wang *et al.*, 2010c]. Wang *et al.* [2010b] found an increase of  $\text{SO}_4^{2-}$  concentrations by 64% with an anticipated decrease of  $\text{SO}_2$  concentrations by 40% during the full emission control period in Beijing in summer 2008. They define two major reasons for this strange circumstance. One reason can be addressed towards the impact of mid- and long-range transported  $\text{SO}_4^{2-}$ , whereas the second reason could be an acceleration of oxidative  $\text{SO}_4^{2-}$  formation by the high ozone concentrations during the Olympic Summer Games. As  $\text{SO}_4^{2-}$  concentrations are very low in the whole model domain, missing transport processes from the surrounding towards Beijing cannot explain the discrepancies between modelled and observed  $\text{SO}_4^{2-}$  concentrations in Beijing. The results rather indicate that a significant source of direct  $\text{SO}_4^{2-}$  emissions has to be missing in the used emission inventory. An underestimation of modelled  $\text{SO}_4^{2-}$  was also found within a modeling study by Gao *et al.* [2011], who, however, assumed an underestimation of  $\text{SO}_2$  concentrations as the major reason.

For validation of modelled  $\text{NH}_4^+$  there are no measurement data available. However, published data of observed  $\text{NH}_4^+$  concentrations are about 6.6  $\mu\text{g m}^{-3}$  [Gao *et al.*, 2011], which is almost twice the value modelled in the present study. It can be assumed that there are some missing sources of  $\text{NH}_4^+$  in the emission inventory which lead to underestimation of modelled values.

A similar conclusion can be drawn for the resulting underestimation of modelled soot. Direct OC emissions are not reconsidered in the inventory which is an indicator for the strong underestimation of modelled soot concentrations. These missing OC emissions should also be a major reason for the underestimation of secondary particles, as a part of the modelled concentrations consists of aged particles, which are a mixture with carbonaceous particles. Duan *et al.* [2006] found monthly average concentrations of OC to be twice as high as BC concentrations, which supports the assumption about the importance of OC as significant direct particle source in Beijing. They reported average OC concentrations of 15  $\mu\text{g m}^{-3}$  in summer in 2001 and 2002. Li *et al.* [2012] found a similar result for their measurements of different aerosol size classes in Beijing during the Olympic Summer Games. OC accounted at least for a relative ratio of 10%, reconsidering water-soluble ions, OC, BC, trace elements and unknown species. According to Li *et al.* [2012], OC is the dominant carbonaceous particulate species during summer 2008, derived from secondary formation, biomass burning and long-range transport. These emission factors are not reconsidered in the current emission inventory.

### 6.5.5 Assessing effects of anthropogenic emission reductions on $\text{NO}_3^-$ and $\text{SO}_4^{2-}$

In this section effects of emission reduction measures on  $\text{NO}_3^-$  and  $\text{SO}_4^{2-}$  concentrations during the Olympic Summer Games are studied. The effects of emission reductions on gaseous atmospheric pollutant concentrations, such as  $\text{NO}_x$  and ozone, were studied in chapter 3.

However, emission reductions also affect atmospheric particulate matter concentrations.  $\text{NO}_3^-$  and  $\text{SO}_4^{2-}$  were chosen for this analysis, as both species clearly show the effect of  $\text{NO}_x$  and  $\text{SO}_2$  emission reductions. A clear emission reduction signal from a specific species on TSP,  $\text{PM}_{10}$  and  $\text{PM}_{2.5}$  would be harder to define, as those are composites of several different species.

Total  $\text{NO}_x$  and  $\text{SO}_2$  concentrations were reduced by 43% and 19% in Beijing and by 21% and 22% in its surrounding during the Olympic Summer Games. Reductions for all sectors are described in chapter 3.

To study emission reduction effects, three model runs were conducted and compared, (1) no  $\text{NO}_x$  and  $\text{SO}_2$  reduction, (2) total  $\text{NO}_x$  and  $\text{SO}_2$  reduction of 50% and 20%, and (3)  $\text{NO}_x$  and  $\text{SO}_2$  reductions according to reduction specific factors shown in chapter 3. The time period for this analysis is from August 4, 08:00 h (Beijing time) to August 8, 19:00 h (Beijing time). The comparison of the three emission set-ups is done for Beijing and the three cities in the surrounding located most far away, namely Shijiazhuang and Yucheng in the south, and Qinhuangdao in the northeast.

The study showed that reduction of total  $\text{NO}_x$  emissions leads to a significant non-linear reduction of  $\text{NO}_3^-$  concentrations. Using the 50% factor leads to a stronger total reduction of atmospheric  $\text{NO}_3^-$  concentrations than applying the specific reduction factors of 43% and 21% for Beijing and its surrounding. However, also the temporal course of  $\text{NO}_3^-$  concentrations is changed compared to the original emission scenario.  $\text{NO}_3^-$  peaks are more pronounced within the original run and more flattened in the two other runs. It can be noted, that there is non-linear dependence between atmospheric concentration reductions and emission reductions. It also showed that  $\text{NO}_x$  reductions in Beijing and Shijiazhuang, which are 43% and 21%, respectively, cause a similar reduction of atmospheric  $\text{NO}_3^-$  concentrations. Outflowing air masses could be the reason for low  $\text{NO}_3^-$  concentrations in Shijiazhuang. In Yucheng,  $\text{NO}_3^-$  concentrations are lowest and show the smallest difference between all runs and among all four sites.

Regarding  $\text{SO}_4^{2-}$ , only a small reduction of concentrations is achieved in Beijing by using the detailed emission factors. In Beijing, strongest differences between the original run and both runs with reduced emissions can be seen for August 7 and 8, whereas there is almost no difference from August 4-7. As differences slightly vary for the first two days, residential and mobile sources seem to be the main active emission factors. Emission reductions of both factors were 0% in Beijing. In Shijiazhuang, which is closest to Beijing among the four sites, a similar behavior of  $\text{SO}_4^{2-}$  concentrations can be seen. In Yucheng and Qinhuangdao,  $\text{SO}_4^{2-}$  concentrations are almost similar for the original run and the run with specific reduction factors. It can be noted that a reduction of  $\text{SO}_2$  concentrations by 19-22% in the whole region

has a negligible effect on atmospheric  $\text{SO}_4^{2-}$  concentrations. It can also be noted that the original  $\text{SO}_2$  emission strengths would probably cause a similar underestimation of  $\text{PM}_{10}$  and  $\text{PM}_{2.5}$  concentrations like modelled concentrations using the emission inventory with specific emission reduction factors. This finding supports the assumption that there is a significant source of direct  $\text{SO}_4^{2-}$  particles missing in the inventory.

The results clearly show that a reduction of  $\text{NO}_x$  and  $\text{SO}_2$  emissions lead to a significant decline of atmospheric  $\text{NO}_3^-$  and  $\text{SO}_4^{2-}$  concentrations, and therefore also to a decline of total  $\text{PM}_x$  concentrations. Differences of  $\text{NO}_3^-$  and  $\text{SO}_4^{2-}$  concentrations are most obvious when in- an outflow of air masses are small at the study sites. Inflowing polluted air masses at the study sites can cause higher levels of  $\text{NO}_3^-$  and  $\text{SO}_4^{2-}$  concentrations within the reduced emission run compared to the original run. Whereas outflowing air masses can lead to stronger differences between the three runs than one would have expected.

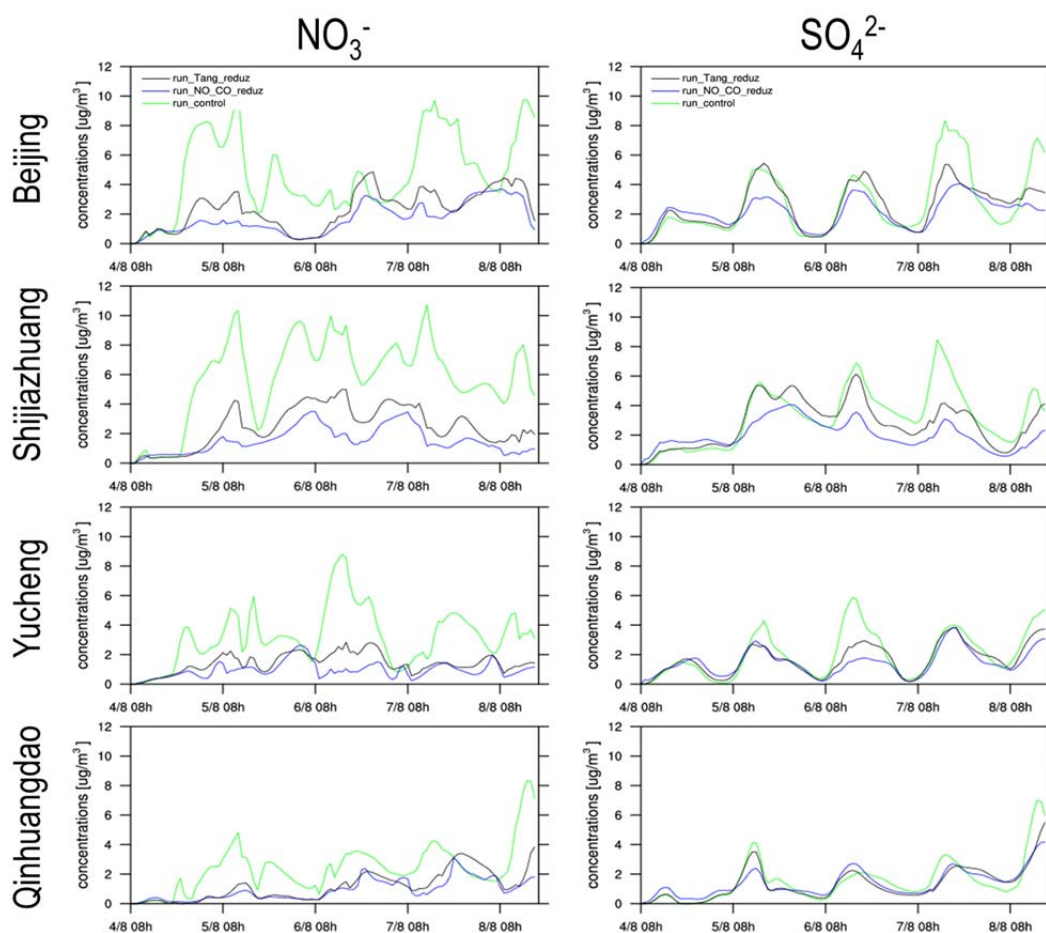


Figure 56: Comparison of  $\text{NO}_3^-$  and  $\text{SO}_4^{2-}$  time-series from three different emission scenarios for Beijing (top row), Shijiazhuang (second row), Yucheng (third row) and Qinhuangdao (bottom row) modelled by using COSMO-ART for August 4, at 08:00 h to August 8, 19:00 h. Time is set to Beijing time (UTC + 8h). Green lines denote  $\text{NO}_3^-$  and  $\text{SO}_4^{2-}$  concentrations from a control run (without emission reductions), blue lines denote the  $\text{NO}_3^-$  and  $\text{SO}_4^{2-}$  concentrations from a run with a  $\text{NO}_x$  reduction of 50% and a  $\text{SO}_2$  reduction of 20%, and black lines denote  $\text{NO}_3^-$  and  $\text{SO}_4^{2-}$  concentrations from a run with specific reduction factors (chapter 3).

### **6.5.6 Spatio-temporal distribution of modelled mineral dust and identification of source regions**

The characterization of the different particulate matter species in section 6.3.3.1 showed that there are varying amounts of mineral dust in the urban atmosphere of Beijing modelled for August 10 to 14 during the Olympic Summer Games. In this section the origin and the spatio-temporal dynamics of this airborne mineral dust are investigated.

For analysis of dust dynamics, AOD is modelled for the total dust mass concentrations in the whole atmospheric column. Anthropogenic aerosols are not reconsidered for this dust-only AOD calculation. This method gives the possibility to study mineral dust distribution separately. In addition, modelled AOD is compared to Deep Blue AOD provided for MODIS-AQUA data. COSMO-ART AOD plots are in temporal accordance with the MODIS records to provide maximum comparability.

The distribution of dust-only AOD for August 6 to 9 in model domain D1 is shown in Figure 57. The first plot in the top left corner shows high AOD values ( $> 1.0$ ) in Badain Jaran Desert in Central China and moderate AOD of 0.2 to 0.7 in Taklimakan Desert on August 6 at 07:00 h (UTC). The strong AOD signal in Badain Jaran Desert is also captured by MODIS. MODIS also captures strong AOD signals over the borders of Taklimakan Desert. Kumtaq Desert and Badain Jaran can be considered as active source regions, as wind speeds are strong enough to cause dust emission. One day later, on August 7, (second plot in the top right corner) modelled AOD in Badain Jaran Desert strongly decrease, but there are still AODs between 0.05 and 0.4 found in this region. There is no information from MODIS for this region. However, model and satellite show increased AOD values in the eastern parts of the Central Chinese Desert and Inner Mongolia. Highest model AODs ( $>1.0$ ) are modelled in South Tengger. Model and satellite also show some AOD in Taklimakan Desert, whereas MODIS AOD is higher than modelled AOD. On August 8 at 07:00 h the amount of modelled airborne mineral dust in Taklimakan Desert and the Central Chinese Deserts decreased. However, MODIS still captures high AODs in Taklimakan Desert. The dust cloud, which built was formed in the eastern Central Chinese Deserts the day before, form a widespread band of low AOD values up to 0.5, stretching from the region north of Beijing and Inner Mongolia towards the Central Chinese Deserts. The northern part of this band is also recorded by MODIS. One day later, on August 9, strong winds cause a dilution of airborne mineral dust in the region of the loess area and the Central Chinese Deserts. During the following two days this dust cloud is pushed towards Beijing (see Figure 58). MODIS AOD in this region is also very low, whereas a strong signal is still present in the Taklimakan Desert.

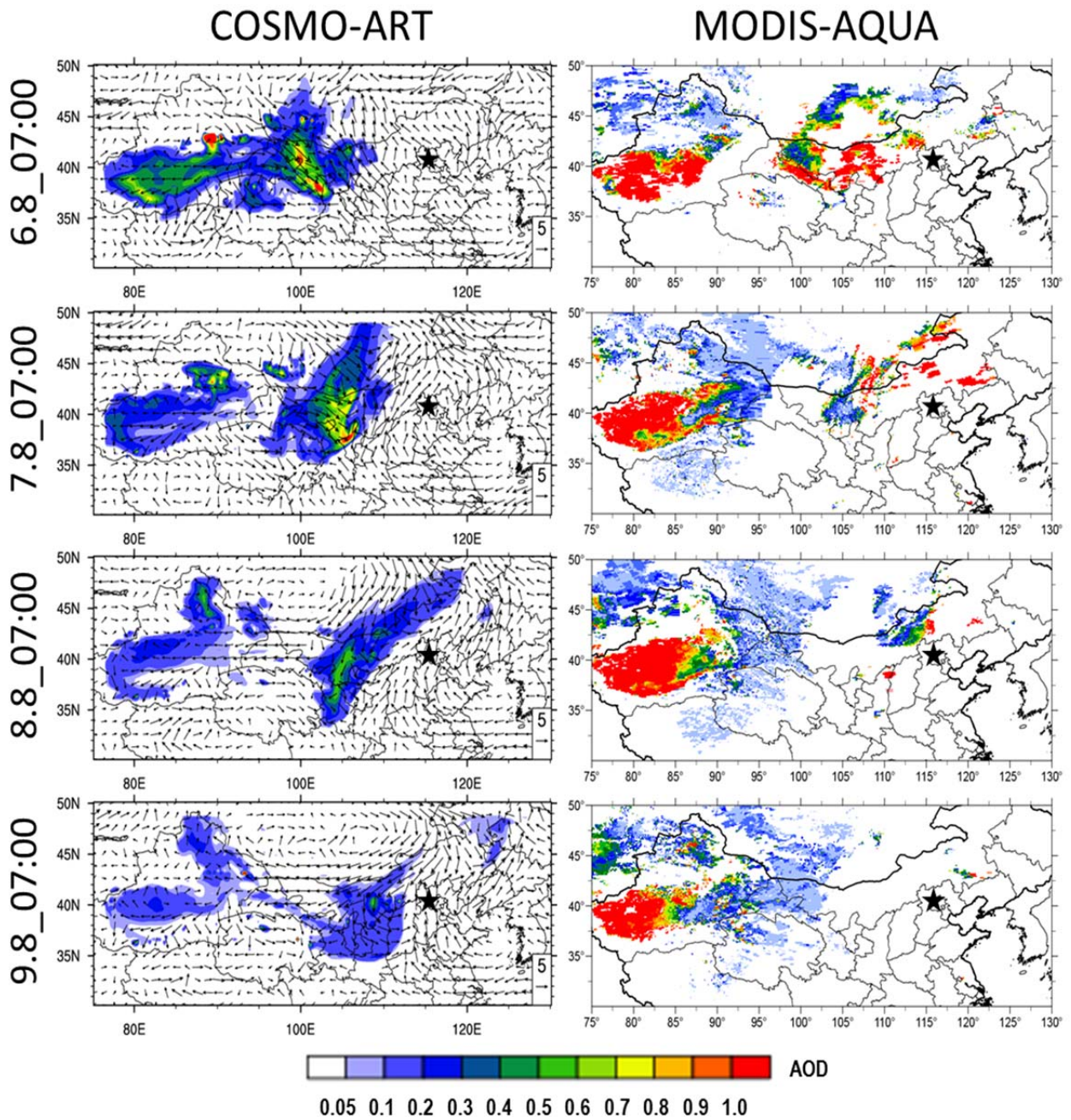


Figure 57: Spatio-temporal dynamics of dust-only AOD and 10-m wind vectors (meridional and zonal wind vectors in  $\text{m s}^{-1}$ ) in model domain D1 from August 6- 9, each at 12:00 h (UTC) in 2008 (from top left to bottom right) modelled by using COSMO-ART. AOD reflects the dust loading of the whole atmospheric column. Anthropogenic aerosols are not reconsidered. White color denotes negligible AOD values, red colors denote AOD > 1.0. Beijing is marked by an asterisk. The reference wind speed vector is shown in the bottom right corner of each plot and is set to  $5 \text{ m s}^{-1}$ . Day and time of the plots (from top left to bottom right): 06.08 12:00 h, 07.08 12:00 h, 08.08 12:00 h, and 09.08 12:00h.

Between August 10 and 13 airborne mineral dust is distributed further over Beijing and its surroundings. On August 10 dust is pushed towards the mountains west of Beijing by winds from northwest.

There is an AOD signal with values  $> 0.3$  modelled in the western part of the domain (at  $40^\circ$  N,  $111^\circ$  E) on this day. The further distribution of dust in the Beijing region is very slow, as the dust-loaded air masses are blocked by air masses from southeast in the area of the mountains. During the following hours AOD is further decreasing, while dust moves slowly forwards to the Chinese East Coast.

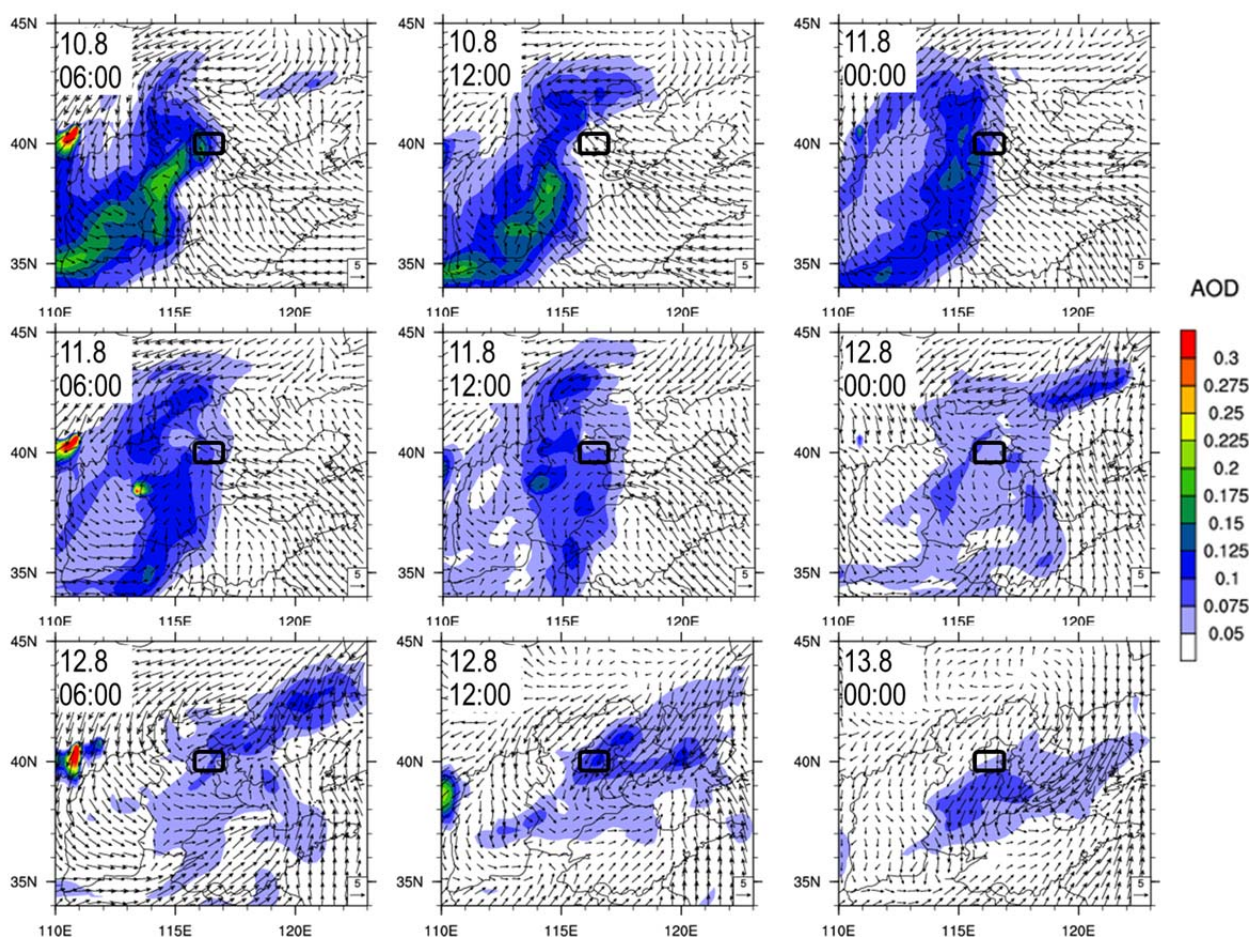


Figure 58: Spatio-temporal dynamics of dust-only AOD and 10-m wind vectors (meridional and zonal wind vectors in  $\text{m s}^{-1}$ ) in model domain D2 for August 10-13 in 2008 (from top left to bottom right) modelled with COSMO-ART. AOD reflects dust loading of the whole atmospheric column. Anthropogenic aerosols are not reconsidered. White color denotes negligible AOD, red colors denote  $\text{AOD} > 0.3$ . Beijing is marked by an asterisk. Reference wind speed vector is shown in the bottom right corner of each plot and is set to  $5 \text{ m s}^{-1}$ . Day and time of the plots (from top left to bottom right): 10.08 06:00 h, 10.08 12:00 h, 11.08 00:00 h, 11.08 06:00 h, 11.08 12:00 h, 12.08 00:00 h, 12.08 06:00 h, 12.08 12:00 h, and 13.08 00:00 h. Time is UTC.

The comparison of modelled and satellite derived AOD showed that COSMO-ART can also be used for dust simulations during summertime. The activation state of Taklimakan Desert from August 6 to 9 is also modelled. Moreover, the AOD signal in the Central Chinese Deserts is reproduced by the model simulations. However, modelled AOD values are much smaller for Taklimakan Desert, than AOD calculated with the MODIS Deep Blue algorithm.

Moreover, this detailed study shows that there is a certain amount of mineral dust emissions released in the source regions in summer. This airborne dust causes AOD above 1.0 in the source regions and dust from the Central Chinese Deserts and Inner Mongolia is distributed to the Chinese East Coast. The amounts of transported dust are not comparable to intense dust storms, but lead to an increase of urban TSP, PM<sub>10</sub> and PM<sub>2.5</sub> levels. The influence of geogenic particles, such as mineral dust, is also observed by chemical analysis of TSP filter samples [Schleicher *et al.*, 2012].

## 6.6 Summary and conclusions

In this chapter a modeling study about the aerosol dynamics during the Olympic Summer Games in Beijing in 2008 was presented.

COSMO-ART was set up to model anthropogenic and geogenic aerosols during nine days in August 2008, stretching over a period before and after the starting point of the Olympic Summer Games on August 8. Data from ground-based measurements and MODIS satellite were used for validation.

The goals of this work focused on (1) analyzing the meteorological conditions during the Olympic Summer Games, (2) characterizing the spatio-temporal distribution of AOD, TSP, PM<sub>10</sub> and PM<sub>2.5</sub> concentrations (2) defining the chemical composition of TSP, PM<sub>10</sub> and PM<sub>2.5</sub>, (3) assessing the interactions between particulate air pollutants and meteorological parameters, (4) defining the effects of emission reductions on air quality, and (5) estimating the impact of mineral dust on air quality in Beijing during the Olympic Summer Games.

The analysis of the meteorological conditions showed a decreasing trend of air temperatures in Beijing and its surrounding starting around August 10. From this day on also several precipitation events were reported. However, relative humidity and wind speeds stayed on a similar level during the whole simulation period. Precipitation and low temperatures lead to significant increase of visibility in Beijing but cannot be seen at the other sites in the region. COSMO-ART shows a good performance of the meteorological conditions during the simulation period. Modelled temperature and humidity fit best with observational data with correlation coefficients > 0.76, and > 0.52, respectively. Wind speeds and wind directions show less agreement due to their stronger abundance towards topographic influences and model constraints, such as grid cell sizes or calculation of the planetary boundary layer. However, compared to published results of modeling studies they are still in a common range of agreement. The proper functionality of the meteorological condition simulation is the basis of aerosol modeling, as aerosols are highly influenced by them.

Simulating AOD, which reflects the anthropogenic and geogenic aerosol loading over the whole column of the atmosphere, showed that there are significant amounts of aerosols in the atmosphere of Beijing and the surrounding provinces in the north, east and south. Highest AOD over a large area can be seen

especially on August 12, when AOD exceeds 1.5 in Tianjin, Southern Hebei Province and North Shandong Province. Highest AOD in Beijing can be found on August 10, when AOD in the northern parts of the city exceed 1.5. Aerosol loadings in the west of Beijing and in the northwestern province Inner Mongolia are very low, as these regions are less urbanized and industrialized. AOD at the border of these two regions drops to very low values. The simulations clearly showed that Taihang Mountains west of Beijing act as a natural barrier towards air pollutant transport from the polluted regions towards the west during stagnant weather conditions with low wind speeds. A transport of pollutants from east to west was not seen in the modelled AOD distributions. Aerosol plumes only moved towards the north, east or south. Beijing, Baoding, Shijiazhuang and Tianjin are main hotspots of air pollution in the region.

As AOD gives no information about air quality close to the ground, TSP, PM<sub>10</sub> and PM<sub>2.5</sub> concentrations were modelled for the lowest model layer. The spatio-temporal distribution of TSP concentrations clearly shows the location of anthropogenic sources in the Beijing-Tianjin-Hebei region. It showed that especially the region between Beijing, Baoding and Shijiazhuang can be considered as a main source area. Also Shandong Province, located south of Hebei Province, has significant anthropogenic sources. Daily TSP concentrations in these regions often exceed 150  $\mu\text{g m}^{-3}$ . High levels of TSP concentrations are always found near the sources, whereas PM<sub>10</sub> and PM<sub>2.5</sub> concentrations show a much more regional distribution. Especially PM<sub>2.5</sub> concentrations clearly reflect the effect of air mass origin and atmospheric transport processes. High amounts of modelled PM<sub>2.5</sub> concentrations are always found in the regions located downwind of the active source regions, whereas they are low within the source regions itself. This behavior shows that particles comprised by PM<sub>2.5</sub> concentrations are mainly formed in the atmosphere by secondary particle formation from gaseous precursors. On several days during the simulation period, a modelled PM<sub>2.5</sub> plume can be observed, which is distributed towards the region north of Beijing.

The spatio-temporal variability of modelled TSP and PM<sub>10</sub> concentrations showed a typical behavior, whereas the low concentrations of PM<sub>2.5</sub> within the major source regions already indicate that there might be some inaccuracies within the emission inventory. The comparison of modelled and observed daily TSP and PM<sub>2.5</sub> concentrations finally showed a good fit for TSP concentrations, but only less agreement for PM<sub>2.5</sub> concentrations. The agreement between modelled and observed hourly PM<sub>2.5</sub> and PM<sub>10</sub> concentrations showed similar inaccuracies. Modelled PM<sub>10</sub> and PM<sub>2.5</sub> concentration levels are most of the time strongly underestimated. A further study about the chemical composition of TSP, PM<sub>10</sub> and PM<sub>2.5</sub> in Beijing showed that the most abundant species of TSP are secondary formed particles ( $\text{NH}_4^+$ ,  $\text{SO}_4^{2-}$ ,  $\text{NO}_3^-$ ), SOA and mineral dust. In PM<sub>2.5</sub> secondary particles ( $\text{NH}_4^+$ ,  $\text{SO}_4^{2-}$ ,  $\text{NO}_3^-$ ) and soot have highest ratios. As modelled TSP showed a much better fit with measured concentrations, soot could be identified as the major reason for the detected inaccuracies. Measurements showed that especially OC has a significant amount within PM<sub>2.5</sub>. However, OC is not included in the emission inventory used in this study, which

should account for a part of the underestimation of  $PM_{2.5}$ . However, as OC concentrations are not that high compared to other species, missing emissions cannot explain the total amount of the missing modelled concentrations. In addition, it can be assumed that especially direct  $SO_4^{2-}$  sources are also missing in the inventory, as modelled and observed  $SO_4^{2-}$  concentrations show the strongest discrepancies of all species. It can be concluded that the emission inventory provided by G. Tang is suitable for simulation of gaseous pollutants and TSP but need extensive modifications for simulations of finer particle fractions, such as  $PM_{2.5}$ . However, it should be noted, that there is only one further inventory (INTEX-B) freely available for the scientific community, which has a much coarser spatial resolution and was prepared for 2006. Aerosol simulations will be limited until these inventories are state-of-the-art again.

The study of the relative chemical composition of TSP also showed that mineral dust has an effect on air quality in Beijing during summer. The AOD simulations already showed that there are three days, when air mass origin in the Beijing region changed from southeast to northeast. During these three days anthropogenic species are drastically lowered at all sites, whereas dust concentrations have maximum concentrations. On these days, modelled and observed daily TSP concentration levels fit very good and chemical analysis show increased concentrations of different elements which are predominantly from geogenic sources, such as potassium, titanium and iron [Schleicher *et al.*, 2011a]. During the same time, element concentrations from major anthropogenic sources, such as copper, arsenic, cadmium, and lead are below mean concentration levels in summer 2008. Gobi Desert can be identified as major source region for this dust. It can be concluded that the conducted simulations highlight the influence of mineral dust on air quality in Beijing in summer. Moreover it was shown that major Asian Deserts are still active in summer and not only in spring.

The presented study clearly showed that aerosols in Beijing and its surrounding are highly dynamic in space and time and that aerosol modeling is a suitable tool to identify typical processes of aerosol distribution. However, better simulation results of finer particle fractions, such as comprised in  $PM_{2.5}$  cannot be achieved with the emission inventory used in this study. A state-of-the-art inventory is necessary for further simulations.

## 7 Conclusions and Outlook

### 7.1 Conclusions

The scope of this work was an in-depth study of the spatio-temporal dynamics of mid-range transported mineral dust and locally produced anthropogenic particulates in Northern China during spring and summer. The aim of this investigation was to improve the understanding about dust emission and distribution within source regions and dust transport and its impact on air quality in downwind regions. In addition, interactions and physical mixing of dust with local anthropogenic particulates were studied under varying weather conditions during a short-term summer episode. To study these processes numerical simulations of airborne particulate load by a meso-scale chemistry-transport model were performed as well as satellite-based and ground-based data were used.

In this section major conclusions from the previous chapters are presented to answer key questions and hypotheses addressed in the beginning.

- Characterization of the spatio-temporal variability of dust and anthropogenic aerosols in Northern China under varying meteorological conditions

It was shown that a significant amount of particulates are present in Northern China during both case studies and that particulate distribution and composition is highly varying in space and time. The analysis of airborne dust variability during the spring 2011 case study clearly showed that there are high amounts of mineral dust in the atmosphere of major Chinese and Mongolian Deserts and in the downwind region of Beijing. Modelled and satellite derived AOD in these regions exceed the global background by far. However, it was also shown that dust load changes fast in its amount and distribution, mainly driven by meteorological conditions.

During summer, anthropogenic particulates are dominating in northeastern China. Highest levels of TSP concentrations during these conditions were always found close to emission sources, whereas  $PM_{10}$  and  $PM_{2.5}$  concentrations show a much more regional distribution. Moreover, a distinct border between areas of high and low AOD and TSP concentrations can be seen in the area along the Taihang Mountain ridge north-west to south-west of Beijing. The Taihang Mountains act as a natural barrier towards anthropogenic air pollutant transport from the polluted regions towards the West during weather conditions with low wind speeds from West to South-West. This study clearly proved the hypothesis that topography has an impact on local and regional air quality in Beijing.

- Definition of active mineral dust source regions and emission strengths

Using modelled and satellite-derived AOD in conjunction with modelled dust emission fluxes highlights emission strengths and the activation state of the dust sources. Taklimakan Desert, Kumtaq Desert, Gobi Desert and Inner Mongolia were the major active dust source regions during the spring and summer case studies. The Central Chinese Deserts and Gobi Desert were the major source regions for dust transported to Beijing during the spring case study, whereas Gobi Desert was identified as major source region during the summer episode. It was shown that the major Asian Deserts are still active as airborne dust source in summer and not only in spring. Strongest emission strengths are modelled for the Central Chinese Deserts and Gobi Desert.

However, during spring the amount of airborne dust modelled in Taklimakan Desert and Inner Mongolia is underestimated, comparing results to satellite data. It showed up that modelled dust emissions in Taklimakan Desert are not as high as expected, due to an underestimation of wind speeds, as the desert is located in a huge topographic low and inaccuracies of soil properties within the soil dataset. For Inner Mongolia, it can be noted, that a certain area of this region is not reconsidered within the soil dataset.

- Analysis of the dynamics of mid-range transport of dust towards Beijing

The in-depth study about dust dynamics and mid-range transport towards downwind regions in Northeastern China showed that Beijing and its surroundings were affected by a moving dust storm event originating in the Central Chinese Deserts and Gobi Desert during the case study period. In Taklimakan Desert a local dust storm event without mid-range or long-range transport was modelled for this specific weather situation.

The moving dust storm event showed a unique profile with two dust fronts moving on a south-eastern path towards Beijing. The plume on the more southern pathway arrives first in the Beijing region, followed by the second front in the North. On April 30 in 2011 both dust plumes merge, covering a huge area from 33° to 42° N and 107° to 120° E. Vertical atmospheric particulate and wind profiles showed that the transport of the dust clouds is highly dynamic due to strong winds and topographic effects in the lee of the Taihang Mountains, west of Beijing. This strong dynamic leads to an uplift of dust up to 10 km. The results of this study again support the hypothesis that topography has a strong effect on dust transport and its transport pathway.

- Determination of the vertical distribution of dust in the atmosphere in the source regions and the downwind located area of Beijing

The strong dynamics of dust transport often cause an uplift of particulates to higher altitudes. COSMO-ART and the spaceborne lidar aboard CALIPSO showed its potential to study vertical profiles of mineral dust

and the health-relevant amount of dust located near the ground. It showed up that dust in Taklimakan Desert, the Central Chinese Deserts and Inner Mongolia is mainly located near the ground up to 6 km and that there are also some thin uplifted layers. However, dust, which is transported from the Central Chinese Desert and Gobi Desert towards Northeastern China, can be lifted up to 10 km due to atmospheric turbulences and topographic effects.

The CALIPSO lidar data highlighted that mineral dust can be located in different heights in the atmosphere due to strong upward winds and topographic effects. The CALIPSO lidar is a suitable tool for such investigations.

- Assessment of the impact of mineral dust on local air quality in the desert areas and in Beijing

The high amounts of dust in the atmosphere of source regions and the downwind region of Beijing during spring 2011 caused a strong increase of near ground particulate concentrations. Particulate concentrations in Beijing reached its highest values throughout the year and lead to a drastic depletion of air quality. During this dust storm event the amount of anthropogenic particulates was negligible.

Simulations of dust distribution in August 2008 highlighted that dust impact on urban air quality can be significant not only in spring but also during summer. However, during such days anthropogenic particulates are still present in the urban atmosphere.

The presented results support the hypotheses that air quality in Beijing is strongly determined by airborne mineral dust, not only in spring but also during summer season. In spring mineral dust is a strong pollutant in Beijing on its own and does not act as substitute to local anthropogenic pollution levels. There is also no significant mixing of airborne mineral dust with locally produced pollutants. Whereas, in summer mineral dust is a substitute pollutant to existing anthropogenic dominated pollution levels.

- Estimation of the impact of anthropogenic emission reductions on air quality in Beijing during the Olympic Summer Games

As the modelled results of anthropogenic particulate concentrations and its spatio-temporal variability showed some inaccuracies, a realistic estimation of the impact of emission reduction measures was strongly limited. However, the comparison of modelled and measured gaseous pollutant concentrations, such as  $\text{NO}_x$  and ozone supported the assumption that emission reductions had a significant impact on local air quality.

However, the comparative analysis of air quality and meteorological parameters, such as precipitation events and wind conditions also showed that a reduction of particulate concentrations in Beijing was supported by the weather conditions.

- Adaptation of COSMO-ART model for aerosol simulations in East Asia

COSMO-ART was adapted for Northern Asia by implementing a soil dataset by *Laurent et al.* [2005] and an emission inventory by *Tang* [2010] and calibrating model parameters. The most reasonable model set-up was defined as result of intensive calibration and validation studies. It showed up that especially factor C, which describes the crusting of the soil, has a strong impact on total dust fluxes. It was set to a value of 0.1, which is much lower than for studies in Sahara Desert [*Vogel et al.*, 2006; *Stanelle et al.*, 2010] and Spain [*Gomes et al.*, 2003]. The spatial resolution of the model was set to 28 x 28 km<sup>2</sup>, mainly due to computation limitations and to reduce spatial discrepancies between model and input datasets.

- Estimation of the accuracy of COSMO-ART model results by validation with measurement data

After implementation of all adaptations, the model showed its ability to reproduce the spatio-temporal variability of Asian airborne mineral dust, whereas, results for the simulation of anthropogenic aerosols are more ambiguous due to inaccuracies of the anthropogenic emission inventory. However, problems of simulating anthropogenic pollutants are a common issue in aerosol modeling. Moreover, it became clear that a direct validation of model data with point based measurement data is highly challenging, due to scale differences.

However, in general spatio-temporal mineral dust distribution and transport can be reproduced by using COSMO-ART. The combined approach of aerosol model, satellite and ground-based measurements is a suitable tool for studying mineral dust dynamics and its impact on air quality

- Analysis of the application of four different passive and active satellite-based sensor data for assessment of mineral dust loads and air quality

The study showed that MODIS Deep Blue AOD is the most appropriate passive satellite product for airborne mineral dust assessment in Asian desert areas. OMI is often in accordance with MODIS, but has a much coarser spatial and temporal resolution. The lack of spatial information is also the main limitation for use of MISR data for such applications. The present study also highlighted that these passive sensor data cannot be used for direct assessment of near-ground air quality as vertical information of the location of aerosol layers is missing [*Schäfer et al.*, 2012b]. Such information can be obtained by using CALIPSO spaceborne lidar data. CALIPSO data were also in good accordance with results from COSMO-ART model runs.

The spaceborne lidar aboard CALIPSO is a suitable tool for determine the vertical location of mineral dust layers. In conjunction with passive satellite sensor data it can help to create a 3D-view of mineral dust in the atmosphere. This 3D-view strongly enhances the assessment of near ground air quality.

## 7.2 Outlook

The present study showed that the use and qualitative analysis of a state-of-the-art meso-scale aerosol model, such as COSMO-ART in combination with multispectral satellite data and ground-based measurements can enhance the knowledge of geogenic and anthropogenic particulate dynamics in Northern China.

However, such a method can only work for short-term case studies of specific events. A long-term analysis of particulates or forecasts of high pollution events need a different kind of methodological approach including quantitative statistical methods. Such methods should also comprise the identification and estimation of model inaccuracies. The present study clearly showed that there are still several uncertainties within the simulation of particulate concentrations. Especially input datasets, such as soil property datasets and emission inventories need to be improved for future applications to achieve best possible modeling results. In addition, available datasets from ground-based and satellite-based measurements for model calibration and validation still need improvements considering spatial and temporal resolution. Some parameters, e. g. dust emission fluxes or dust deposition amounts are in China not measured at all. Quantification of these parameters is only possible by using available data of AOD or particulate concentrations. Until such data will be available only top-down estimates of emissions are possible. These limiting factors could be reduced by some extent using the future satellite-based data products which provide much higher resolutions than currently available. Technical improvements in the satellite sector, such as new hyperspectral sensors or operational spectroradiometer sensors with a focus on atmosphere, should also be used for model improvement and calibration/ validation.

In addition, new ground-based particulate measurement techniques could be used in conjunction with aerosol models to get a closer look into the chemical composition of the urban aerosol load. Comprehensive chemical analysis, as conducted within a study by R. R. Shen at KIT/IMK can be used to detect specific discrepancies between modelled and measured  $PM_x$  concentrations, as all relevant chemical species are analyzed. Especially the organic species, which are to date not routinely analyzed, can give more information.

Moreover, it can also be concluded from the present study that the spatial resolution of the model set-up is too coarse for detailed analysis of particulate concentrations on an urban scale. However, limiting factors are still the coarse resolution of input datasets and computing time. The simulation of meteorological conditions and dust distribution for nine days takes at least six hours for a full run, without considering waiting time. Including anthropogenic particulates already doubles the computing time. Improvement within the computing sector should also lead to an improvement of model resolutions and modelled time spans.

## Appendix

### A Visualization of dust storm movement

The horizontal movement of dust clouds during the dust storm event in April 2011 is shown by visualizing single plots of modelled dust particle mass concentrations of the smallest particle mode near the ground.

The movie is available on dvd. See attachment.

## List of figures

Figure 1: Desert areas in Northern China and Southern Mongolia according to Laurent et al. [2005].	13
Figure 2: Schematic overview of the relevant impact factors, parameters, properties, processes, effects and methodological approaches used within the framework of the present work. The impact of primary and secondary geogenic and anthropogenic aerosols are studied over their whole lifetime from emission to transport and their formation during transport, to their impact on air quality. Relevant parameters are emission fluxes, total particle mass concentrations, AOD and near-ground PM <sub>x</sub> . Emission strengths, source locations and their activation state are identified by using COSMO-ART and satellite data. The horizontal and vertical distribution and transport of aerosols are also analyzed by using COSMO-ART and satellite data, whereas the transport and impact of aerosols on urban air quality are mainly studied by using COSMO-ART in conjunction with ground-based measurement data to get information about spatio-temporal variability and aerosol composition.	26
Figure 3: Location of all available ground-based measurement sites. Black flags mark meteorological sites, crosses mark air quality sites. Names of sites are abbreviated (see Table 1 and Table 2 for site names). D1 refers to model domain 1 located between 75°-130° E and 30.25°-50.25° N, D2 refers to model domain 2 located between 113.5°-120.25° E and 35°-42° N.	27
Figure 4: Feedback processes between aerosol and meteorological parameters included in the current COSMO-ART version. The dashed lines indicate cloud feedback processes which are newly included in the upcoming model version.	35
Figure 5: Schematic overview of mineral dust emission fluxes in COSMO-ART. $F_h$ represents the horizontal saltation flux and $F_v$ describes the vertical emission flux [Vogel et al., 2006].	35
Figure 6: Map of regions comprising similar soil types and soil properties according to the soil dataset of Laurent et al. [2005]. 12 Regions are defined: Gobi Desert, loess areas, sandy Loess areas, Taklimakan Desert, Badain Jaran Desert, Tengger Desert, Ulan Buh Desert, Qubqi Desert, Mu Us Sandy Land, Hoqin Sandy Land, desert areas east of Xinjiang, and Hexi Corridor.	43
Figure 7: Differences of vertical dust flux intensities of the different soil types in the study domain (soil dataset of Laurent et al. [2005]) under changing wind friction velocities between 0.3 and 1.0 m s <sup>-1</sup> (Figure 7a) and changes of vertical dust flux intensity of dust modes 1, 2 and 3 for different wind friction velocities between 0.3 and 1.0 m s <sup>-1</sup> (Figure 7b).	48
Figure 8: Dimension $\alpha$ as function of $u_*$ for soil type Gobi (Figure 8a) and soil type Loess (Figure 8b) with erodible fractions of 0.75, and 0.07, respectively.	49
Figure 9: Total dust emission fluxes of the Gobi Desert soils (soil type 'Gobi') with $C = 0.02$ and $C = 2.5$ and an erodible fraction of 0.75 (Figure 9a) and 0.9 (Figure 9b) for varying wind friction velocities between 0.3 and 1.0. Vertical dust flux in $\mu\text{g m}^{-2} \text{s}^{-1}$ (y-axis) is presented in logarithmic scale.	50
Figure 10: Total dust emissions (in $\mu\text{g m}^{-2} \text{s}^{-1}$ ) on April 29, 06:00 h (UTC) modelled with COSMO-ART. The left plot shows emissions modelled with $C = 0.25$ and the right plot shows emissions modelled with $C = 0.1$ . The bottom plot shows emission	

- changes for both runs from April 23 to May 2 in one grid cell at 41.875° N/ 103.875° E (black circles). The blue line indicates total dust emissions modelled with  $C = 0.25$  and the red line denotes emissions modelled with  $C = 0.1$ . ..... 51
- Figure 11: Daily variations of modelled and measured NO (left plot) and ozone (right plot) concentrations (both in ppbv) in Beijing for August 4 at 08:00 h up to August 8 at 19:00 h (local time)..... 53
- Figure 12: Comparison of observed NO and NO<sub>2</sub> concentrations with three different simulation runs of NO and NO<sub>2</sub> (both in ppbv) in Beijing for August 4, 08:00 h to August 8, 19:00 h (local time). The green lines (NO\_runC and NO<sub>2</sub>\_runC) denote the control runs without emissions reductions, the blue lines (NO\_runB and NO<sub>2</sub>\_runB) represent total NO<sub>x</sub> emission reductions of 50%, the black lines (NO\_runA and NO<sub>2</sub>\_runA) show NO<sub>x</sub> emission reductions according to G. Tang [Tang, 2010], and the red lines denote observed NO and NO<sub>2</sub> concentrations at the measurement site Beijing. .... 55
- Figure 13: Map of the geo-location of the model domain (30-50.25° N, 75-130.25° E), country and province boundaries and main desert areas superimposed with a surface elevation map. Elevation in the study domain ranges between 0 and 8848 m. Topographic data is taken from the global digital elevation model provided by the Earth Resources Observation and Science Center (EROS) ([www.eros.usgs.gov](http://www.eros.usgs.gov)). ..... 57
- Figure 14: Example of MODIS 5-minute-granules available over the study domain during one day and their times of recording. .... 58
- Figure 15: Multi-sensor AOD data for April 28, 29 and 30, 2011 (date is shown on the left hand side of the plot). Color indicates retrieved AOD values; the white color denotes missing or negligible (< 0.1) low AOD data due to clouds or snow/ ice cover. The first column shows MODIS Deep Blue AOD for April 28 (a), April 29 (d), and April 30 (g). The second column shows OMI 500 nm AOD for April 28 (b), April 29 (e), and April 30 (h). The third column shows MISR 555 nm AOD for April 28 (c), April 29 (f), and April 30 (i). The colored lines in images (a), (d) and (g) represent CALIPSO overpass paths for each day; the pink line for April 28, the green line for April 29 and the red line for April 30 (data is analyzed in section 4.4.2 and 4.4.3). The AOD range of MODIS and OMI is 0.1 to 3.5; and 0 to 0.9 for MISR. .... 61
- Figure 16: Horizontal distribution of AOD modelled using COSMO-ART for April 28 to 30, 2011. The date is displayed on the left hand side of the plots. AOD range is 0.1 to 3.5. The white color denotes missing or negligible low (< 0.1) AOD data due to low aerosol loadings, clouds or snow/ ice cover. Images are composited of up to three single images to fit temporally towards the MODIS composite images. April 28 is composed of images from 06:00 and 08:00 UTC (first plot); April 29 05:00, 07:00 and 08:00 UTC (second plot) and April 30 06:00 and 07:00 UTC (third plot). .... 63
- Figure 17: MODIS Deep Blue AOD (left column) and modelled COSMO-ART AOD (center column) for April 28, 06:00 and 08:00 UTC (first row); April 29, 05:00, 07:00 and 08:00 UTC (second row) and April 30, 06:00 and 07:00 UTC (third row). Increasing values of AOD are color coded from blue to red. AOD range is 0 to 4. The white color denotes missing or negligible low (< 0.1) AOD due to clouds or snow/ ice cover. CALIPSO overpass paths are shown by colored lines for April 28 (pink line), April 29 (green line) and April 30 (red line). Differences between modelled and satellite derived AOD for April 28 to 30 are shown in the right column. Blue colors denote AOD < 0.1 which occur when MODIS AOD is higher than COSMO-ART AOD and red colors are AOD > 0.0 representing higher values of COSMO-ART than

- derived by MODIS; the light beige color shows AOD similar for MODIS and COSMO-ART ..... 65
- Figure 18: Modelled COSMO-ART AOD (red line), MODIS Deep Blue AOD (blue line with dots) and CALIPSO total AOD (black line with asterisk) captured along the three selected CALIPSO overpass paths from south (30° N) to north (50° N). The overpass regions are Taklimakan Desert on April 28 07:30 UTC (first plot), Central China on April 29 06:30 UTC (second plot) and Inner Mongolia/ Beijing on April 30, 05:30 UTC (third plot). ..... 67
- Figure 19: Modelled COSMO-ART total mineral dust emissions summarized of all dust modes in  $\mu\text{g m}^{-2} \text{s}^{-1}$  for April 28, 06:00 and 08:00 UTC (first plot); April 29, 05:00, 07:00 and 08:00 UTC (second plot) and April 30, 06:00 and 07:00 UTC (third plot). White color denotes negligible emissions  $< 1 \mu\text{g m}^{-2} \text{s}^{-1}$ . Date is shown on left hand side of the plot. The bottom scale is valid for all plots. .... 68
- Figure 20: The first three plots of the first row show the vertical location of aerosol and cloud types found by the CALIPSO feature mask algorithm for the three paths over Taklimakan Desert on April 28, 07:30 UTC, Central China on April 29, 06:30 UTC, and Inner Mongolia/Beijing on April 30, 05:30 UTC. The second row represents vertical profiles of CALIPSO feature AOD for each transect. The scale for the first plot is 0.01 to 1.0, scales of the second and third plot are 0.1 to 3.0. The white color donates missing AOD due to inexistence of aerosol, clouds or algorithm failures. The third row shows COSMO-ART layer AOD for the three paths with an AOD range of 0.02 to 0.3. .... 71
- Figure 21:  $\text{PM}_{2.5}$  (left column) and  $\text{PM}_{10}$  (right column) mass concentrations (in  $\mu\text{g m}^{-3}$ ) modelled for the lowest model layer for April 28, 06:00 and 08:00 UTC (first row); April 29, 05:00, 07:00 and 08:00 UTC (second row) and April 30, 06:00 and 07:00 UTC (third row) in the study domain modelled with COSMO-ART. Study time is shown on the left hand side of the plot. .... 73
- Figure 22: Ranges of differences (expressed as AOD values) of satellite derived and modelled AOD during April 28 to 30, 2011. The blue colored dots denote an underestimation of modelled AOD; orange colored dots denote an overestimation of modelled AOD. The central beige dot denotes no significant difference between COSMO-ART and MODIS (-0.5 – 0.5). The size of the dots is increasing with increasing difference. .... 76
- Figure 23: Horizontal distribution of total dust mass concentrations (sum of all dust modes) (in  $\text{mg m}^{-3}$ ) in the lowest model layer and 10-m height wind vectors (meridional and zonal wind vectors in  $\text{m s}^{-1}$ ) from April 28 to 30, 2011 (from top left to bottom right) modelled using COSMO-ART. The reference wind speed vector is shown in the bottom right corner of each plot and is set to  $10 \text{ m s}^{-1}$ . Beijing is marked by a black asterisk. The scale on the right hand side refers to dust concentrations and is valid for all plots. Time is always UTC. Day and time of the plots (from top left to bottom right): 28.04 12:00 h, 29.04 00:00 h, 29.04 06:00 h, 29.04 12:00 h, 29.04 18:00 h, 30.04 00:00 h, 30.04 06:00 h, 30.04 12:00 h, and 30.04 18:00 h. .... 87
- Figure 24: Total soil roughness length  $z_{01}$  (in cm) for the Chinese and South Mongolian Deserts included in the soil dataset of *Laurent et al.* [2005] and taken as input dataset for COSMO-ART simulations. Beijing is marked by a black asterisk. .... 89
- Figure 25: Total dust emissions (sum of all dust modes) (in  $\mu\text{g m}^{-2} \text{s}^{-1}$ ) and 10-m height wind vectors (meridional and zonal wind vectors in  $\text{m s}^{-1}$ ) for Northeast China for April 28 to 30 in 2011, modelled with COSMO-ART. Reference wind speed vector is shown in the bottom right corner of each plot and set to  $10 \text{ m s}^{-1}$ . Beijing is marked by a black asterisk. The scale on the right hand side refers to dust emissions and is

- valid for all plots. Time is UTC. Day and time of the plots (from top left to bottom right): 28.04 12:00 h, 29.04 00:00 h, 29.04 06:00 h, 29.04 12:00 h, 29.04 18:00 h, 30.04 00:00 h, 30.04 06:00 h, 30.04 12:00 h and 30.04 18:00 h..... 90
- Figure 26: Wind speed (in  $\text{m s}^{-1}$ ) in 10 m above ground for Northeast China from April 28 to 30 in 2011, modelled with COSMO-ART. Beijing is marked by a black asterisk. The scale on the right hand side refers to wind speed and is valid for all plots. Time is UTC. Day and time of the plots (from top left to bottom right): 28.04 12:00 h, 29.04 00:00 h, 29.04 06:00 h, 29.04 12:00 h, 29.04 18:00 h, 30.04 00:00 h, 30.04 06:00 h, 30.04 12:00 h and 30.04 18:00 h..... 90
- Figure 27: The first plot shows wind direction (in  $^{\circ}$ ) (black dashed line with triangles) and wind speed (in  $\text{m s}^{-1}$ ) (black line with asterisk) in 10 m height from April 29 at 12:00 h to April 30 at 18:00 h in 2011 measured in Beijing. The second plot shows air temperature (in  $^{\circ}\text{C}$ ) (black line with dots) and sea level pressure (in hPa) (black stars) in 2 m height from April 28 at 12:00 h to April 30 at 18:00 h in 2011 measured in Beijing. Reported dust events are shown in grey. Time is UTC..... 91
- Figure 28: Horizontal movement of dust plumes from Gobi Desert to the Chinese East Coast from April 28 to 30 in 2011 modelled using COSMO-ART. The grey shaded areas show the area covered by modelled total dust mass concentrations  $> 2 \text{ mg m}^{-3}$  summarized over all model layers. The colored lines show the dust plums at different times (in UTC). The black line shows the initial dust plume on 28.04 12:00 h, purple stands for 29.04 00:00 h, blue for 29.04 12:00 h, green for 29.04 18:00 h, red for 30.04..... 92
- Figure 29: Location of cross-section paths A and B. Cross-section A is located between  $44^{\circ}\text{N}/100^{\circ}\text{E}$  and  $34^{\circ}\text{N}/120^{\circ}\text{E}$  (solid line); cross-section B is located between  $44^{\circ}\text{N}/108^{\circ}\text{E}$  and  $37^{\circ}\text{N}/122^{\circ}\text{E}$  (dashed line). Beijing is marked by a black asterisk..... 93
- Figure 30: Profiles of total dust mass concentrations (in  $\text{mg m}^{-3}$ ) and wind vectors (wind speed and vertical wind velocity in  $\text{m s}^{-1}$ ) for cross-section A ( $44^{\circ}\text{N}/100^{\circ}\text{E}$  to  $34^{\circ}\text{N}/120^{\circ}\text{E}$ ) from April 28 to 30, 2011. The vertical wind velocity is multiplied by a factor of 20 to make vertical movement visible. The reference vector is shown in the top right corner of the plots and set to  $15 \text{ m s}^{-1}$ . The scale on the right hand side refers to total dust mass concentrations and is valid for all plots. Time is UTC. Day and time of the plots from the top left to the bottom right: 28.04 12:00 h, 29.04 00:00 h, 29.04 06:00 h, 29.04 12:00 h, 29.04 18:00 h, 30.04 00:00 h, 30.04 06:00 h, 30.04 12:00 h and 30.04 18:00 h..... 95
- Figure 31: Profiles of total dust mass concentrations (in  $\text{mg m}^{-3}$ ) and wind vectors (wind speed and vertical wind velocity in  $\text{m s}^{-1}$ ) for cross-section B ( $44^{\circ}\text{N}/108^{\circ}\text{E}$  to  $37^{\circ}\text{N}/122^{\circ}\text{E}$ ) from April 28 to 30, 2011. The vertical wind velocity is multiplied by a factor of 20 to make vertical movement visible. The reference vector is shown in the top right corner of the plots and set to  $15 \text{ m s}^{-1}$ . The scale on the right hand side refers to total dust mass concentrations and is valid for all plots. The location of Beijing is marked by the thick black bar. Time is UTC. Day and time of the plots from the top left to the bottom right: 28.04 12:00 h, 29.04 00:00 h, 29.04 06:00 h, 29.04 12:00 h, 29.04 18:00 h, 30.04 00:00 h, 30.04 06:00 h, 30.04 12:00 h and 30.04 18:00 h..... 96
- Figure 32: CALIPSO vertical feature mask profiles for three cross-sections passing Beijing on April 29 at 18:30 h (blue line on map, first cross-sectional plot), April 30 at 05:30 h (red line on map, second cross-sectional plot), and May 1 at 18:30 h (pink line on map, third cross-sectional plot). Time is in UTC. The locations of the cross-sections are shown in the map at the top on the right hand side. Beijing is marked by a black

asterisk. The cross-sectional plots are located between 35° and 45° N. The legend of CALIPSO features are shown on the right hand side. ....	98
Figure 33: PM <sub>2.5</sub> (top panel plot) and PM <sub>10</sub> (bottom panel plot) mass concentrations (in $\mu\text{g m}^{-3}$ ) from April 29 at 12:00 h to April 30 at 18:00 h in the lowest model layer modelled with COSMO-ART. Date and time is shown in the top left of the plots and all times are in UTC. Beijing city is marked by a black cuboid. Small black dots show the horizontal COSMO-ART grid cell raster. ....	100
Figure 34: Locations of NOAA meteorological measurement sites and CAS-IAP air quality measurement sites providing PM <sub>10</sub> and PM <sub>2.5</sub> data for April 24 to May 2 in 2011. Air quality sites are marked with a colored cross, meteorological sites are marked with a black flag. Black lines show country and province boundaries, superimposed with a surface elevation map (data source: see chapter 4) and the grid cell raster of the COSMO-ART model setup. ....	101
Figure 35: Comparison of PM <sub>10</sub> and PM <sub>2.5</sub> (in $\mu\text{g m}^{-3}$ ) measured at sites in Beijing, Baoding and Tianjin with PM <sub>10</sub> and PM <sub>2.5</sub> (in $\mu\text{g m}^{-3}$ ) modelled for the according locations with COSMO-ART for April 24 at 00:00 h to May 2 at 00:00 h in 2011. Time is in UTC. In addition observed visibility (in km) and dust events are shown. The comparison of modelled and observed PM <sub>2.5</sub> is shown on the left hand side of the plot, and the comparison of PM <sub>10</sub> on the right hand side. The red line denotes modelled PM <sub>10</sub> and PM <sub>2.5</sub> , the black line denotes observed PM <sub>10</sub> and PM <sub>2.5</sub> . The purple crosses show observed visibility and reported dust events are shaded in light grey.....	104
Figure 36: Same figure as Figure 34 but for the measurement sites Xianghe, Tangshan and Xinglong. Meteorological data for Xianghe and Xinglong are taken from the site Beijing as there are no active NOAA meteorological sites near Xinglong and Xianghe for this time period.....	105
Figure 37: Modelled and observed wind speed (in $\text{m s}^{-1}$ ) and wind direction (in °) for Beijing, Baoding, Tianjin and Tangshan between April 24 at 00:00 h and May 2 at 00:00 h in 2011. The blue line denotes modelled wind speeds; the blue cross denotes observed wind speeds, the black line shows modelled wind directions and the black asterisk shows observed wind directions. Reported dust events are shaded in grey.....	110
Figure 38: Vertical profiles of total dust concentrations (in $\text{mg m}^{-3}$ ) up to 6 km height for a part of cross-section B between 37° and 42° N for April 30, 00:00 h to 05:00 h. Time is UTC. The vertical wind velocity is multiplied by a factor of 20 to make vertical movement visible. The reference vector is shown in the top right corner of the plots and set to $15 \text{ m s}^{-1}$ . The scale on the right hand side refers to total dust mass concentrations and is valid for all plots. Beijing is located at 40° N.....	112
Figure 39: Map (36-42° N, 113.5-120.25° E) of location of NOAA meteorological measurement sites, CAS-IAP and CRAES air quality measurement sites providing data for August 4 to 14 in 2008 in model domain 2. Air quality sites are marked with colored crosses and meteorological sites are marked with a black flag. Black lines show country and province boundaries, superimposed with a surface elevation map (data source: see chapter 4). ....	122
Figure 40: Time-series of wind speed (black line with asterisk), visibility (red line with cross), temperature (green line with dot), and precipitation (blue bulk) measured at NOAA sites in Beijing, Baoding, Shijiazhuang, Potou, and Tangshan from August 4 at 00:00 h to August 14 at 00:00 h in 2008. Wind speed in $\text{m s}^{-1}$ , visibility in km, temperature in °C, and precipitation in mm. The dashed grey boxes mark the Olympic period during the case study. ....	124

- Figure 41: Comparison of observed and modelled meteorological parameters at sites Beijing, Baoding, Shijiazhuang, Potou, and Tangshan from August 4 to 14. Asterisk always describe measurement date and solid lines describe modelled data. Black denotes wind speeds (both in  $\text{m s}^{-1}$ ), red denotes relative humidity (both in %), and blue denotes temperature (both in  $^{\circ}\text{C}$ ). The scale of wind speed is on the left hand side of the plot, temperature and relative humidity on the right hand side of the plots. .... 126
- Figure 42: Spatio-temporal distribution of total AOD and 10-m wind vectors (meridional and zonal wind vectors in  $\text{m s}^{-1}$ ) in model domain D2 from August 5 to 13 in 2008 (from top left to bottom right) modelled by using COSMO-ART. AOD reflects the aerosol loading of the whole atmospheric column. White color denotes negligible ( $< 0.05$ ) or missing AOD values; red colors denote  $\text{AOD} > 1.5$ . Beijing is marked by a black box. The reference wind speed vector is shown in the bottom right corner of each plot and is set to  $5 \text{ m s}^{-1}$ . Time of every plot is 06:00 h (UTC) which corresponds with 14:00 h local Beijing time. .... 128
- Figure 43: Spatio-temporal distribution of daily TSP concentrations (in  $\mu\text{g m}^{-3}$ ) and 10-m wind vectors (meridional and zonal wind vectors in  $\text{m s}^{-1}$ ) in model domain D2 from August 5 to 13 in 2008 (from top left to bottom right) modelled by using COSMO-ART. TSP comprises anthropogenic aerosols and mineral dust and is calculated for the lowest model layer. White color denotes negligible ( $< 2.5$ ) or missing TSP values; red colors denote  $\text{TSP} > 160 \mu\text{g m}^{-3}$ . Beijing is marked by a black box. The reference wind speed vector is shown in the bottom right corner of each plot and is set to  $5 \text{ m s}^{-1}$ . TSP is average over 24 hours for every day, beginning at 01:00 h UTC ( $\sim 09:00$  h Beijing time) for temporal accordance with daily measurement data from CRAES site (see section 6.3.2.3). .... 131
- Figure 44: Spatio-temporal distribution of daily  $\text{PM}_{10}$  concentrations (in  $\mu\text{g m}^{-3}$ ) and 10-m wind vectors (meridional and zonal wind vectors in  $\text{m s}^{-1}$ ) in model domain D2 from August 5 to 13 in 2008 (from top left to bottom right) modelled by using COSMO-ART. TSP comprises anthropogenic aerosols and mineral dust and is calculated for the lowest model layer. White color denotes negligible ( $< 2.5$ ) or missing  $\text{PM}_{10}$  concentration values; red colors denote  $\text{PM}_{10}$  concentrations  $> 50 \mu\text{g m}^{-3}$ . Beijing is marked by a black box. The reference wind speed vector is shown in the bottom right corner of each plot and is set to  $5 \text{ m s}^{-1}$ .  $\text{PM}_{10}$  is averaged over 24 hours for every day, beginning at 01:00 h UTC ( $\sim 09:00$  h Beijing time) for temporal accordance with daily measurement data from CRAES site (see section 6.3.2.3). .... 132
- Figure 45: Spatio-temporal distribution of daily  $\text{PM}_{2.5}$  concentrations (in  $\mu\text{g m}^{-3}$ ) and 10-m wind vectors (meridional and zonal wind vectors in  $\text{m s}^{-1}$ ) in model domain D2 from August 5 to -13 in 2008 (from top left to bottom right) modelled using COSMO-ART. TSP comprises anthropogenic aerosols and mineral dust and is calculated for the lowest model layer. White color denotes negligible ( $< 0.1$ ) or missing  $\text{PM}_{2.5}$  concentration values; red colors denote  $\text{PM}_{2.5}$  concentrations  $> 16 \mu\text{g m}^{-3}$ . Beijing is marked by a black box. The reference wind speed vector is shown in the bottom right corner of each plot and is set to  $5 \text{ m s}^{-1}$ .  $\text{PM}_{2.5}$  is average over 24 hours for every day, beginning at 01:00 h UTC ( $\sim 09:00$  h Beijing time) for temporal accordance with daily measurement data from CRAES site (see section 6.3.2.3). .... 133
- Figure 46: Comparison of hourly  $\text{PM}_{10}$  (top plot, left column) and  $\text{PM}_{2.5}$  concentrations (bottom plot, left column) and daily TSP (top plot, right column) and  $\text{PM}_{2.5}$  (bottom plot, right column) concentrations (all in  $\mu\text{g m}^{-3}$ ) observed at CAS site Aoyuncun in Beijing and CRAES site in Beijing and modelled with COSMO-ART for August 4-13, 2008. Red lines denote modelled data and black lines define observed data. The grey box indicates the start of the Olympic period. .... 134

- Figure 47: Temporal variability of PM<sub>10</sub> and PM<sub>2.5</sub> concentrations (in  $\mu\text{g m}^{-3}$ ) at site Aoyuncun (Beijing), Baoding, Shijiazhuang, Yucheng, Xianghe, Xinglong, Tangshan, Qinhuangdao, and Cangzhou for August 4-14 in 2008 modelled with COSMO-ART. Time is local Beijing Time. Purple lines define PM<sub>10</sub> and PM<sub>2.5</sub> concentrations at Aoyuncun (Beijing) site, pink lines stand for Baoding, red lines stand for Shijiazhuang, orange lines stand for Yucheng, yellow lines stand for Cangzhou, green lines stand for Tangshan, blue lines stand for Qinhuangdao, bright grey lines stand for Xinglong, and dark grey lines stand for Xianghe..... 135
- Figure 48: Modelled chemical compositions of TSP for all available sites averaged for August 4-14. White color denotes NH<sub>4</sub><sup>+</sup>, blue denotes SO<sub>4</sub><sup>2-</sup>, yellow denotes NO<sub>3</sub><sup>-</sup>, green denotes SOA, brown denotes soot, purple denotes primary PM<sub>10</sub>, and orange denotes mineral dust. All ratios are in % and refer to specific total mass concentrations. The location of all sites is shown in the central plot..... 138
- Figure 49: Same figure as Figure 48 but showing modelled chemical compositions of PM<sub>10</sub> for all sites averaged for August 4-14. .... 138
- Figure 50: Same figure as figure 48 but showing modelled chemical compositions of PM<sub>10</sub> for all sites averaged for August 4-14. .... 139
- Figure 51: Temporal changes of TSP, PM<sub>10</sub> and PM<sub>2.5</sub> composition at Beijing (top row), Baoding (second row), Shijiazhuang (central row), Yucheng (forth row), and Cangzhou (bottom row) for August 4-14, 2008 modelled by using COSMO-ART. Time is always Beijing time (UTC + 8h). White defines NH<sub>4</sub><sup>+</sup> concentrations, yellow defines NO<sub>3</sub><sup>-</sup>, blue defines SO<sub>4</sub><sup>2-</sup>, brown defines soot, green defines SOA, purple defines direct PM<sub>10</sub>, and orange defines mineral dust. All species are described in  $\mu\text{g m}^{-3}$ ..... 140
- Figure 52: Same figure as figure 51 but showing temporal changes of TSP, PM<sub>10</sub> and PM<sub>2.5</sub> composition at Tangshan (top row), Qinhuangdao (second row), Xinglong (third row), and Xianghe (bottom row) for August 4-14, 2008 modelled by using COSMO-ART. .... 141
- Figure 53: Comparison of daily averaged NO<sub>3</sub><sup>-</sup> (top row), SO<sub>4</sub><sup>2-</sup> (central row) and BC (bottom row) concentrations (in  $\mu\text{g m}^{-3}$ ) observed at CRAES-Beijing site and modelled with COSMO-ART for August 4-13, 2008. Red lines denote modelled data and black lines define observational data. .... 142
- Figure 54: Demonstration of selected observed and modelled hourly and daily meteorological parameters, TSP concentrations and its chemical species in Beijing during August 4-14. Selected meteorological parameters are wind speed (in  $\text{m s}^{-1}$ ), relative humidity (in %), temperature (in ° C) (all shown in top plot), and precipitation (in mm) (second plot). Observed wind speed, humidity and temperature are represented by asterisks, modelled values by closed lines. Modelled and observed TSP concentrations (in  $\mu\text{g m}^{-3}$ ) and chemical species concentrations (in  $\mu\text{g m}^{-3}$ ) of modelled TSP are shown in the third plot and the bottom plot. The black line with asterisk denotes observed TSP and the red line with asterisk denotes modelled TSP, whereas chemical species NH<sub>4</sub><sup>+</sup>, NO<sub>3</sub><sup>-</sup>, SO<sub>4</sub><sup>2-</sup>, soot, SOA, PM<sub>10</sub> and dust are represented by white, yellow, blue, brown, green, purple, and orange colors. The grey boxes show two specific meteorological conditions with low TSP concentrations..... 144
- Figure 55: Spatio-temporal distribution of total AOD and 10-m wind vectors (meridional and zonal wind vectors in  $\text{m s}^{-1}$ ) in model domain D2 from August 10-13 in 2008 (from top left to bottom right) modelled by using COSMO-ART. White color denotes negligible or missing AOD, red colors denote AOD > 1.5. Beijing is marked by a

- black box. The reference wind speed vector is shown in the bottom right corner of each plot and is set to  $5 \text{ m s}^{-1}$ . Day and time of the plots (from top left to bottom right): 10.08 06:00 h, 11.08 06:00 h, 12.08 12:00 h, 10.08 12:00 h, 11.08 12:00 h, and 13.08 00:00 h. Time is UTC. .... 147
- Figure 56: Comparison of  $\text{NO}_3^-$  and  $\text{SO}_4^{2-}$  time-series from three different emission scenarios for Beijing (top row), Shijiazhuang (second row), Yucheng (third row) and Qinhuangdao (bottom row) modelled by using COSMO-ART for August 4, at 08:00 h to August 8, 19:00 h. Time is set to Beijing time (UTC + 8h). Green lines denote  $\text{NO}_3^-$  and  $\text{SO}_4^{2-}$  concentrations from a control run (without emission reductions), blue lines denote the  $\text{NO}_3^-$  and  $\text{SO}_4^{2-}$  concentrations from a run with a  $\text{NO}_x$  reduction of 50% and a  $\text{SO}_2$  reduction of 20%, and black lines denote  $\text{NO}_3^-$  and  $\text{SO}_4^{2-}$  concentrations from a run with specific reduction factors (chapter 3). .... 151
- Figure 57: Spatio-temporal dynamics of dust-only AOD and 10-m wind vectors (meridional and zonal wind vectors in  $\text{m s}^{-1}$ ) in model domain D1 from August 6- 9, each at 12:00 h (UTC) in 2008 (from top left to bottom right) modelled by using COSMO-ART. AOD reflects the dust loading of the whole atmospheric column. Anthropogenic aerosols are not reconsidered. White color denotes negligible AOD values, red colors denote  $\text{AOD} > 1.0$ . Beijing is marked by an asterisk. The reference wind speed vector is shown in the bottom right corner of each plot and is set to  $5 \text{ m s}^{-1}$ . Day and time of the plots (from top left to bottom right): 06.08 12:00 h, 07.08 12:00 h, 08.08 12:00 h, and 09.08 12:00h. .... 153
- Figure 58: Spatio-temporal dynamics of dust-only AOD and 10-m wind vectors (meridional and zonal wind vectors in  $\text{m s}^{-1}$ ) in model domain D2 for August 10-13 in 2008 (from top left to bottom right) modelled with COSMO-ART. AOD reflects dust loading of the whole atmospheric column. Anthropogenic aerosols are not reconsidered. White color denotes negligible AOD, red colors denote  $\text{AOD} > 0.3$ . Beijing is marked by an asterisk. Reference wind speed vector is shown in the bottom right corner of each plot and is set to  $5 \text{ m s}^{-1}$ . Day and time of the plots (from top left to bottom right): 10.08 06:00 h, 10.08 12:00 h, 11.08 00:00 h, 11.08 06:00 h, 11.08 12:00 h, 12.08 00:00 h, 12.08 06:00 h, 12.08 12:00 h, and 13.08 00:00 h. Time is UTC. .... 154

## List of tables

Table 1:	Summary of data availability and temporal resolution of selected meteorological parameters from the WMO official measurement network for both case studies in August 2008 (abbreviated as '08') and April 2011 (abbreviated as '11'). T = Temperature, RH = Relative humidity, U = Wind speed, V = Wind direction, PR = Precipitation, Vis = Visibility, Con = Conditions.....	28
Table 2:	Summary of the availability of trace gas, PM <sub>10</sub> and PM <sub>2.5</sub> data for the Beijing-CRAES measurement site and the Beijing-Tianjin-Hebei-Measurement Network, for both case studies in August 2008 and April 2011.....	29
Table 3:	Overview presenting the specific aerosol modes (row 1), their chemical compositions (row 2-5), mixing states (row 6), initial diameters in $\mu\text{m}$ (row 7) and standard deviations (last row).....	33
Table 4:	Properties of the three mineral dust modes following <i>Alfaro and Gomes</i> [2001].....	38
Table 5:	Overview of emission sectors and available reduction factors of NO <sub>x</sub> , SO <sub>2</sub> , PM <sub>10</sub> , NMVOCs and NH <sub>3</sub> (in %) in Beijing and its direct surrounding, being valid for August 2008. In addition the total reductions are summarized for every species. ....	54
Table 6:	Performance statistics of modelled NO, NO <sub>2</sub> and ozone concentrations in Beijing, for August 4, 08:00 h to August 8, 19:00 h (local time) in 2008. The following statistical parameters are calculated: mean average of modelled parameters (ave_mod), mean average of observed parameters (ave_obs), number of data points used for calculations (npt) and the Spearman correlation coefficient (r).....	55
Table 7:	Statistical indicators of CALIPSO and MODIS total AOD for the three CALIPSO cross tracks over Taklimakan Desert on April 28, Central China on April 29 and Inner Mongolia/ Beijing on April 30, 2011. AOD mean (aod_ave), median (aod_med), minimum (aod_min), maximum (aod_max), standard deviation (aod_dev) and number of data values (npt) are shown.....	67
Table 8:	Performance statistics of modelled 10-m wind speed (WS), 10-m wind direction (WD) and 2-m temperature (T) at Beijing, Baoding, Tianjin and Tangshan from April 24 at 00:00 h to May 2 at 00:00 h in 2011. The following statistical parameters are calculated: mean average of modelled parameters (ave_mod), mean average of observed parameters (ave_obs), number of data points used for calculations (npt) and the Spearman correlation coefficient (r).....	109
Table 9:	Performance statistics of the modelled 10-m wind speed (WS), 10-m wind direction (WD), 2-m temperature (T), 2-m relative humidity (RH), and precipitation (PRP) at Beijing, Baoding, Shijiazhuang, Potou, and Tangshan from August 4 at 00:00 h to August 14 at 00:00 h in 2008. Following statistical parameters are calculated: mean average of modelled parameters (ave_mod), mean average of observed parameters (ave_obs), data points used for calculations (npt) and Spearman correlation coefficient (r). ....	126
Table 10:	Performance statistics of modelled PM <sub>10</sub> and PM <sub>2.5</sub> at Aoyuncun (Beijing), Baoding, Shijiazhuang, Yucheng, Xianghe, Xinglong, Tangshan, Qinhuangdao, and Cangzhou for August 4-14 in 2008, and comparison with measurement data. The following statistical parameters are calculated: mean average of modelled parameters (ave_mod), mean average of observed parameters (ave_obs), number of data points used for calculations (npt) and the Spearman correlation coefficient (r). – means that no observational data are available, preventing a further comparison. ....	136

## References

- Ahn, C., Torres, O., and Bhartia, P. K. (2008), Comparison of ozone monitoring instrument UV aerosol products with Aqua/Moderate Resolution Imaging Spectroradiometer and Multiangle Imaging Spectroradiometer observations in 2006, *Journal of Geophysical Research: Atmospheres (1984–2012)*, *113*(D16), 2156-2202.
- Alfaro, S. C., and Gomes, L. (1995), Improving the large-scale modeling of the saltation flux of soil particles in presence of nonerodible elements, *Journal of Geophysical Research: Atmospheres*, *100*(D8), 16357-16366.
- Alfaro, S. C., and Gomes, L. (2001), Modeling mineral aerosol production by wind erosion: Emission intensities and aerosol size distributions in source areas, *Journal of Geophysical Research: Atmospheres*, *106*(D16), 18075-18084.
- Amiridis, V., Giannakaki, E., Balis, D., Gerasopoulos, E., Pytharoulis, I., Zanis, P., Kazadzis, S., Melas, D., and Zerefos, C. (2010), Smoke injection heights from agricultural burning in Eastern Europe as seen by CALIPSO, *Atmospheric Chemistry and Physics*, *10*(23), 11567-11576.
- Amiridis, V., Wandinger, U., Marinou, E., Giannakaki, E., Tsekeri, A., Basart, S., Kazadzis, S., Gkikas, A., Taylor, M., and Baldasano, J. (2013), Optimizing Saharan dust CALIPSO retrievals, *Atmospheric Chemistry and Physics Discussions*, *13*(6), 14749-14795.
- An, X., Zhu, T., Wang, Z., Li, C., and Wang, Y. (2007), A modeling analysis of a heavy air pollution episode occurred in Beijing, *Atmospheric Chemistry and Physics*, *7*(12), 3103-3114.
- Andreae, M. O., Hegg, D. A., and Baltensperger, U. (2009), Sources and Nature of Atmospheric Aerosols, in *Aerosol Pollution Impact on Precipitation*, edited by Levin, Z. and Cotton, W., pp. 45-89, Springer Netherlands.
- Ansmann, A., Petzold, A., Kandler, K., Tegen, I., Wendisch, M., Müller, D., Weinzierl, B., Müller, T., and Heintzenberg, J. (2011), Saharan Mineral Dust Experiments SAMUM-1 and SAMUM-2: what have we learned?, *Tellus B*, *63*(4), 403-429.
- Bangert, M., Nenes, A., Vogel, B., Vogel, H., Barahona, D., Karydis, V. A., Kumar, P., Kottmeier, C., and Blahak, U. (2012), Saharan dust event impacts on cloud formation and radiation over Western Europe, *Atmospheric Chemistry and Physics*, *12*(9), 4045-4063.
- Bäumer, D., Vogel, B., Versick, S., Rinke, R., Möhler, O., and Schnaiter, M. (2008), Relationship of visibility, aerosol optical thickness and aerosol size distribution in an ageing air mass over South-West Germany, *Atmospheric Environment*, *42*(5), 989-998.
- Bell, M. L., Levy, J. K., and Lin, Z. (2008), The effect of sandstorms and air pollution on cause-specific hospital admissions in Taipei, Taiwan, *Occupational and environmental medicine*, *65*(2), 104-111.
- Bian, H., Tie, X., Cao, J., Ying, Z., Han, S., and Xue, Y. (2011), Analysis of a severe dust storm event over China: Application of the WRF-Dust Model, *Aerosol and Air Quality Research*, *11*(4), 419-428.
- Binkowski, F. S., and Shankar, U. (1995), The regional particulate matter model: 1. Model description and preliminary results, *Journal of Geophysical Research: Atmospheres (1984–2012)*, *100*(D12), 26191-26209.
- Breitner, S., Liu, L., Cyrys, J., Brüske, I., Franck, U., Schlink, U., Lette, A. M., Herbarth, O., Wiedensohler, A., and Wehner, B. (2011), Sub-micrometer particulate air pollution and cardiovascular mortality in Beijing, China, *Science of The Total Environment*, *409*(24), 5196-5204.
- Burton, S., Ferrare, R., Vaughan, M., Omar, A., Rogers, R., Hostetler, C., and Hair, J. (2013), Aerosol classification from airborne HSRL and comparisons with the CALIPSO vertical feature mask, *Atmospheric Measurement Techniques*, *6*(5), 1397-1412.

- Cao, G., Zhang, X., and Zheng, F. (2006), Inventory of black carbon and organic carbon emissions from China, *Atmospheric Environment*, 40(34), 6516-6527.
- Cao, J.-j., Wang, Q.-y., Chow, J. C., Watson, J. G., Tie, X.-x., Shen, Z.-x., Wang, P., and An, Z.-s. (2012), Impacts of aerosol compositions on visibility impairment in Xi'an, China, *Atmospheric Environment*, 59(0), 559-566.
- Cermak, J., and Knutti, R. (2009), Beijing Olympics as an aerosol field experiment, *Geophysical Research Letters*, 36(10), L10806.
- Chan, C. K., and Yao, X. (2008), Air pollution in mega cities in China, *Atmospheric Environment*, 42(1), 1-42.
- Chang, D., Song, Y., and Liu, B. (2009), Visibility trends in six megacities in China 1973–2007, *Atmospheric Research*, 94(2), 161-167.
- Chatenet, B., Marticorena, B., Gomes, L., and Bergametti, G. (1996), Assessing the microped size distributions of desert soils erodible by wind, *Sedimentology*, 43(5), 901-911.
- Chen, D., Cheng, S., Liu, L., Chen, T., and Guo, X. (2007), An integrated MM5–CMAQ modeling approach for assessing trans-boundary PM<sub>10</sub> contribution to the host city of 2008 Olympic summer games—Beijing, China, *Atmospheric Environment*, 41(6), 1237-1250.
- Chen, D., Wang, Y., McElroy, M., He, K., Yantosca, R., and Sager, P. L. (2009), Regional CO pollution and export in China modelled by the high-resolution nested-grid GEOS-Chem model, *Atmospheric Chemistry and Physics*, 9(11), 3825-3839.
- Chen, Z., Torres, O., McCormick, M. P., Smith, W., and Ahn, C. (2012), Comparative study of aerosol and cloud detected by CALIPSO and OMI, *Atmospheric Environment*, 51, 187-195.
- Cheng, S., Chen, D., Li, J., Wang, H., and Guo, X. (2007), The assessment of emission-source contributions to air quality by using a coupled MM5-ARPS-CMAQ modeling system: A case study in the Beijing metropolitan region, China, *Environmental Modelling & Software*, 22(11), 1601-1616.
- Chin, M., Diehl, T., Dubovik, O., Eck, T., Holben, B., Sinyuk, A., and Streets, D. (2009), Light absorption by pollution, dust, and biomass burning aerosols: A global model study and evaluation with AERONET measurements, *Annales geophysicae: atmospheres, hydrospheres and space sciences*, 27, 3439.
- Colbeck, I., and Lazaridis, M. (2010), Aerosols and environmental pollution, *Naturwissenschaften*, 97(2), 117-131.
- Cuesta, J., Marsham, J. H., Parker, D. J., and Flamant, C. (2009), Dynamical mechanisms controlling the vertical redistribution of dust and the thermodynamic structure of the West Saharan atmospheric boundary layer during summer, *Atmospheric Science Letters*, 10(1), 34-42.
- Darmenova, K., Sokolik, I. N., Shao, Y., Marticorena, B., and Bergametti, G. (2009), Development of a physically based dust emission module within the Weather Research and Forecasting (WRF) model: Assessment of dust emission parameterizations and input parameters for source regions in Central and East Asia, *Journal of Geophysical Research: Atmospheres*, 114(D14), D14201.
- Diner, D., Abdou, W., Bruegge, C., Conel, J., Crean, K., Gaitley, B., Helmlinger, M., Kahn, R., Martonchik, J., and Pilorz, S. (2001), MISR aerosol optical depth retrievals over southern Africa during the SAFARI2000 Dry Season Campaign, *Geophysical Research Letters*, 28(16), 3127-3130.
- Diner, D. J., Beckert, J. C., Reilly, T. H., Bruegge, C. J., Conel, J. E., Kahn, R. A., Martonchik, J. V., Ackerman, T. P., Davies, R., and Gerstl, S. A. (1998), Multi-angle Imaging SpectroRadiometer (MISR) instrument description and experiment overview, *Geoscience and Remote Sensing, IEEE Transactions on*, 36(4), 1072-1087.
- Ding, R., Li, J., Wang, S., and Ren, F. (2005), Decadal change of the spring dust storm in northwest China and the associated atmospheric circulation, *Geophysical Research Letters*, 32(2), L02808.
- Doms, G., and Schättler, U. (2002), A description of the nonhydrostatic regional model LM, *Deutscher Wetterdienst*.

- Donkelaar, A. v., Martin, R. V., Leaitch, W. R., Macdonald, A., Walker, T., Streets, D. G., Zhang, Q., Dunlea, E. J., Jimenez, J. L., and Dibb, J. E. (2008), Analysis of aircraft and satellite measurements from the Intercontinental Chemical Transport Experiment (INTEX-B) to quantify long-range transport of East Asian sulfur to Canada, *Atmospheric Chemistry and Physics*, 8(11), 2999-3014.
- Duan, F., He, K., Ma, Y., Yang, F., Yu, X., Cadle, S., Chan, T., and Mulawa, P. (2006), Concentration and chemical characteristics of PM<sub>2.5</sub> in Beijing, China: 2001–2002, *Science of The Total Environment*, 355(1), 264-275.
- Eck, T., Holben, B., Reid, J., Dubovik, O., Smirnov, A., O'Neill, N., Slutsker, I., and Kinne, S. (1999), Wavelength dependence of the optical depth of biomass burning, urban, and desert dust aerosols, *Journal of Geophysical Research: Atmospheres (1984–2012)*, 104(D24), 31333-31349.
- Eguchi, K., Uno, I., Yumimoto, K., Takemura, T., Shimizu, A., Sugimoto, N., and Liu, Z. (2009), Trans-pacific dust transport: integrated analysis of NASA/CALIPSO and a global aerosol transport model, *Atmospheric Chemistry and Physics*, 9(9), 3137-3145.
- Emmons, L., Walters, S., Hess, P., Lamarque, J.-F., Pfister, G., Fillmore, D., Granier, C., Guenther, A., Kinnison, D., and Laepple, T. (2010), Description and evaluation of the Model for Ozone and Related chemical Tracers, version 4 (MOZART-4), *Geoscientific Model Development*, 3(1), 43-67.
- Engel-Cox, J. A., Hoff, R. M., and Haymet, A. (2004), Recommendations on the use of satellite remote-sensing data for urban air quality, *Journal of the Air & Waste Management Association*, 54(11), 1360-1371.
- Fang, M., Chan, C. K., and Yao, X. (2009), Managing air quality in a rapidly developing nation: China, *Atmospheric Environment*, 43(1), 79-86.
- Fécan, F., Marticorena, B., and Bergametti, G. (1998), Parametrization of the increase of the aeolian erosion threshold wind friction velocity due to soil moisture for arid and semi-arid areas, *Annales Geophysicae*, 17, 149-157, Springer.
- Fenger, J. (1999), Urban air quality, *Atmospheric Environment*, 33(29), 4877-4900.
- Filip, L., and Stefan, S. (2011), Study of the correlation between the near-ground PM<sub>10</sub> mass concentration and the aerosol optical depth, *Journal of Atmospheric and Solar-Terrestrial Physics*, 73(13), 1883-1889.
- Fu, J. S., Streets, D. G., Jang, C. J., Kebin He, J. H., He, K., Wang, L., and Zhang, Q. (2009), Modeling regional/urban ozone and particulate matter in Beijing, China, *Journal of the Air & Waste Management Association*, 59(1), 37-44.
- Fu, X., Wang, S., Cheng, Z., Xing, J., Zhao, B., Wang, J., and Hao, J. (2013), Source, transport and impacts of a heavy dust event in the Yangtze River Delta, China in 2011, *Atmospheric Chemistry and Physics Discussions*, 13(8), 21507-21540.
- Gao, Y., Liu, X., Zhao, C., and Zhang, M. (2011), Emission controls versus meteorological conditions in determining aerosol concentrations in Beijing during the 2008 Olympic Games, *Atmospheric Chemistry and Physics*, 11(23), 12437-12451.
- Ge, C., Zhang, M., Han, Z., and Liu, Y. (2011), Episode simulation of Asian dust storms with an air quality modeling system, *Advances in Atmospheric Sciences*, 28, 511-520.
- Ginoux, P., Chin, M., Tegen, I., Prospero, J. M., Holben, B., Dubovik, O., and Lin, S.-J. (2001), Sources and distributions of dust aerosols modelled with the GOCART model, *Journal of Geophysical Research: Atmospheres*, 106(D17), 20255-20273.
- Gomes, L., Rajot, J. L., Alfaro, S. C., and Gaudichet, A. (2003), Validation of a dust production model from measurements performed in semi-arid agricultural areas of Spain and Niger, *CATENA*, 52(3–4), 257-271.
- Gong, S., Zhang, X., Zhao, T., McKendry, I., Jaffe, D., and Lu, N. (2003), Characterization of soil dust aerosol in China and its transport and distribution during 2001 ACE-Asia: 2. Model simulation and validation, *Journal of Geophysical Research: Atmospheres (1984–2012)*, 108(D9), 2156-2202.

- Gong, S., and Zhang, X. (2008), CUACE/Dust—an integrated system of observation and modeling systems for operational dust forecasting in Asia, *Atmospheric Chemistry and Physics*, 8(9), 2333-2340.
- Grenier, P., Blanchet, J. P., and Muñoz-Alpizar, R. (2009), Study of polar thin ice clouds and aerosols seen by CloudSat and CALIPSO during midwinter 2007, *Journal of Geophysical Research: Atmospheres* (1984–2012), 114(D9).
- Guinot, B., Cachier, H., Sciare, J., Tong, Y., Xin, W., and Jianhua, Y. (2007), Beijing aerosol: Atmospheric interactions and new trends, *Journal of Geophysical Research: Atmospheres*, 112(D14), D14314.
- Guo, J.-P., Zhang, X.-Y., Che, H.-Z., Gong, S.-L., An, X., Cao, C.-X., Guang, J., Zhang, H., Wang, Y.-Q., and Zhang, X.-C. (2009a), Correlation between PM concentrations and aerosol optical depth in eastern China, *Atmospheric Environment*, 43(37), 5876-5886.
- Guo, S., Hu, M., Guo, Q., Zhang, X., Schauer, J., and Zhang, R. (2013), Quantitative evaluation of emission controls on primary and secondary organic aerosol sources during Beijing 2008 Olympics, *Atmospheric Chemistry and Physics*, 13(16), 8303-8314.
- Guo, Y., Jia, Y., Pan, X., Liu, L., and Wichmann, H. (2009b), The association between fine particulate air pollution and hospital emergency room visits for cardiovascular diseases in Beijing, China, *Science of The Total Environment*, 407(17), 4826-4830.
- Guo, Y., Tong, S., Zhang, Y., Barnett, A. G., Jia, Y., and Pan, X. (2010), The relationship between particulate air pollution and emergency hospital visits for hypertension in Beijing, China, *Science of The Total Environment*, 408(20), 4446-4450.
- Gupta, P., and Christopher, S. A. (2008), An evaluation of Terra-MODIS sampling for monthly and annual particulate matter air quality assessment over the Southeastern United States, *Atmospheric Environment*, 42(26), 6465-6471.
- Gurjar, B., Butler, T., Lawrence, M., and Lelieveld, J. (2008), Evaluation of emissions and air quality in megacities, *Atmospheric Environment*, 42(7), 1593-1606.
- Han, L., Zhuang, G., Cheng, S., and Li, J. (2007), The mineral aerosol and its impact on urban pollution aerosols over Beijing, China, *Atmospheric Environment*, 41(35), 7533-7546.
- Han, X., Ge, C., Tao, J., Zhang, M., and Zhang, R. (2012a), Air quality modeling for a strong dust event in East Asia in March 2010, *Aerosol and Air Quality Research*, 12(4), 615-628.
- Han, Z., Li, J., Xia, X., and Zhang, R. (2012b), Investigation of direct radiative effects of aerosols in dust storm season over East Asia with an online coupled regional climate-chemistry-aerosol model, *Atmospheric Environment*, 54(0), 688-699.
- Hao, J., Tian, H., and Lu, Y. (2002), Emission inventories of NO<sub>x</sub> from commercial energy consumption in China, 1995-1998, *Environmental science & technology*, 36(4), 552-560.
- He, K., Yang, F., Ma, Y., Zhang, Q., Yao, X., Chan, C. K., Cadle, S., Chan, T., and Mulawa, P. (2001), The characteristics of PM<sub>2.5</sub> in Beijing, China, *Atmospheric Environment*, 35(29), 4959-4970.
- Hsu, N. C., Tsay, S.-C., King, M. D., and Herman, J. R. (2004), Aerosol properties over bright-reflecting source regions, *IEEE Transactions on Geoscience and Remote Sensing*, 42(3), 557-569.
- Hsu, N. C., Tsay, S.-C., King, M. D., and Herman, J. R. (2006), Deep blue retrievals of Asian aerosol properties during ACE-Asia, *IEEE Transactions on Geoscience and Remote Sensing*, 44(11), 3180-3195.
- Huang, J., Minnis, P., Yi, Y., Tang, Q., Wang, X., Hu, Y., Liu, Z., Ayers, K., Trepte, C., and Winker, D. (2007), Summer dust aerosols detected from CALIPSO over the Tibetan Plateau, *Geophysical Research Letters*, 34(18).
- Huang, X.-X., Wang, T.-J., Jiang, F., Liao, J.-B., Cai, Y.-F., Yin, C.-Q., Zhu, J.-L., and Han, Y. (2013), Studies on a Severe Dust Storm in East Asia and Its Impact on the Air Quality of Nanjing, China, *Aerosol and Air Quality Research*, 13(1), 179-193.

- Huneus, N., Schulz, M., Balkanski, Y., Griesfeller, J., Kinne, S., Prospero, J., Bauer, S., Boucher, O., Chin, M., and Dentener, F. (2010), Global dust model intercomparison in AeroCom phase I, *Atmospheric Chemistry and Physics Discussions*, 10(10), 23781-23864.
- Husar, R. B., Prospero, J. M., and Stowe, L. L. (1997), Characterization of tropospheric aerosols over the oceans with the NOAA advanced very high resolution radiometer optical thickness operational product, *Journal of Geophysical Research: Atmospheres (1984–2012)*, 102(D14), 16889-16816,16909.
- Husar, R. B., et al. (2001), Asian dust events of April 1998, *Journal of Geophysical Research: Atmospheres (1984–2012)*, 106(D16), 18317-18330.
- Ichoku, C., Chu, D. A., Mattoo, S., Kaufman, Y. J., Remer, L. A., Tanré, D., Slutsker, I., and Holben, B. N. (2002), A spatio-temporal approach for global validation and analysis of MODIS aerosol products, *Geophysical Research Letters*, 29(12), MOD1-1-MOD1-4.
- Jiang, F., Liu, Q., Huang, X., Wang, T., Zhuang, B., and Xie, M. (2012), Regional modeling of secondary organic aerosol over China using WRF/Chem, *Journal of Aerosol Science*, 43(1), 57-73.
- Jugder, D., Shinoda, M., Sugimoto, N., Matsui, I., Nishikawa, M., Park, S.-U., Chun, Y.-S., and Park, M.-S. (2011), Spatial and temporal variations of dust concentrations in the Gobi Desert of Mongolia, *Global and Planetary Change*, 78(1), 14-22.
- Kaskaoutis, D., and Kambezidis, H. (2006), Investigation into the wavelength dependence of the aerosol optical depth in the Athens area, *Quarterly Journal of the Royal Meteorological Society*, 132(620), 2217-2234.
- Kaufman, Y. J., Tanré, D., and Boucher, O. (2002), A satellite view of aerosols in the climate system, *Nature*, 419(6903), 215-223.
- Kim, J. (2008), Transport routes and source regions of Asian dust observed in Korea during the past 40 years (1965–2004), *Atmospheric Environment*, 42(19), 4778-4789.
- Klimont, Z., Cofala, J., Xing, J., Wei, W., Zhang, C., Wang, S., Kejun, J., Bhandari, P., Mathur, R., and Purohit, P. (2009), Projections of SO<sub>2</sub>, NO<sub>x</sub> and carbonaceous aerosols emissions in Asia, *Tellus B*, 61(4), 602-617.
- Knippertz, P., and Todd, M. C. (2012), Mineral dust aerosols over the Sahara: Meteorological controls on emission and transport and implications for modeling, *Reviews of Geophysics*, 50(1).
- Knote, C., Brunner, D., Vogel, H., Allan, J., Asmi, A., Äijälä, M., Carbone, S., Gon, H., Jimenez, J., and Kiendler-Scharr, A. (2011), Towards an online-coupled chemistry-climate model: evaluation of trace gases and aerosols in COSMO-ART, *Geoscientific Model Development*, 4(4), 1077-1102.
- Laurent, B., Marticorena, B., Bergametti, G., Chazette, P., Maignan, F., and Schmechtig, C. (2005), Simulation of the mineral dust emission frequencies from desert areas of China and Mongolia using an aerodynamic roughness length map derived from the POLDER/ADEOS 1 surface products, *Journal of Geophysical Research: Atmospheres (1984–2012)*, 110(D18), 2156-2202.
- Laurent, B., Marticorena, B., Bergametti, G., and Mei, F. (2006), Modeling mineral dust emissions from Chinese and Mongolian deserts, *Global and Planetary Change*, 52(1–4), 121-141.
- Lee, E.-H., Munkhtsetseg, E., Kim, S.-B., Ha, J.-C., Lee, S.-S., and Chun, Y. (2013), Numerical simulation and evaluation of Asian dust events observed in Mongolia in spring 2011, *Asia-Pacific Journal of Atmospheric Sciences*, 49(1), 111-120.
- Li, C., Hsu, N. C., and Tsay, S.-C. (2011), A study on the potential applications of satellite data in air quality monitoring and forecasting, *Atmospheric Environment*, 45(22), 3663-3675.
- Li, X., Wang, L., Wang, Y., Wen, T., Yang, Y., Zhao, Y., and Wang, Y. (2012), Chemical composition and size distribution of airborne particulate matters in Beijing during the 2008 Olympics, *Atmospheric Environment*, 50, 278-286.

- Li, X., He, K., Li, C., Yang, F., Zhao, Q., Ma, Y., Cheng, Y., Ouyang, W., and Chen, G. (2013), PM<sub>2.5</sub> mass, chemical composition, and light extinction before and during the 2008 Beijing Olympics, *Journal of Geophysical Research: Atmospheres*, 118(21), 12,158-112,167.
- Li, Z., Xia, X., Cribb, M., Mi, W., Holben, B., Wang, P., Chen, H., Tsay, S. C., Eck, T., and Zhao, F. (2007), Aerosol optical properties and their radiative effects in northern China, *Journal of Geophysical Research: Atmospheres (1984–2012)*, 112(D22).
- Liu, L., et al. (2013), Size-fractionated particulate air pollution and cardiovascular emergency room visits in Beijing, China, *Environmental Research* 121, 52-63.
- Liu, Y., Paciorek, C. J., and Koutrakis, P. (2009), Estimating regional spatial and temporal variability of PM<sub>2.5</sub> concentrations using satellite data, meteorology, and land use information, *Environmental Health Perspectives.*, 117(6), 886.
- Liu, Y., He, K., Li, S., Wang, Z., Christiani, D. C., and Koutrakis, P. (2012), A statistical model to evaluate the effectiveness of PM<sub>2.5</sub> emissions control during the Beijing 2008 Olympic Games, *Environment international*, 44, 100-105.
- Lundgren, K. (2010), *Direct radiative effects of sea salt on the regional scale*, KIT Scientific Publishing.
- Luo, C., Mahowald, N. M., and Del Corral, J. (2003), Sensitivity study of meteorological parameters on mineral aerosol mobilization, transport, and distribution, *Journal of Geophysical Research: Atmospheres (1984–2012)*, 108(D15).
- Marticorena, B., Bergametti, G., Aumont, B., Callot, Y., N'Doumé, C., and Legrand, M. (1997), Modeling the atmospheric dust cycle 2. Simulation of Saharan dust sources, *Journal of Geophysical Research: Atmospheres (1984–2012)*, 102(D4), 4387-4404.
- Martonchik, J., Diner, D., Kahn, R., Gaitley, B., and Holben, B. (2004), Comparison of MISR and AERONET aerosol optical depths over desert sites, *Geophysical Research Letters*, 31(16).
- Matsui, H., Koike, M., Kondo, Y., Takegawa, N., Kita, K., Miyazaki, Y., Hu, M., Chang, S. Y., Blake, D., and Fast, J. D. (2009), Spatial and temporal variations of aerosols around Beijing in summer 2006: Model evaluation and source apportionment, *Journal of Geophysical Research: Atmospheres (1984–2012)*, 114(D2).
- McKendry, I., Hacker, J., Stull, R., Sakiyama, S., Mignacca, D., and Reid, K. (2001), Long-range transport of Asian dust to the Lower Fraser Valley, British Columbia, Canada, *Journal of Geophysical Research: Atmospheres (1984–2012)*, 106(D16), 18361-18370.
- Mei, F., Zhang, X., Lu, H., Shen, Z., and Wang, Y. (2004), Characterization of MASDs of surface soils in north China and its influence on estimating dust emission, *Chinese Science Bulletin*, 49(20), 2169-2176.
- Mijling, B. (2009), Reductions of NO<sub>2</sub> detected from space during the 2008 Beijing Olympic Games, *Geophysical Research Letters*, 36(13), L13801.
- NBSC(2011), Communiqué of the National Bureau of Statistics of People's Republic of China on Major Figures of the 2010 Population Census (No. 2), Communiqué, National Bureau of Statistics of People's Republic of China.
- Nickovic, S., Kallos, G., Papadopoulos, A., and Kakaliagou, O. (2001), A model for prediction of desert dust cycle in the atmosphere, *Journal of Geophysical Research: Atmospheres (1984–2012)*, 106(D16), 18113-18118,18129.
- Norra, S., Schleicher, N., Stüben, D., Chai, F., Chen, Y., and Wang, S. (2010), Assessment of aerosol concentration sampled at five sites in Beijing from 2005 till 2007, in *Highway and Urban Environment*, edited, pp. 133-140, Springer.
- Odum, J. R., Hoffmann, T., Bowman, F., Collins, D., Flagan, R. C., and Seinfeld, J. H. (1996), Gas/particle partitioning and secondary organic aerosol yields, *Environmental science & technology*, 30(8), 2580-2585.

- Ohara, T., Akimoto, H., Kurokawa, J.-i., Horii, N., Yamaji, K., Yan, X., and Hayasaka, T. (2007), An Asian emission inventory of anthropogenic emission sources for the period 1980–2020, *Atmospheric Chemistry and Physics*, 7(16), 4419-4444.
- Omar, A. H., Winker, D. M., Tackett, J. L., Giles, D. M., Kar, J., Liu, Z., Vaughan, M. A., Powell, K. A., and Trepte, C. R. (2013), CALIOP and AERONET aerosol optical depth comparisons: One size fits none, *Journal of Geophysical Research: Atmospheres*, 118(10), 4748-4766.
- Park, S.-U., and Lee, E.-H. (2004), Parameterization of Asian dust (Hwangsa) particle-size distributions for use in dust emission models, *Atmospheric Environment*, 38(14), 2155-2162.
- Park, Y.-K., and Park, S. H. (2013), Estimation of Threshold Friction Velocity Using a Physical Parameterization Over the Asian Dust Source Region, *Particulate Science and Technology*, 31(2), 119-127.
- Pasqui, M., Taramelli, A., Barbour, J., Kirschbaum, D., Bottai, L., Busillo, C., Calastrini, F., Gualtieri, G., Guarnieri, F., and Small, C. (2013), Dust emission in northern China: atmospheric emission–dispersion modelling of a major dust event, *Earth Surface Processes and Landforms*, 38(12), 1354-1368.
- Penner, J. E., Hegg, D., and Leaitch, R. (2001), Peer Reviewed: Unraveling the role of aerosols in climate change, *Environmental science & technology*, 35(15), 332A-340A.
- Pope, C. A. (2000), Epidemiology of fine particulate air pollution and human health: biologic mechanisms and who's at risk?, *Environmental Health Perspectives*, 108(Suppl 4), 713.
- Pope, C. A., Ezzati, M., and Dockery, D. W. (2009), Fine-particulate air pollution and life expectancy in the United States, *New England Journal of Medicine*, 360(4), 376-386.
- Prospero, J. M. (1999), Long-range transport of mineral dust in the global atmosphere: Impact of African dust on the environment of the southeastern United States, *Proceedings of the National Academy of Sciences*, 96(7), 3396-3403.
- Qian, Y., Ruby Leung, L., Ghan, S. J., and Giorgi, F. (2003), Regional climate effects of aerosols over China: modeling and observation, *Tellus B*, 55(4), 914-934.
- Qu, W., Arimoto, R., Zhang, X., Zhao, C., Wang, Y., Sheng, L., and Fu, G. (2010), Spatial distribution and interannual variation of surface PM<sub>10</sub> concentrations over eighty-six Chinese cities, *Atmospheric Chemistry and Physics*, 10(12), 5641-5662.
- Remer, L. A., Kaufman, Y., Tanré, D., Mattoo, S., Chu, D., Martins, J., Li, R.-R., Ichoku, C., Levy, R., and Kleidman, R. (2005), The MODIS aerosol algorithm, products, and validation, *Journal of the Atmospheric Sciences*, 62(4), 947-973.
- Riemer, N., Vogel, H., Vogel, B., and Fiedler, F. (2003), Modeling aerosols on the mesoscale-y: Treatment of soot aerosol and its radiative effects, *Journal of Geophysical Research: Atmospheres (1984–2012)*, 108(D19), 4601.
- Rinke, R. (2008), Parametrisierung des Auswaschens von Aerosolpartikeln durch Niederschlag, Karlsruhe, Univ., Diss., 2008.
- Ritter, B., and Geleyn, J.-F. (1992), A comprehensive radiation scheme for numerical weather prediction models with potential applications in climate simulations, *Monthly Weather Review*, 120(2), 303-325.
- Schäfer, K., Emeis, S., Jahn, C., Münkel, C., Suppan, P., and Tuma, M. (2012a), Results from long-term detection of mixing layer height: ceilometer and comparison with Radio-Acoustic Sounding System, *SPIE Remote Sensing*, 853408, 1, International Society for Optics and Photonics.
- Schäfer, K., Wagner, P., Emeis, S., Jahn, C., Muenkel, C., and Suppan, P. (2012b), Mixing layer height and air pollution levels in urban area, *SPIE Remote Sensing*, 853409, 1, International Society for Optics and Photonics.

- Schleicher, N., Norra, S., Chai, F., Chen, Y., Wang, S., and Stüben, D. (2010a), Seasonal trend of water-soluble ions at one TSP and five PM<sub>2.5</sub> sampling sites in Beijing, China, in *Highway and Urban Environment*, edited, pp. 87-95, Springer.
- Schleicher, N., Norra, S., Chai, F., Chen, Y., Wang, S., and Stüben, D. (2010b), Anthropogenic versus geogenic contribution to total suspended atmospheric particulate matter and its variations during a two-year sampling period in Beijing, China, *Journal of Environmental Monitoring*, 12(2), 434-441.
- Schleicher, N., Norra, S., Dietze, V., Yu, Y., Fricker, M., Kaminski, U., Chen, Y., and Cen, K. (2011a), The effect of mitigation measures on size distributed mass concentrations of atmospheric particles and black carbon concentrations during the Olympic Summer Games 2008 in Beijing, *Science of The Total Environment*, 412, 185-193.
- Schleicher, N., Norra, S., Chen, Y., Chai, F., and Wang, S. (2012), Efficiency of mitigation measures to reduce particulate air pollution—A case study during the Olympic Summer Games 2008 in Beijing, China, *Science of The Total Environment*, 427–428(0), 146-158.
- Schleicher, N. J., Norra, S., Chai, F., Chen, Y., Wang, S., Cen, K., Yu, Y., and Stüben, D. (2011b), Temporal variability of trace metal mobility of urban particulate matter from Beijing—A contribution to health impact assessments of aerosols, *Atmospheric Environment*, 45(39), 7248-7265.
- Seinfeld, J. H., Carmichael, G. R., Arimoto, R., Conant, W. C., Brechtel, F. J., Bates, T. S., Cahill, T. A., Clarke, A. D., Doherty, S. J., and Flatau, P. J. (2004), ACE-ASIA-Regional climatic and atmospheric chemical effects of Asian dust and pollution, *Bulletin of the American Meteorological Society*, 85(3), 367-380.
- Senlin, L., Zhenkun, Y., Xiaohui, C., Minghong, W., Guoying, S., Jiamo, F., and Paul, D. (2008), The relationship between physicochemical characterization and the potential toxicity of fine particulates (PM<sub>2.5</sub>) in Shanghai atmosphere, *Atmospheric Environment*, 42(31), 7205-7214.
- Shao, Y., and Lu, H. (2000), A simple expression for wind erosion threshold friction velocity, *Journal of Geophysical Research: Atmospheres (1984–2012)*, 105(D17), 22437-22443.
- Shao, Y. (2004), Simplification of a dust emission scheme and comparison with data, *Journal of Geophysical Research: Atmospheres (1984–2012)*, 109(D10).
- Shao, Y., and Dong, C. (2006), A review on East Asian dust storm climate, modelling and monitoring, *Global and Planetary Change*, 52(1), 1-22.
- Sibson, R. (1981), Interpreting multivariate data, *A Brief Description of Natural Neighbor Interpolation*, Wiley, New York, 21-36.
- Singh, H., Brune, W., Crawford, J., Flocke, F., and Jacob, D. (2009), Chemistry and transport of pollution over the Gulf of Mexico and the Pacific: spring 2006 INTEX-B campaign overview and first results, *Atmospheric Chemistry and Physics*, 9(7), 2301-2318.
- Slinn, S., and Slinn, W. (1980), Predictions for particle deposition on natural waters, *Atmospheric Environment (1967)*, 14(9), 1013-1016.
- Solomon, S. (2007), *Climate change 2007-the physical science basis: Working group I contribution to the fourth assessment report of the IPCC*, Cambridge University Press.
- Song, Y., Zhang, M., and Cai, X. (2006), PM<sub>10</sub> modeling of Beijing in the winter, *Atmospheric Environment*, 40(22), 4126-4136.
- Song, Z., Wang, J., and Wang, S. (2007), Quantitative classification of northeast Asian dust events, *Journal of Geophysical Research: Atmospheres (1984–2012)*, 112(D4), D04211.
- Stanelle, T., Vogel, B., Vogel, H., Bäumer, D., and Kottmeier, C. (2010), Feedback between dust particles and atmospheric processes over West Africa during dust episodes in March 2006 and June 2007, *Atmospheric Chemistry and Physics*, 10(22), 10771-10788.
- Streets, D., and Waldhoff, S. (2000), Present and future emissions of air pollutants in China: SO<sub>2</sub>, NO<sub>x</sub>, and CO, *Atmospheric Environment*, 34(3), 363-374.

- Streets, D. G., et al. (2007), Air quality during the 2008 Beijing Olympic Games, *Atmospheric Environment*, 41(3), 480-492.
- Su, J., Shao, M., Lu, S., and Xie, Y. (2011), Non-methane volatile organic compound emission inventories in Beijing during Olympic Games 2008, *Atmospheric Environment*, 45(39), 7046-7052.
- Su, L., and Toon, O. (2011), Saharan and Asian dust: similarities and differences determined by CALIPSO, AERONET, and a coupled climate-aerosol microphysical model, *Atmospheric Chemistry and Physics*, 11(7), 3263-3280.
- Sugimoto, N., Hara, Y., Shimizu, A., Nishizawa, T., Matsui, I., and Nishikawa, M. (2013), Analysis of dust events in 2008 and 2009 using the lidar network, surface observations and the CFORS model, *Asia-Pacific Journal of Atmospheric Sciences*, 49(1), 27-39.
- Sun, J., Zhang, M., and Liu, T. (2001), Spatial and temporal characteristics of dust storms in China and its surrounding regions, 1960–1999: Relations to source area and climate, *Journal of Geophysical Research: Atmospheres (1984–2012)*, 106(D10), 10325-10310,10333.
- Sun, Y., Zhuang, G., Wang, Y., Han, L., Guo, J., Dan, M., Zhang, W., Wang, Z., and Hao, Z. (2004), The airborne particulate pollution in Beijing—concentration, composition, distribution and sources, *Atmospheric Environment*, 38(35), 5991-6004.
- Sun, Y., Wang, L., Wang, Y., Quan, L., and Zirui, L. (2011), In situ measurements of SO<sub>2</sub>, NO<sub>x</sub>, NO<sub>y</sub>, and O<sub>3</sub> in Beijing, China during August 2008, *Science of The Total Environment*, 409(5), 933-940.
- Tanaka, T. Y., and Chiba, M. (2006), A numerical study of the contributions of dust source regions to the global dust budget, *Global and Planetary Change*, 52(1), 88-104.
- Tang, G. (2010), Modelling of ozone spatial-temporal distribution in the vicinity of Beijing during Olympics, PhD. thesis, 153 pp, Chinese Academy of Sciences.
- Taramelli, A., Pasqui, M., Barbour, J., Kirschbaum, D., Bottai, L., Busillo, C., Calastrini, F., Guarnieri, F., and Small, C. (2013), Spatial and temporal dust source variability in northern China identified using advanced remote sensing analysis, *Earth Surface Processes and Landforms*, 38(8), 793-809.
- Tegen, I., and Fung, I. (1994), Modeling of mineral dust in the atmosphere: Sources, transport, and optical thickness, *Journal of Geophysical Research: Atmospheres (1984–2012)*, 99(D11), 22897-22914.
- Tegen, I., and Fung, I. (1995), Contribution to the atmospheric mineral aerosol load from land surface modification, *Journal of Geophysical Research: Atmospheres (1984–2012)*, 100(D9), 18707-18718,18726.
- Tegen, I., Schepanski, K., and Heinold, B. (2013), Comparing two years of Saharan dust source activation obtained by regional modelling and satellite observations, *Atmospheric Chemistry and Physics*, 13(5), 2381-2390.
- Torres, O., Tanskanen, A., Veihelmann, B., Ahn, C., Braak, R., Bhartia, P. K., Veefkind, P., and Levelt, P. (2007), Aerosols and surface UV products from Ozone Monitoring Instrument observations: An overview, *Journal of Geophysical Research: Atmospheres (1984–2012)*, 112(D24).
- Uno, I., Carmichael, G., Streets, D., Tang, Y., Yienger, J., Satake, S., Wang, Z., Woo, J. H., Guttikunda, S., and Uematsu, M. (2003), Regional chemical weather forecasting system CFORS: Model descriptions and analysis of surface observations at Japanese island stations during the ACE-Asia experiment, *Journal of Geophysical Research: Atmospheres (1984–2012)*, 108(D23).
- Uno, I., Satake, S., Carmichael, G. R., Tang, Y., Wang, Z., Takemura, T., Sugimoto, N., Shimizu, A., Murayama, T., and Cahill, T. A. (2004), Numerical study of Asian dust transport during the springtime of 2001 modelled with the Chemical Weather Forecasting System (CFORS) model, *Journal of Geophysical Research: Atmospheres (1984–2012)*, 109(D19).
- Uno, I., Wang, Z., Chiba, M., Chun, Y., Gong, S., Hara, Y., Jung, E., Lee, S. S., Liu, M., and Mikami, M. (2006), Dust model intercomparison (DMIP) study over Asia: Overview, *Journal of Geophysical Research: Atmospheres (1984–2012)*, 111(D12).

- Uno, I., Yumimoto, K., Shimizu, A., Hara, Y., Sugimoto, N., Wang, Z., Liu, Z., and Winker, D. (2008), 3D structure of Asian dust transport revealed by CALIPSO lidar and a 4DVAR dust model, *Geophysical Research Letters*, 35(6), L06803.
- van Donkelaar, A., Martin, R. V., Brauer, M., Kahn, R., Levy, R., Verduzco, C., and Villeneuve, P. J. (2010), Global estimates of ambient fine particulate matter concentrations from satellite-based aerosol optical depth: development and application, *Environmental health perspectives*, 118(6), 847.
- Vogel, B., Hoose, C., Vogel, H., and Kottmeier, C. (2006), A model of dust transport applied to the Dead Sea area, *Meteorologische Zeitschrift*, 15(6), 611-624.
- Vogel, B., Vogel, H., Baumer, D., Bangert, M., Lundgren, K., Rinke, R., and Stanelle, T. (2009), The comprehensive model system COSMO-ART - Radiative impact of aerosol on the state of the atmosphere on the regional scale, *Atmospheric Chemistry and Physics*, 9(22), 8661-8680.
- Wang, F., Chen, D., Cheng, S., Li, J., Li, M., and Ren, Z. (2010a), Identification of regional atmospheric PM<sub>10</sub> transport pathways using HYSPLIT, MM5-CMAQ and synoptic pressure pattern analysis, *Environmental Modelling & Software*, 25(8), 927-934.
- Wang, L., Hao, J., He, K., Wang, S., Li, J., Zhang, Q., Streets, D. G., Fu, J. S., Jang, C. J., and Takekawa, H. (2008a), A modeling study of coarse particulate matter pollution in Beijing: regional source contributions and control implications for the 2008 Summer Olympics, *Journal of the Air & Waste Management Association*, 58(8), 1057-1069.
- Wang, S.-H., et al. (2011), First detailed observations of long-range transported dust over the northern South China Sea, *Atmospheric Environment*, 45(27), 4804-4808.
- Wang, S., Yuan, W., and Shang, K. (2006), The impacts of different kinds of dust events on PM<sub>10</sub> pollution in northern China, *Atmospheric Environment*, 40(40), 7975-7982.
- Wang, S., Zhao, M., Xing, J., Wu, Y., Zhou, Y., Lei, Y., He, K., Fu, L., and Hao, J. (2010b), Quantifying the air pollutants emission reduction during the 2008 Olympic games in Beijing, *Environmental science & technology*, 44(7), 2490-2496.
- Wang, T., Nie, W., Gao, J., Xue, L., Gao, X., Wang, X., Qiu, J., Poon, C., Meinardi, S., and Blake, D. (2010c), Air quality during the 2008 Beijing Olympics: secondary pollutants and regional impact, *Atmospheric Chemistry and Physics*, 10(16), 7603-7615.
- Wang, W., Primbs, T., Tao, S., and Simonich, S. L. M. (2009a), Atmospheric particulate matter pollution during the 2008 Beijing Olympics, *Environmental science & technology*, 43(14), 5314-5320.
- Wang, W., Li, L., Pan, B., Chen, S., Wang, R., Li, J., and Zheng, H. (2013), Influence of DSSs on urban air quality in China during 2005–2010 and analysis of a severe DSS event, *Asia-Pacific Journal of Atmospheric Sciences*, 49(1), 67-71.
- Wang, X., Xia, D., Wang, T., Xue, X., and Li, J. (2008b), Dust sources in arid and semiarid China and southern Mongolia: Impacts of geomorphological setting and surface materials, *Geomorphology*, 97(3–4), 583-600.
- Wang, Y., Hao, J., McElroy, M. B., Munger, J. W., Ma, H., Chen, D., and Nielsen, C. (2009b), Ozone air quality during the 2008 Beijing Olympics: effectiveness of emission restrictions, *Atmospheric Chemistry and Physics*, 9, 5237-5251.
- Weingartner, E., Burtscher, H., and Baltensperger, U. (1997), Hygroscopic properties of carbon and diesel soot particles, *Atmospheric Environment*, 31(15), 2311-2327.
- Whitby, E. R., McMurry, P. H., Shankar, U., and Binkowski, F. S. (1991), Modal aerosol dynamics modeling, Report, Computer Sciences Corp., Research Triangle Park, NC (USA).
- White, B. R. (1979), Soil transport by winds on Mars, *Journal of Geophysical Research: Solid Earth (1978–2012)*, 84(B9), 4643-4651.

- WHO (2006), Air quality guidelines - Global update 2005. Particulate matter, ozone, nitrogen, dioxide and sulfur dioxide, Report, 484 pp.
- Wiegner, M., Emeis, S., Freudenthaler, V., Heese, B., Junkermann, W., Münkler, C., Schäfer, K., Seefeldner, M., and Vogt, S. (2006), Mixing layer height over Munich, Germany: Variability and comparisons of different methodologies, *Journal of Geophysical Research: Atmospheres* (1984–2012), 111(D13).
- Winker, D. M., Vaughan, M. A., Omar, A., Hu, Y., Powell, K. A., Liu, Z., Hunt, W. H., and Young, S. A. (2009), Overview of the CALIPSO mission and CALIOP data processing algorithms, *Journal of Atmospheric and Oceanic Technology*, 26(11), 2310-2323.
- Witte, J., Schoeberl, M., Douglass, A., Gleason, J., Krotkov, N., Gille, J., Pickering, K., and Livesey, N. (2009), Satellite observations of changes in air quality during the 2008 Beijing Olympics and Paralympics, *Geophysical Research Letters*, 36(17), L17803.
- Wong, M. S., Shahzad, M. I., Nichol, J. E., Lee, K. H., and Chan, P. (2013), Validation of MODIS, MISR, OMI, and CALIPSO aerosol optical thickness using ground-based sunphotometers in Hong Kong, *International Journal of Remote Sensing*, 34(3), 897-918.
- WPR(2013), Population of Beijing 2013, online article, World Population Review.
- Wu, Q., Wang, Z., Gbaguidi, A., Gao, C., Li, L., and Wang, W. (2011), A numerical study of contributions to air pollution in Beijing during CAREBeijing-2006, *Atmospheric Chemistry and Physics*, 11(12), 5997-6011.
- Xiao, N., Shi, T., Calder, C. A., Munroe, D. K., Berrett, C., Wolfenbarger, S., and Li, D. (2009), Spatial characteristics of the difference between MISR and MODIS aerosol optical depth retrievals over mainland Southeast Asia, *Remote Sensing of Environment*, 113(1), 1-9.
- Xin, J., Wang, Y., Wang, L., Tang, G., Sun, Y., Pan, Y., and Ji, D. (2012), Reductions of PM<sub>2.5</sub> in Beijing-Tianjin-Hebei urban agglomerations during the 2008 Olympic Games, *Advances in Atmospheric Sciences*, 29(6), 1330-1342.
- Xuan, J., and Sokolik, I. N. (2002), Characterization of sources and emission rates of mineral dust in Northern China, *Atmospheric Environment*, 36(31), 4863-4876.
- Xuan, J., Sokolik, I. N., Hao, J., Guo, F., Mao, H., and Yang, G. (2004), Identification and characterization of sources of atmospheric mineral dust in East Asia, *Atmospheric Environment*, 38(36), 6239-6252.
- Yang, G., Xiao, H., and Tuo, W. (2001), Black windstorm in northwest China: a case study of the strong sand-dust storm on May 5th 1993, *Global Alarm: Dust and Sandstorms from the World's Drylands*, United Nations, Bangkok, Thailand, 49-73.
- Young, S. A., and Vaughan, M. A. (2009), The retrieval of profiles of particulate extinction from Cloud-Aerosol Lidar Infrared Pathfinder Satellite Observations (CALIPSO) data: Algorithm description, *Journal of Atmospheric and Oceanic Technology*, 26(6), 1105-1119.
- Young, S. A., Vaughan, M. A., Kuehn, R. E., and Winker, D. M. (2013), The Retrieval of Profiles of Particulate Extinction from Cloud-Aerosol Lidar and Infrared Pathfinder Satellite Observations (CALIPSO) Data: Uncertainty and Error Sensitivity Analyses, *Journal of Atmospheric and Oceanic Technology*, 30(3), 395-428.
- Yu, H., Chin, M., Winker, D. M., Omar, A. H., Liu, Z., Kittaka, C., and Diehl, T. (2010), Global view of aerosol vertical distributions from CALIPSO lidar measurements and GOCART simulations: Regional and seasonal variations, *Journal of Geophysical Research: Atmospheres* (1984–2012), 115(D4).
- Yu, Y., Schleicher, N., Norra, S., Fricker, M., Dietze, V., Kaminski, U., Cen, K., and Stüben, D. (2011), Dynamics and origin of PM<sub>2.5</sub> during a three-year sampling period in Beijing, China, *Journal of Environmental Monitoring*, 13(2), 334-346.
- Zender, C. S., Bian, H., and Newman, D. (2003), Mineral Dust Entrainment and Deposition (DEAD) model: Description and 1990s dust climatology, *Journal of Geophysical Research: Atmospheres* (1984–2012), 108(D14), 4416.

- Zender, C. S., Miller, R., and Tegen, I. (2004), Quantifying mineral dust mass budgets: Terminology, constraints, and current estimates, *Eos-Transactions American Geophysical Union*, 85(48), 509-512.
- Zhang, J., Song, H., Tong, S., Li, L., Liu, B., and Wang, L. (2000), Ambient sulfate concentration and chronic disease mortality in Beijing, *Science of The Total Environment*, 262(1), 63-71.
- Zhang, L., Jacob, D. J., Boersma, K., Jaffe, D., Olson, J., Bowman, K., Worden, J., Thompson, A., Avery, M., and Cohen, R. (2008a), Transpacific transport of ozone pollution and the effect of recent Asian emission increases on air quality in North America: an integrated analysis using satellite, aircraft, ozonesonde, and surface observations, *Atmospheric Chemistry and Physics Discussions*, 8(2), 8143-8191.
- Zhang, M., Song, Y., Cai, X., and Zhou, J. (2008b), Economic assessment of the health effects related to particulate matter pollution in 111 Chinese cities by using economic burden of disease analysis, *Journal of Environmental Management*, 88(4), 947-954.
- Zhang, Q., Streets, D. G., Carmichael, G. R., He, K., Huo, H., Kannari, A., Klimont, Z., Park, I., Reddy, S., and Fu, J. (2009), Asian emissions in 2006 for the NASA INTEX-B mission, *Atmospheric Chemistry and Physics*, 9(14), 5131-5153.
- Zhang, Q., Zhang, J., and Xue, H. (2010), The challenge of improving visibility in Beijing, *Atmospheric Chemistry and Physics*, 10(16), 7821-7827.
- Zhang, X. Y., Gong, S. L., Shen, Z. X., Mei, F. M., Xi, X. X., Liu, L. C., Zhou, Z. J., Wang, D., Wang, Y. Q., and Cheng, Y. (2003a), Characterization of soil dust aerosol in China and its transport and distribution during 2001 ACE-Asia: 1. Network observations, *Journal of Geophysical Research: Atmospheres (1984–2012)*, 108(D9), 4261.
- Zhang, X. Y., Gong, S. L., Zhao, T. L., Arimoto, R., Wang, Y. Q., and Zhou, Z. J. (2003b), Sources of Asian dust and role of climate change versus desertification in Asian dust emission, *Geophysical Research Letters*, 30(24), 2272.
- Zhang, Y., Zhu, X., Slanina, S., Shao, M., Zeng, L., Hu, M., Bergin, M., and Salmon, L. (2004), Aerosol pollution in some Chinese cities (IUPAC Technical Report), *Pure and Applied Chemistry*, 76(6), 1227-1239.
- Zhang, Y., Guo, Y., Li, G., Zhou, J., Jin, X., Wang, W., and Pan, X. (2012), The spatial characteristics of ambient particulate matter and daily mortality in the urban area of Beijing, China, *Science of The Total Environment*, 435, 14-20.
- Zhao, C., and Wang, Y. (2009), Assimilated inversion of NO<sub>x</sub> emissions over east Asia using OMI NO<sub>2</sub> column measurements, *Geophysical Research Letters*, 36(6), L06805.
- Zhao, C., Wang, Y., and Zeng, T. (2009), East China plains: a “basin” of ozone pollution, *Environmental science & technology*, 43(6), 1911-1915.
- Zhao, X. (2012), Asian Dust Detection from the Satellite Observations of Moderate Resolution Imaging Spectroradiometer (MODIS), *Aerosol and Air Quality Research*, 12(6), 1073-1080.
- Zhao, Y., Nielsen, C., Lei, Y., McElroy, M., and Hao, J. (2011), Quantifying the uncertainties of a bottom-up emission inventory of anthropogenic atmospheric pollutants in China, *Atmospheric Chemistry and Physics*, 11(5), 2295-2308.
- Zhou, Y., Wu, Y., Yang, L., Fu, L., He, K., Wang, S., Hao, J., Chen, J., and Li, C. (2010), The impact of transportation control measures on emission reductions during the 2008 Olympic Games in Beijing, China, *Atmospheric Environment*, 44(3), 285-293.

## List of abbreviations

(Ordered in logical groups)

DWD	German Weather Service
NASA	National Aeronautics and Space Administration
CNAAQ5	Chinese National Ambient Air Quality Standard
WHO	World Health Organization
WMO	World Meteorological Organization
ECMWF	European Centre for Medium-Range Weather Forecasts
CAS	Chinese Academy of Sciences
IAP	Institute of Atmospheric Physics
AERONET	Aerosol Robotic Network
INTEX-B	Intercontinental Chemical Transport Experiment-Phase B
COSMO-ART	Consortium for Small Scale Modeling – Aerosols and Reactive Trace Gases
NCL	NCAR Command Language
BC	elemental carbon
OC	organic carbon
BC	black carbon
CO	carbon monoxide
O <sub>3</sub>	ozone
NO	nitrogen monoxide
NO <sub>2</sub>	nitrogen dioxide
NO <sub>x</sub>	nitrogen oxides
NO <sub>3</sub> <sup>-</sup>	nitrate
SO <sub>2</sub>	sulfur dioxide
SO <sub>4</sub> <sup>2-</sup>	sulfate
NH <sub>3</sub>	ammonia
NH <sub>4</sub> <sup>+</sup>	ammonium
VOC	volatile organic compounds
NMVOC	non-methane volatile organic compounds
SOA	secondary organic aerosols

PM <sub>10</sub>	particulate matter with an aerodynamic diameter smaller 10 µm
PM <sub>2.5</sub>	particulate matter with an aerodynamic diameter smaller 2.5 µm
TSP	total suspended particulates
CALIPSO	Cloud-Aerosol Lidar and Infrared Pathfinder Satellite Observations
CALIOP	Cloud-Aerosol Lidar with Orthogonal Polarization
OMI	Ozone Monitoring Instrument
MODIS	Moderate Resolution Imaging Spectroradiometer
MISR	Multi-angle Imaging Spectroradiometer
POLDER	Polarization and Directionality of the Earth's Reflectance
API	Air Pollution Index
UTC	Coordinated universal time
AOD	aerosol-optical thickness
TOA	top of atmosphere
CCN	cloud condensation nuclei
UV	ultraviolet
MLH	mixing layer height
PBL	planetary boundary layer

## Danksagung

Mein Dank geht an PD Dr. Stefan Norra für die Übernahme des Hauptreferats und für die wissenschaftliche Betreuung. Er stand auch in den sehr turbulenten Zeiten an KIT und IfGG stets hinter mir und meiner Arbeit und ermöglichte mir dadurch die erfolgreiche Durchführung meiner Promotion.

Ein ebenso großes Dankeschön geht an Prof. Dr. Klaus Schäfer, der mich nicht nur während meines ersten Jahres am IMK-IFU sehr gut betreut und unterstützt hat, sondern dies auch während der folgenden Jahre stets getan hat. Deine Unterstützung während meiner Diplomarbeit und Promotion waren nicht nur von unschätzbarem fachlichem sondern auch persönlichem Wert für mich.

Dr. Peter Suppan vom IMK-IFU danke ich für die Betreuung meiner Arbeit, den Aufbau der Chinesischen Kontakte und die Unterbringung am IMK-IFU.

Ich möchte mich außerdem ganz herzlich bei Dr. Bernhard Vogel und Heike Vogel vom IMK-TRO bedanken. Ohne eure Unterstützung bei der Arbeit mit COSMO-ART wäre diese Arbeit nicht möglich gewesen. Insbesondere dir, Heike, möchte ich danken, nicht nur für deine Hilfe in fachlichen und technischen Dingen, auch dafür immer ein offenes Ohr für mich gehabt zu haben. Euer positives Denken hat mich stets aufs Neue motiviert weiterzumachen und nicht aufzugeben.

Ein großer Dank geht auch an Prof. Dr. Irina Sokolik am Georgia Institute of Technology für die Aufnahme in ihre Arbeitsgruppe während meines 5 monatigen Forschungsaufenthaltes. Dein Fachwissen und deine Unterstützung waren für meine Arbeit und mich persönlich von unschätzbarem Wert.

Ein großer Dank geht außerdem an meine ehemaligen Bürokollegen in Garmisch-Partenkirchen, die mich während des ersten Jahres meiner Doktorarbeit begleitet haben. Ein weiteres Dankeschön geht an meine ‚Teilzeit‘ Kollegen am IMK-TRO, die stets ein offenes Ohr für meine Fragen zu den Mysterien des Programmierens hatten. Des Weiteren danke ich den Mitgliedern meiner Doktorandengruppe für die stets informativen und lustigen Mittwochstreffen. Einen ganz besonderen Dank möchte ich dabei meinen Bürokolleginnen Mira, Denise, Fabienne und Nina, sowie meinen Büro-Nachbarinnen Annette und Angela aussprechen. Eure Unterstützung, Motivation und die unglaublich positive Arbeitsatmosphäre haben mich stets motiviert. Ich danke euch auch für all die Gespräche, Stammtische und die zahlreichen sonstigen Aktivitäten die wir gemeinsam in den drei Jahren erlebt haben.

Zu guter Letzt möchte ich noch einen großen Dank an meine Eltern richten, die mich stets bei meinem Weg unterstützt haben. Und zu guter Letzt möchte ich Dominik danken. Ich denke nicht, dass ich hier in wenigen Worten ausdrücken kann, wie viel mir deine Unterstützung während der letzten 5 Jahre bedeutet und wie froh ich bin, dass du damals im Mai im Regen so viel Mut bewiesen hast.

## **Erklärung**

Hiermit erkläre ich, dass ich die vorliegende Arbeit selbstständig verfasst, keine anderen als die angegebenen Quellen und Hilfsmittel benutzt und alle wörtlichen und sinngemäßen Entlehnungen deutlich als solche gekennzeichnet habe. Des Weiteren wurden die Grundsätze des Karlsruher Instituts für Technologie (KIT) zur Sicherung guter wissenschaftlicher Praxis stets eingehalten.

Bonn, Mai 2014